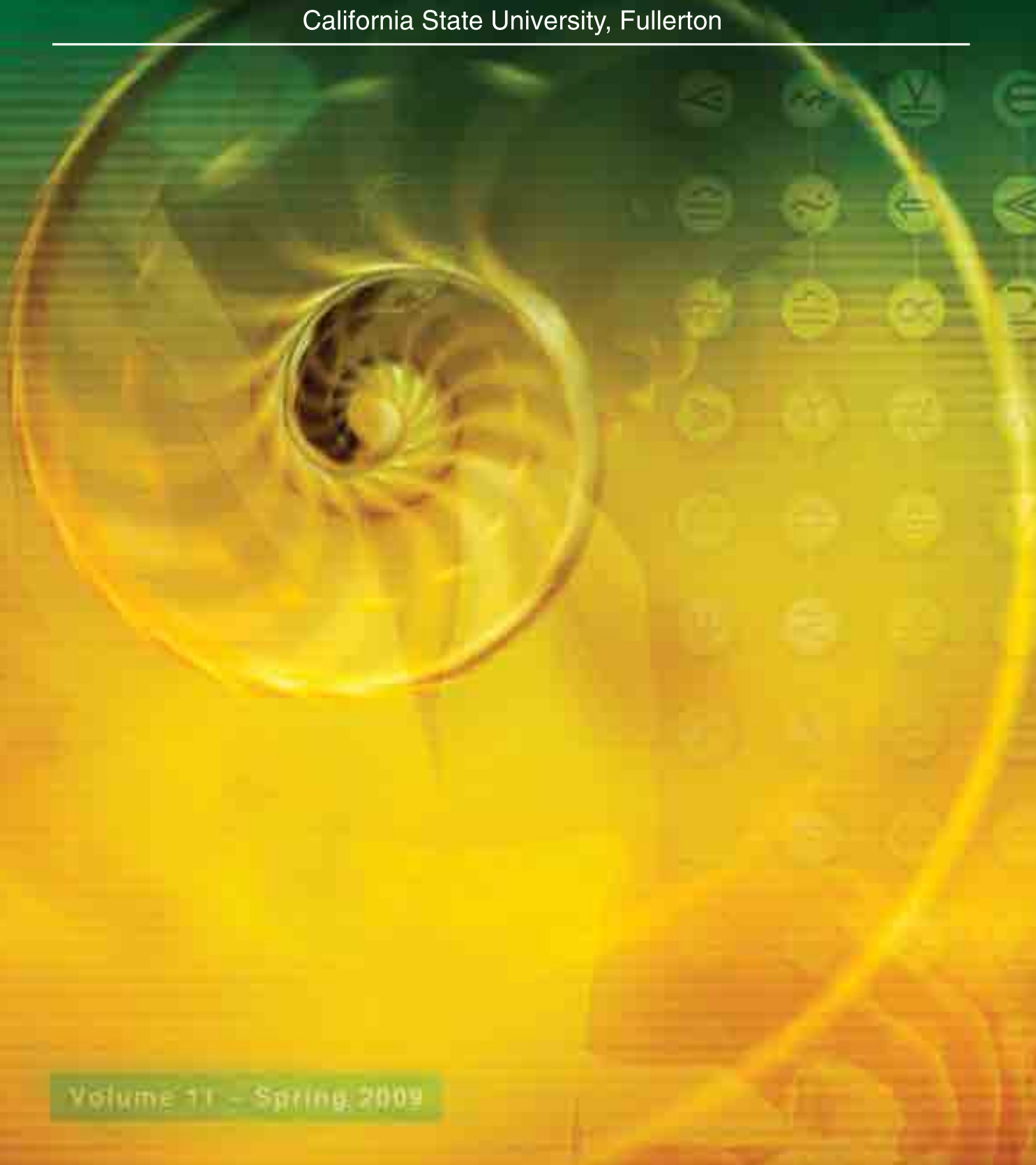




DIMENSIONS

The Journal of Undergraduate Research in Natural Sciences and Mathematics

California State University, Fullerton



Volume 11 – Spring, 2009

11TH EDITION

[ur] DIMENSIONS

The Journal of Undergraduate Research in Natural Sciences and Mathematics

California State University, Fullerton

Spring 2009

Marks of a CSUF Graduate from the College of Natural Sciences and Mathematics

Graduates from the College of Natural Sciences and Mathematics:

Understand the basic concepts and principles of science and mathematics.

Are experienced in working collectively and collaboratively to solve problems.

Communicate both orally and in writing with clarity, precision and confidence.

Are adept at using computers to do word processing, prepare spreadsheets and graphs, and use presentation software.

Possess skills in information retrieval using library resources and the Internet.

Have extensive laboratory/workshop/field experience where they utilize the scientific method to ask questions, formulate hypotheses, design experiments, conduct experiments, and analyze data.

Appreciate diverse cultures as a result of working side by side with many people in collaborative efforts in the classroom, laboratory and on research projects.

In many instances have had the opportunity to work individually with faculty in conducting research and independent projects. In addition to the attributes of all NSM students, these students generate original data and contribute to the research knowledge base.

Have had the opportunity to work with very modern, sophisticated equipment including advanced computer hardware and software.

About the cover: The central focus of the cover art is the Fibonacci sequence, a mathematical pattern found throughout nature and represented here in the cross section of a nautilus shell. As we follow the spiral outward we travel through the masthead and the cooler colors of the Earth down through an array of math symbols finally to the warm colors of the Earth's interior. The faint image of the student represents the research and hard work the students put into this publication.

Dimensions: The Journal of Undergraduate Research in Natural Sciences and Mathematics is an official publication of California State University, Fullerton. Dimensions is published annually by CSUF, 800 N. St. College Blvd., Fullerton, CA 92834. Copyright ©2009 CSUF. Except as otherwise provided, Dimensions: The Journal of Undergraduate Research in Natural Sciences and Mathematics grants permission for material in this publication to be copied for use by non-profit educational institutions for scholarly or instructional purposes only, provided that 1) copies are distributed at or below cost, 2) the author and Dimensions are identified, and 3) proper notice of the copyright appears on each copy. If the author retains the copyright, permission to copy must be attained directly from the author.

Table of Contents

Acknowledgments

► Biological Sciences

RNase P-based Antisense Strategy to Combat Resistance to Antibiotics in Pathogenic Bacteria By: Doreen Emilee Carpio	7
Effects Of Trampling On Aquatic Invertebrate Communities At Bell Creek Within Starr Ranch Audubon Sanctuary, Ca By: Ernesto Casillas & Allyson Degrassi	8
Ethnobotanical Investigation: Traditional use of <i>Hydrocotyle ranunculoides</i> L.f. (Apiaceae) in the higher Lerma River Region, Mexico By: Carmen J. Cortez	9
Pollination Efficiency in Major Trunk and Branch Axis of the Cauliflorous <i>Theobroma cacao</i> L. By: Carmen J. Cortez	15
Aquatic Insects as Bioindicators for Sustainable Water Use: A Comparative Analysis of Three Water Reservoirs in Thailand By: Kimberly Nelson & Songyot Kullasoot	23
Feeding Preferences of the Marine Gastropod <i>Aplysia vaccaria</i> By: Meredith R. Raith	28
Environmental Factors that Affect Delayed Hatching on Development and Swimming Speed in the California Grunion, <i>Leuresthes tenuis</i> By: Tracie Treybig	36

►	Chemistry and Biochemistry	
	Molecular Dynamics of Human Butyrylcholinesterase towards the Design of Selective Inhibitors By: Tejas Bondade	43
	Determining Binding affinity of an Iron (III) corrole complex with Pyridine and Imidazole Derivatives By: Po-Yu Fang	49
	Molecular Modeling and Dynamics of Zinc Loaded Metallothionein By: Steven K. Hoang	59
►	Geological Sciences	
	Subsurface Modeling of Low Porosity Units Restricting Groundwater Recharge to the Regional Aquifer, El Mirage Valley, Mojave Desert, San Bernardino County, California By: Dale R. Dailey	63
	Dynamic Rupture Propagation path of a Complex fault Geometry By: Melissa Nunley	88
►	Mathematics	
	The Unveiling of Math's Two Most Secret Societies By: Christine Renéé Martin	97
►	Physics	
	Nuclear Spin Relaxation via Hole Spins in Semiconductor Nanostructures By: Alyssa Rodd	102
	Near Threshold Electron Impact Doubly Differential Cross Sections for the Ionization of Neon and Xenon By: Brent R. Yates	103
	Author Biographies	119

Acknowledgements ►

Editor in Chief

Ali Forghani

Editors

Yareli Sanchez, Biology

Joyce Park, Chemistry/Biochemistry

Kelly Kathe, Geology

Troy Cannon, Mathematics

Bahar Ajdari, Physics

Advisor

Dr. Rochelle Woods, Assistant
Dean for Student Affairs

Graphic Design

Ricardo Ulloa, Layout Editor

Brian Bouskel, Cover Designer

Graphic Design Advisor

Arnold Holland,
Associate Professor

Pre-Press and Printing

Reprographics

College of the Arts

Jerry Samuelson, Dean

Andi Sims, Assistant
Dean for Student Affairs

College of Natural Sciences and Mathematics

Dr. Steven Murray, Dean

Dr. Mark Filowitz,
Associate Dean

Dr. Robert Koch, Chair,
Department of Biological Science

Dr. Maria Linder, Chair,
Department of Chemistry/Biochem-
istry

Dr. David Bowman, Chair,
Department of Geological Sciences

Dr. Paul De Land, Chair,
Department of Mathematics

Dr. Murtadha Khakoo, Chair,
Department of Physics

Special Thanks

To **President Milton A. Gordon**
and **Dean Steven Murray** for
their support and dedication
to Dimensions.

RNase P-based Antisense Strategy to Combat Resistance to Antibiotics in Pathogenic Bacteria

► Doreen Emilee Carpio¹, Alfonso Soler Bistué¹, Jonathan Joaquín¹, Hongphuc Ha², Angeles Zorreguieta¹, and Marcelo E. Tolmasky²

¹Fund. Inst. Leloir, IIBBA-CONICET y Dto.Qca.Biol., FCEN-UBA, Argentina

²Center for Applied Biotechnology Studies, Department of Biological Science, CNSM, California State University, Fullerton

Background

Aminoglycoside (Ag) antibiotics are commonly used for the treatment of serious bacterial infections. Unfortunately, the success rate of treatments with Ags has gone down due to the spread of Ag 6'-N-acetyltransferases type I enzymes. One of them, AAC(6')-Ib, is present in over 70% of AAC(6')-I-producing gram-negative clinical isolates. A strategy to overcome this problem is to silence aac(6')-Ib by designing antisense oligonucleotides, known as external guide sequences (EGSs), that induce RNase P-mediated digestion of the aac(6')-Ib mRNA. However, since oligonucleotides are rapidly degraded by nucleases in body fluids, the therapeutic use of EGSs requires the development of nuclease resistant analogs.

Methods

Efficiency of EGSs to promote cleavage of the target mRNA was performed by cloning the DNA segments under the control of the T7 promoter and transformation of *Escherichia coli* BL21 harboring aac(6')-Ib. RNase P activity experiments were carried out in

the presence of the EGSs, 5'-end-radiolabeled aac(6')-Ib mRNA, RNase P, and the reaction products were analyzed by 6% denaturing GTG-PAGE.

Results

Recombinant plasmids coding for selected EGSs were introduced into *E. coli* harboring aac(6')-Ib, and the strains were tested to determine their resistance to Ags. This analysis permitted us to identify two of them, EGSC3 and EGSA2, that interfered with expression of the resistance. However, in these experiments the EGSs were transcribed from plasmids inside the cytoplasm where they bind the target mRNA and elicit cleavage by RNase P. Therefore, this is not a viable strategy as the final stage in development of a RNase P-based antisense technology. To deal with this problem, we designed antisense compounds with the EGSC3 sequence using non-hydrolyzable nucleic acid analogs. Out of a variety of analogs assayed, only Locked Nucleic Acids were able to direct RNase P-mediated precise cleavage of aac(6')-Ib mRNA.

Conclusion

Our results prove that phenotypic conversion to susceptibility to Ags induced by EGS analogs is a feasible strategy to overcome the problem of antibiotic resistance.

Acknowledgments

Funding has been provided by grant 2R15AI047115 from NIH. D.C. and J.J. were supported by LA Basin MHIRT 5T37MD001368 (National Center on Minority Health and Health Disparities, NIH).

EFFECTS OF TRAMPLING ON AQUATIC INVERTEBRATE COMMUNITIES AT BELL CREEK WITHIN STARR RANCH AUDUBON SANCTUARY, CA

► Ernesto Casillas, Allyson Degrassi, Elizabeth Hessom, Elaine Ramos, Tracie Treybig, Sean Walker, Darren Sandquist.

Advisor: Dr. William Hoese

California State University, Fullerton

Abstract

Trampling through streams may disrupt aquatic ecosystems by altering the landscape and displacing wildlife, including aquatic invertebrates, which are often used as indicators of water quality in stream ecosystems. We examined the effects of trampling on the aquatic invertebrate communities at two (upper and lower) sites on Bell Creek in Orange County, CA. We used the California Streamside Biosurvey Protocol of aquatic invertebrates as a guide for sampling and to determine creek health. We calculated absolute abundance, relative abundance, species richness, and species diversity of these communities. We hypothesized that trampling would decrease diversity and absolute abundance of the aquatic invertebrates and would lower water quality in this stream. We simulated a 20-person hiking group trampling through the treatment plots. Samples of aquatic invertebrates were collected from control (n=6) and trampled (n=12) plots. Treatment plots were sampled 12 and 36 hours after trampling. Nine samples were collected from each site using a D frame net. Trampled plots in

the upper sites had a significant decline in absolute abundance, a decrease in diversity, a decrease in richness, and a decrease in water quality 12 hours after trampling, relative to the control plots. The lower site had a decrease in absolute abundance, decrease in diversity, an increase in richness, and an increase in water quality 12 hours after trampling. Similar trends were observed 36 hours after trampling except for species in the mayfly (Ephemeroptera) and caddisfly (Trichoptera) orders, which increased in abundance. Our results show that trampling adversely affects the short-term community composition of aquatic invertebrates within this creek.

Ethnobotanical Investigation: Traditional use of *Hydrocotyle ranunculoides* L.f. (Apiaceae) in the higher Lerma River Region, Mexico

► Carmen J. Cortez

Advisor: Dr. Sandra A. Banack

California State University, Fullerton

Abstract

Hydrocotyle ranunculoides L.f. (Apiaceae) is a small aquatic plant found in the wetlands that are prominent in the higher Lerma River region in the Valley of Toluca, Mexico. The Valley of Toluca is the ancestral home to the indigenous Otomi, Matlatzinca, Mazahua, and the Mexica groups. Since the 16th century *H. ranunculoides*, known by the Mexica as “amamalacotl,” meaning swirl of water in Nahuatl, was used as a condiment and medicine to treat minor illnesses. Formal documentation of the knowledge and use of this plant in Mexico is limited. The overexploitation of groundwater resources from this valley, pollution, and further development are recent threats to the loss of habitat and the valuable cultural knowledge of harvesting aquatic plants including *H. ranunculoides*. In this study we investigated the current use and ethnobotanical knowledge of *H. ranunculoides* in four municipalities surrounding the higher Lerma River region. Although these wetlands are changing, local people continue to consume and use this plant as the Mexica indigenous people once did before the 16th century in Mexico.

Introduction

Hydrocotyle ranunculoides L.f. (Apiaceae) known as the marsh pennywort, water pennywort, or floating pennywort, is a small perennial aquatic plant native to North America (Preston & Croft, 1997). It is a stoloniferous plant with round deeply lobed floating leaves that are 2-6 cm in diameter and submerged stems and roots (Martin, 1981). *H. ranunculoides* is generally found near slow-moving and shallow pools, lakes, and ponds growing in an interwoven mat of roots and stems that can reach down to 50 cm (Newman & Dawson, 1999). These mats can get very dense and in some instances may exclude other aquatic plants from emerging in the same sites. In Europe and Australia *H. ranunculoides* was initially imported as an aquarium or garden plant and is found in aquatic centers, private lakes, and ponds (Dawson, 1999). In recent years its effective vegetative propagation has resulted in successful invasion of various natural water systems.

In Western Uganda, Oates (1978) observed and documented the consumption of *H. ranunculoides* by Guereza monkeys. Guereza monkeys ate the rooted *H. ranunculoides* from shallow pools to supplement their diet

with additional minerals not regularly found in their regular terrestrial plant diet. Interestingly, in the western hemisphere, *H. ranunculoides* was harvested from Lake Texcoco in Mexico City by the Mexica indigenous people and was known as *amamalacotl*, in the Nahuatl language, which translates to swirl of water (Pico and Nuez, 2000). It was not considered to be an ordinary weed, but rather an edible *verdura*, vegetable appreciated for its aromatic scent. It is believed that this plant was consumed and used medicinally to treat fevers and infections of the liver (Hernandez, 1943). Additionally, *H. ranunculoides* was used for forage, as an ornament in rituals, and for the construction of “chinampas”, narrow, rectangular beds or platforms used for agriculture, which are constructed by alternating layers of lake mud and thick mats of decaying vegetation over shallow lake bottoms (Albores, 1995; Calnek, 1972).

Currently in Mexico, *Hydrocotyle ranunculoides* can be found in the wetlands of the Valley of Toluca in the State of Mexico. *H. ranunculoides* surrounds the cattails, *Typha latifolia* L. (*Typhaceae*), and grows near the shoreline of the wetland pools of the higher basin Lerma River region. This area is a sub-basin of the Lerma

River that starts near Almoloya del Rio near the Texcalyacac municipality in the state of Mexico and flows out to the Pacific Ocean (Munoz et al., 2001). Located just west of Mexico City, the higher Lerma River basin is the ancestral home to the indigenous groups of the Otomi, Matlatzinca, Mazahuaz, and the Mexica (Flores, 1999). For centuries the traditional people of this region have commonly engage in the collection of aquatic flora and fauna, fishing and hunting (Esteller et al., 2002). In this study, we investigated the current use and ethnobotanical knowledge of *H. ranunculoides* in four municipalities surrounding the higher Lerma River region in the Valley of Toluca.

Study Area

Just east of Mexico City, in the valley of Toluca, the Lerma River emerges creating a unique wetland area encompassing about 20 municipalities including San Mateo Texcalyacac, Temoaya, San Pedro, Tlaltizapan, Ixtlahuaca, and Toluca (Fig. 1). The higher Lerma river region has been the ancestral home to various traditional people who have used this lacustrine zone and its surroundings to obtain food, shelter, water, medicine, and other material goods. The people of this area continue to make use of their immediate environment including the three major bodies of water: Chiconahuapan, Lerma or Chimaliapán, and Chignahuapan. These three bodies of water are a reduction of a 27, 000 ha of wetland region once found at the end of the XIX century (Albores, 1995). In recent years these bodies of water have slowly diminished in size, which biologist attribute to ground water exploitation. The increase in the population in Mexico



Figure 1. Chiconahuapan wetland San Mateo, Texcalyacac Mexico July, 2007.

City has resulted in a greater demand for water, which in the 1960's was supplemented with an increase in groundwater extraction from the Valley of Mexico Lerma River basin (Esteller et al., 2002). Since the 1970's, there has been an attempt to restore the wetlands particularly Chiconahuapan, but the desiccation of the wetlands and loss of aquatic flora and fauna is still a threat (Estellar et al., 2002). The diminishing water in this area today can potentially have an impact on how their aquatic flora are used traditionally by local people.

Water pollution is yet another concern. According to Avila-Perez et al. (1999) the Lerma River receives urban wastewater discharges from 29 municipalities, as well as industrial water discharges, treated and untreated, mainly from the industrial zones of Toluca. There has yet to be a published study on the quality of water of the three major bodies of water and the severity of pollution is unknown.

Furthermore, this region is facing urban development. State authorities

plan to construct a private highway through which will negatively impact the three major bodies wetlands. Plans are also underway for developing the Chiconahuapan wetland by constructing a tourist zone similar to that of Lago Xochimilco in Mexico City.

Methods

This investigation was conducted in the higher Lerma river region located in the Valley of Toluca, Mexico one week during early January of 2007 and three weeks during mid July to early August of 2007. Semi-structured interviews were conducted using ethnographic interviewing techniques as specified by Spradley (1980) with a local family, farm workers, and traveling vendors at weekly "tianguis" or farmer's markets. Interviews were conducted in the towns of San Mateo Texcalyacac, San Pedro Tlaltizapan, Temoaya, and Ixtlahuaca, municipalities surrounding the river basin region of the Lerma River. An open-ended questionnaire that



Figure 2. a.) Lerma River and the wetland region in the Ejido de San Pedro Tlatizapan, Mexico July, 2007. b.) Collection of *H. ranunculoides* with wood stick and metal fork attached to the end. c.) *H. ranunculoides* ‘berro amarillo’ San Pedro, Tlatizapan, Mexico. d.) *H. ranunculoides* ‘quelites sanreje’ purchased from farmer’s market in Temoaya, Mexico.

included questions on the use of the local wetland flora was used to obtain information from all participants. No compensation was given to any participant interviewed. Before data collection, permission for interviews was acquired from each participant and from the Institutional Review Board (Assurance # FWA00000135.) Confidentiality was guarded for those participants that wished to remain anonymous. Interviews were conducted in Spanish and information was documented using a notebook and if specific permission was granted, tape recorders were also used.

Results

Hydrocotyle ranunculoides is found in slow-moving water in the higher Lerma River wetland region of the Valley of Toluca including the major bodies of water Chiconahuapan, Lerma or Chimaliapan, and Chignahuapan. It is collected from different areas of the Valley of Toluca including San Pedro, Tlatizapan municipality (19°12'36"N, 99°03'55"W). *Hydrocotyle ranunculoides* is harvested from the shorelines of the wetlands by pulling the plant by the stems and leaves, this is done with ones hands or a wooden

stick with a forked end that enables collectors to hold and pull plants out of the water (Fig. 2). Approximately 20 plants can be extracted from the water at one time with this method. *H. ranunculoides* is gathered from the wetlands all year long and is most abundant during the rainy season in the months of July through September. During collection, attention is paid to the types of *H. ranunculoides* being collected because it is believed there are three types present: “berro colorado,” “berro Amarillo,” and “berro blanco” (Fig. 2c). The first two are believed to have a bitter fibrous taste, more roots present,

and is difficult to chew. The latter is known to have a sweeter taste and much softer in texture than the other two. Knowing how to identify these three different types of *H. ranunculoides* is knowledge acquired by collectors from their previous generations. A collector may spend 2 to 3 days in order to collect approximately 50 kg that are then taken to local “tianguis”, or market, to sell to vendors who will ultimately sell the product to consumers. Plant material collected is taken to “tianguis” or farmer’s markets in Temoaya, Mexico City, and the “Central de Abastos,” the largest weekly “tianguis” in the valley of Toluca. Majority of the vendors conducted the collection of *H. ranunculoides* themselves. These vendors all used the same method for removing *H. ranunculoides* from the wetlands. Collection sites for this plant were mainly found in the Lerma River region near the municipality of San Mateo, Atenco between Lerma, Chimaliapan wetlands, and the wetland region of Chiconahuapan near the municipality of San Antonia la Isla and San Pedro, Tlaltizapan. Some collectors however, indicated that *H. ranunculoides* was gathered only from springs around the wetlands to avoid the pollution found in the larger three bodies of waters.

After collection, *H. ranunculoides* is either sold directly by the collector at weekly “tianguis” or is sold to vendors at these farmer’s markets. Similar to the sale of *Sagittaria macrophylla*, “papa de agua,” another aquatic plant of this region whose tubers are edible and eaten in tacos Zepeda-Gomez & Lot (2005), the sale of *H. ranunculoides* is mainly done by female vendors referred to as “ambulantes,” traveling vendors, that frequently assist the weekly “tian-

guis” or “mercados,” markets (Fig. 3). Vendors clean plants by rinsing them and selling them in pieces of approximately 30 cm that include stems, roots, and leaves (Fig. 3). The average price for approximately 15 pieces is \$5 pesos and \$10 pesos for approximately 30 pieces. *H. ranunculoides* was found to be sold in “tianguis” located in Teomoya, Toluca, and Ixt-

lahuaca. *Hydrocotyle ranunculoides* is sold with other plants such as cactus pads, cilantro, *Lilaeopsis schaffneriana*, *Hydroyistria laeviata*, *Myriophyllum aquaticum*, *Lilaea scilloides*, *Rorippa nasturtium-aquaticum*, *Ludwigia peploides*, *Jaegeria bellidiflora*, *Potamogeton pusillus*, *Typha latifolia*, and *Sagittaria macrophylla* (Zepeda-Gomez & Lot, 2005). Some of the common



Figure 3. *H. ranunculoides* for sale in the weekly mercado, market in Temoya, Mexico July, 2007.

names used to identify *H. ranunculoides* included: “quelites sanreje” in native Otomi language, “sanreje”, “sombrilla”, “tripa de pato”, “berro”, “berro redondo”, “berro amarillo”, “berro blanco”, and “berro colorado”.

The primary use of *H. ranunculoides* is for consumption. The stems and leaves are the only part of the plant that is eaten (Fig. 2d). This plant can be eaten raw, with the exception of the roots, or is diced, chopped and eaten in salads. These salads usually consist of tomato, avocado, and onion and *H. ranunculoides* to add a stimulant and aromatic smell and taste. *H. ranunculoides* is used for its medicinal properties and is used to treat minor ailments that include: urinary track infections, ailments in of the lungs and kidney, and can help decrease the effect of gastritis. For this purpose, *H. ranunculoides* is prepared as a shake with lemon and cactus pads.

There are only a few individuals in the communities surrounding the wetlands that currently use *H. ranunculoides*. A local family interviewed, in San Mateo, Texcalyacac had knowledge of the aquatic flora from their immediate wetland Chiconahuapan. They were able to identify *H. ranunculoides* as “berro redondo” and were aware that others knew of its presence in Chiconahuapan (Fig. 1). Although this family was not using this plant, they had obtained knowledge of it through oral history. They knew their ancestor took this plant from the waters and used it as a condiment. There were no observed uses of *H. ranunculoides* in the town of San Mateo, Texcalyacac. In Ixtlahuaca *H. ranunculoides* is identified as “quelites san reje” and only the older generation in this community still have use for this plant. Similar to

how the Mexica once harvested and use *H. ranunculoides*, many traditional people of this area still harvest and eat this plant as a condiment, but there is an increase concern over the quality of water quality where this plant is harvested.

Discussion

Although an invasive species and pest in parts Europe and Australia, *Hydrocotyle ranunculoides* continues to be consumed by the people of Mexico as they once did before the 16th century. The ethnobotanical knowledge of this plant is not widespread in various municipalities of the higher Lerma River region and is limited to traditional people that still have many ties to their indigenous ancestry. In addition, many people have become aware of the unsanitary quality of the water and have fear of consuming this and other aquatic vegetation, this has lead to a decrease of commerce for this plant (Moctezuma et al., 2007).

There have been efforts to grow *H. ranunculoides* for sustainable farming of native flora in this region. In a study conducted by Moctezuma et al. (2007) *H. ranunculoides* were planted in irrigation ponds and found that an average of 1,000 plants per m² could potentially be grown. The objective of that study was to establish cultures under a system of some native species, in irrigation ponds in the higher Lerma River region wetlands as an alternative to common carp (*Ciprinus carpio*) monoculture (Moctezuma et al., 2007).

If these sustainable farming techniques are efficient and are welcomed by the community they could be a way to potentially bridge the generational gap of ethnobotanical

knowledge of this and other aquatic vegetation of the region while creating food alternatives. However, the limiting factor to the continual use of *H. ranunculoides* is the decrease in water levels, pollution, and development of the region all of which desperately need to be addressed.

Acknowledgements

I would like to thank Dr. Sandra Anne Banack for her guidance, feedback, and for allowing me to learn more about the study of people and plants. The Ronald E. McNair Program for funding this opportunity and helping me demystify higher education. I would also like to thank Mr. Gabriel Diaz Alcaraz and Ms. Nayelli Madero for assisting me in making connections in Mexico. I am grateful and thankful to the communities in the higher Lerma River region that participated in this study particularly the family, Mr. Juan Garcia Rivera and Mrs. Yolanda Cristina Madero Reyes who open to me their home and their hearts.

References

Albores-Zarate, B.A. 1995. Tules y Sirenas, El impacto ecologico y cultural de la industrializacion en el Alto Lerma. El Colegio Mexiquense: Gobierno del Estado de Mexico.

Avila-Perez, P., Garcia-Aragon, J.A., Diaz-Delgado, C., Tejada-Vega, S., and Reyes-Guitierrez, R. 2002. Heavy metal distribution in bottom sediments of a Mexican reservoir. *Aquatic Ecosystem Health and Management* 5: 205-216.

Avila-Perez, P., Balcazar, M., Zarazua-Ortega, G., Barcelo-Quintal,

- I., Diaz-Delgado, C. 1999. Heavy metal concentration in water and bottom sediments of a Mexican reservoir. *The Science of the Total Environment* 234: 185-196
- Calnek E. E. 1972. Settlement Pattern and Chinampa Agriculture at Tenochtitlan American Antiquity 37(1): 104-115.
- Esteller, M.V., and Diaz-Delgado C. 2002. Environmental Effects of Aquifer Overexploitation: A Case Study in the Highlands of Mexico. *Environmental Management* 29(2): 266-278.
- European and Mediterranean Plant Protection Organization Data sheets on quarantine pests, Fiches Hydorcotyle ranunculoides. 2006. OEPP/EPPO Bulletin 36: 3-6.
- Flores, O.L. 1999. Texcalyacac Monografía Municipal. Toluca, Mexico. Instituto Mexiquense de Cultura Morelos Ote.
- Guilizzoni, P. 1991. The Role of Heavy Metals and Toxic Materials in the Physiological Ecology of Submersed Macrophytes. *Aquatic Botany* 41: 87-109
- Hernández, F. 1790, ed. 1942-46. *Historia de las plantas de Nueva España*. Vol. 3. UNAM. Instituto de Biología. Imprenta Universitaria, Mexico, Mexico.
- Martin, W.C. and Hutchins, C.R. 1981. *A Flora of New Mexico*. Lubrecht & Cramer U.S.A
- Moctezuma Malagón A., de la Lanza Espino G., González-Rebeles Islas C., and González Esquivel C. 2007. Multiculture of native species in irrigation ponds in central Mexico. *Livestock Research for Rural Development* 19(14).
- Munoz, M.B. and Encina, G.P. ed 2001. Community-science-traditional knowledge: a common but differentiated approach. The case of the higher basin of Lerma River wetlands, Mexico. *Science and local communities: Strengthening partnerships for effective wetland management*. Ducks Unlimited, Inc., USA.
- Newman, J.R., and Dawson, H.F. 1999. Ecology, distribution and chemical control of *Hydrocotyle ranunculoides* in the U.K. *Hydrobiologia* 415: 295-298.
- Oates J. F. 1978. Water-Plant and Soil Consumption by *Guereza* Monkeys (*Colobus guereza*): A Relationship with Minerals and Toxins in the Diet? *Biotropica* 10(4): 241-253.
- Preston, C. D. and Croft, J. M. 1997. *Aquatic Plants in Britain and Ireland*. Harley Books, Colchester, Essex.
- Pico, B. and Nuez, F. 2000. Minor crops of Mesoamerica in early sources (II). Herbs used as condiments. *Genetic Resources and Crop Evolution* 47: 541-552.
- Ruiz-Avila, R.J. and Klemm, V.V. 1996. Management of *Hydrocotyle ranunculoides* L.f., an aquatic invasive weed of urban waterways in Western Australia. *Hydrobiologia* 340: 187-190.
- Spradley, J.P. 1980. *Participant Observation*. New York. Holt, Rinehart and Winston.
- Zepeda-Gomez C., Lot A. 2005. Distribucion y uso tradicional de *Sagittaria macrophylla* Zucc S. *latifolia* Willd. en el Estado de Mexico. *Ciencias Naturales y Agropecuarias* 12(003):282-290.

Pollination Efficiency in Major Trunk and Branch Axis of the Cauliflorous *Theobroma cacao* L.

► Carmen J. Cortez

Advisor: Dr. Peter K. Kwapong

University of Florida-University of Cape Coast, Ghana

NSF-Research Experience for Undergraduates

Abstract

Theobroma cacao L. (Sterculiaceae), cacao is one of the major crops exported from various tropical regions, primarily Ghana. Every cacao bean produced by the cacao tree is the product of effective pollination and therefore research to further understand this biological process in this economically important crop is crucial. We investigated the pollination efficiency of the major trunk and branch axis, trunk and canopy segments, of two cocoa varieties, Upper Amazon and CRIG series II hybrid, possible pollinators for these two varieties, and morphological differences between flowers of the West African Amelonado, Upper Amazon, and the CRIG series II hybrid located in two local Ghanaian farms. Farms were divided into four plots where two cocoa trees were semi-randomly selected. A one meter trunk segment, 0.03 m above the ground and a one meter canopy segment, 1.8-2.1 m height range, were identified for each tree in both farms. Open flowers in these segments were quantified and marked. After 72 h the number of previously marked flowers no longer present, or dropped, was recorded and used to measure pollination efficiency. Possible pollinators were col-

lected using a motorized aspirator in one tree for each plot in both farms. Observations for flower morphology were made for all three cocoa varieties. Results suggested that pollination efficiency was significantly higher in the trunk segments than the canopy segments in both the Upper Amazon and the CRIG series II hybrid. Collections for possible pollinators found four genera, *Oecophylla*, *Camponotus*, *Simulium*, and *Synip*. Qualitative observations did not find any major differences in flower morphology of the three varieties. Although, these preliminary results suggest further investigations need to be conducted. Additionally, significantly higher pollination efficiency in the trunk versus the canopy segments of the two cocoa varieties maybe influenced by the concentration of principal pollinators in the farm grounds.

Introduction

Pollinator-plant interactions have influenced a mutual diversification of floral structures and pollinators; more importantly pollinators played an important role in the evolution and speciation of many land plants (Kearns et al., 1998; Ollerton & Dafni, 2005). Globally, a great deal of ecologically and economically important plants

are dependent upon biotic agents for pollination. It is estimated that there are approximately 25,000 different species of angiosperms worldwide, 90% of which are animal-pollinated particularly by insects (Heywood, 1993; Buchmann & Nabhan, 1996). Insect pollinators assist in pollination of major cash crops such as cotton (*Gossypium spp.*), soya (*Glycine max*), strawberry (*Fragaria x ananassa*), aubergine (*Solanum melanocarpum*), pepper (*Capsicum annum*), tomato (*Lyco-persicon esculentum*), olives (*Olea europea*), grapes (*Vitis vinifera*), and avocado (*Persea americana*) (Richards, 2001). Other important crops such as carrots, alfalfa, and clover are dependent on insect pollinators for seed production, and in some crops (i.e. cotton), efficient pollination service can improve yield and fruit quality (Free, 1993; Allen-Wardell et al., 1998).

One economically important crop of the tropics and an obligately insect-pollinated plant is *Theobroma cacao* L. (Sterculiaceae), also known as cocoa. Cocoa has hermaphroditic flowers that consist of 5 stamens, and 5 sterile staminodes (Wood, 1975). The stigma is surrounded by fleshy reddish-purple vertically positioned sterile staminodes, the five stamen filaments are bent outwards and



Figure 1. a.) *Theobroma cacao* CRIG Series II hybrid in Ghanaian farm, Abrafo-Odumase June, 2008. b.) CRIG Series II hybrid flower and flower buds emerging from flower cushions on the trunk of *Theobroma cacao*, Abrafo-Odumase June, 2008.

are hidden within pouched petals, and all 5 petals have reddish-purple guidelines (Murray, 1975). Cocoa is a cauliflorous plant that grows new flower buds in old leaf scars that through time create knot-like structures known as flower cushions. These flower cushions are found directly on the trunk and major branch axis (Lent, 1966; McKelvie, 1962). Pollination studies of the cocoa conducted by Ibrahim (1988) found that with less than 35 pollen grains in the stigma, fertilization does not occur. Other studies by Falque (1995) found that more than 35 pollen grains are needed for high fruit set and bean production in pods. Additionally, Young (1982a) established that pollination in cocoa is a system that is dependent on the frequency of pollinator visits to the flower and

the ability of pollinators to correctly deposit clusters of pollen in or around the stigma. In the absence of effective pollination, cocoa flowers abscise within 24-48h after opening (Murray, 1975; Young, 1982a; Falque et al., 1995). It is believed that throughout various parts of the tropics Diptera midges in the Ceratopogonidae family are the cocoa effective and principal pollinators (Winder, 1977; Posnette & Entwistle, 1957; Kaufmann, 1975; Young, 1983; Brew, 1985).

Up to the 16th century, the Mayan people of Central America harvested *Theobroma cacao*. After European colonization of the tropical Americas, cocoa trade expanded around the world. By the 19th and 20th century, cocoa production reached various parts of the tropics including West Africa (Hunter, 1990). In 1879,

cocoa was introduced to Ghana and during most of the early 20th century, the cocoa industry flourished making Ghana one of the richest countries in Sub-Saharan Africa (Nyanteng, 1995). The favorable tropical climate conditions made Ghana an ideal location for cocoa production. In 1960, census data in Ghana revealed that 20% of the labor force was employed in the cocoa industry and by the 1970's, 47% of farmers were cultivating cocoa as their major cash crop (Nyanteng, 1995).

In 1938, 90% of all cocoa trees grown in Ghana were of the West African Amelonado variety, ideal because of its self-compatibility and higher fruit yield under optimal conditions (Sumner, 1962; Hammond, 1962; Murray, 1975; Edwin & Masters, 2005). However, in 1941

with the growing problem of the cocoa swollen shoot disease (CSSD), a search began through 1951 for a virus resistant variety until the Upper Amazon variety from Peru was found to be tolerant and resistant and was subsequently introduced to the Ghanaian farmer (Edwin & Masters, 2005; Ponsette, 1951). In many Ghanaian farms, multiple cocoa varieties can be found including the West African Amelonado, the Upper Amazon, and the CRIG series II hybrids which is a bi-parental cross of Upper Amazon, Amelondao, and Local Trinitario crosses (Edwin & Masters, 2005).

Cocoa productivity relies on various environmental factors, one being effective pollination, which results in fruit set. A study conducted by Frimpong, E. (unpubl. data) suggests that approximately 3.6% of the flowers produced by the cocoa tree are successfully pollinated and produce fruit while 96.4% of the flowers drop after unsuccessful pollination. Ibrahim (1988) investigated the percentage of fruit set and the role of insects as pollinating agents in Malaysia and found an average of $4,553 \pm 687$ flowers per tree were produced over a six month period by Sabah hybrid cocoa trees, only 5.2% were observed to be effectively pollinated or set fruit. Earlier work by Kaufmann (1975) found a higher percentage of effective fertilization by ceratopogonid pollinators in Ghana through experiments segments of a cocoa branches were caged with 1 to 2 midges. Of the 2,160 flowers examined in one plot over a three-year period, in Tafo Cocoa Plantation, 750 (34.6%) had been effectively pollinated; they bore 35 or more pollen grains on the stigma (Kaufmann, 1975). Work by Winder (1977) suggested that increasing

pollinator populations by having increasing suitable midge breeding sites might increase pollination efficiency and fruit set. Various studies thereafter further explored this subject particularly understanding pollinator availability in cocoa plantations, seasonal pollinator availability, and understanding breeding site preference for these main pollinators (Diptera: Ceratopogonidae) (Young, 1982; Young, 1983; Ibrahim, 1988; Brew, 1988). Young (1986) concluded that ceratopogonid midge breeding sites are often found in rotting banana/plantain stems, rotting cocoa husks, and in leaf litter. As a result, studies have focused on evaluating pollination efficiency by investigating cocoa tree proximity to midge breeding sites. However, work on pollination efficiency of cocoa has not investigated if there are differences between pollination efficiency of canopy versus trunk segments of cocoa trees. Winder (1977) worked with Diptera and cocoa flowers and found that an equal number of ceratopogonids were collected from flowers below 1 m and between 1 and 2 m and none were collected above 2 m on 2.5 m high trees. Pollination efficiency might be higher in the trunk sections of the cocoa trees than that in the canopy.

Additionally, limited work has been done to investigate flower structure differences between different cocoa varieties. Kaufmann (1975) suggests that ceratopogonids midges visit cocoa flowers to feed on some substances found on the staminode surface. Their thorax brush against the style as the insect crawls up the staminodes in the process depositing clumps of pollen on the style and effecting pollination. He further suggests that staminodes should be oriented parallel to the style to

facilitate contact between the ceratopogonid midges and the style. Brew (1988) also investigated possible color or flower part preference by the pollinators of cocoa and found that there was no significant difference in the percentage of pollination for different colors, but with the use of flower traps, he found that the initial attraction to *T. cacao* flowers by midges may be due to the vertical orientation of the staminodes rather than the “guide lines” in the petal hoods that are not vertical. Specific studies investigating the possible difference between floral structures and color of different hybrids have yet to be conducted.

Objective

The objective of this study was threefold: 1.) Documenting pollination efficiency in two cocoa varieties (Upper Amazon and CRIG II series hybrid) in two Ghanaian farms by identifying possible difference in flower drop of the trunk and canopy segments 2.) To collect possible pollinators from each variety in each farm 3.) To make observation on possible differences in flower structure between these two varieties specifically looking at staminode positions, guideline differences in the petals, and color differences in the sepals and petals.

Materials and Methods

This study was conducted in two farms in the community of Abrafo-Odumase, 1.8-2 km west of Kakum National Forest (05°19'N; 001°22'W), a tropical rain forest region of Ghana during the month of June 2008. Both farms are within 150 m of each other and one farm

grows Upper Amazon cocoa while the other farm grows CRIG series II hybrid variety of cocoa. These are small-scale open canopy farms that are bordered by cornfields and by the tropical forest region. Each farm was divided into four plots where two trees 3.5-4 m in height in each plot were sampled. All trees were divided into two segments, trunk and canopy; a one-meter length segment of the trunk, 0.3 meters from the ground was marked (Moses & Enriquez, 1979). A one-meter segment of a branch in the canopy, 1.8-2.1 meters from the ground, was also marked. In all trees, metal pins were gently placed adjacent to the flower cushions where open flowers were observed (Young, 1982b). The number of open flowers was then recorded on 6 June 2008 and approximately 72 hours later, 9 June 2008, the tagged positions without fruit were recorded to give an estimate of total flower drop for each tree (Young, 1982b). Thereafter, small marks were made with markers on one sepal of all open flowers and on the side of their corresponding flower cushion. After 72 hours, the number of fertilized flowers and dropped flowers were recorded; this process was repeated two additional times. Cocoa flowers identified as fertilized were those with dried brownish sepals and petals along with an enlarged ovary.

Mean percent flower drop was calculated for both canopy and trunk segments of both cocoa varieties and data was analyzed using MINITAB statistical analysis software.

Possible pollinators were collected using a motorized aspirator. For approximately one minute the aspirator was gently placed over cocoa flowers, marked trunk, and canopy regions of the tree. All organisms collected

were then placed in 35 mm empty film bottles and capped. This process was carried out on one tree from each plot for both farms. Insects collected were identified to the order level with the exception of Diptera, which was identified to the family level.

The flower structure of ten flowers from the Upper Amazon, ten from the CRIG series II hybrid, and ten flowers from the self-compatible West African Amelonado were examined and staminode position, "guidelines" within the petals, and sepal shape were compared. Flowers from the West African Amelonado were collected from a closed canopy cocoa farm near Abrafo-Odumase and collection of flowers from the Upper Amazon and the CRIG series II hybrid were carried out in the study sites. Flower samples were kept fresh by placing them in different small plastic containers each containing wet paper lining and observations were made a day after collection under a dissecting scope.

Results

Flower drop in trunk and canopy segments

There was a significant difference in mean percent flower drop between the canopy and trunk segments in the Upper Amazon. A similar pattern was observed in the CRIG series II hybrid, a significant difference in mean percent flower drop of the canopy and trunk segments was found. The difference in mean percent flower drop in the canopy of the Upper Amazon and the CRIG series II hybrid was not significantly different. Results also show no significant difference between the mean percent flower drop of the trunk segments

in the Upper Amazon and the CRIG series II hybrid. A higher percentage of flower drop in the canopy of the CRIG series II hybrid compared to the Upper Amazon was found, but a lower percentage of flower drop was observed for the trunk segment when compared to the Upper Amazon variety.

Insect collections

Insects in the ceratopogonidae family were not found in either farm, however, qualitative observations found midge larvae in various midge breeding sites including rotting plantain stems, rotting leaf litter, and rotting cocoa husk. With the use of the motorized aspirator the genera found in both varieties included the following: *Oecophylla* (arboreal ant), *Camponotus* (garden ant), *Simulium* (black fly), *Synip* (gall wasp).

Flower structure observations

Qualitative observations revealed that flower color for all ten flowers sampled was similar. Sepal color was white, while the petals appeared to be cupped around the stamen and slightly transparent. In each of the petals two reddish deep purple "guidelines" were observed and a slightly lighter reddish purple guideline towards the top cupped part of the petal. This was observed in all flowers of the three varieties. Petals end in a broad spatulate tip that is often pastel yellow in color. Staminodes are reddish deep purple in color with a slight white tip and are attached to a base along the outer whorl of stamen. Staminodes were covered in trichomes surrounding the stigma and were observed to be vertically position although in some flowers,

	Mean % Flower Drop \pm SE		Mean % Flower Drop Range	
	Canopy	Trunk	Canopy	Trunk
Upper Amazon	95.61 \pm 3.33	82.30 \pm 6.95	75-100	36-100
CRIG series II hybrid	98.08 \pm 2.45	80.43 \pm 7.59	75-100	40-100

Table 1. Significant results from one-way ANOVA with unequal sample size (General Linear Model) mean percent flower drop and mean percent flower drop range for the canopy and trunk segments of the Upper Amazon and the CRIG series II hybrid.

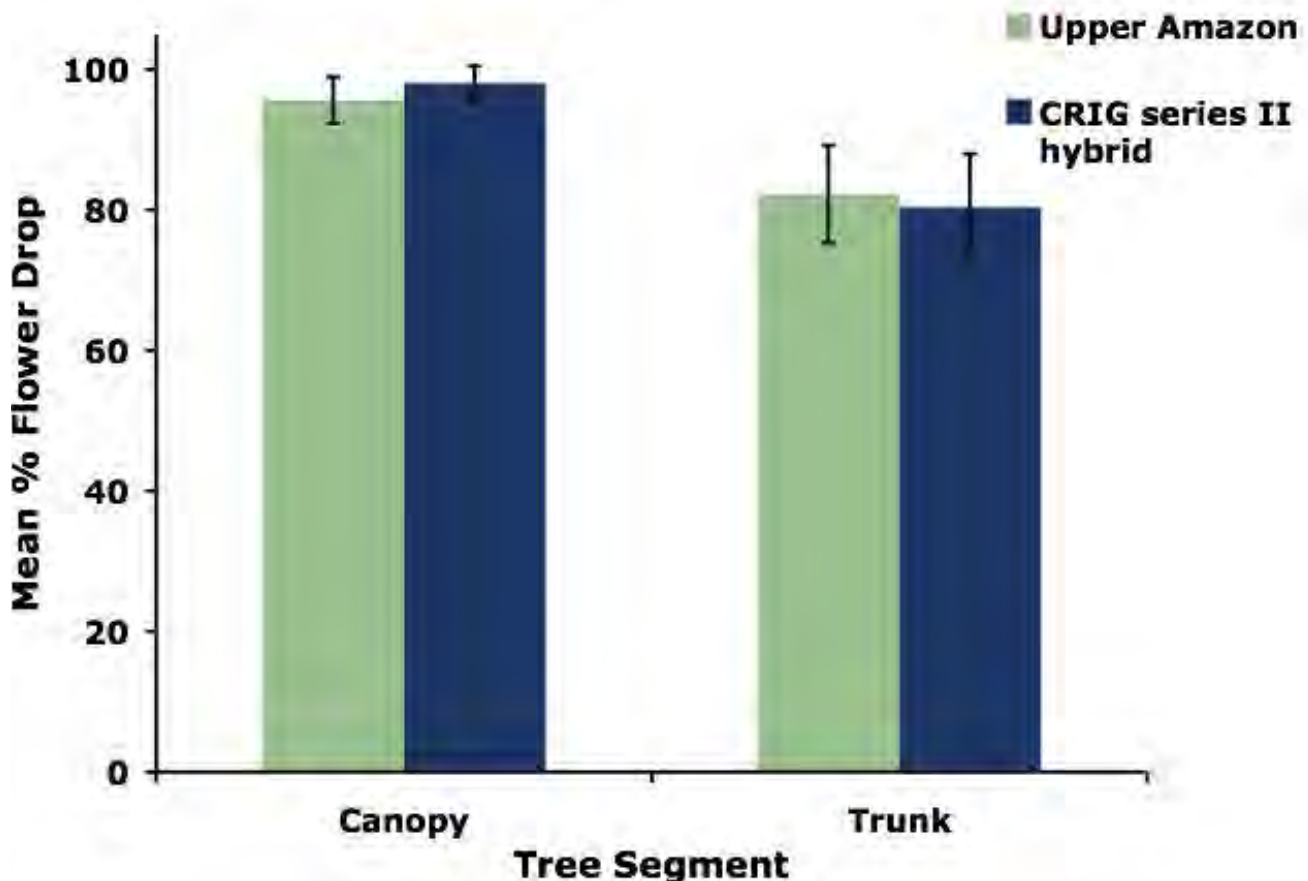


Figure 2. Mean percent flower drop for the canopy and trunk segments of the Upper Amazon and the CRIG series II hybrid.

staminode tips seemed to be flared in some flowers from all three varieties. The stigma was white in color and its tip was flared out into five segments, this was observed in some flowers for all three varieties.

Discussion

Pollination efficiency in canopy and tree segments

Studies where branch segments of cocoa trees were caged with ceratopogonid midges conducted by Kaufman (1975) and Young (1983) found an increase in the percent of fertilized flowers in those branch segments. Furthermore, pollinator abundance has been observed to be one limiting factor of effective pollination along with the presence or absence of midge breeding sites (Winder, 1977; Young, 1982; Young,

1983). The results of this study suggest that the higher pollination efficiency in the trunk segments of both cocoa varieties maybe due to a higher concentration of principal pollinators (Dipteria: Ceratopogonidae) below 1.8 meters. This was observed in Winder (1977) were no ceratopogonids were collected above 2 meters in cocoa trees. Midge breeding sites are found in the moist rotting substrates of the cocoa farm floors a

possible explanation for why there might be a concentration of these pollinators near the substrates of the farm. Researchers have also reported that these cocoa pollinating midges may be “distracted” by a number of understorey flowers by surrounding plants many of which persist in these farms due to availability of sunlight that penetrates through the open canopy of these cocoa farms (Young, 1982; Young 1983). Furthermore, the open-canopy in the two farm sites may play a role in the unevenness in pollination efficiency between canopy and trunk segments. During the dry season, small-bodied insects tend to experience more water stress in less shaded habitats (Janzen & Schoener 1968; Young 1982). The open canopy of these two farms may inhibit these pollinating midges from pollinating flowers in the canopy of these cocoa trees. More studies could be conducted to identify whether this is also observed in closed-canopy cocoa farms.

Flower structures

Qualitative observations on the morphology of the observed flowers are consistent with the scientific literature (Murray, 1975; Young, 1982a; Posnette, 1944). An interesting observation for all flowers of all three varieties was the flared tips of the staminodes. Murray (1975), however, described the movement of the staminodes away from the stigma occurring naturally over time when flowers are not fertilized. Flower structure observations, should then be made within a few hours after collection. Brew (1988) suggested that the vertical position of the staminodes is what attracts the cocoa principal pollinators, ceretopogonid midges,

which is an important aspect of the flower structure to be considered for further observation. Future studies should include a bigger sample size and specific preservation method for flowers.

Insects collected

Results reported for the insect collections reflect specimens collected from both farms. Overall, a small sample size of specimens was collected. This was in part due to weather conditions. It has been concluded by some studies that the outside activity of ceratopogonids in the rain decreases (Kaufman, 1975). Additionally, the collections were not exclusively focused on the cocoa flowers and therefore other organisms from the trunk and branch areas were collected such as the *Oecophylla* (tree ant) and *Camponotus* (garden ant). These are organisms that other researchers have documented as being natural enemies of cocoa pests including mirids and other insect pest herbivores (Anikwe et al., 2007). There was only one *Simulium* (black fly) and one *Synip* (gall wasp) and the specimen collection. There are no studies that suggest either of these genera to be potential pollinators or have a specific plant-insect interaction with the cocoa tree. Future studies should focus on collecting possible pollinators directly from the cocoa flower. More collections need to be undertaken and must consider pollinator concentrations between the canopy and the trunk segments.

Conclusion

In conclusion, there is a pollination efficiency difference between the canopy and the trunk segments of

both Upper Amazon and CRIG series II hybrid cocoa trees. This difference in pollination efficiency between segments may be attributed to the pollinator concentrations in the farm floor substrates. Moreover, the open-canopy in the two farms may decrease the number of ceretopogonid midges from accessing flowers found in the canopy. A pollination efficiency study in a closed-canopy cocoa farm can bring forth evidence that may support this idea. More pollinator collections exclusively on the flower can also bring forth more evidence on where the ceretopogonid midges are being vertically concentrated on cocoa trees.

Acknowledgements

This study was made possible with funding and support from the National Science Foundation, the University of Florida-University Cape Coast research for undergraduates program and Dr. Daniel Wubah. I am indebted to Eric Frimpong, Rofella Combey, Danquah Percy Opoku Ahwenee, and the rest of the Ghana pollination group at the University of Cape Coast for their guidance, mentoring, and assistance in the field. I am very thankful to Ajaku and Wofa Yaw for allowing me to conduct this study in their farms. Thank you Dr. Peter Kwapong for your guidance and mentoring.

References

Allen-Wardell G., P. Bernhardt, R. Bitner, A. Burquez, S. Buchmann, J. Cane, P.A. Cox, V. Dalton, P. Feinsinger, M. Ingram, D. Inouye, C.E. Jones, K. Kennedy, P. Kevan, H. Koopowitz, R. Medellin, S. Medellin-Morales, G.P. Nabhan, B. Pavlik,

- V. Tepedino, P. Torchio, S. Walker 1998. The potential consequences of pollinator declines on the conservation of biodiversity and stability of food crop yields. *Conservation Biology* 12: 8-17.
- Anikwe J.C., A.A. Omoloye, and F.A. Okelana. 2007. Studies of the Ant-plant Mutualism in the Nigerian Cocoa Agroecology. *Middle-East Journal of Scientific Research* 2(2): 69-72.
- Brew A.H. 1988. The effect of colours and specific features of floral parts on the pollination of cocoa by ceratopogonid midges in Ghana. 10th International Cocoa Research Conference, Santo Domingo, Costa Rica 1987: 307.
- Brew A.H. 1988 Cocoa pod husk as a breeding substrate for *Forcipomyia* midges and related species which pollinate cocoa in Ghana. *Cocoa Growers' Bulletin* 40:40-42.
- Brew A.H. 1985. Studies on cocoa pollination in Ghana. 9th International Cocoa Research Conference Lome Togo: p 543.
- Buchmann, S.L., and G.P. Nabhan. 1996. *The Forgotten Pollinators*. Washington, DC: Island. p 292.
- Edwin J. and W.A. Masters. 2005. Genetic improvement and cocoa yields in Ghana. *Experimental Agriculture*. 41: 491-503.
- Falque M., Vincent A., B. E. Vaissiere, and A.B. Eskes. 1995. Effect of pollination intensity on fruit and seed set in cacao (*Theobroma cacao* L.) *Sex Plant Reproduction* 8: 354-360.
- Free J.B. (1993) *Insect Pollination of Crops*, Academic Press In: Dewenter, I.S., Potts, S.G., and Packer, L. 2005. Pollinator diversity and crop pollination services are at risk. *Trends in Ecology and Evolution* 20(12): 651.
- Glendinning D.R. 1972. Natural pollination of cocoa. *New Phytologist* 71(4):719-729.
- Hammond P.S. 1962. Agriculture and land use in Ghana; *Cocoa Agronomy*. Eds. Wills J.B. Oxford University Press, London: p 252.
- Heywood V.H., ed. 1993. *Flowering Plants of the World*. New York: Oxford Univ. Press In: Kearns, C.A., Inouye D.W., and Waser, N.M. 1998. Endangered mutualism: The conservation of plant-pollinator interactions. *Annual Review Ecological Systems* 29: 83-112.
- Hunter J.R. 1990. The Status of Cacao (*Theobroma cacao*, Sterculiaceae) in the Western Hemisphere. *Economic Botany* 44(4): 425-439.
- Ibrahim A.G. 1988. The effect of colours and specific features of floral parts on the pollination of cocoa by ceratopogonid midges in Ghana. 10th International Cocoa Research Conference, Santo Domingo, Costa Rica 1987. Oxford University Press, London: pp 252.
- Janzen D.H. and S.W. Thomas. 1968. Differences in Insect Abundance and Diversity Between Wetter and Drier Sites During a Tropical Dry Season. *Ecology* 49(1): 96-110.
- Kaufmann T. 1975. Ecology and behavior of cocoa pollinating ceratopogonidae in Ghana, West Africa. *Environmental entomology* 4(2): 347-351.
- McKelvie A.D. 1962. Agriculture and land use in Ghana; *Physiology*. Eds Wills J.B. Oxford University Press, London: p 256.
- Moses D.D. and G.A. Enriquez. 1979. Calibrating varieties for yield of cocoa, as well as the relationships of several cacao features with the environment. 7th International Cocoa Research Conference. Doula, Cameroon.
- Murray D.B. 1975. *Cocoa; The Botany of Cocoa*. 3rd ed. Longman Group Ltd, London: pp 55.
- Nyanteng V.K. 1995. Prospects for Ghana's Cocoa industry in the 21st century In: Francois R.P.S., 1995. *Cocoa Cycle: The economics of cocoa supply; Prospects for Ghana's Cocoa industry in the 21st century*. Woodhead Press p 180.
- Ollerton J. and A. Dafni, 2005. Functional Floral Morphology and Phenology In: Dafni, A., Kevan, P.G., Husband B.C. 2005. *Practical Pollination Biology*. Enviroquest, Ltd. Ontario Canada.
- Posnette A.F. 1944. Pollination of Cocoa in Trinidad. *Tropical Agriculture* 21(6):115-117.
- Posnette A. F. and J. McA. Todd. 1951. Virus diseases of cacao in West Africa. The search for a virus resistant cacao. *Annals of Applied Biology* 38: 785-800.

Posnette A.F. and H.M. Entwistle. 1957. Planting material and methods. Cocoa Conference London: p 66-69.

Richards A.J. 2001. Does low biodiversity resulting from modern agricultural practice affect crop pollination and yield? *Annals of Botany* 88:165-172.

Sumner M.H. 1962. Agriculture and land use in Ghana; C. Pollination. Eds. Wills J.B. Oxford University Press, London: p 260.

Winder J.A. 1977. Field observations on Ceratopogonidae and other Diptera: Nematrochera associated with cocoa flowers in Brazil. *Bulletin of entomological research* 67(1):57-63.

Young A.M. 1982a, Population Biology of Tropical Insects. Plenum Press, New York: p 511.

Young A.M. 1982b. Effects of shade cover and availability of midge breeding sites on pollinating midge populations and fruit set in two cocoa farms. *Journal of Applied Ecology* 19:47-63.

Young A.M. 1983. Seasonal differences in abundance and distribution of cocoa-pollinating midges in relation to flower and fruit set between shaded and sunny habitats of the la lola cocoa farm in Costa Rica. *The Journal of Applied Ecology* 20(3):801-831.

Aquatic Insects as Bioindicators for Sustainable Water Use: A Comparative Analysis of Three Water Reservoirs in Thailand

► Kimberly Nelson¹, Songyot Kullasoot²

Advisors: Dr. Richard Deming¹, Dr. Chitchol Phalaraksh²

¹California State University, Fullerton ²Chiang Mai University, Chiang Mai, Thailand

Abstract

Water quality in three reservoirs at the Banpu coal mines in Northern Thailand were monitored using aquatic insects as bioindicators, along with pond net sampling of submerged vegetation, acidity measurements and chemical analysis. Despite the low pH of 4 at site BP2, many more insects (1605) were found in this pond compared to site BP1-G (308) and BP1-B (242). Seventy five specimens in the family Baetidae were found in BP2, but only five Baetidae were found in sites BP1-B and two in BP1-G, indicating poor water quality in BP2. Chemical analysis indicated high levels of dissolved solids in all sites (433-580 mg.L⁻¹), but site B2 had high ammonia (1.47-1.97 mg.L⁻¹) and dissolved oxygen (6.6-7.6 mg.L⁻¹). Since the ponds are used by the local villagers, these results indicate that site BP2 is unsuitable for use, while sites BP1-B and BP1-G may be acceptable.

Introduction

One of the greatest challenges for countries around the world is the development of safe and reliable water sources (creeks, rivers and ponds) to improve local living conditions while

maintaining the ecological health of the water supplies. Regular monitoring the water quality of natural sources will help protect aquatic life and improve human health (Sangpradub and Boonsoong, 2006) and biological techniques, including the study of aquatic insects as bioindicators, can be used to monitor the overall health of water sources to allow for sustainable water usage. A bioindicator is a group of species that reflects abiotic or biotic factors in an environment that shows the impact

of an environmental change on an ecosystem (McGeoch, 1998). Aquatic insects have characteristics that make them good bioindicators (Paradise and Dunson, 1997): they are high in abundance, highly diverse, and their wide distribution allows them to occupy different trophic categories in many aquatic systems (Sangpradub and Boonsoong, 2006; Paradise and Dunson, 1997).

The village of Banpu in Li district of Lamphun Province Northern is situated near extensive soft coal

Appendix A



Figure 1. Map of Thailand (left) and map of Lamphun Province (right) with Li district shaded.



Figure 2. Banpu reservoir study sites BP1-G, BP1-B, and BP2
 BP1-G Location: N 17° 46.979, E 99° 00.067; BP1-B Location: N 17° 48.091, E 99° 00.921;
 BP 2 Location: N 17° 48.091 E 99° 00.921 (www.pointasia.com)

(lignite) deposits which have been mined since 1983 (Figure 1). The village recently closed the coal mines and turned the empty mine sheds into water reservoirs, named BP1-G, BP1-B, and BP2 (Figure 2). These man-made reservoirs were a way to provide villagers with access to water and aide in developing a sustainable food source for local villagers. The high sulfur content of the coal deposits, residual fly ash and the SO₂ emissions from the nearby coal-fired power plant in neighboring Lampang province have resulted in significant degradation of water quality that has lead to health concerns.

To better assess the quality of water in the three reservoirs, a insects were collected using the submergent vegetation technique were conducted to compare the water quality of the three sites. The high sulfur content of the deposits in the area would likely increase the acidity of the water, and it was predicted that the most acidic site would have the largest numbers of insects and that their species distribution would reflect the overall water quality. In addition to monitoring

of insect populations and diversity, measurements of pH, total dissolved solids (TDS), dissolved oxygen (D), biological oxygen demand (BOD), nitrate, ammonia, and conductivity were carried out at different depths, down to 20 meters.

Methods

Banpu village lies in the Li district in the southern part of the Lamphun province, about 105 km southeast of Chiang Mai, in Northern Thailand. Sampling was conducted in three nearby water reservoirs named Banpu 1-B (BP1-B), Banpu 1-G (BP1-G), and Banpu 2 (BP2) as shown in the aerial satellite photo in Figure 2.

Chemical Techniques

Water samples were taken using a Van Doren water sampler at the surface and at depths of 5, 10, 15, and 20 meters. These water samples were then taken to the chemistry lab at Chiang Mai Rajabhat University, and Levels of dissolved oxygen (DO), ammonia (NH₃), temperature in

degrees Celsius, total dissolved solids (TDS), biological oxygen demand (BOD), conduct, and nitrate (NO₃) were determined for the samples from each of the reservoirs. These results were compared values that would be considered as normal water quality factors.

Biological Techniques

Using a pond net, a technique called submergent vegetation was performed on July 26, 2008 during the rainy season. The pond net was used to rub the vegetation along the surface and under the water to collect aquatic insects that inhabit the water reservoir. In areas inaccessible by foot, a boat was used for collection. The items on the net were emptied into a pan and placed into a plastic bag and labeled. Next, the contents were mixed with alcohol to preserve the specimens. Samples were taken at BP1-B, BP1-G and BP2 and brought back to the aquatic insect lab at Chiang Mai University, in Chiang Mai, Thailand, where the insects were sorted, identified, and analyzed.

Insects were identified in the lab of Dr. Chitchol Phalaraksh using an aquatic insect key (Sangpradub and Boonsoong, 2006) and a key developed by the participants of the aquatic insects laboratory. Results were then analyzed using a paired mean sample t-test to see differences between insect orders and among the three water reservoirs. Aquatic insect families were also compared with the Thailand Stream Invertebrates handbook (Kanjanavanit, 2002) which is a guide available in English. In addition, local villagers aided in the identification of aquatic insects.

Table 1

BP1-B Physical-Chemical Parameters of Banpu Coal Mine Reservoirs

Depth (m)	Water Temp($^{\circ}$ C)	pH	TDS (mg.l ⁻¹)	DO (mg.l ⁻¹)	BOD (mg.l ⁻¹)	NO ₃ ⁻ (mg.l ⁻¹)	NH ₃ (mg.l ⁻¹)	Conduct. μ S.cm ⁻¹
0	32.5	7.10	505	4.6	0	0.9	0.09	1052
5	31.5	7.05	503	4.6	0.2	0.7	0.16	1044
10	29.0	6.64	510	0.8	0	1.4	0.21	1054
15	28.5	6.82	517	1.2	0	1.3	0.22	1070
20	28.0	6.86	521	1.4	0	1.0	0.37	1069

BP1-G Physical-Chemical Parameters of Banpu Coal Mine Reservoirs

Depth (m)	Water Temp($^{\circ}$ C)	pH	TDS (mg.l ⁻¹)	DO (mg.l ⁻¹)	BOD (mg.l ⁻¹)	NO ₃ ⁻ (mg.l ⁻¹)	NH ₃ (mg.l ⁻¹)	Conduct. μ S.cm ⁻¹
0	32	6.40	455	4.8	0	1.2	0.03	957
5	31	6.13	440	1.6	0	1.4	0.04	924
10	29	6.03	470	1.8	0	1.1	0.14	973
15	28	6.07	433	4.4	0	1.0	0.14	975
20	28	6.47	472	0.6	0	1.1	0.22	982

BP2 Physical-Chemical Parameters of Banpu Coal Mine Reservoirs

Depth (m)	Water Temp($^{\circ}$ C)	pH	TDS (mg.l ⁻¹)	DO (mg.l ⁻¹)	BOD (mg.l ⁻¹)	NO ₃ (mg.l ⁻¹)	NH ₃ (mg.l ⁻¹)	Conduct. μ S.cm ⁻¹
0	29	4.04	538	6.6	0	1.2	1.80	905
5	28	4.13	570	6.6	0	1.1	1.97	960
10	25.5	4.04	532	6.6	0	1.0	1.86	906
15	25.0	4.05	560	7.6	2.2	1.2	1.47	980
20	25.0	4.04	580	6.6	1.7	1.2	1.96	980

Table 1. Physical-chemical parameters of water from Banpu Coal Mine water reservoirs, BP1-B, BP1-G, and BP2. BP2 is known as the acidic reservoir due to its average pH of 4.6.

Results

Chemical Techniques

Physical-chemical characteristics of water from BP1-B, BP1-G, and BP2 are in Table 1. While moderate to neutral/slightly acidic water conditions exist in BP1-B and BP1-G, the pH survey shows that severe acidic conditions exist in BP2. This can be due to the large amounts of sulfur, which is known to be acidic, visible in the surrounding areas of BP2.

The temperature of the water of all 3 reservoirs ranged from 25-32 $^{\circ}$ C at all depths. The total dissolved solids (TDS) showed high to medium concentrations of dissolved solids and sulfur with BP1-B having an average of 511.2 and BP2 having an average of 556. BP1-G shows the TDS levels being comparatively lower in their concentrations of dissolved solids having an average of 454. The Dissolved oxygen (DO) levels were higher in the more acidic BP2 reservoir than the other two sample sites,

showing the promising capability of sustaining more aquatic life. Nitrate levels did not show a significant difference between all three sites, but the ammonia levels were highest in the acidic reservoir BP2.

Biological Techniques

Table 2 reflects the distribution of insects collected from the three sites. Seventy-four percent of the insects collected from the three reservoirs were found in the acid reservoir

Appendix C

Aquatic insect of Banpu coal mine on 07/26/2008

Aquatic insect (family)	BP1G	Reservoir BP1B	BP2 (acid reservoir)
Order Hemiptera ***			
Corixidae	6	-	123
Belostomatidae	-	-	3
Hydrometridae	-	-	1
Notoecetidae	-	-	69
Veliidae	-	-	2
Psephenidae	-	-	1
Mesoveliidae	-	1	16
Nepidae	1	-	17
Gerridae	-	34	46
Order Odonata			
Zygoptera			
Corduliidae	5	40	35
Libellulidae	-	-	2
Coenagrionidae	3	2	128
Gomphidae**	5	3	-
Macromiidae	1	1	-
Order Diptera			
Chironomidae	225	131	723
Chironomidae (pupa)	27	16	56
Culicidae	-	-	209
Culicidae (pupa)	-	-	17
Ceratopogonidae (pupa)	1	6	51
Tabanidae	1	-	-
Order Ephemeroptera			
Baetidae*	3	5	75
Caenidae	26	10	-
Order Coleoptera			
Hydrophilidae	1	1	2
Dytiscidae	-	-	1
Order Lepidoptera			
Pyralidae	-	-	2
Order Trichoptera			
Polycentropodidae	3	1	25
Odonoceridae	-	1	1

Table 2. Total Aquatic insects from the Banpu coal mine reservoirs on July 26, 2008. *Insects in these families are known to thrive in polluted waters and are indicators of poor water quality. ** Insects in these families are known to not be able to survive in polluted waters and high levels indicate good water quality.

BP2. Most of the insects sampled were from the Order Diptera. In this order, the family Culicidae made up 226 of the BP2 sample, but none were in the BP1-G or BP1-B. Mayflies in the order Ephemeroptera are considered as an indicator of poor water quality. These mayflies were sig-

nificantly more abundant in BP2. In the mayfly family, Baetidae, BP2 had 75, but only 3 were in BP1-G, and 5 were found in BP1-B. The other family found in the order Ephemeroptera at these sites was Caenidae, which had 26 in BP1-G and 10 in BP1-B, but none were found in the

acid reservoir BP2. Caenidae is not an indicator of good water quality, but are known to not be able to survive in high levels of water pollution. The samples containing the order Hemiptera had 7 individuals in BP1-G, 35 (34 in the family Gerridae) in BP1-B, and 278 samples in BP2.

Discussion

The reservoir with the highest acidity, BP2, had the highest levels of dissolved oxygen, total dissolved solids, sulphur, ammonia nitrate levels. These parameters indicate that more aquatic life can be sustained within this reservoir. Seventy four percent of the aquatic insects came from BP2. Many studies have shown acidification of water sources to have negative effects on biodiversity (Petřin et al. 2007), but some feel that in naturally acidic water sources invertebrates have adapted to tolerate the low pH (Cherry et al. 1979; Petřin et al. 2007). It has been documented that specific groups of aquatic invertebrates, specifically the Odonates and Dipterans, have been more tolerant to stress such as coal ash and acidic water sources (Cherry et al. 1979). On the other hand, Ephemeroptera have been repeatedly documented for undergoing extreme loss of taxa due to shifts in water conditions (Pond et al. 2008). In a study by Pond et al. (2008), sampling was conducted in an unmined site and a mined site and results indicated a decline in the total richness and relative abundance of aquatic invertebrates with increasing mining disturbance. In the present study in the Banpu ponds, more Ephemeroptera were found in the highly acidic reservoir BP2, than the other two sites. A description in Kanjanavanit's (2002) identification

guide to stream invertebrates as an indicator for water quality, states that both of the Ephemeroptera families Baetidae and Caenidae both indicate moderate to poor water quality. Baetidae that were found mostly in the BP2 reservoir are known to live in harsher conditions due to their ability to swim rapidly from excess pollutants. The other family, Caenidae, is known to tolerate slightly poorer water quality, but none were found in the acidic reservoir BP2.

It was also noted that the only fish surviving in the water reservoir, BP2, was the climbing perch. Although no other fish has been able to survive in this reservoir, the climbing perch possess an extra accessory, an air-breathing organ, which enables them to survive in areas with lower pH levels. The climbing perch is known to survive on land in periods of low or no water.

In BP1 where pH levels are considered normal, multiple fish thrive. The walls of the BP1 water reservoir contained sulfur and ash that are not as visible as in BP2 where rocks are yellow and large amounts of leftover coal-ash can be seen bordering all sides of the water reservoir.

This study did find significant differences between the three reservoirs besides the extreme differences in pH between the more acidic BP2 reservoir and the BP1 and BP3 reservoirs. Some of the aquatic insects that are found in the acidic BP2 reservoir are indicators of poor water quality for human use. The high levels of sulfur in the area, the fact that only one fish species lives in this acid reservoir, and the occurrence of acid rain all indicate that there are significant threats to water quality in the BP2 reservoir. The fact that there are more varieties of fish in BP1-B and BP1-G

and fewer indications of poor water quality suggests that these are more suitable reservoirs.

Acknowledgements

We thank the Associated Students/IRA fund at California State University Fullerton for support of the Environmental Science Research in Thailand (ESRT) summer program; the aquatic insects laboratory, Chiang Mai University, Thailand; Ronald Nelson, Beverly Nelson, Ashley Nelson, Erica Pickett, Ronald Nelson II, Don Lundy, Dr. Chai, Dream and Nok.

References

Cherry, D., Guthrie, R., Sherberger, F., and Larrick, S. 1979. The Influence of Coal Ash and Thermal Discharges upon the Distribution and Bioaccumulation of Aquatic Invertebrates. *Hydrobiologia* 62(3): 257-267.

Kanjanavanit, O. 2002. Identification Guide to Stream Invertebrates. The Green World Foundation. 56pp.

Mc Geoch, M., and Chown, S. 1998. Scaling Up the Value of Bioindicators. *Trends in Ecology and Evolution* 13(2): 46-47.

Paradise, C.J., and Dunson, W.A. 1997. Effects of pH and Sulfate on Insects and Protozoans Inhabiting Treeholes. *Arch. Environ. Contam. Toxicology* 33: 182-187.

Petrin, Z., Laudon, H., and Malmqvist, B. 2007. Does Freshwater Macroinvertebrate Diversity along a PH- Gradient Reflect Adaptation to Low PH? *Freshwater Biology* 52:

2172-2183.

Pond, G., Passmore, M., Borsuk, F., Reynolds, L., Rose, C. 2008. Downstream Effects of Mountaintop Coal Mining: Comparing Biological Conditions using Family- and Genus-level Macroinvertebrate Bioassessment Tools. *Journal of the North American Benthological Society* 27(3): 717-737.

Sangpradub, N., and Boonsoong, B. 2006. Identification of Freshwater Invertebrates of the Mekong River and its Tributaries. Mekong River Commission, Vientiane. 274pp.

Singh, G. 1988. Impact of Coal Mining on Mine Water Quality. *International Journal of Mine Water* 7(3): 49-59.

Feeding Preferences of the Marine Gastropod *Aplysia Vaccaria*

► **Meredith R. Raith**

Advisor: **Dr. Danielle C. Zacherl**

California State University, Fullerton

Abstract

Understanding marine herbivore feeding preferences provides insight into how these organisms impact algal community structure. *Aplysia vaccaria*, the black sea hare, is a large herbivorous marine gastropod native to the California coast. Little is known about this species regarding its feeding ecology due to its temporally and spatially patchy distribution. To determine if *A. vaccaria* exhibits feeding preferences, we performed a series of paired-choice feeding trials. We used algae commonly found in its habitat including two brown kelps, *Egrecia menziesii* and *Macrosystis pyrifera*, along with the red alga *Plocamium cartilagineum* and the green alga *Ulva lobata*. We hypothesized *E. menziesii* would be preferred over other algal species because it is prevalent in *A. vaccaria*'s habitat and is thought to induce larval metamorphosis. After feeding trials, we analyzed for preference by comparing percent loss of mass (g) of algae consumed using paired t-tests. *E. menziesii*, *M. pyrifera* and *U. lobata* were significantly preferred over *P. cartilagineum*, while there was no significant dif-

ference in consumption between *E. menziesii*, *M. pyrifera*, and *U. lobata*. These three algal species were also eaten in ratios similar to each other regardless of the size of the individuals used in trials. Further studies on the feeding ecology of *A. vaccaria* may shed light on its importance as a grazer in marine communities.

Introduction

Marine herbivores feed on algal species for a variety of reasons including availability, edibility, palatability and nutritional value (Wakefield & Murray, 1998). If a food source is rare, then organisms will not graze on it extensively or exclusively, but resort to other, more readily available sources. A food item that is edible can be physically broken down by the organism while palatable food items taste good (Wakefield & Murray, 1998). In addition, nutritionally rich food items give the organism greater energy acquisition (Lubchenco, 1978). An especially desirable food item, then, would be readily available, digestible, palatable, and nutritious. However, multiple studies have found preference for food that does not meet these criteria (Cox and Murray, 2006; Wakefield and Murray, 1998),

suggesting there are additional factors determining why organisms graze upon certain foods.

For instance, many herbivores are considered generalists such as *Norrisia norrisii*, which feed on multiple kelp species (Wakefield and Murray, 1998). Other herbivores feed heavily on only a limited number of species. Extreme examples of these specialists are the slugs *Alderia modesta* and *A. willowi* which rely exclusively on the alga *Vaucheria longicualis*. This is probably because the alga is not only a food source, but also provides primary habitat for the slug (Krug, 1998). In addition, the alga provides the metamorphosis cue for the planktonic larvae. This phenomenon of specialization occurs with many other marine herbivores (Hay et al., 1990) and may lead to heavy utilization of specific algal species. It is necessary to determine which algal species are useful to herbivores and how the overall community structure may be affected.

Previous research has shown that molluscs are major herbivores in temperate habitats (Barry & Ehret, 1993) and have direct effects on benthic algal populations (Steinberg, 1985; Lubchenco, 1978). Therefore, understanding herbivore feeding preferences may elucidate how algal

communities change or the distributions of other organisms change. In addition, determining the preferences of little known species is especially useful because new insight can be gained in describing food choices, species interactions, abundance and effects on community structure.

The giant black sea hare, *Aplysia vaccaria*, is found in the low intertidal and in subtidal habitat along the Pacific Coast from Monterey Bay, CA to the Gulf of California (Behrens, 1991; Sept, 2002). Individuals are thought to live for only one year yet they reach lengths up to 99 cm and weights of 14 kg (Behrens, 1991). These animals must feed intensively to grow so quickly, yet little is known about their feeding strategies. In addition, this species is temporally and spatially patchy with individuals congregating in kelp beds and rocky areas along the intertidal and subtidal (Angeloni, 1999), perhaps making their feeding habits and impacts quite dynamic. From February to March, and sometimes into summer months, large aggregates of these sea hares move into shallower waters to mate (Angeloni, 1999), creating a potential for them to exert a significant impact on the intertidal community of algae. Because feeding preferences of this relatively understudied species are unknown, making predictions about their impact on intertidal communities is difficult. Here, we explored whether *Aplysia vaccaria* exhibits feeding preferences among four algal species common to southern California intertidal and shallow subtidal communities. Because this species is thought to settle preferentially onto *Egregia menziesii* (Angeloni, 1999), we hypothesized that *A. vaccaria* will preferentially consume this kelp over *Macrocystis pyrifera*, *Ulva lobata* and

Plocamium cartilagineum.

Materials and Methods

Collection and Care of A. vaccaria

During the months of February 2007 through August 2007, animals were collected from Wilder Annex in San Pedro, CA. Approximately 6-10 individuals were collected every two weeks during spring tides. Animals were brought back to the laboratory in a cooler and placed in individual feeding arenas in one re-circulating aquarium on a 12:12 hr light:dark cycle in 15°C ± 1°C filtered seawater. Nitrate, nitrite, ammonia and pH levels were checked daily to track water quality; feces were also removed daily. The animals acclimated to the lab environment for seven days, while being fed only romaine lettuce. This ensured that the previous algal species consumed were flushed from their system, and any feeding biases they had experienced in their natural habitat would be reduced (Cox & Murray, 2006). The animals were starved for 48 hours and then used in paired feeding trials for 48 hours. Each sea hare was used in only one feeding trial and after the trial was measured using volume displacement as a proxy for length or weight. After trials and measurements they were tagged before release back into the field to ensure they were not recaptured and used in future feeding trials.

Algal Species

The algae were collected from two field sites: Dana Point, CA and San Pedro, CA. The algal species used in this experiment included *Macrocystis pyrifera*, *Egregia menziesii*, *Ulva lobata*, and *Plocamium cartilagineum*.

These algal species are commonly found within the known range of *A. vaccaria* and could be potential food sources for the organism.

M. pyrifera is a large brown alga that can grow up to 60 m in length. It is found from Alaska to Baja, California in depths of less than 40 m and water temperatures of less than 20°C. Because it is available year-round and is a primary food source for many subtidal and intertidal organisms (Steinberg, 1985), it is a likely component of *A. vaccaria*'s diet. It is known to form dense kelp forests which create diverse ecosystems and suitable nursery habitats for young organisms (Leighton, 1966; Hay & Fenical, 1988).

E. menziesii is a common low intertidal that typically inhabits shallower depths than *M. pyrifera*. It is known to be a food source for many species including *A. vaccaria*'s congener *A. californica* and the limpet *Acamea inessa* (Kitting, 1980). This species is also thought to induce metamorphosis of the veliger larvae of *A. vaccaria* (Angeloni, 1999). *E. menziesii* grows primarily in the summer months, when *A. vaccaria* moves to shallower waters to mate, and provides some protection from wave action as well as lush nursery areas (Leighton, 1966).

Ulva lobata is a perennial green alga found throughout the intertidal as well as in the subtidal in calm waters (Hay & Fenical, 1988). It also grows prolifically near and around docks during the summer months at the field sites in this study (*M. Raith*, personal observation). Many organisms are known to eat this alga and it is especially useful when caring for marine organisms in captivity (Pennings, 1991). At both field sites utilized for collecting *U. lobata*

and *A. vaccaria*, the alga was most prevalent from July to September with the supply tapering off in late fall (M. Raith, personal observation). There was also noticeable grazing on this algal species by various organisms at the field sites. Typically *Ulva* spp. does not grow large blades because of constant grazing, but in and around docks herbivores are limited and larger blades are prolific.

Lastly, *Plocamium cartilagineum* is a red alga preferred by the congener *A. californica* (Korb, 2003), whose geographic and intertidal ranges overlaps with that of *A. vaccaria* (Morris Abbott & Haderlie, 1980). This alga is known to trigger metamorphosis of *A. californica* larvae (Pennings, 1991). *P. cartilagineum* is the least common alga in the field among those provided in the feeding trials.

Feeding Trials and Volume Displacement

Rather than use single or mixed-algal trials, paired feeding trials were used in order to determine which algal species would be the most preferred. This allowed for a simple analysis of choice. If more than two food items are presented it is possible that more than one difference will act on the species, so consumption of one type is not independent of consumption of another type (Peterson & Renaud, 1989). Furthermore, mixed feeding trial studies focus extensively on foraging theory aimed at determining why herbivores pick one food item over another (Peterson & Renaud, 1989). As a starting point we simply set out to determine if *Aplysia vaccaria* exhibits a preference using paired feeding trials which have proven successful in multiple other studies (Cox and Murray, 2006;

Wakefield and Murray, 1998, Steinberg, 1985).

Once collected, the algae were transported to the laboratory immersed in a cooler of fresh seawater. In the laboratory the algae were rinsed with fresh water, cleaned of any visible epiphytes, weighed to the nearest 0.1 g and presented to the individuals after their starvation interval. Sea hares were given 25-100 g of blades from each alga depending on body size. During feeding trials each animal and the algae pairs were placed in 15 cm x 10 cm polyurethane feeding arenas with 1.5 mm mesh screen sides to allow ample water flow. The feeding arena was weighted to the bottom of the tank while the algae were free floating in the arena. The animals had 48 hours to feed before the algae were reweighed. Each individual was observed for approximately 10 minutes at the beginning of the trial to determine if individuals would initially choose to feed on one alga over the other. There were a total of six algal pairs tested throughout the study: *E. menziesii* versus *M. pyrifera*, *E. menziesii* versus *U. lobata*, *E. menziesii* versus *P. cartilagineum*, *M. pyrifera* versus *U. lobata*, *M. pyrifera* versus *P. cartilagineum* and *U. lobata* versus *P. cartilagineum*. In addition, control arenas were also used to account for autogenic tissue loss. These consisted of the algal pairs in 25-100g amounts in feeding arenas for 48 hours in the absence of *Aplysia*.

After feeding trials were finished, I measured the volume (mL) of each animal using a large graduated cylinder. Each animal was measured approximately 10 times and the volumes averaged. Stressed animals would sometimes release large amounts of water which led

to dramatic size variation within an individual. If this occurred, individuals were allowed to recuperate for approximately 15-20 minutes before re-measuring displacement.

Data Analysis

Consumption of algae was compared by determining the percent consumed of each algal species. Because algae have different mass properties and lose mass at different rates (Peterson and Renaud, 1989; Cox and Murray, 2006), it is more accurate to determine percent losses over time than to rely solely on mass losses. Also it is important to ensure that the difference in percent loss of the algae consumed is greater than the difference in percent loss due to autogenic tissue loss. For that reason, t-tests comparing consumption of algal species between experimental and control setups were run on the data rather than directly comparing percent tissue loss due to grazing activity (*sensu* Cox and Murray, 2006). Since this study extended across seven months, experimental organisms generally increased in size throughout the time period. Thus, I determined the relationship between *A. vaccaria* size and average algal consumption using regression analysis to explore whether ontogenetic shifts in preference were evident.

Results

Aplysia vaccaria consumed three of the four algal species presented in paired feeding trials. A significantly greater percentage of tissue loss due to consumption occurred in *E. menziesii* (t-test, $p=0.0001$), *M. pyrifera* (t-test, $p=0.0001$) and *U. lobata* (t-test, $p=0.0006$) than

in *P. cartilagineum* after 48 hours in feeding trials (Fig 1). *Aplysia vaccaria* consumed similar amounts of *E. menziesii* and *M. pyrifera* (t-test, $p=0.259$), *E. menziesii* and *U. lobata* (t-test, $p=0.197$) and *M. pyrifera* and *U. lobata* (t-test, $p=0.068$) during paired feeding trials. Although there was no statistical significance in the amount consumed, 8 of 10 individuals consumed more *E. menziesii* over *M. pyrifera*, 5 of 7 consumed more *U. lobata* over *M. pyrifera* and 6 of 7 individuals consumed more *E. menziesii* over *U. lobata*.

Algae was consumed at a 1:1 ratio across size classes, and did not vary significantly (Regression, $p=0.066$; Fig 2). During trials, larger animals were found to consume more algae than smaller animals (Regression, $p<0.001$; Fig 3).

After feeding trials, the animals

were fed algae until they were released. Those given only *P. cartilagineum* during this interim consumed nothing, but given any of the other three algal species consumption was immediate.

Discussion

In two-choice feeding trials *Aplysia vaccaria* preferred to feed on the brown algae *E. menziesii*, and *M. pyrifera* and the green alga *U. lobata* over the red alga *P. cartilagineum*. Between the three most preferred algal species, there was no significant rank order in preference, though experimental animals did consistently eat a greater percentage of *E. menziesii* than *M. pyrifera* or *U. lobata*. As a follow up to determine if any preference exists between these three algal species, feeding trials using

mixed-algal diets could be performed. In many cases, organisms do not feed exclusively on only one food source (Leighton, 1966) but a mixture of food items which may provide increased nutrients and better growth (Wantanabe, 1984). In mixed-algal trials it is possible to observe decreases in what could be termed normal consumption of algal species observed in two-choice feeding trials. This is an artifact of organisms feeding not only on what is thought to be their preferred food source, but on other food sources as well (Wantanabe, 1984). Mixed-algal trials can also help determine various chemoreceptive responses, discriminatory behavior and ingestion rates (Wantanabe, 1984).

In all feeding trials *P. cartilagineum* mass decreased, but decreases matched autogenic tissue loss in the

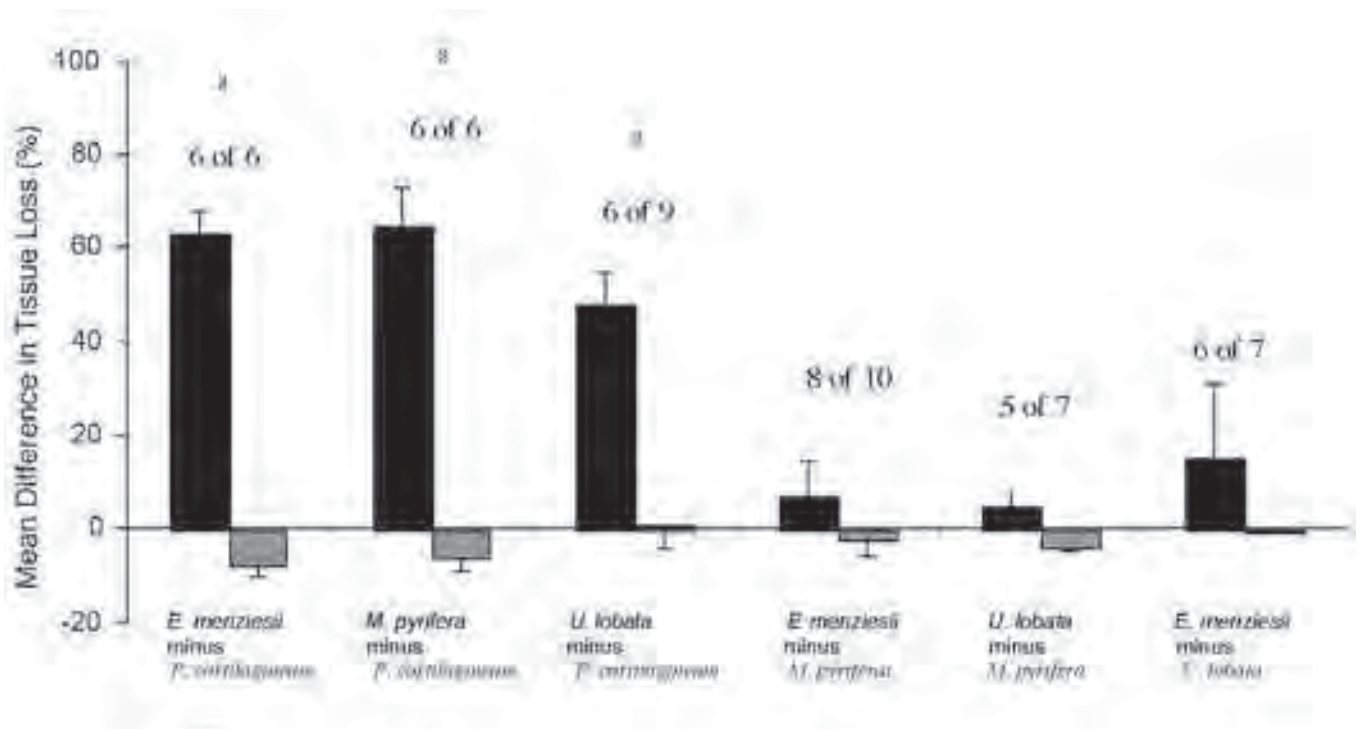


Figure 1. Results of two-choice feeding experiments with *Aplysia vaccaria* among algal species including *Plocamium cartilagineum*, *Egrecia menziesii*, *Macrocystis pyrifera*, and *Ulva lobata*. Data are mean (± 1 SE) percent differences in tissue loss when two algal species were offered together for consumption (black bars) and as controls in the absence of *A. vaccaria* (gray bars). Numbers above bars indicate number of individuals that consumed more of the first species listed. Star indicates significant preference ($p<0.05$) for the first alga in each pair.

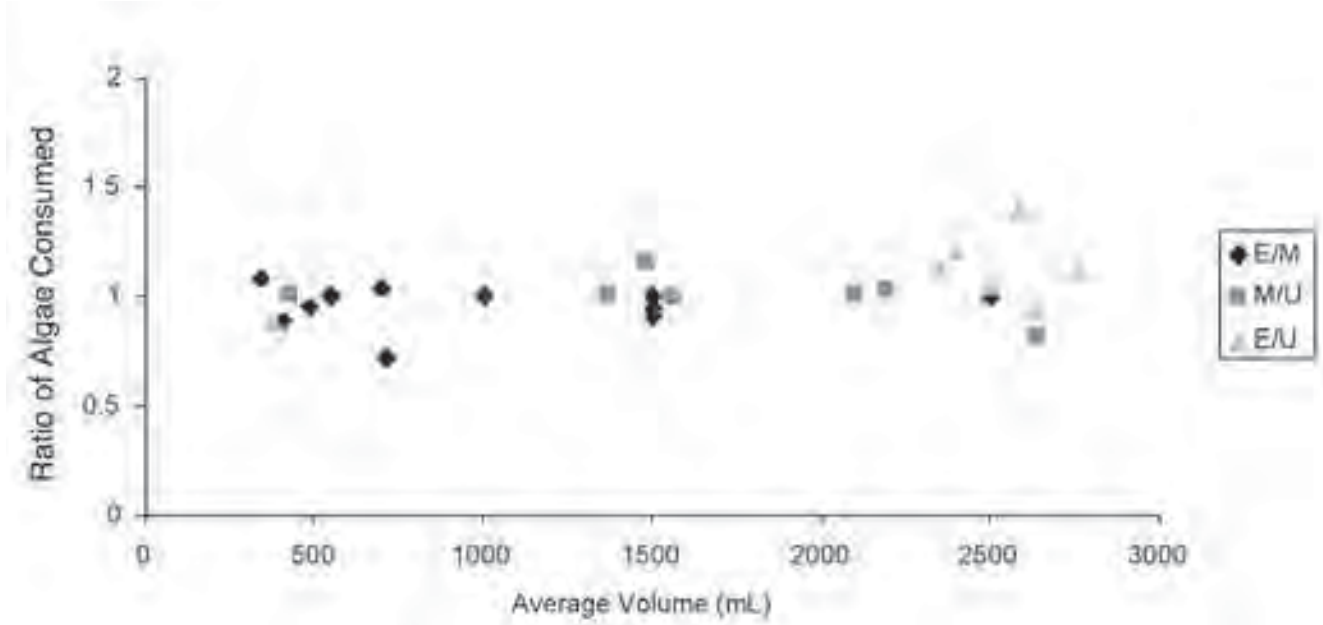


Figure 2. Ratios of algae consumed during paired feeding trials as a function of consumer volume. Consumption of *E. menziesii* : *M. pyrifera* (black diamonds), *E. menziesii* : *U. lobata* (dark grey squares) and *M. pyrifera* : *U. lobata* (light grey triangles) showed no significant change across size ranges of individuals (Regression, $n = 24$, $p = 0.066$).

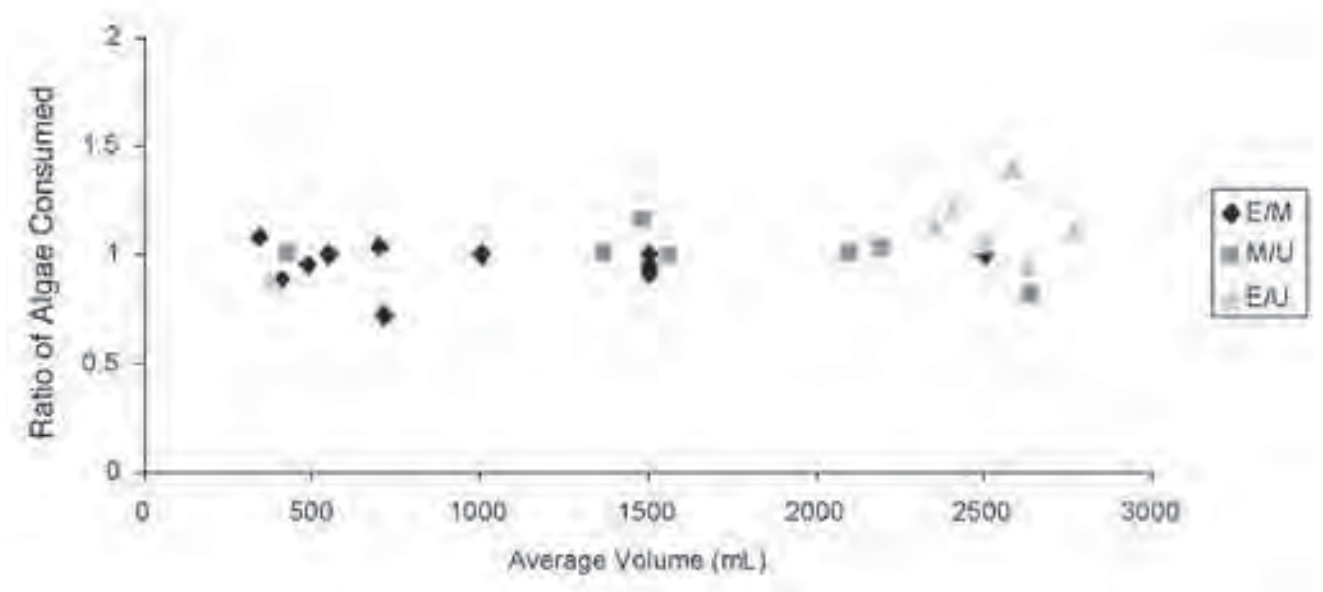


Figure 3. Relationship between the average volume of *Aplysia vaccaria* individuals and their average total algal consumption during feeding trials with all algal species that were consumed. Average total consumption of algae increased with greater volume (Regression, $p < 0.001$, $n = 41$, $R^2 = 0.45$).

controls, indicating very little to no consumption by *A. vaccaria*. Interestingly, even after trials were finished, individuals were kept in the aquaria up to a week before being released. Some were given *P. cartilagineum* for this interim and there was still no consumption observed despite immediate consumption of any of the other three algae offered. In addition, if the trial animals were given brown or green algae in pairs, they were eaten in nearly equal amounts. These observations concur with the experimental findings and suggest little specialization, but with a marked avoidance of *P. cartilagineum*.

The presumed dislike for *P. cartilagineum* by *A. vaccaria* may be due to its high secondary metabolite content (Korb 2003). Although many herbivores, such as *Aplysia californica* and *Aplysia parvula*, prefer algal species containing secondary metabolites such as terpenes, phenols or tannins (Pennings, 1990; Steinberg, 1985), some organisms cannot tolerate these chemicals. Interestingly, *P. cartilagineum* is the preferred food source for *Aplysia californica* with the secondary metabolites of this alga being incorporated into the ink and skin of this animal for defensive purposes. *A. vaccaria* may not have the cellular processes allowing successful break down of these chemicals, but this sea hare has been shown to sequester halogenated diphenols in its tissue. These compounds are obtained from brown algae in the family Dictyotaceae (Fenical, Sleeper, Paul, Stallard & Sun, 1979). The compound Pachydictyol A has been found within the digestive gland of *A. vaccaria*. Pachydictyol A is a chemical produced in the alga *Pachydictyon coriaceum* (Fenical et al., 1979), a brown algal species that is accessible to *A. vaccaria*.

It is possible that although there are no known predators to *A. vaccaria*, these and other compounds may be used as defense for younger or smaller individuals, or as a way to shunt toxicities of the algae into benign forms. Both *Navanax inermis* and *Panulirus interruptus* are known to prey upon *A. californica* (Pennings, 1991), so *A. vaccaria* juveniles or small adults may be susceptible to these predators as well. Chemical defense could be especially important to smaller individuals. For example, algal species most beneficial to specific age classes have been determined for *A. californica*, where more individuals survive when feeding on *P. cartilagineum* compared to other algal species (Winkler, 1961). Further, younger or smaller sized *A. californica* were only able to grow successfully to adulthood when reared on *P. cartilagineum* and sometimes *Laurencia pacifica* (Winkler, 1963) because individuals were less susceptible to predation when they consumed those algal species (Winkler & Dawson, 1963). *A. californica* juveniles are monophagous or oligophagous (Nadeau et al. 1989) and feed almost exclusively on *P. cartilagineum* or *L. pacifica* in order to build up toxins within their skin (Korb, 2003). However, as adults, their choices in food broaden and a repertoire of algal species are consumed (Carefoot, 1991). Juvenile *A. vaccaria* may similarly rely upon terpenes or tannins within *M. pyrifera* or *E. menziesii* for defense against predators. Further studies should explore whether the youngest life stages of *A. vaccaria* (smaller than used in this study) are chemically defended.

Besides chemical deterrents, the avoidance of *P. cartilagineum* displayed by *A. vaccaria* could also be

an artifact of resource partitioning in an effort to avoid competition with *A. californica* since the ranges and habitats of these species overlap (Kupfermann and Carew, 1974). *A. californica* uses *P. cartilagineum* not only for camouflage and direct access to food, but also as a method of allowing their veliger larvae to be in the presence of a food source (Pennings 1990). *A. vaccaria* may show a similar affinity for *E. menziesii*, because it is convenient for adults and larvae to stay close to food sources. The presence of this seaweed may then induce metamorphosis while also allowing for an immediate food source increasing their chances of survival (Nadeau, Paige, Starczak, Capo, Lafler & Bidwell, 1989). However, in our study there seemed to be no substantial preference for *E. menziesii* across the size classes of *A. vaccaria* studied suggesting other factors determine what, if any, algal species this sea hare consumes preferentially.

Other studies have noted that characteristics of a given food source, such as mechanical structure and "toughness" (Wakefield & Murray, 1998) also affect grazer choice. For example, *Aplysia punctata* specializes on the delicate red alga *Delesseria* when young and then migrates to the tougher *Laminaria* when older (Eales, 1921). In addition, some herbivores only eat certain portions of algae, such as the fronds or fleshy blades (Frings & Frings, 1965). The algal species presented to *A. vaccaria* were very different in their structures with *M. pyrifera* and *E. menziesii* having firm blades, *U. lobata* having large, soft blades and *P. cartilagineum* having thin rigid blades. The blades of *P. cartilagineum* could perhaps be too small or tough for *A. vaccaria* to consume. In addition, since only

blades were consumed, stipes may be too tough for consumption, not chemically attractive enough, or *A. vaccaria*'s feeding preference could be for blades instead of other portions of algae. There are many factors still unknown in dictating why *A. vaccaria* consumes specific algal species while avoiding others.

Lastly, considering the experimental design of this study, the subset of animals used in trials was quite small, and the time period was abbreviated. It would be valuable to extend experimentation using additional algae available within *A. vaccaria*'s habitat such as *Laminaria*, *Pterygophora*, *Eisenia*, *Silvetia*, *Codium* and *Dictyota* to further define feeding preferences. This would also allow for determination of any seasonal shifts this species may exhibit. In addition, because algal communities change seasonally and consumption may then vary depending on the algal species available, nutrient content of algal species and isotopic analysis may provide additional insight into the feeding habits of *A. vaccaria*.

This study provided a foundation for determining feeding preferences among common algae eaten by *A. vaccaria*. However, there are still many more food sources *A. vaccaria* has the ability to utilize. Future studies should also aim to uncover what impacts this massive grazer might have on community structure when it aggregates in shallow subtidal or intertidal habitats.

Acknowledgements

I wish to thank the Southern California Ecosystems Research Program (SCERP)/ Undergraduate Mentoring in Environmental Biology (UMEB), National Science Founda-

tion (NSF) #0602922 for the funding and guidance provided during the course of this research project. I also wish to thank the California Department of Fish and Game for providing collecting permits, the Cabrillo Marine Aquarium for helping with the acquisition of algal species. I also want to thank Dr. Bill Hoese for input on experimental and draft revisions. Thank you also to the lab and field assistants including: J. Chappell, A. Carrillo, C. Navarro, K. Walker, S. Kelley, J. Brum and L. Sam.

References

- Angeloni, L. 1999. Growth, seasonality, and dispersion of a population of *Aplysia vaccaria*. Winkler, 1955. *The Veliger*, 42(11), 1-9.
- Barry, J.P., Egret, M.J. 1993. Diet, food preference, and algal availability for fishes and crabs on intertidal reef communities in southern California. *Environmental Biology of Fishes*, 37(1), 75-95.
- Behrens, D.W. "Pacific coast nudibranchs." Monterey, CA: Sea Challengers, 1991. 42-3.
- Carefoot, T.H. 1967. Studies on a sublittoral population of *Aplysia punctata*. *Journal of Marine Biology*, 47, 335-50.
- Cox, T.E., Murray, S.N. 2006. Feeding preferences and the relationships between food choice and assimilation efficiency in the herbivorous marine snail *Lithoopoma undosum* (Turbinidae). *Marine Biology*, 148(6), 1295-306.
- Eales, N.B. "Aplysia." University of Michigan, MI: University Press, 1921. 81-3.
- Fenical, W., Sleeper, H.L., Paul, V.J., Stallard, M.O., Sun, H.H. (1979). Defensive chemistry of *Navanax* and related opisthobranch mollusks. *Pure and Applied Chemistry*, 51, 1865-74.
- Frings, H., Frings, C. (1965). Chemosensory bases of food-finding and feeding in *Aplysia Juliana* (Mollusca, Opisthobranchia). *Biological Bulletin of Marine Biology*, 128, 211-7.
- Hay M.E., Fenical, W. (1988). Marine plant-herbivore interactions: The ecology of chemical defense. *Annual Review of Ecology and Systematics*, 19, 111-45.
- Hay, M.E. J.E. Duffy and W. Fenical (1990) Host-plant specialization decreases predation on a marine amphipod: an herbivore in plant's clothing. *Ecology*, 71(2), 733-43.
- Kitting, C.L. (1980). Herbivore-plant interactions of individual limpets maintaining a mixed diet of intertidal marine algae. *Ecological Monographs*, 50(4), 527-50.
- Korb, R. 2003. Lack of dietary specialization in adult *Aplysia californica*: Evidence from stable carbon isotope composition. *Journal of the Marine Biological Association of the United Kingdom*, 83, 501-505.
- Krug, P.J. 1998. Peocilgony in an estuarine opisthobranch: Planktotrophy, lecithotrophy, and mixed clutches in a population of the ascoglossan *Alderia modesta*. *Marine Biology*, 132 (3):483-94.

- Kupfermann, I., Carew, T.J. (1974). Behavior patterns of *Aplysia californica* in its natural environment. *Behavioral Biology*, 12(3), 317-37.
- Leighton, D. 1966. Studies of food preference in algivorous invertebrates of southern California kelp beds. *Pacific Science*, 20, 104-13.
- Lubchenco, J. 1978. Plant species diversity in a marine intertidal community: importance of herbivore food preference and algal competitive abilities. *The American Naturalist*, 112, (983), 23-39.
- Morris, R.H., Abbott, D.P., Hadlerlie, E.C. "Intertidal invertebrates of California." Stanford, CA: Stanford University Press, 1980. 233-5.
- Nadeau, L., Paige, J.A., Starczak, V., Capo, T.R., Lafler, J., Bidwell, J.P. 1989. Metamorphic competence in *Aplysia californica* Cooper. *Journal of Experimental Marine Biology and Ecology*, 131(2), 171-93.
- Pennings, S.C. 1990. Size related shifts in herbivory: Specialization in the sea hare *Aplysia californica* Cooper. *Journal of Experimental Marine Biology and Ecology*, 142(1-2), 43-61.
- Pennings, S.C. 1991. Spatial and temporal variation in recruitment of *Aplysia californica* Cooper: Patterns, mechanisms and consequences. *Journal of Experimental Marine Biology and Ecology*, 146(2), 253-74.
- Peterson, C.H., Renaud, P.E. 1989. Analysis of feeding preference experiments. *Oecologia*, 80(1), 82-6.
- Sept, J.D. "The beachcomber's guide to seashore life of California." B.C. Canada: Harbour Publishing, 2002. 143.
- Steinberg, P.D. 1985. Feeding preferences of *Tegula funebris* and chemical defenses of marine brown algae. *Ecological Monographs*, 55 (3), 333-49.
- Wakefield, R.L., Murray, S.N. 1998. Factors influencing food choice by the seaweed-eating marine snail *Norrisia norrisii* (Trochidae). *Marine Biology*, 130(4), 631-42.
- Wantanabe, J.M. 1984. Food preference, food quality and diets of three herbivorous gastropods (Trochidae: *Tegula*) in a temperate kelp forest habitat. *Oecologia*, 62(1), 47-52.
- Winkler, L.R. 1961. Preliminary tests of the toxin extracted from California sea hares of the genus *Aplysia*. *Pacific Science*, 15, 211-4.
- Winkler, L.R., Dawson, E.Y. 1963. Observations and experiments on the food habits of California sea hares of the genus *Aplysia*. *Pacific Science*, 17, 102-5.

Environmental Factors that Affect Delayed Hatching on Development and Swimming Speed in the California Grunion, *Leuresthes Tenuis*

► Tracie Treybig, Allyson Degrassi, Ernesto Casillas, Elizabeth Hessom, and Elaine Ramos

Advisor: Dr. Kathryn A. Dickson

California State University, Fullerton

Abstract

The California grunion, *Leuresthes tenuis*, spawns on shore during spring high tides and fertilized eggs incubate 9-14 days until wave action stimulates hatching during the next spring high tide series. Embryos that are not washed out can remain viable for at least 35 days and may hatch during subsequent spring high tides. We hypothesized that larvae fertilized at two different also monitored the environmental conditions that grunion embryos experience on three beaches in southern California. Egg masses were located, their depths recorded, and tidal heights measured. Sand movements and temperatures at two depths (15 and 25 cm) were monitored at each beach for 32 h during a spring tide series. Mean sand temperature at depths where we found grunion egg masses ranged from 17.5°C to 23.7°C. Temperature fluctuated by as much as 11.4°C and varied more at shallower depths. These differences in temperature will affect the rate of grunion embryonic development and when they are ready to hatch. Based on measured tidal heights of the egg masses, predicted tides

and sand movements within the environment, embryos at all three beaches may be forced to delay hatching. We compared development and swimming speed in 30-days-post-fertilization (dpf) larvae and 14-dpf larvae. The 30-dpf larvae were significantly longer, had less yolk, and fewer myotomes than the 14-dpf larvae, but swimming speed did not differ between the two groups. Delayed hatching resulted in larger, more developed larvae with reduced energy reserves, which may impact post-hatching survival in *Leuresthes tenuis*.

Introduction

The California grunion, *Leuresthes tenuis*, is one of the few species of fish known to leave the ocean to spawn on sandy beaches (Walker, 1952; Symder and Martin, 2001). Their spawning season begins in March and extends until August (Walker, 1952; Symder and Martin, 2001). *L. tenuis* typically spawns twice a month, during new and full moons, just after the highest high tides (Walker, 1952; Thomson, 1972). During this time, *L. tenuis* adults ride the waves ashore, the female wiggles into the liquid sand tail first until only her head is visible,

and she then deposits her eggs approximately 5 cm deep (Thompson, 1976). Meanwhile, multiple males encircle her and release sperm into the sand to fertilize the eggs within the sand.

From the time the eggs are laid in the sand until it is time for the eggs to hatch, sand particles are continuously shifting due to wind and receding tides. This process either exposes or further buries the eggs, anywhere from 15 to 20 cm (Thomson and Muench, 1976). At 18°C the grunion eggs are developmentally ready to hatch 9-10 days post-fertilization (David, 1939; Darken et al., 1998). If the first high-tide series after spawning does not trigger the eggs to hatch, for instance, the embryos can delay hatching and extend incubation. During that time, the embryos use their yolk as a source of energy to survive (Smyder and Martin, 2002). In the laboratory, grunion embryos can extend incubation time up to 35 days and still be viable (Darken et al., 1998). Therefore, in the field, grunion should be able to extend hatching for two subsequent spring high tide series.

Environmental variables can reduce the probability of survival for grunion embryos. First, the tidal height and the depth of embryos

in the sand on the beach determine whether a spring high tide will reach the incubating embryos to trigger hatching. Second, temperature during incubation affects the rate of development and the minimum incubation time (Smyder and Martin, 2002).

The purpose of our field and laboratory research was (a) to characterize the environment in which grunion embryos develop and (b) to investigate how delayed hatching affects *L. tenuis* development and swimming performance. Three environmental variables were measured: the depth of incubating grunion embryos, tidal height of embryos, and temperature of sand at depths of 15 cm and 25 cm (within the range of depths of incubating embryos). In the laboratory four variables were measured in grunion larvae hatched at 14 days post-fertilization (dpf) and 30 dpf: number of myotomes, surface area of yolk, notochord length, and swimming speed. We hypothesized that grunion larvae hatched at 30 dpf (delayed hatching) would be in a later development stage than 14-dpf grunion larvae; thus, they would have more myotomes, less yolk, greater notochord lengths, and faster swimming speeds.

Methods

Environmental data were collected to provide more extensive knowledge of habitat conditions experienced by *L. tenuis* embryos. In this study three different sandy beach environments in Los Angeles and Orange Counties were investigated: Doheny Beach in Dana Point (33.46147°N, 117.68859°W), Seal Beach in Huntington Beach (33°44417°N, 118.06900°W), and Cabrillo Beach in San Pedro (33.70916°N,

118.28419°W). One day prior to a spring high tide, *L. tenuis* egg masses from recent spawns were located and their depths in the sand, tidal heights, sand temperature, and sand movements were measured.

Tidal heights of egg masses were measured at three sites on each beach using a survey tripod. The water height (cm) was measured at different times, at different beaches, and at variable tidal heights; therefore, the Tide and Current Predictor of the University of South Carolina Department of Biological Sciences provided the actual tidal height at the given hour of the day. This information was used to calculate the tidal height of the egg masses relative to mean low low water (MLLW) = water height (cm) – [(tidal height of plots (cm) - grunion egg mass depth (cm)) + actual tidal height (cm)].

Sand temperature was measured using temperature loggers (Onsite Tidbit model TBI32-05+37) deployed at depths of 15 cm and 25 cm for a 32-h period at three different sites on each of the three beaches. The two depths were chosen because most of the egg masses were found within this depth range. Sand temperature was recorded at 30-min intervals. When the temperature loggers were recovered, the depth of each data logger was recorded in order to estimate the change in depth of grunion embryos due to sand movement.

During two separate spawning runs at Cabrillo Beach, eggs and sperm from adult grunion were collected separately by gently pressing on the ventral body surface. Eggs were collected in filtered sea water, whereas sperm were collected in dry beakers. The eggs and sperm from multiple males and females were combined in filtered sea water for 15-20 min. The

fertilized eggs were then rinsed with filtered sea water to remove excess sperm. Lastly, the fertilized eggs were placed on moist paper towels in plastic containers which were maintained in temperature-controlled incubators at California State University, Fullerton (CSUF).

Grunion larvae used in the experiment were hatched from two groups of embryos by agitation in filtered sea water. The larvae representing delayed hatching, hatched at 30 dpf, were from eggs fertilized on May 20, 2008. These fertilized eggs were first kept at approximately 22-23°C for 13 days at Cabrillo Marine Aquarium, followed by incubation at 20°C for 17 days, until they were hatched and used in experiments on June 19 (n=20). The 14-dpf larvae were from eggs fertilized on June 5, 2008, and incubated continuously at 20°C until hatched and used in experiments on June 19 (n=20).

The 30-dpf and 14-dpf groups were hatched five at a time, so that the time elapsed between when the embryos were hatched and when the larvae were experimented upon was similar. First, swimming speed was measured in a metal channel “swim track,” 1.3 m x 12.8 mm x 14.2 mm (l x w x h). The channel was filled to a depth of 11.2 mm with 240 mL of room temperature (21°C ± 2) filtered sea water with a salinity of 31 ppm. The channel was cleaned eight times throughout the experiment. One of the ten newly hatched fish from 30 dpf or 14 dpf was randomly chosen and placed at the beginning of the channel using a pipette. The time it took each larval fish to swim 0.5 m was recorded and converted to speed (mm s⁻¹). Relative speed for each fish was calculated by dividing by notochord length in mm. If the fish swam

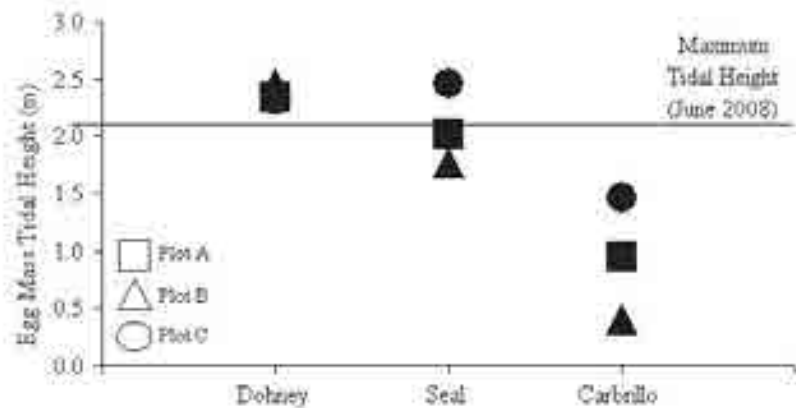


Figure 1. Tidal height of grunion egg masses at three plots on each of the three beaches sampled in June 2008. The horizontal line is the maximum tidal height in June, based on the MLLW.

too close to the side of the channel, switched directions, or did not swim the full 0.5 m, that fish was excluded from the comparison.

After each fish completed the swimming trial, it was anesthetized in Tricaine methanesulfonate (MS-222; 1g: 2.5L). The notochord length (mm) of each *L. tenuis* was measured using a dissecting microscope with a calibrated ocular micrometer. The yolk surface area (mm²) was calculated as the area of an ellipse based on measurements of the major and minor axes of the yolk using the ocular micrometer. The number of myotomes, or muscle segments, of each fish was counted three times and averaged. Effects of delayed hatching were assessed by testing for significant differences between the 14-dpf and 30-dpf larvae in the four variables measured.

Results

We determined that the depths of the grunion egg masses corresponded to tidal heights ranging from 0.39 cm to 2.46 cm above MLLW (Fig. 1).

Grunion egg masses were found higher on shore at Doheny Beach than at either Seal Beach or Cabrillo Beach and were higher than the maximum tidal height for June (Fig. 1). After 32 h, the temperature data loggers had been covered by an additional 7.16 cm of sand at Cabrillo Beach and 4.66 cm at Seal Beach, but were uncovered and therefore made shallower by 5.43 cm at Doheny Beach (Fig. 2). Sand temperature fluctuated during the 32-h monitoring period at the two depths (Fig. 3). At all three

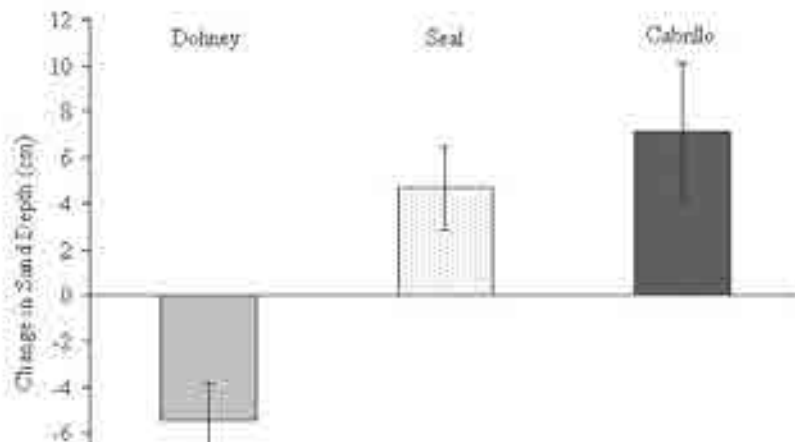


Figure 2. Mean (\pm S.D.) change in depth of temperature loggers after 32 h in the sand at the three beaches studied. Sand movement is represented by sand deposition (+) and sand erosion (-).

beaches the temperature recorded varied more at 15 cm than at 25 cm, with an overall average temperature of approximately 20°C. Seal Beach had the highest temperature range at both depths (Fig. 4).

The state of larval development varied between the two groups. The yolk surface area was significantly smaller in the 30-dpf larvae ($n=20$ per group, $t=4.55 \times 10^{-10}$, $P<0.001$; Fig. 5). Significantly more muscle segments (myotomes) were found in the 14-dpf larvae ($n=20$ per group, $t=0.045$, $P<0.05$; Fig. 6). Notochord length was significantly greater in the 30-dpf larvae ($n=20$ per group, $t=1.80 \times 10^{-5}$, $P<0.001$; Fig. 7). The swimming speed did not differ significantly between the two groups, ($n=9$ for 14-dpf and $n=15$ for 30-dpf; $t=0.37$; $P>0.05$; Fig. 8).

Discussion

The major findings of this study are that the variable environmental conditions that grunion embryos encounter, specifically the heights of the spring high tides, temperature, and sand movements, may affect grunion development and may lead to delayed

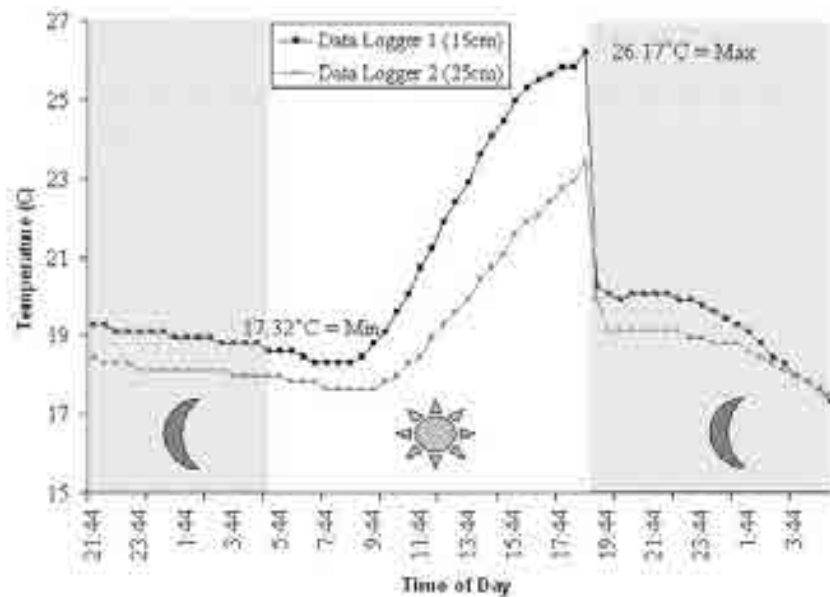


Figure 3. Sand temperature at 15 cm and 25 cm below the surface measured every 30 min over a 32-h period at Cabrillo Beach.

hatching. Furthermore, if hatching is delayed, these grunion larvae will be more developmentally advanced, but will have similar swimming speeds and less yolk as an energy reserve than grunion hatched earlier.

The egg masses at Doheny Beach were found higher on shore than the maximum tidal height for June, whereas the egg masses at Seal Beach and Cabrillo Beach were found to be lower than the maximum tidal height (Fig. 1). Thus, some embryos at Doheny Beach may not have been stimulated to hatch because the water would not have reached them. Another variable that may affect the probability of wave action from stimulating the embryos to hatch is the sand movement above developing embryos. At Seal and Cabrillo Beaches, egg masses experienced sand deposition, whereas embryos at Doheny Beach were found shallower in the sand due to sand removal as a result of erosion or wind, making the embryos at Doheny Beach more likely to be stimulated to hatch.

The temperature at which the

embryos incubate affects the length of time embryos can delay hatching because it alters the rate of development (Smyder and Martin, 2002). Our results show that sand temperatures varied more at 15-cm than at 25-cm depth and that temperatures at Seal

Beach are greater than at the other two beaches. Therefore the embryos at Seal Beach would not be able to delay hatching for as long as these other two beaches.

In our laboratory experiments, two of our hypotheses were supported: delayed hatching resulted in significantly less yolk (Fig. 4) and a greater notochord length (Fig. 6) in the 30-dpf larvae compared with the 14-dpf larvae. The number of myotomes also differed significantly between the two groups (Fig. 5), but not in the direction predicted. The 14-dpf larvae had more muscle segments than did the 30-dpf larvae. This observation can be explained because the number of myotomes that form during early development is inversely related to incubation temperature (Ehrlich and Farris, 1970). The 30-dpf larvae were initially incubated at a slightly higher temperature during stages when myotome number is established and thus had fewer myo-

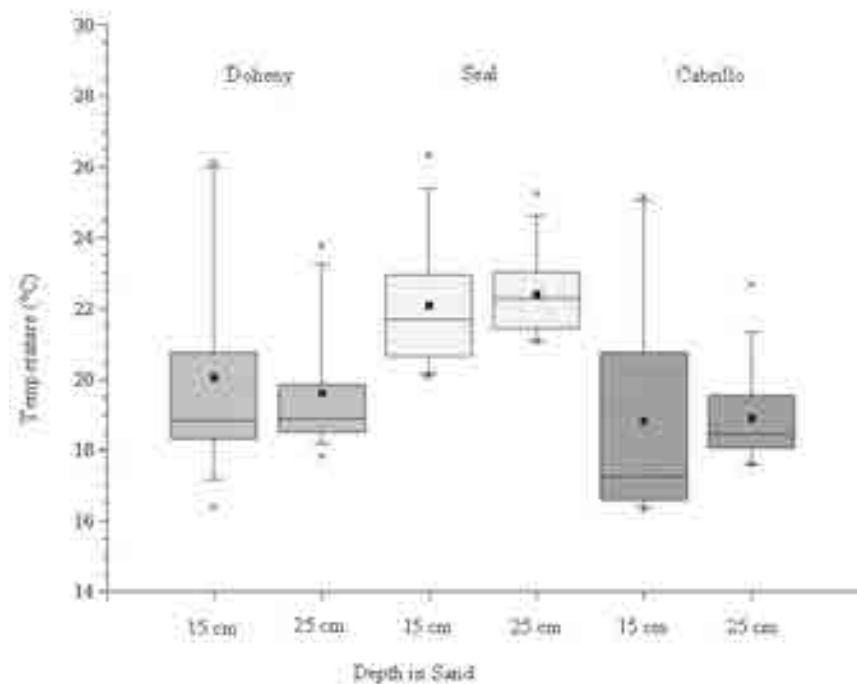


Figure 4. Median (solid line), mean (black square), (x marks are the minimum and maximum temperatures) middle 50% (filled) and 80% (open), sand temperatures at 15 cm and 25 cm depths, recorded over 32 h at three beaches sampled in June 2008.

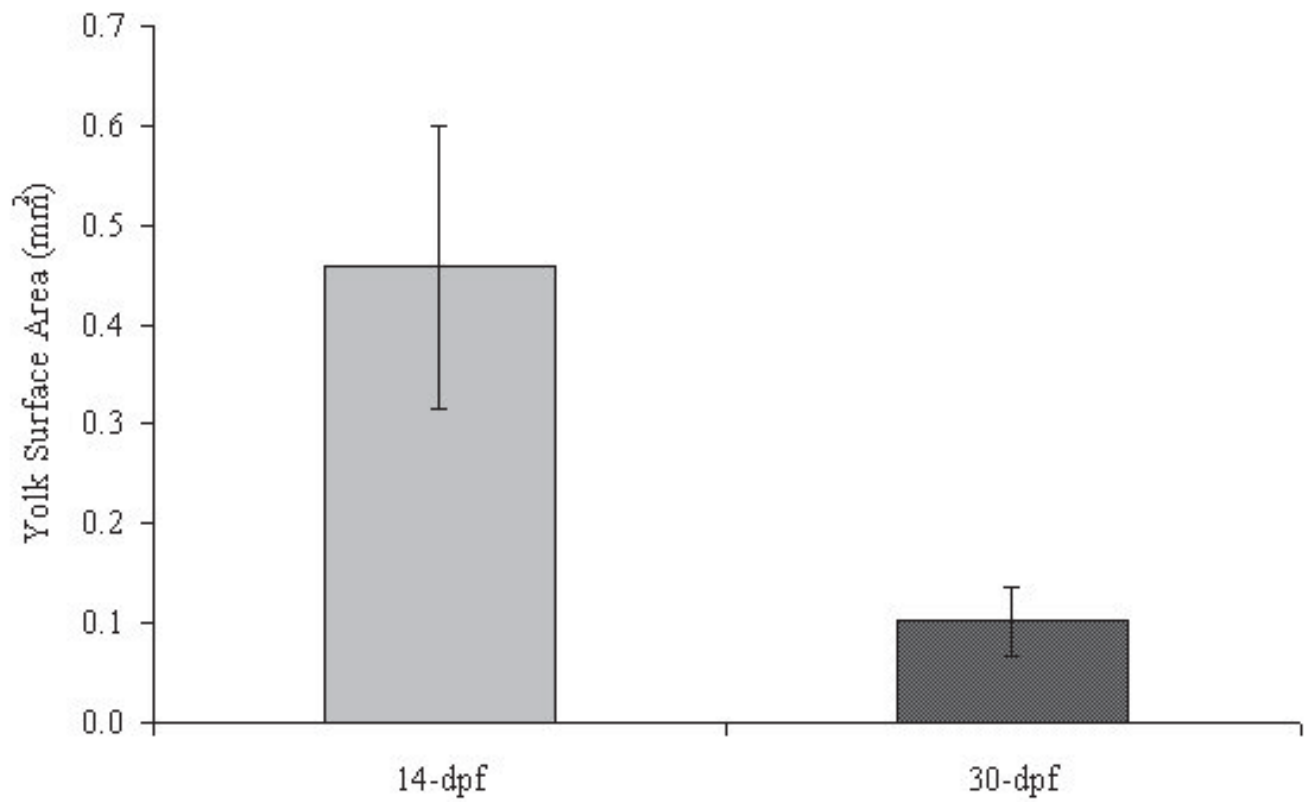


Figure 5. Mean (\pm S.D.) yolk surface area of each larva was measured for the 14-dpf and 30-dpf larvae. The 30-dpf larvae had significantly more yolk ($n=20$ per group, $t=4.55 \times 10^{-10}$, $P<0.001$).

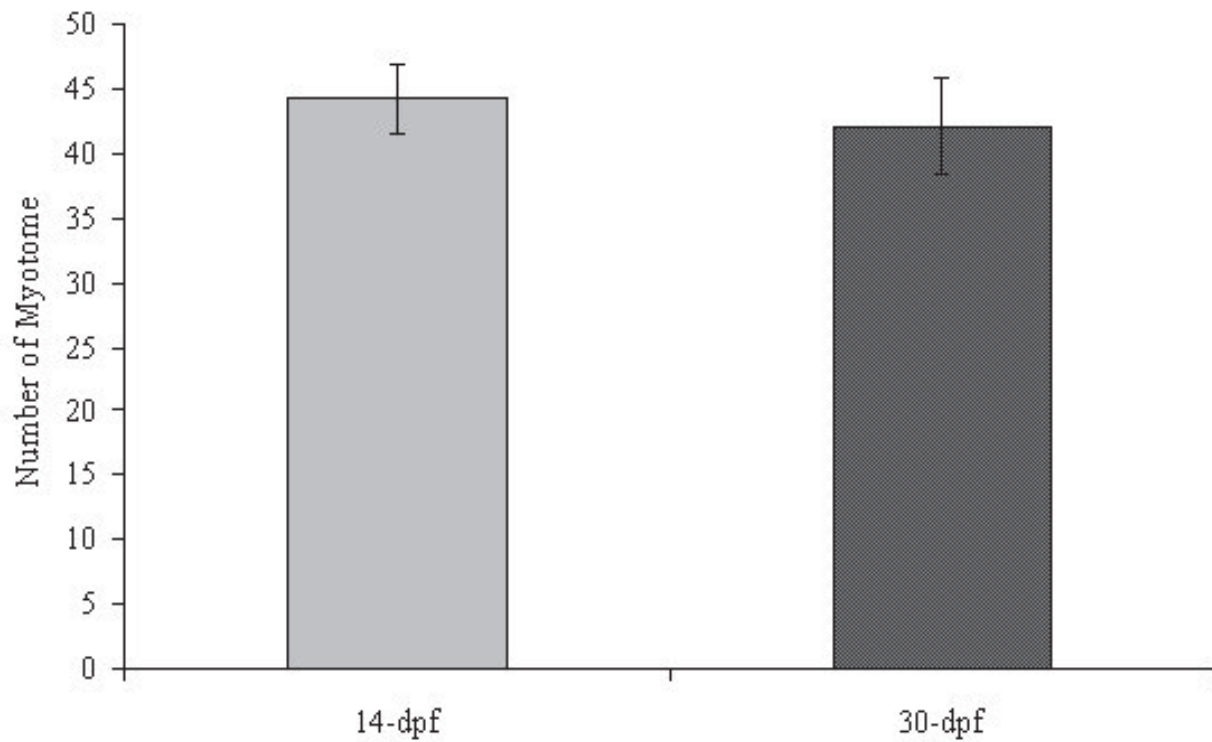


Figure 6. Mean (\pm S.D.) segments of muscle (myotome number) for the 14-dpf and 30-dpf larvae. The 30-dpf larvae had significantly fewer number of myotomes ($n=20$ per group, $t=0.045$, $P<0.05$).

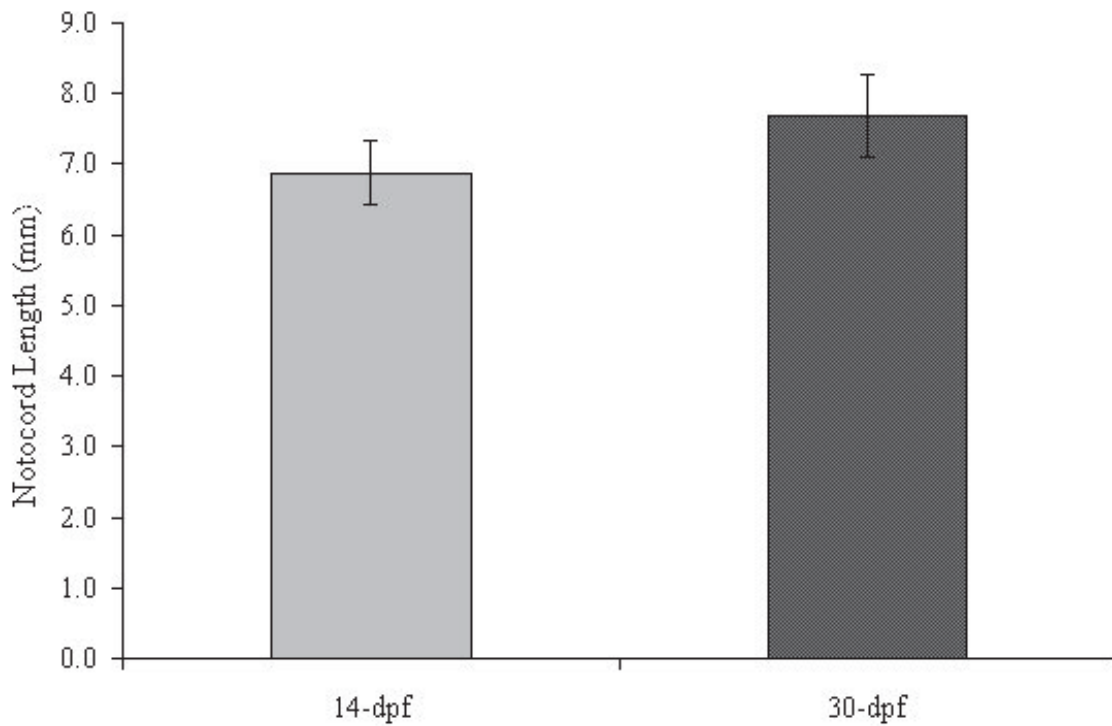
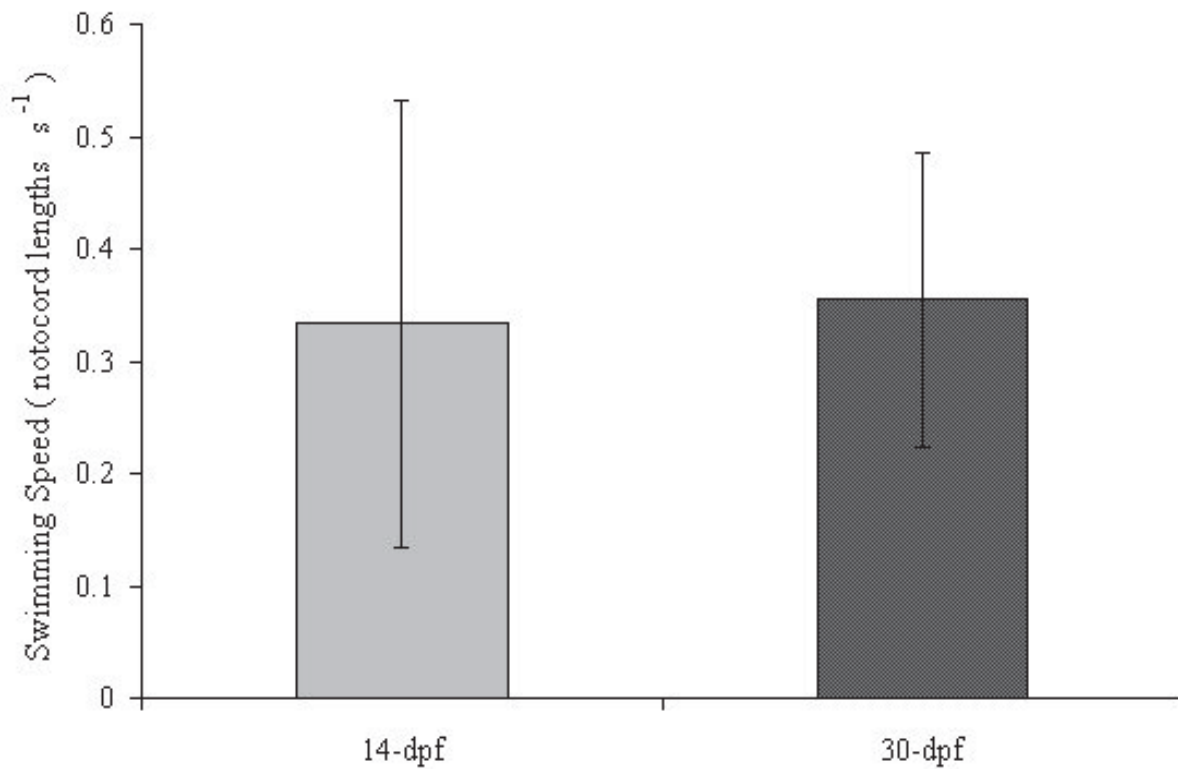


Figure 7. Mean (\pm S.D.) notocord length of the 14-dpf and 30-dpf larvae. The 30-dpf larvae had a significantly greater notocord length ($n=20$ per group, $t=1.80 \times 10^{-5}$, $P<0.001$).



comes at hatching than the 14-dpf larvae (Smyder and Martin, 2002). The greater notocord length of

Figure 8. Mean (\pm S.D.) swimming speed of each larvae, calculated over a distance of 0.5 m, for the 14-dpf and 30-dpf larvae ($n=20$, $t=0.37$, $P>0.05$). No significant difference was found between the two groups.

the 30-dpf larvae in this study suggests that they are more developmentally advanced than the 14-dpf larvae. If the 30-dpf larvae also have more developed sensory systems, muscle, and skeleton, they may have more keen perception of their environment, may be better able to capture prey and escape predators, and thus have an advantage over larvae that hatch after shorter incubation periods. Despite this difference, the swimming speeds of the two groups did not differ significantly. Furthermore, there may be disadvantages to delayed hatching. The 30-dpf larvae had less yolk and thus lower energy reserves and less time before they would have to feed once they hatched, compared to the 14-dpf larvae.

Although we examined effects of delayed hatching, the two groups of grunion larvae we compared also differed in incubation temperature and had different parents. These two factors could also contribute to differences in the variables that we measured. Thus, we are repeating and expanding these experiments to isolate effects of delayed hatching by investigating larval muscle and skeleton development and feeding performance. When these ongoing experiments are completed, we should gain a better understanding of the costs and benefits of delayed hatching in the California grunion.

References

- Darken, R.S., Martin K.L.M., and M.C. Fisher. 1998. Metabolism during delayed hatching in terrestrial eggs of a marine fish, the grunion *Leuresthes tenuis*. *Physiological Zoology* 71: 400-406.
- David, L.R. 1939. Embryonic and early larval stages of the grunion, *Leuresthes tenuis*, and of the sculpin, *Scorpaena guttata*. *Copeia* 1939: 75-81.
- Ehrlich, K.F. and D.A. Farris. 1970. Effect of temperature on number of myomeres in newly hatched grunion (*Leuresthes tenuis*). *Copeia* 1970: 774-775.
- Griem, J.N. and K.L.M. Martin. 2000. Wave action: the environmental trigger for hatching in the California grunion *Leuresthes tenuis* (Teleostei: Atherinopsidae). *Marine Biology* 137: 177-181.
- Martin, K.L.M. 1999. Ready and waiting: delayed hatching and extended incubation of anamniotic vertebrate terrestrial eggs. *American Zoologist* 39: 279-288.
- Reynolds, W.W., Thompson, D.A. and M.E. Casterlin. 1977. Responses of young California grunion, *Leuresthes tenuis*, to gradients of temperature and light. *Copeia* 1977: 144-149.
- Snyder, E.A. and K.L.M. Martin. 2002. Temperature effects on egg survival and hatching during the extended incubation period of California grunion, *Leuresthes tenuis*. *Copeia* 2002: 313-320.
- Thomson, D.A. and K.A. Muench. 1976. Influence of tides and waves on the spawning behavior of the Gulf of California grunion, *Leuresthes sardina*. *Bulletin of the Southern California Academy of Sciences* 75: 198-203.
- Walker, B.W. 1949. The periodicity of spawning by the grunion, *Leuresthes tenuis*, an atherine fish. Unpublished Ph.D. dissertation, University of California Los Angeles.

Molecular Dynamics of Human Butyrylcholinesterase towards the Design of Selective Inhibitors

► Tejas Bondade

Advisor: Dr. Katherine Kantardjieff
California State University, Fullerton

Abstract

Butyrylcholinesterase (BChE), an enzyme found to have increased activity levels in Alzheimer's disease (AD) patients, is studied by methods of molecular dynamics (MD). Although no cure exists for the disease, therapeutic treatments can be produced to improve the quality of life of the patients. One treatment involves selectively inhibiting BChE. To determine whether design of such a therapeutic is possible, we must examine the binding of compound libraries of potential inhibitors, and the mechanics of the functional response of the enzyme. Previous studies in our laboratory have suggested that it may be possible to exploit the binding of compounds to both the active site gorge and a peripheral (P') site tethered by a linker chain, to create a potent and selective BChE inhibitor. Docking and subsequent MD simulations are used to study the BChE structure and better understand the chemistry of putative bound inhibitors. Simulations are performed with the enzyme free of substrates and bound to a known selective inhibitor, di-*n*-butyl phenyl phosphate. Trajectories are analyzed with particular attention given to the active site, the P' site, and the adjoining region. Based

on the movements of the catalytic triad and the side chains between the active site gorge and the P' site, it may be possible to design tethered compounds with linker lengths of ~10 C-C bonds, capable of binding to both the active site gorge and P' site to create a highly competitive selective BChE inhibitor.

Keywords

Alzheimer's Disease, Butyrylcholinesterase, simulated docking, molecular dynamics

Introduction

Alzheimer's disease poses a significant threat to the aging population as the most common type of adult-onset dementia [1]. Although no cure exists yet for the disease, one form of treatment involves the reversible inhibition of acetylcholinesterase (AChE) and butyrylcholinesterase (BChE), two enzymes which hydrolyze the neurotransmitter acetylcholine (ACh) [2]. In patients diagnosed with AD, ACh levels decrease within the brain, coupled with a decrease in AChE activity (45%) and an increase in BChE activity (40-90%) [3,4]. Selective inhibition of these two enzymes is based on the concept that by preventing the

rapid hydrolysis of ACh, interneuron communication can still occur despite the decreased levels of ACh in the brain.

Specifically, ACh is known to be released from the axon terminals of the pre-synaptic cell to bind to cholinergic receptors of the post-synaptic cell, allowing action potentials (APs) to be propagated from one neuron to another. AChE and BChE are enzymes that rapidly break down ACh to terminate signal transmission, and allow new APs to be sent. Due to neuritic plaques that build up in patients with AD, axon terminals containing ACh become destroyed which reduces the amount of ACh found within the brain [6]. Thus, in order to compensate for the reduction of ACh levels, inhibition of AChE and BChE allows smaller levels of ACh to bring the post synaptic cell to threshold in order to generate an AP without being hydrolyzed too rapidly.

Two computational methods are used in the experiment: flexible docking [7,8] and molecular dynamics [9,10]. Flexible docking simulations involve docking compounds to identified pockets on the enzyme. In flexible docking, the enzyme is treated as a rigid object while the compound being docked is allowed

to rotate about its bonds in order to bind to the pocket. One of the weaknesses of flexible docking simulations is that the enzyme is treated as a rigid object, while in reality the enzyme experiences conformational change. Molecular dynamics compensates for this weakness because it considers the many conformations an enzyme can experience over a specified duration of time. In addition, MD allows researchers to understand proteins in terms of structure and microscopic interactions between the molecules [11]. In general, molecular dynamics consists of using classical equations of motion to calculate forces acting on the atoms. This involves calculating potential energy to represent the non-bonded interactions, determining the bonding potentials for the intramolecular bonding interactions, and finally calculating the atomic forces [11]. A MD algorithm is applied to solve Newton's equations of motion. In addition, constraints are commonly used to have rigidly constrained bond lengths [11].

In relation to this experiment, flexible docking and molecular dynamics were two methods used to develop possible drug lead compounds. Previous docking simulations in our laboratory have shown that di-*n*-butyl phenyl phosphate has a high affinity to bind in the active site gorge of BChE. Furthermore, a second binding site (designated the P' site) was also identified at the top of the gorge [1] (Figure 1). This project explores the possibility for developing a competitive selective inhibitor for BChE that can bind both the active site gorge and the P' site, if the ligands to each site are linked by a tether (Figure 2). Molecular dynamic simulations are used in this experiment to study the movements of the side chains and

the loop region between the active site gorge and the P' site with the purpose of better understanding how the proposed tethered compound would interact with the enzyme, upon which a library of compounds based on the DAPP inhibitor and various tether constructs will be examined *in silico*.

Methods

Molecular dynamics simulations were performed on human BChE free of substrates, and bound to the known selective inhibitor di-*n*-butyl phenyl phosphate. The crystal structure of human BChE was obtained from the PDB (PDB code: 1P0I) and modified to remove all heteroatoms excluding the crystallographic waters.

Preliminary simulations were performed with MacroModel [9], using the AMBER* force field for minimization [12]. The simulation was performed in the absence of solvent. The minimization step used a maximum iteration value of 5000 and a convergence threshold of 0.002. One hundred conformations were sampled over 1 ns. Dynamics were performed under the following conditions: simulation temperature of 300 K, time step of 1.5 fs, and equilibration time of 1 ps. The output trajectory was analyzed by comparing the extent of flexibility of the catalytic triad, the P' site, and the adjoining region. Side chain movements and loop movements were examined as well.

More sophisticated simulations were performed with Desmond [10]. Steps included: optimizing the structure, setting up a solvent box, performing minimization, and obtaining a trajectory from the dynamics. Optimizing the structure involved using The Protein Preparation Wizard

in the Maestro suite to assign bond orders, add hydrogen atoms, cap termini, and optimize hydrogen atoms. Setting up the solvent box involved using the SPC solvent model [10] to create an orthorhombic, 601,892 Å³ volume solvent box to immerse the enzyme. In addition, chloride ions were added to the system for neutralization. Crystallographic water was preserved in the simulations to retain the catalytically important water molecule found within the gorge. Minimization was performed to relax the model system. Molecular dynamics were performed for BChE free of substrates and bound to di-*n*-butyl phenyl phosphate. The latter was obtained by flexible docking with ICM-Pro 3.4.5d [7,8]. The obtained trajectory file was analyzed using Desmond's simulation event analysis tool. RMSD values and radius of gyration were calculated to interpret the output trajectories.

Results

The preliminary trajectory obtained using MacroModel (Figure 3) provided information regarding the movement and the interactions found within the active site gorge and specifically the catalytic triad. The three catalytically important residues (S198, E325, and H438) within the active site gorge were observed to have a fairly planar rigidity throughout the simulation, as has been suggested previously [2]. His 438 forms hydrogen bonds with Ser 198 and Glu 325 which solidifies the network between the catalytic triad. A water molecule found within the triad is also observed to hydrogen bond tightly within the gorge confirming its importance for hydrolysis. Regions on the surface of the protein

were generally observed to be more flexible than regions within the core of the protein, such as the catalytic triad. There was some side chain movement observed in the loop region bridging the active site gorge to the P' site. Overall however, the preliminary simulation did not clearly depict an opening between the active site and P' site that would allow the tethered compound to bind between the loop region.

The results from the longer and more sophisticated MD simulation using Desmond further support the results observed from the preliminary simulation. The trajectory obtained for BChE free of substrates shows the catalytic triad as relatively rigid. The trajectory obtained for the BChE bound to di-*n*-butyl phenyl phosphate also depicts the rigidity of the catalytic triad, but also shows significant flexibility of the docked inhibitor within the active site gorge. The calculated RMSD values for the enzyme free of substrates were observed to fluctuate between 0.6 and 1.6 Å (Figure 4). The radius of gyration was observed to fluctuate between 22.95 and 23.3 Å (Figure 5). Examination of the loop region between the active site and P' site also did not show an opening that would allow the tethered compound to bind between the loop region. The implication of the results is that a tethered compound would need to be designed that would go above the loop region. This means that the designed tethered compound would have to be at least 10 carbon-carbon bonds long (most likely more).

Discussion

It is important to recognize that the length of the preliminary simula-

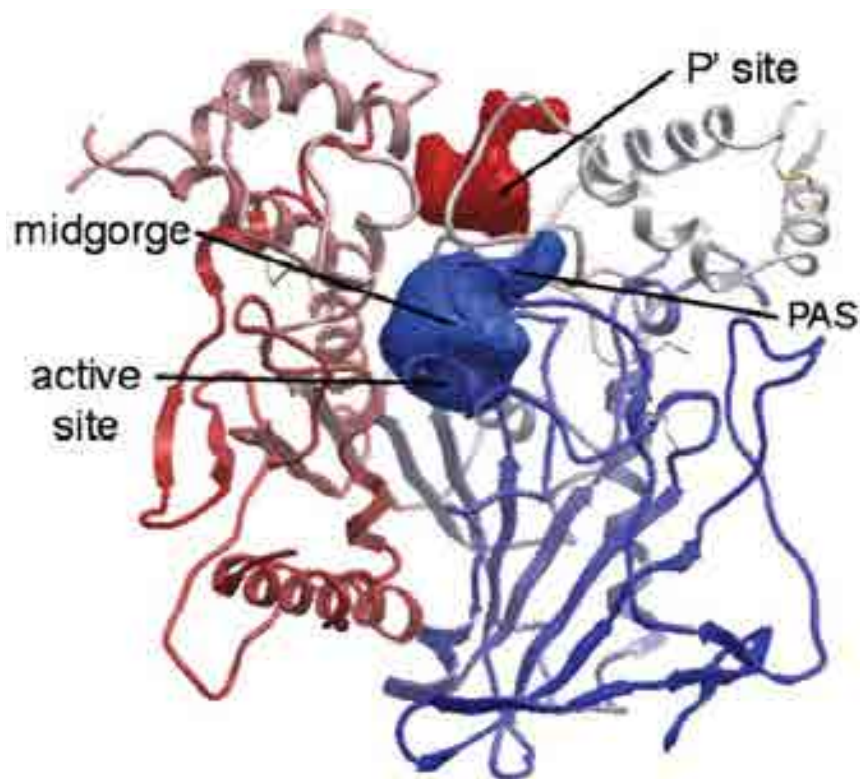


Figure 1. Human BChE used for both docking simulation and molecular dynamics. Identified in the blue solid region is the active site. The observed P' site at the top of the gorge is identified by the red solid region. Also labeled are the midgorge region and the peripheral anion site (PAS) which is believed to be involved with allostery. [1]

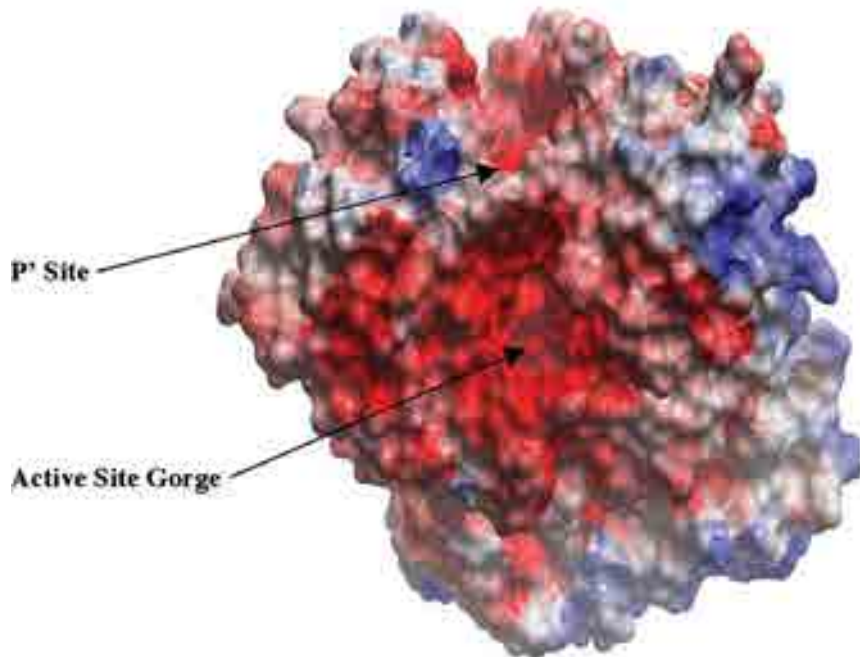


Figure 2. Active site gorge. The electrostatic potential surface depicts the active site gorge and the P' site.

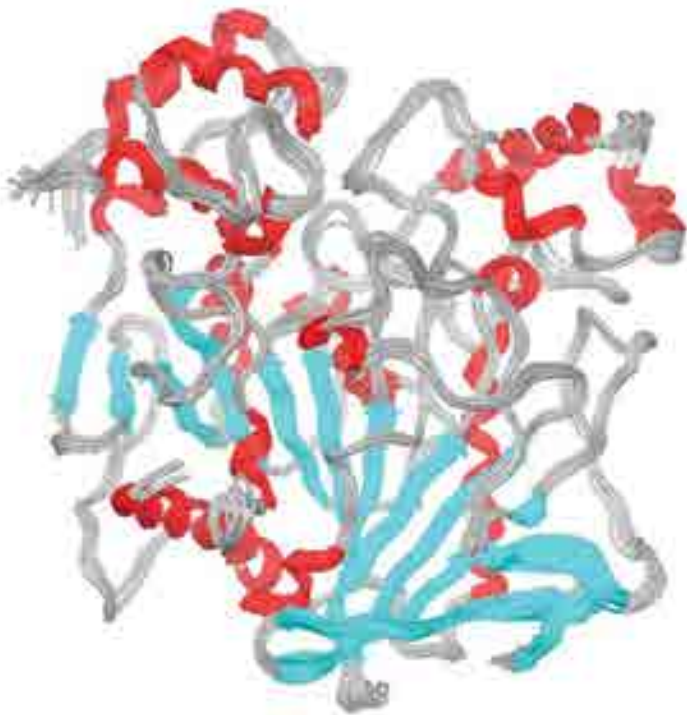


Figure 3. Preliminary trajectory obtained using MacroModel. Several conformations of the simulation are shown superimposed on each other. Residues on the surface of the protein were observed to be more flexible than those found within the active site gorge. The catalytic triad was observed to retain a certain planar conformation with H438 hydrogen bonding to S198 and E325. A catalytically important water molecule was also observed to remain fairly rigid.

tions so far can be increased in duration in future simulations to allow for more fully, statistically reliable observations. One of the concerns in molecular dynamic simulations is that longer simulation times need to be set to ensure that the trajectory includes all of the major conformations the enzyme assumes over time. Although Desmond relaxes the system prior to simulation, the simulation may not include all of these conformations. Thus, future simulations should be run for at least 5-10 ns to ensure that statistically reliable observations are obtained.

When looking at the deviations in the backbone movement of the BChE enzyme with respect to the relaxed state, it is observed that the RMSD values for the enzyme docked to di-*n*-butyl phenyl phosphate have higher values compared to the non-docked

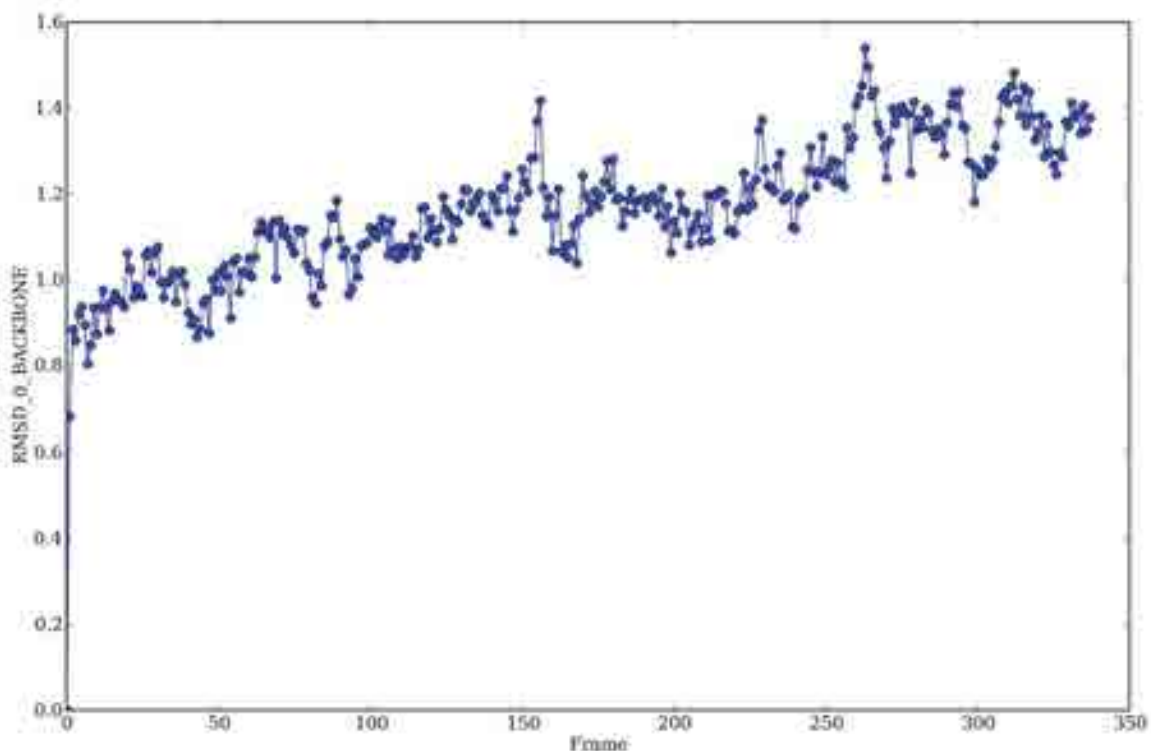


Figure 4. RMSD plot obtained from Desmond simulations of BChE free of substrates. Deviations in the backbone are depicted with respect to the relaxed system at frame 0.

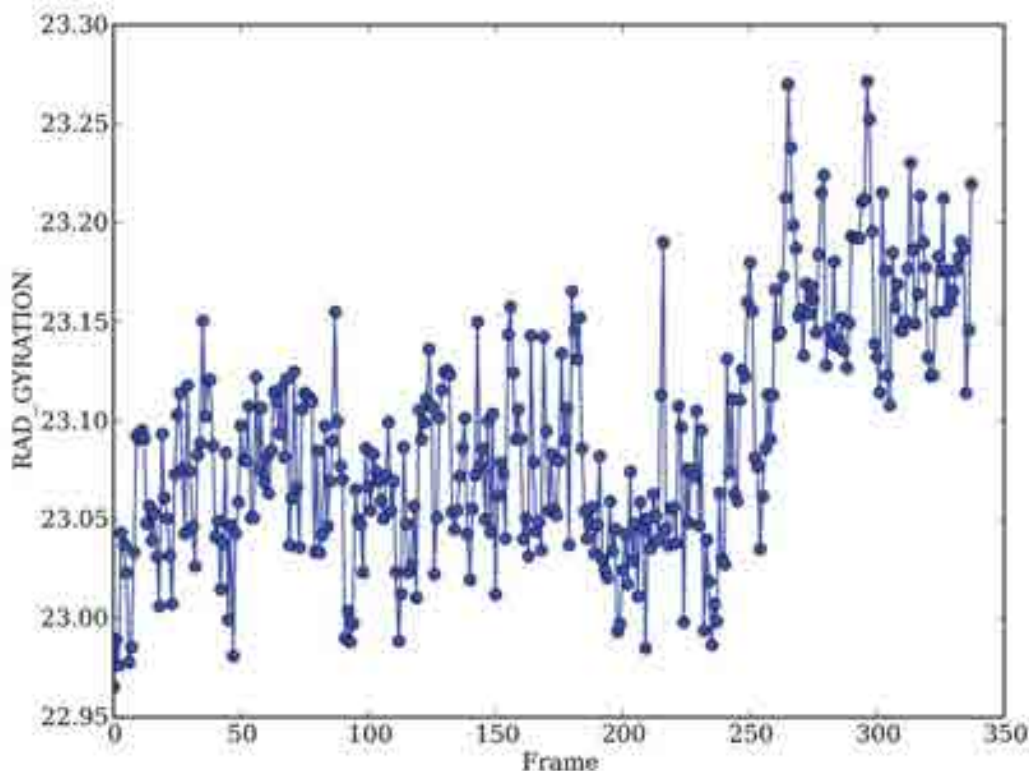


Figure 5. Radius of gyration plot obtained from Desmond simulations of BChE free of substrates. The radius of gyration observed to fluctuate between 22.95 and 23.3 Å.

enzyme. The greater RMSD values obtained for the docked enzyme imply that the backbone experiences greater conformational change as compared to the non-docked enzyme. This can be an effect of greater conformational change in the loop regions involved in allostery or signaling [1]. To better understand this effect, analysis of specific regions of the backbone need to be conducted.

Based on estimations of the length between the active site gorge and the P' site that suggested a ~10 carbon-carbon bond length tether to be created, a docking simulation was performed to test whether a somewhat smaller length may dock in the proposed manner. Docking of two di-*n*-butyl phenyl phosphates linked by a 7 C-C linker chain was performed to see how the compound would in-

teract with the active site. Due to the size of the active site gorge, the entire tethered compound docked completely within the gorge. This suggests that the chain needs to be even longer and perhaps more rigid in order to give the tether direction towards the P' site. It may also be possible to make one of the ends of the tether have a bulky group that will block the active site gorge while a smaller group on the other end can bind to the P' site, but not the other way around. The tether could be designed to have shape/rigidity enabling it to go up the gorge and around the loop region to reach the P' site, or, if MD simulations do reveal an opening between the loop regions separating the gorge opening from the P' site, a different compound could be designed that conforms to the shape and charge of

that region. Furthermore, to test what types of tethered compounds will facilitate docking to both the active site gorge and the P' site as proposed, a library of tethered compounds can be designed and docked using flexible docking simulations in ICM-Pro. In addition to DAPPs, existing drugs that are known to be dual cholinesterase inhibitors may be used to gain an idea of what types of compounds can be used as part of the tether designed.

Conclusion

Based on the preliminary trajectories obtained for BChE using both MacroModel and Desmond, an opening between the active site and P' site that would allow the tethered compound to bind between the loop

region is not observed. Thus, it may be possible to design a tethered compound with linker lengths equal to or greater than ~10 C-C bonds that will bind to both the active site gorge and P' site, but will go above the loop region instead of between it.

Acknowledgements

We thank our collaborators Drs. Roger Acey and Kensaku Nakayama. Department of Chemistry and Biochemistry, CSU Long Beach, and Dr. James Zhao.

References

1. Law K., Acey R. A., Smith C. R., Benton D. A., Soroushian S., Eckenrod B., Stedman R., Kantardjieff K. A., & Nakayama K. 2007. Di-alkyl phenyl phosphates as novel and selective inhibitors of butyrylcholinesterase. *Biochem Biophys Res Comm.* 355: 371–378.
2. Suarez D. & Field M. 2005. Molecular Dynamics Simulations of Human Butyrylcholinesterase. *Proteins: Struct Func Bioinf.* 59: 104-117.
3. Arendt T., Bruckner M.K., & Lange V. 1992. Changes in acetylcholinesterase and butyrylcholinesterase in Alzheimer's disease resemble embryonic development – a study of molecular forms. *Neurochem.* 21: 381-396.
4. Perry E.K. & Tomlinson B.E. 1978. Changes in brain cholinesterase in senile dementia of Alzheimer's disease. *Appl Neurobiol.* 4: 273-277.
5. Patocka J., Kuca K., & Jun D. 2004. Acetylcholinesterase and Butyrylcholinesterase – Important Enzymes of Human Body. *ACTA.* 47: 215-228.
6. Ballard C.G., Greig N.H., Guillozet-Bongaartz A.L., Enz A., & Darvesh S. 2005. Cholinesterases: Roles in the Brain During Health and Disease. *Current Alzheimer Research.* 2: 307-318.
7. Schapira M., Abagyan R., & Totrov M. 2003. Nuclear hormone receptor targeted virtual screening. *J Med Chem.* 46: 3045-3059.
8. Schapira M., Raaka B.M., Das S., Fan L., Totrov M., Zhou Z., Wilson S.R., Abagyan R., & Samuels H.H. 2003. Discovery of diverse thyroid hormone receptor antagonists by high-throughput docking. *Proc Nat Acad Sci USA.* 100: 7354-7359.
9. MacroModel, version 9.0; Schrodinger, LLC: New York, NY, 2005.
10. Desmond, version 2.3.4; D E. Shaw Research, 2007.
11. Allen M. P. 2004. Introduction to Molecular Dynamics Simulation. *NIC Series.* 23: 1-28.
12. Kollman. *Acc. Chem. Res.* (1996); 29: 461-469.

Determining Binding affinity of an Iron (III) corrole complex with Pyridine and Imidazole Derivatives

► Po-Yu Fang, Karn Sorasaenee

Advisor: Dr. Richard Deming

California State University, Fullerton

Abstract

Corroles are comparable to porphyrins because of their similarities in structure; since both are macrocyclic (macrocyclic) and highly conjugated. Because of this similarity, corroles may have a comparable interaction with porphyrins. However, despite their structural similarity, corroles can stabilize metal complexes in high oxidation state. According to this unique feature, they have begun to interest inorganic chemists in recent years. In order to complete this work, $\text{Fe}^{\text{III}}(\text{tpfc})(\text{OEt}_2)_2$ was essential. In a previous experiment, tpfc, Tris (pentafluorophenyl) corrole, an important molecule was used to synthesize $\text{Fe}^{\text{III}}(\text{tpfc})(\text{OEt}_2)_2$ compound. The purpose of this experiment was to determine the binding affinity, and the binding constant of iron corroles $\text{Fe}^{\text{III}}(\text{tpfc})(\text{OEt}_2)_2$ with pyridine and imidazole molecules. The extinction coefficient of $\text{Fe}^{\text{III}}(\text{tpfc})(\text{OEt}_2)_2$ in toluene solvent were determined using Beer's Law with known concentrations and absorbance readings of the Soret and Q bands. The extinction coefficients measured 3.5×10^4 at 385 nm and 8.8×10^3 at 546 nm. Spectrometric titrations were performed with different pyridine and imidazole derivatives. The affinity for

$\text{Fe}^{\text{III}}(\text{tpfc})(\text{OEt}_2)_2$ with electron-donor ligands performance in this study is as follows:

4-dimethylamino pyridine > 4-methylimidazole > 1-methylimidazole > imidazole > 4-methylpyridine > pyridine

The 2-methylimidazole and 1, 2-dimethylimidazole did not exhibit any binding.

The stronger base, imidazoles, in general shows stronger binding than pyridines, except for 4-dimethylamino pyridine. The dimethylamino group of 4-dimethylamino pyridine best stabilizes the binding complexes due to the inductive effects of the ligands. Moreover, the position of electron donating groups is another factor to affect the binding. According to the results, when an electron donating group was at the C-4 position of pyridine or imidazole derivatives, it demonstrated stronger binding affinity. However, when an electron donating group was at the C-2 position of these derivatives, the binding did not take place, despite the presence of another electron donating group at the C-4 position.

Introduction

Corroles are modified porphyrins, which are of increasing interest to

chemists in recent years. Both are macrocyclic and highly conjugated (Figure 1); yet, corroles contain one fewer carbon atom than porphyrins. Corroles can also stabilize a metal complex in high oxidation states,

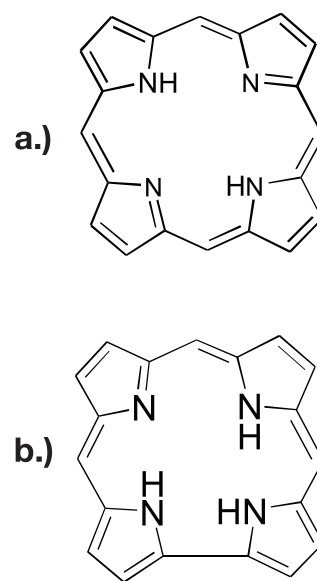
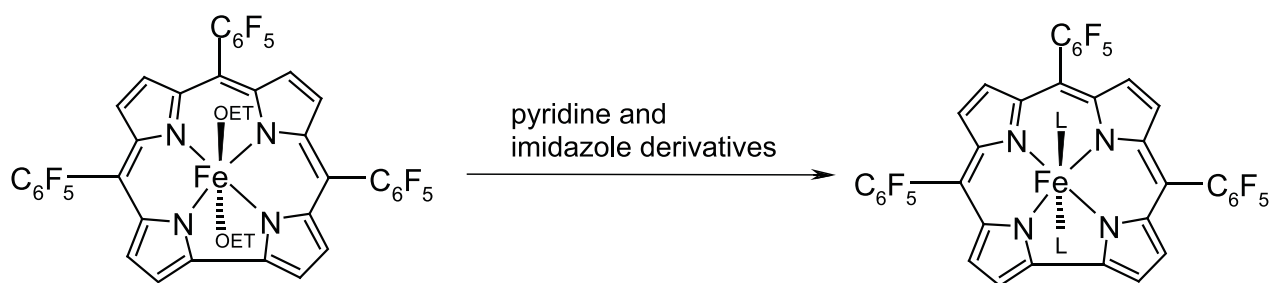


Figure 1. Structures of a porphyrin (a), and a corrole (b)

such as iron (IV) and cobalt (IV) due to their tribasic nature.

This work focuses on the binding of pyridine and imidazole derivatives to the axial positions of the iron complex $\text{Fe}^{\text{III}}(\text{tpfc})(\text{OEt}_2)_2$, where OEt_2 equals diethyl ether. The displacement of diethyl ether by pyridine or imidazole molecules is illustrated in



Scheme 1. The binding of $\text{Fe}^{\text{III}}(\text{tpfc})(\text{OEt}_2)_2$ with pyridine and imidazole derivatives

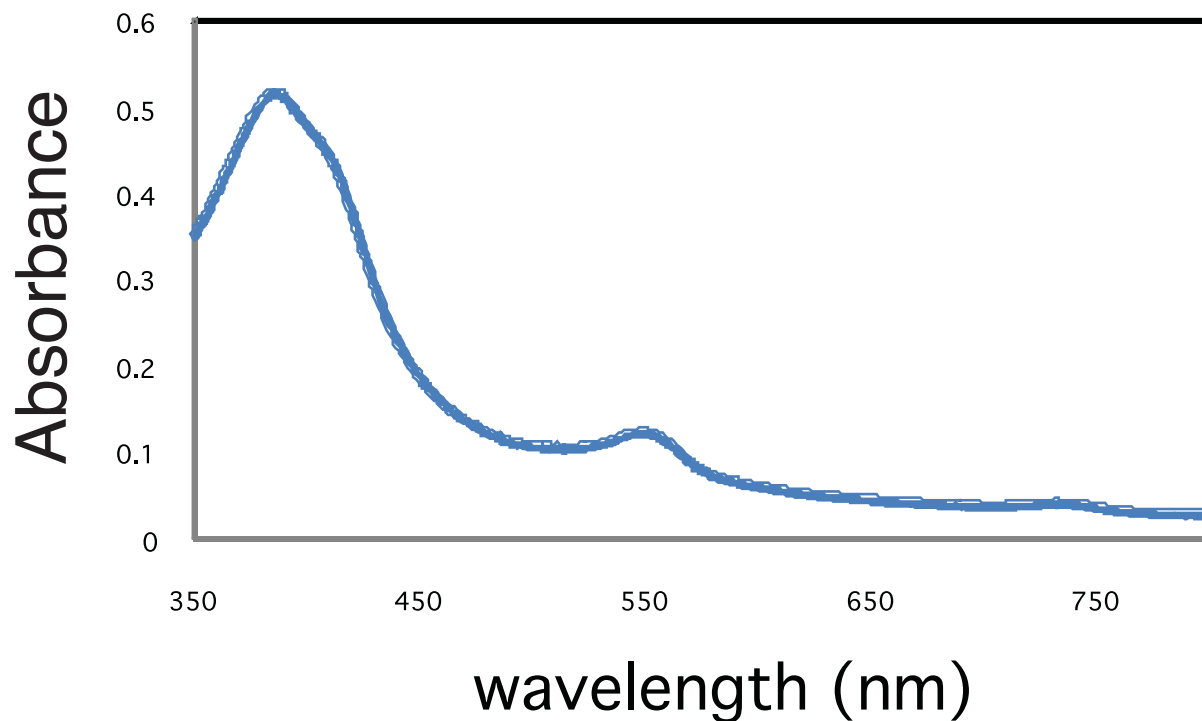


Figure 2. The UV-Vis electronic absorption spectrum of $\text{Fe}^{\text{III}}(\text{tpfc})(\text{OEt}_2)_2$ in toluene

Scheme 1. During preparation and isolation of the complex, the pyridine or imidazole molecules are expected to coordinate to the iron (III) complex ion as the ligands. (Scheme1). This reaction between ligands and a metal ion is treated as a Lewis acid-base interaction. Qualitatively, we aim to discover a set of pyridine and imidazole molecules that exhibits strong affinity toward the iron center. Once the appropriate ligands are qualitatively identified, the binding affinity between $\text{Fe}^{\text{III}}(\text{tpfc})(\text{OEt}_2)_2$

and the ligands can be further assessed quantitatively.

$\text{Fe}^{\text{III}}(\text{tpfc})(\text{OEt}_2)_2$ in toluene solution has two characteristic absorption bands. The Soret band is located between 400 nm and 450 nm in the blue wavelength region of the visible spectrum. The second band, the Q band, absorbs a fraction of the light that the Soret band absorbs and ranges from 500 nm to 600 nm. The toluene solvent, as a non-polar solvent, is used in this experiment to avoid competition of ligands with

$\text{Fe}^{\text{III}}(\text{tpfc})(\text{OEt}_2)_2$. If polar solvent is used, it may bind $\text{Fe}^{\text{III}}(\text{tpfc})(\text{OEt}_2)_2$ more tightly than ligands, thereby causing interference. The UV-Vis spectrum of $\text{Fe}^{\text{III}}(\text{tpfc})(\text{OEt}_2)_2$ in toluene solution is presented in Figure 2.

Materials

Imidazole (99%), 2-methylimidazole (99%), and 4-dimethylimidazole pyridine (99%), were obtained from Sigma Aldrich. 4-picolin (98%), 1, 2-dimethylimidazole (98%) and

	Pyridine	4-dimethylamino pyridine	4-picoline	Imidazole
Original peak of Soret Band (nm)	385	385	386	385
Newly formed peak of Soret Band (nm)	417	420	420	426
Initial concentration of sample ligand (M)	1.24×10^{-1}	8.56×10^{-2}	1.03×10^{-1}	6.23×10^{-2}
Initial concentration of corrole (M)	1.26×10^{-5}	1.20×10^{-5}	1.09×10^{-5}	1.35×10^{-5}
Ratio (ligand:corrole)	20000/1	800/1	12000/1	1800/1

Table 1. This table represents the results of soret band peak shifts of the pyridine derivatives (pyridine, 4-dimethylamino pyridine, and 4-picoline) in toluene solution.

	1-methylimidazole	4 methylimidazole	2-methylimidazole	1,2-dimethylimidazole
Original peak of Soret Band (nm)	385	384	387	386
Newly formed peak of Soret Band (nm)	426	428	-	-
Initial concentration of sample ligand (M)	6.27×10^{-2}	6.04×10^{-2}	7.19×10^{-2}	7.09×10^{-2}
Initial concentration of corrole (M)	9.87×10^{-6}	1.44×10^{-5}	1.39×10^{-5}	2.44×10^{-5}
Ratio (ligand:corrole)	1300/1	1000/1	-	-

Table 2. This table represents the results of soret band peak shifts of the imidazole derivatives, which are imidazole, 1-methylimidazole, and 4-methylimidazole.

	2-methylimidazole	1,2-dimethylimidazole
Original peak of Soret Band (nm)	387	386
New Forming peak of Soret Band (nm)	-	-
Concentration of sample ligand (M)	7.14E-02	7.09E-02
Concentration of corrole (M)	1.39E-05	2.44E-05
Total volume of added sample ligand in cuvet (uL)	220	180
Final mol of ligand in cuvet (mol)	1.57E-05	1.28E-05
Final mol of corrole in cuvet (mol)	2.79E-08	4.89E-08
Ratio (ligand:corrole)	-	-

Table 3. This table shows the data of the remaining imidazole derivatives, 2-methylimidazole and 1,2-dimethylimidazole. The newly formed peaks of these Soret Bands did not shift from their original peaks of 386 nm and the binding ratio of these two imidazole derivatives could not be determined.

4-methylimidazole (98%), were purchased from Alfa Aesar. 1-methylimidazole (99%) was received from Acros Organic. Pyridine (99%) and chloroform (99%) were obtained from stock room at CSUF. Using a micropipette, pyridines and imidazoles were added into a cuvet containing $\text{Fe}^{\text{III}}(\text{tpfc})(\text{OEt}_2)_2$ and toluene during UV/Vis titration. The toluene

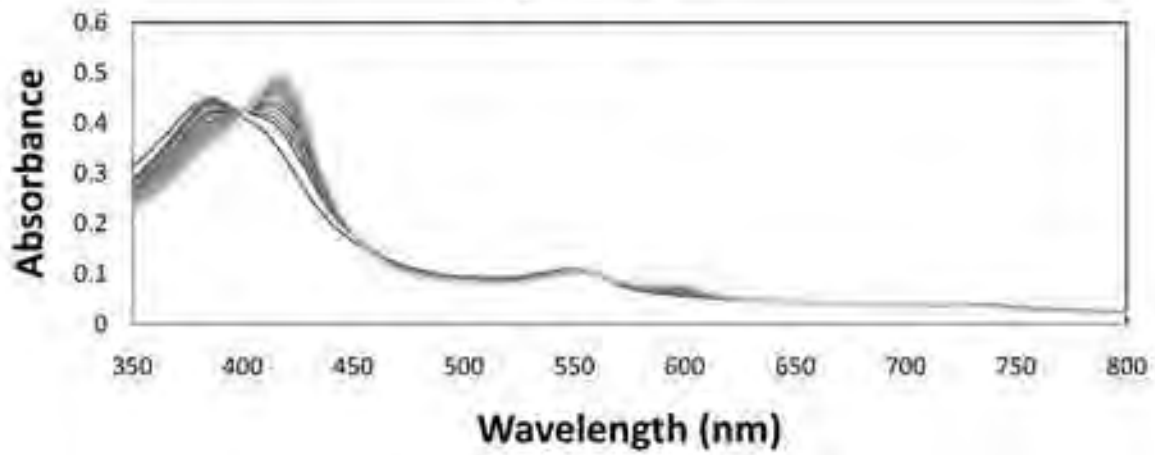
was acquired from OmniSolv and the $\text{Fe}^{\text{III}}(\text{tpfc})(\text{OEt}_2)_2$ compound was previously prepared. All organic ligands were used as received. All absorption spectra were collected from a Shimadzu UV-2101PC spectrophotometer.

Determination of extinction coefficients of $\text{Fe}^{\text{III}}(\text{tpfc})(\text{OEt}_2)_2$ in toluene solvent:

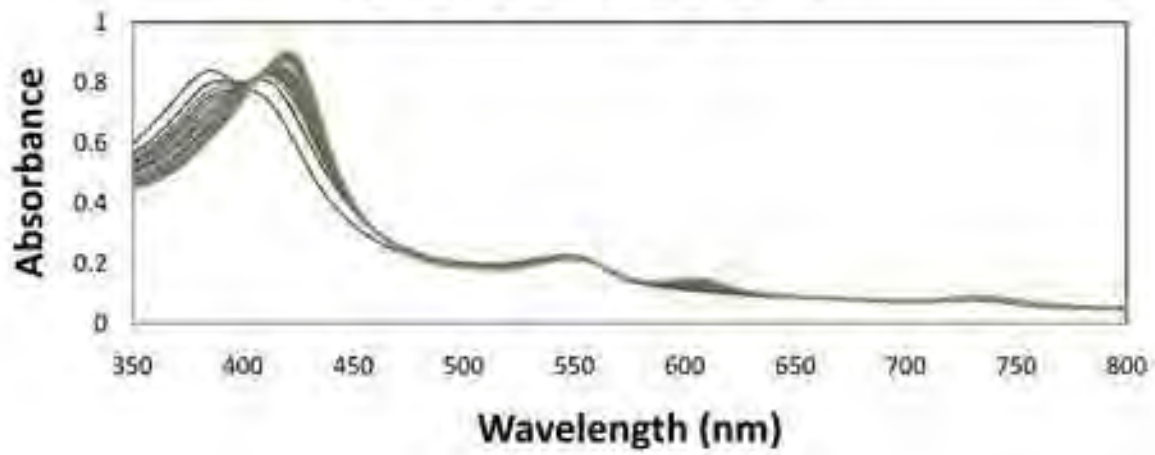
In order to prepare a primary sample solution, 0.0023g of $\text{Fe}^{\text{III}}(\text{tpfc})(\text{OEt}_2)_2$ was dissolved in 8.0 mL of toluene solvent. An aliquot of 360 μL of $\text{Fe}^{\text{III}}(\text{tpfc})(\text{OEt}_2)_2$ in toluene was further diluted with

UV/VIS Spectra:

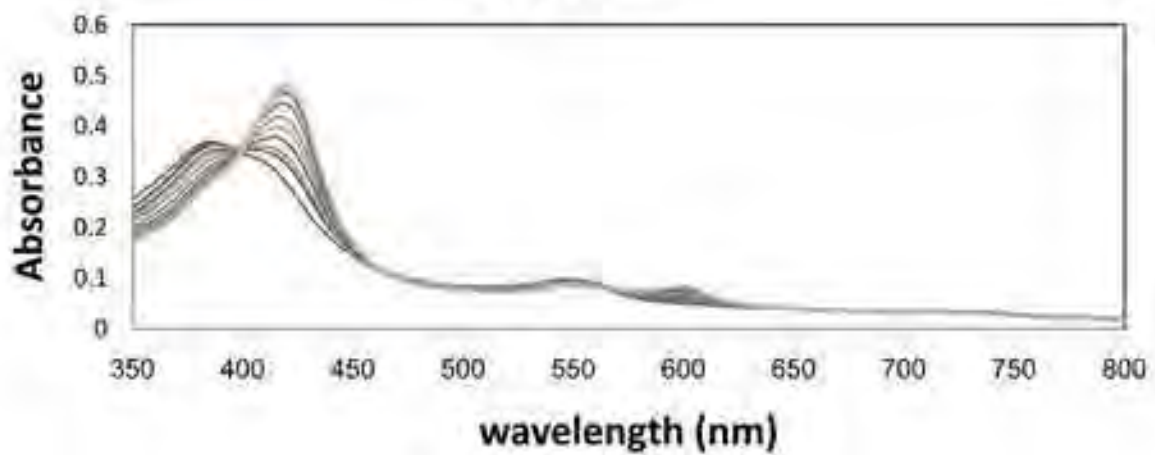
Pyridine



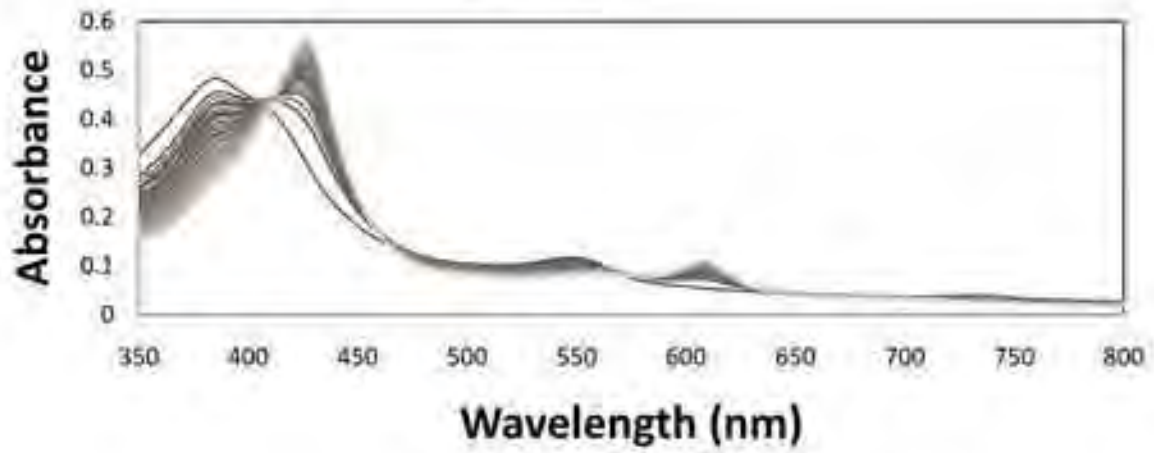
4-dimethylamino pyridine



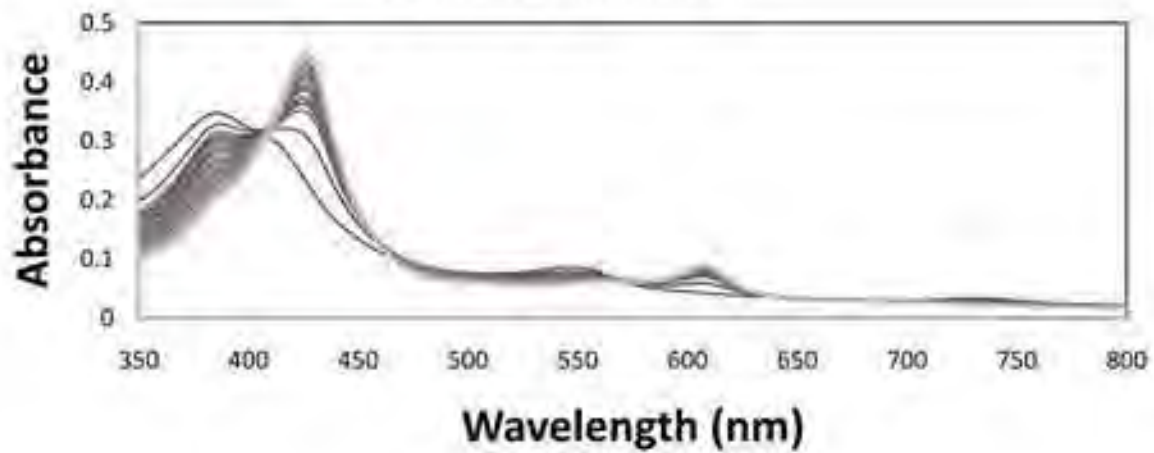
4-picoline



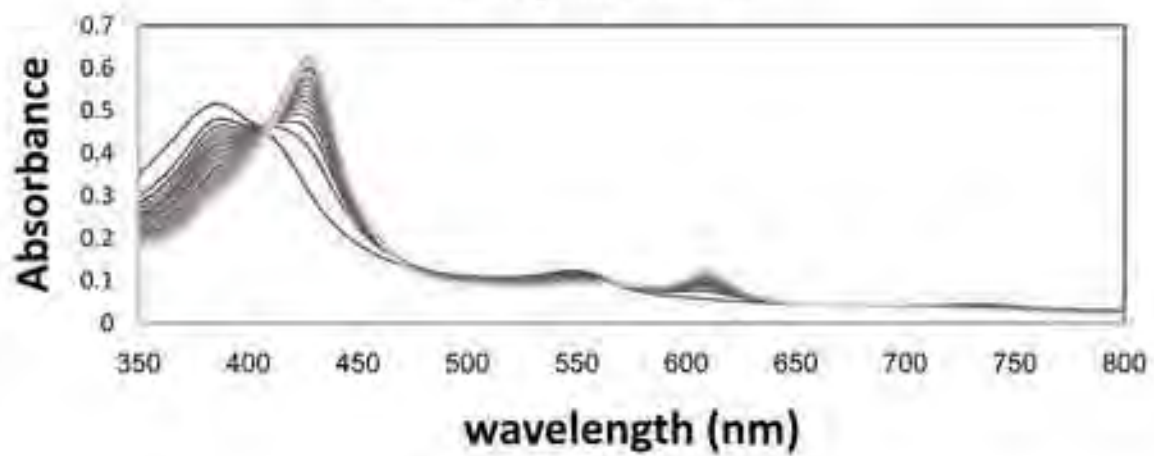
imidazole



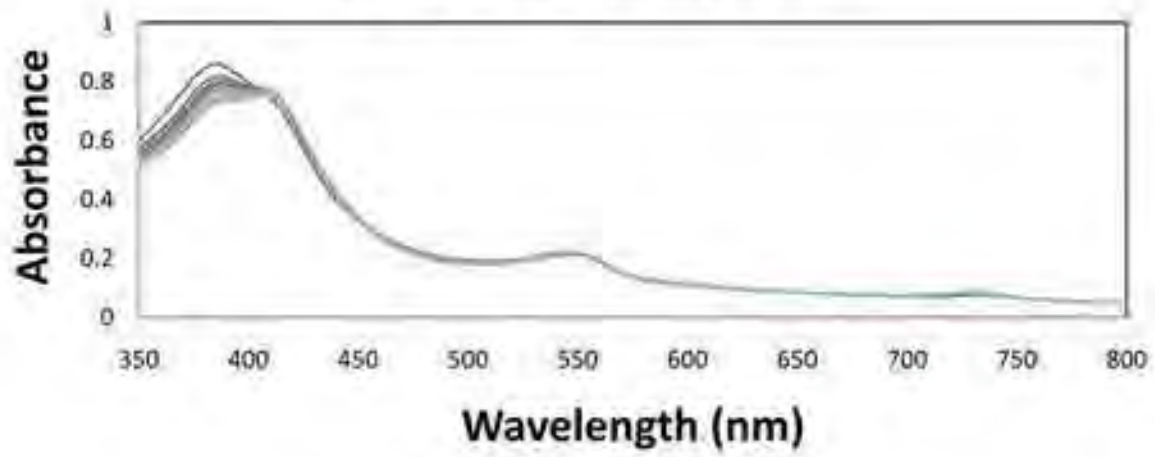
1-methylimidazole



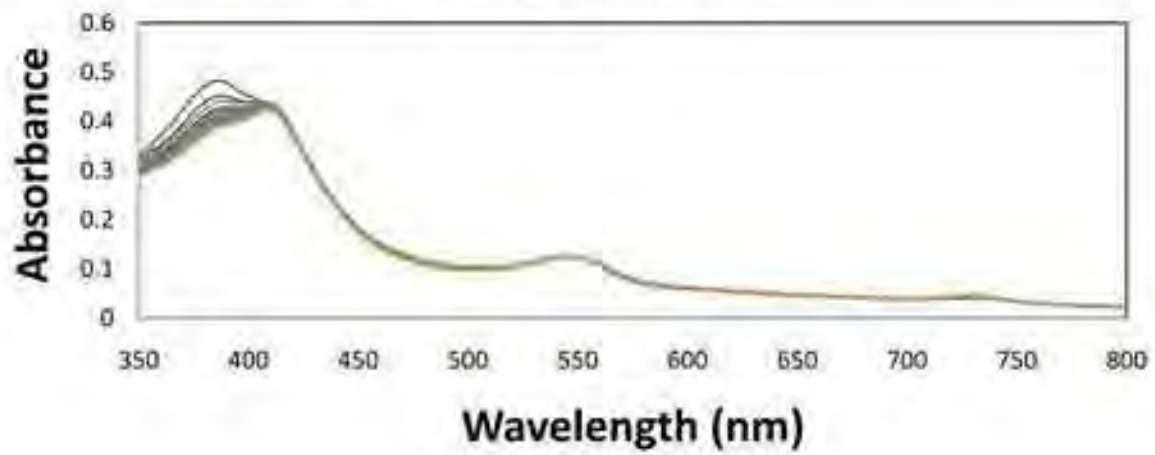
4-methylimidazole



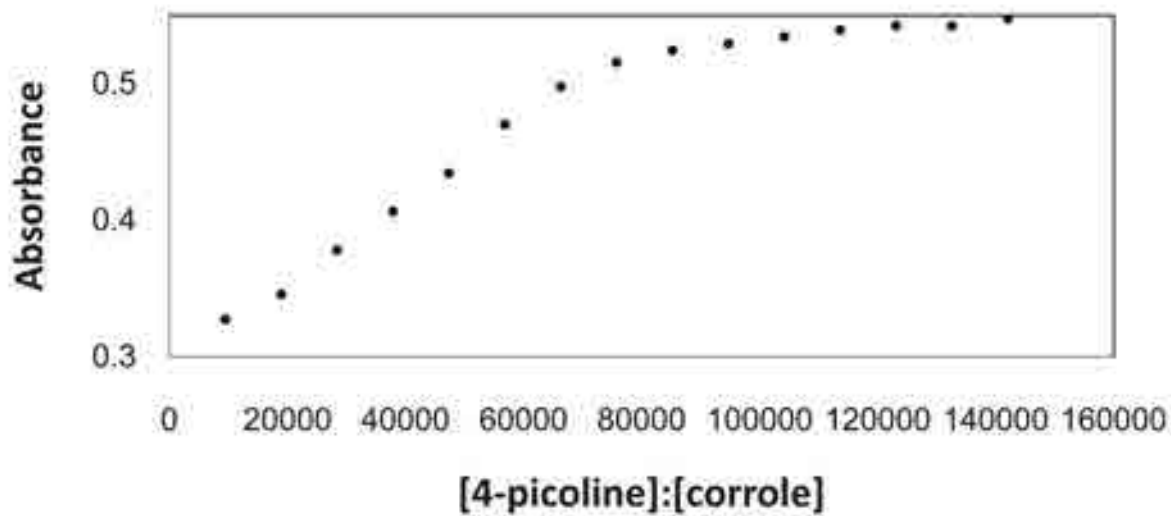
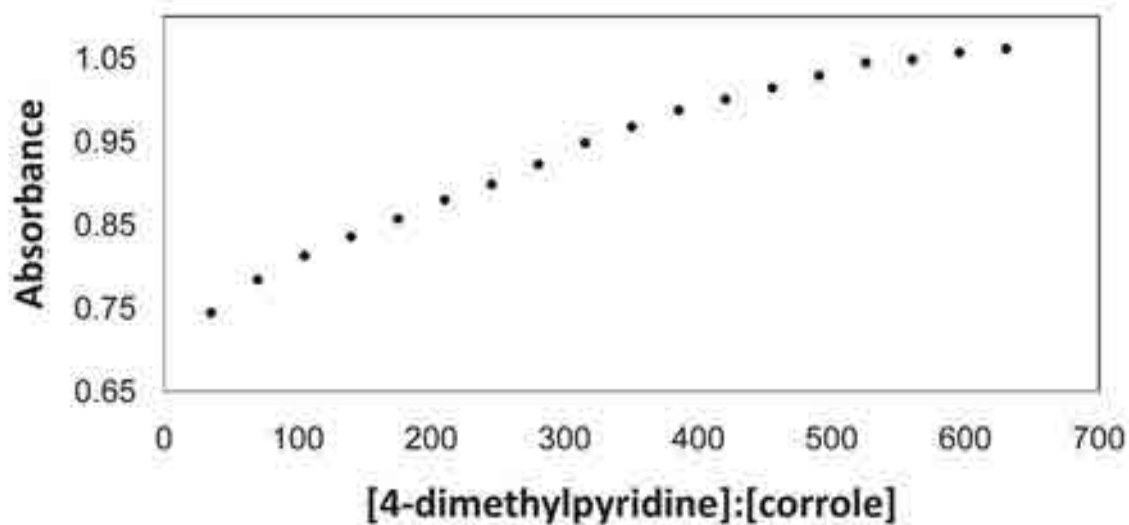
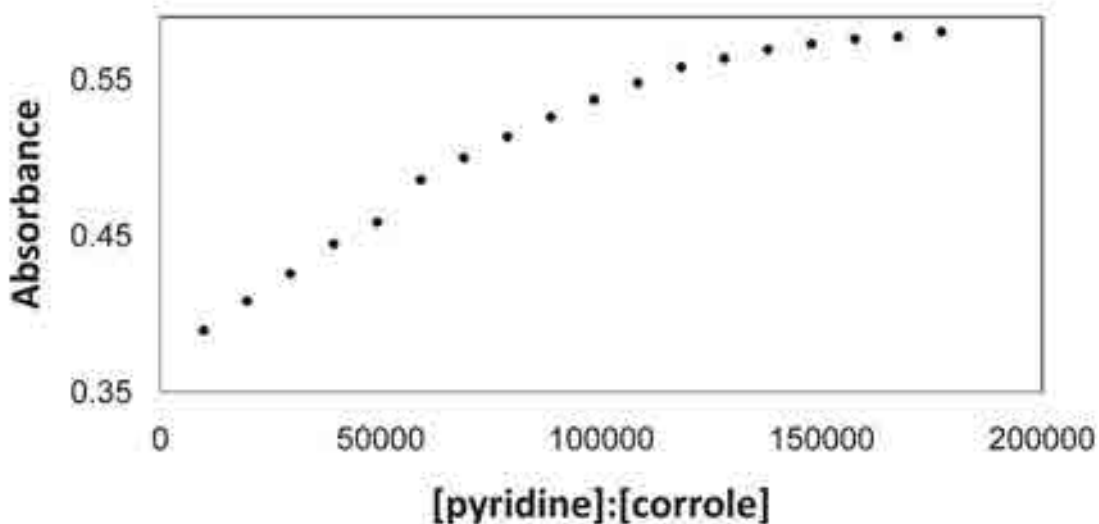
1,2-Dimethylimidazole

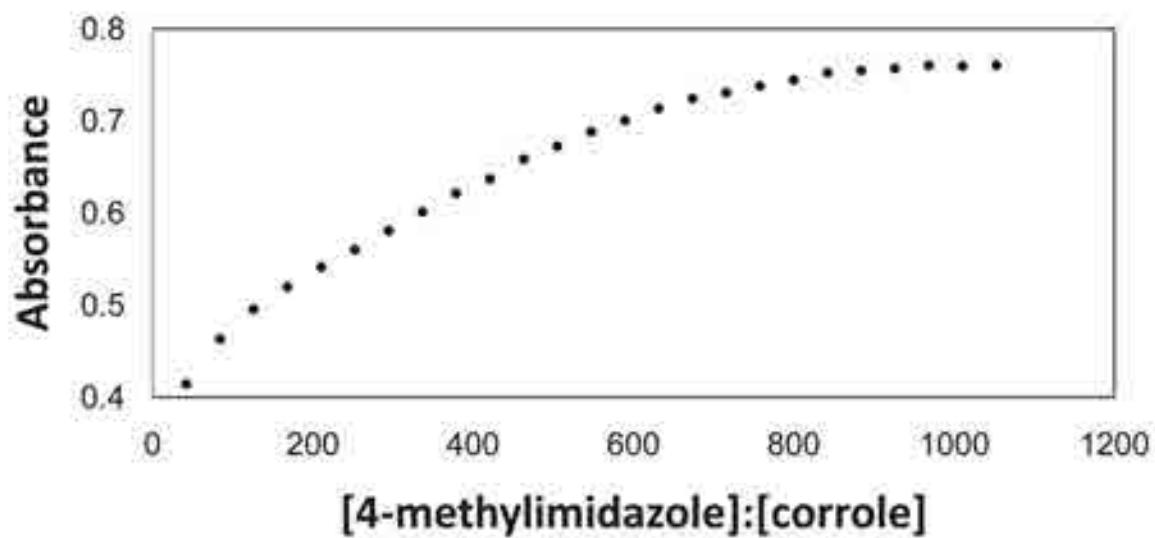
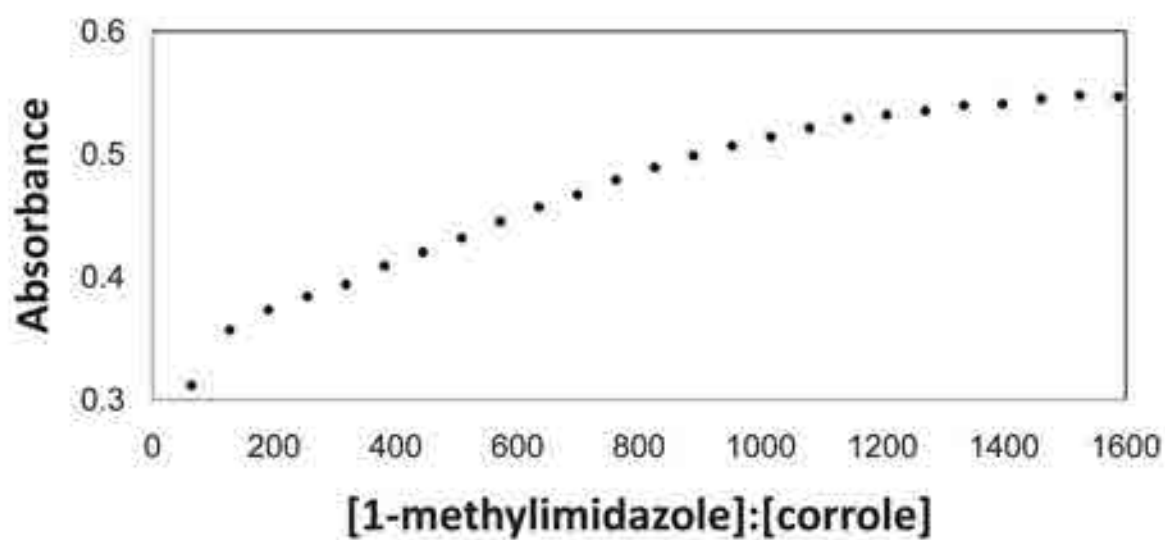
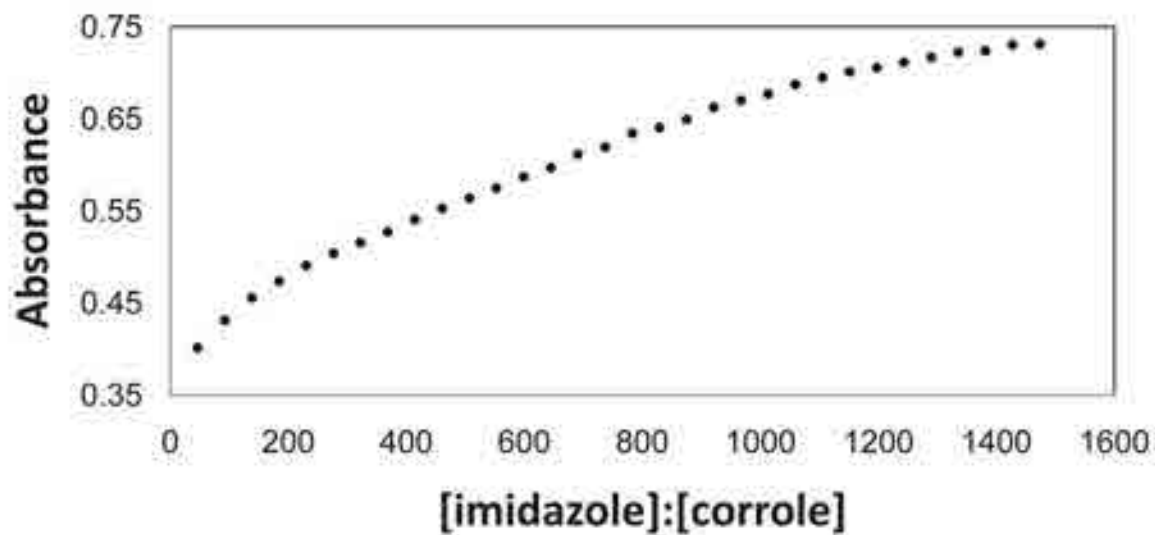


2-methylimidazole



Graphs of reaching maximum binding ratio:





additional toluene to yield a 5 ml diluted solution. The concentration of the diluted solution was found to be 2.08×10^{-5} M. The extinction coefficients of $\text{Fe}^{\text{III}}(\text{tpfc})(\text{OEt}_2)_2$ in toluene were determined by applying Beer's law.

Spectrometric titrations:

To establish a baseline spectrum, toluene was first recorded via both cuvetts. A small amount of $\text{Fe}^{\text{III}}(\text{tpfc})(\text{OEt}_2)_2$ was then dissolved in the sample cuvet containing 2.0 mL of toluene. The concentration of $\text{Fe}^{\text{III}}(\text{tpfc})(\text{OEt}_2)_2$ must be preserved between $11 \mu\text{M}$ and $20 \mu\text{M}$ to obtain reliable absorption readings ($\text{Abs} \sim 0.4\text{--}0.9$); if the sample is overly concentrated, or too diluted, the intensity of light becomes too difficult to measure due to the detection limits of the Shimadzu UV-2101PC spectrophotometer. All pyridines and imidazoles were initially diluted or dissolved in toluene solvent, except pyridine and 4-methylpyridine which were titrated directly into the cuvet as a liquid. Besides these, the concentrations of all other pyridine and imidazole derivatives were preserved between 0.06 M and 0.09 M. After each titration, the absorption reading was recorded using an increment of $20 \mu\text{L}$ in each trial. When the absorption of the new Soret band ceased to increase significantly, no further ligand was added to the sample.

Discussion

Tables 1, 2, and 3 show the wavelengths of the shifting-Soret peaks, final moles of ligands, total moles of $\text{Fe}^{\text{III}}(\text{tpfc})(\text{OEt}_2)_2$, and the ratio of binding between ligands and the Iron corrole. The affinity for

$\text{Fe}^{\text{III}}(\text{tpfc})(\text{OEt}_2)_2$ toward electron-donor ligand performance in this study is as follows:

4-dimethylamino pyridine >
4-methylimidazole > 1-methylimidazole > imidazole > 4-methylpyridine > pyridine

The 2-methylimidazole and 1, 2-dimethylimidazole did not exhibit any binding.

The electron donating groups on the pyridine and each imidazole derivative were the most important factors in this experiment. When the solid $\text{Fe}^{\text{III}}(\text{tpfc})(\text{OEt}_2)_2$ was dissolved in toluene, the molar absorptivities were 3.5×10^4 at 385nm and 8.8×10^3 at 546nm on the UV/Vis spectrum report. Since the extinction coefficients of $\text{Fe}^{\text{III}}(\text{tpfc})(\text{OEt}_2)_2$ were very large ($\epsilon > 10,000$), we may presume that this species would exhibit charge transfer absorption in this experiment. In order to reveal the charge transfer spectrum, it is essential for one component to have electron-donor properties, and for another component to have electron-accepter feature. Therefore, this reaction could be considered as a Lewis acid-base interaction. In this experiment, Iron (III) complex ion served as the electron acceptor, and pyridine and imidazole derivatives were the electron donors. Under normal conditions, the electron would be transferred from the electron rich group to a *d* orbital of an electron acceptor group.

In this work, the nitrogen atom on the simplest pyridine had a lone pair of electrons. These electrons were not delocalized in the aromatic π -system. For this reason, these pyridines were viewed as Lewis bases which are capable of electron donation which commit its lone pair of electrons to the *d* orbital. In addition, all the other pyridine derivatives substituted

a Hydrogen atom at the C-4 position despite containing several different electron donating groups. Theoretically, these more complex pyridine derivatives should have stronger affinity toward our Iron (III) corrole complex.

The structure of the Imidazole was similar to the pyridines. In the imidazole, two C-H groups in a five-membered ring were replaced by two nitrogen atoms, instead of the replacement of one C-H group in the six-membered ring of the pyridine derivatives. Because of the increased electron number resulting from the two lone pairs of electrons on the nitrogen atoms of the imidazole ring, the imidazole derivatives were considered stronger electron donors than the pyridine derivatives. This tendency was demonstrated in the results of this experiment, where all imidazole derivatives showed stronger binding than other pyridine derivatives, excluding 4-dimethylamino pyridine. The ratio of 4-dimethylamino pyridine to Iron (III) corrole complex was the smallest (1000:1). The dimethylamino group of pyridine was an important factor to elicit the strongest binding in this work. The dimethylamino group contained a lone pair on its nitrogen atom, which was distributed to stabilize the ligand. The partial positive charge of the nitrogen atom was also stabilized by two adjacent methyl groups. The electron density of the methyl groups were able to move through the σ -bond to the partial positive nitrogen atom due to inductive effects. Thus, this effect not only stabilized the 4-dimethylamino pyridine itself but also provided stronger binding with Iron (III) corrole complex than other imidazole derivatives, which only possessed methyl donating groups at

different positions of the five-member ring of the imidazole derivatives. However, the positions of the electron donating groups were also another factor contributing to the binding strength.

In this experiment, 1-methyl, 2-methyl, and 4-methylimidazole were used, and all of these imidazole derivatives were isomers with the same molecular formula ($C_4H_6N_2$) but different structural formula. Although each possessed one methyl group, the binding ratio dramatically differed. When the methyl group was at the C-4 position of the imidazole ring, it had the strongest binding as compared with the other two derivatives. Because the ratio of ligands to Iron (III) corrole complex was smaller at the C-4 position (1000:1) than at other imidazole positions, the ratio indicated a stronger affinity toward the Iron (III) complex than other imidazole derivatives in this experiment. However, when the methyl group was positioned at C-2 of the imidazole ring, the binding between $Fe^{III}(tpfc)(OEt_2)_2$ and the ligand was not formed at all. The 1, 2-dimethylimidazole exhibited the same result as 2-methylimidazole, in which the binding did not develop even though there was another methyl group located at the C-1 position. In short, the electron donating group at the C-4 position exhibited stronger binding than other positions. Once an electron donating group existed at the C-2 position, the formation of bond was inhibited completely. It remains unclear whether it was or was not caused by steric effect. Future researchers are encouraged to use crystallography to conduct experiments in order to visualize the structure of the binding complexes.

From UV/Vis spectra, we dis-

covered that during spectrometric titration every spectrum except that of 2-methylimidazole and 1, 2-dimethylimidazole crossed at a certain point, called an isobestic point. In our results the isobestic points, located approximately between 400 nm and 410 nm, indicated that only two principle species were present while the binding was formed. Once the new principle species was formed, the Soret band shifted from 385 nm to approximately 420 nm. However, the larger transformation of the Soret band did not represent stronger binding: for example, compared to imidazole derivatives, 4-dimethylamino pyridine had the strongest affinity to $Fe^{III}(tpfc)(OEt_2)_2$, but the shift of the new-formed Soret band (420 nm) was smaller than that of Imidazole derivatives, which was contrary to expectation. Furthermore, the binding ratio of imidazole was roughly twice that of 4-dimethylamino pyridine, reinforcing that the 4-dimethylamino pyridine had the stronger affinity toward the Iron (III) complex than the imidazole derivatives.

Conclusion

The affinity for $Fe^{III}(tpfc)(OEt_2)_2$ with electron-donor ligand performances in this study is as follows:

4-dimethylamino pyridine > 4-methylimidazole > 1-methylimidazole > imidazole > 4-methylpyridine > pyridine

The 2-methylimidazole and 1, 2-dimethylimidazole did not exhibit any binding.

The formation of a bond was not only elicited by the existence of an electron donating group, but also affected by the position of the electron donating group on either the five-membered ring of the imidazole

derivatives or six-membered ring of pyridine derivatives. Since the ratios of reaching maximum binding were approximately 1000:1 or larger, it suggests that the bindings between $Fe^{III}(tpfc)(OEt_2)_2$ and the ligands were unstable. Consequently, further research will better identify the stoichiometry of the predominant complex using the method of continuous variation.

References

Gross, Z., Nitsa Galili, and Irena Saltsman, *Angew. Chem, Int. Ed.*, 1999,38, No.10

Gross, Z., Nista Galili, Liliya Simkhovich, Irena Saltsman, Mark Botoshansky, Dieter Blaser, Roland Boese, and Israel Goldberg, *ACS*, 1999, Vol.1, No.4, 1999

Simkhovich, L., Atif Mahammed, Israel Goldberg, and Zeev Gross, *Chem. Eur. J.*, 2001, 7, No5

Walker, F.A., Man-Wai Lo, and Molly Tutran Ree, *J.Am. Chem.Soc.*, 98:18, 1976

Molecular Modeling and Dynamics of Zinc Loaded Metallothionein

► **Steven K. Hoang**

Advisor: **Dr. Katherine Kantardjieff**
California State University, Fullerton

Abstract

Using the x-ray crystal structure of rat (*Rattus rattus*) metallothionein (MT), a protein sequence homology alignment, based on rat PDB 4mt2 with rabbit (*Oryctolagus cuniculus*) SwissProt P18055, was made to discern the molecular structure and molecular dynamics of zinc loaded MT. Comparatively, in ICM-Pro, the primary alignment structure of the homology differed from the original by less than 15%, showing a good fit for structural prediction after loading zinc ions in α and β domains. A resultant dynamics simulation in Schrodinger's Maestro/Desmond was executed specifically to observe the Na binding site on the β -domain at the N-terminus. Using an OPLS2001 force field in an optimized solution box, one 12 ns long, all-atom trajectory was recovered with configurations showing high flexibility and motility through the targeted areas, suggesting the possibility of mediated intra-molecular metal-ion transfer.

Keywords

Metallothionein, thionein, 4mt2, P18055, x-ray, crystallography, molecular dynamics, modeling, apo-, zinc, loaded, simulation, trajectory,

heavy-metals, ion-transfer

Introduction

Metallothionein is a superfamily of small, low-molecular weight, cysteine-rich proteins whose residual thiol groups allow the binding of xenobiotic (Cd, Hg, Ag) and physiological (Zn, Cu, Se) metals. The unique quality inherent in metallothionein is the capacity to serially bind metals of varying sizes from apo-thionein to form loaded metallothionein. Metallothionein is composed of two anti-parallel β -domains with 3 metal binding sites at the N-terminus and one α -domain with 4 metal-binding sites at the C-terminus, for a total of seven equivalents of divalent metal ions (Henkel).

First derived from horse kidney by Margoshes and Vallee in 1957, metallothionein has since been isolated in the cytoplasm of eukaryotes and the periplasm of bacteria; it appears ubiquitous in nature (Wikipedia). Currently, the system of classification for MT has 16 families with each family based on the primary structure of the protein (a definitive set of sequence-specific characters). These are further subdivided into subfamilies and isoforms. Subfamilies share "more stringent phylogenetic features such

as specific monophyletic relationships among the sequences of proteins and/or of nucleotide segments in the genes" (Henkel).

AZ Mason's prior work with metallothionein brought into question the specific pathways and processes in which metal ions were transferred in-situ in rabbit MT from domain to domain. This project aims to extensively discuss and predict the ramifications of those findings, specifically the processes of basic mechanics for trajectory calculations of fully loaded metallothionein.

Further elucidation focuses most notably on molecular modeling and dynamics of metallothionein rather than on specific zinc-centered mechanisms or processes, in-vivo or otherwise. This basic science research may offer insights into specific biological processes involving zinc-regulated pathways, protective cellular capacities regarding free radicals, the removal of heavy metals, a "correlation between metallothionein synthesis and amplified oncogene" expression, and resistance to therapeutic pharmaceuticals (Doz).

Experiment and Results

Dr. Katherine Kantardjieff's discourse regarding metallothionein be-

gan the experimental process and all subsequent procedural work derives from the advice and guidance given.

As a molecular modeling and dynamics project focusing on AZ Mason's work with zinc loaded rabbit liver (Zn_7MTII), a protein structure was needed for study. Rabbit liver metallothionein was unavailable for direct download using the Protein Data Bank offered by RCSB (<http://www.rcsb.org/>); however, a close relative in the mammalian MT-2 family was available in x-ray crystal structure. Rat MT-2 was downloaded through Molsoft's ICM-Pro as the PDB entry, 4mt2 (Figure 1). Slight modifications were made to the core of the PDB file before insertion into ICM-Pro; the coding for cadmium was replaced to represent seven zinc ions (Figure 2) to closely replicate the parameters of the previous study by Mason et al.



Figure 1. Original PDB of 4mt2



Figure 2. Modified PDB of 4mt2 with zinc substitution

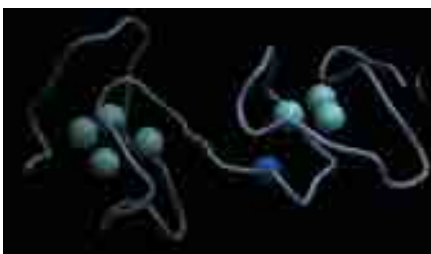


Figure 3. Modified PDB of 4mt2 with Na point of interest



Figure 4. Homology Sequence between 4mt2 (with zinc) and rabbit liver MT-2

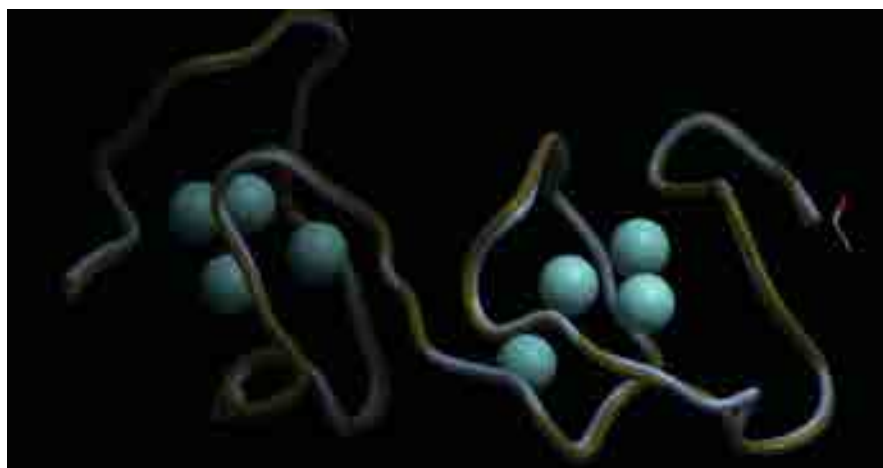


Figure 5. Interactive Modeling Build of 4mt2-rabbit homology. The original 4mt2 is in olive. The new model appears in turquoise. Noticeable differences lie in the boxed section.



Figure 6. Build Model: Sequence variation highlighted

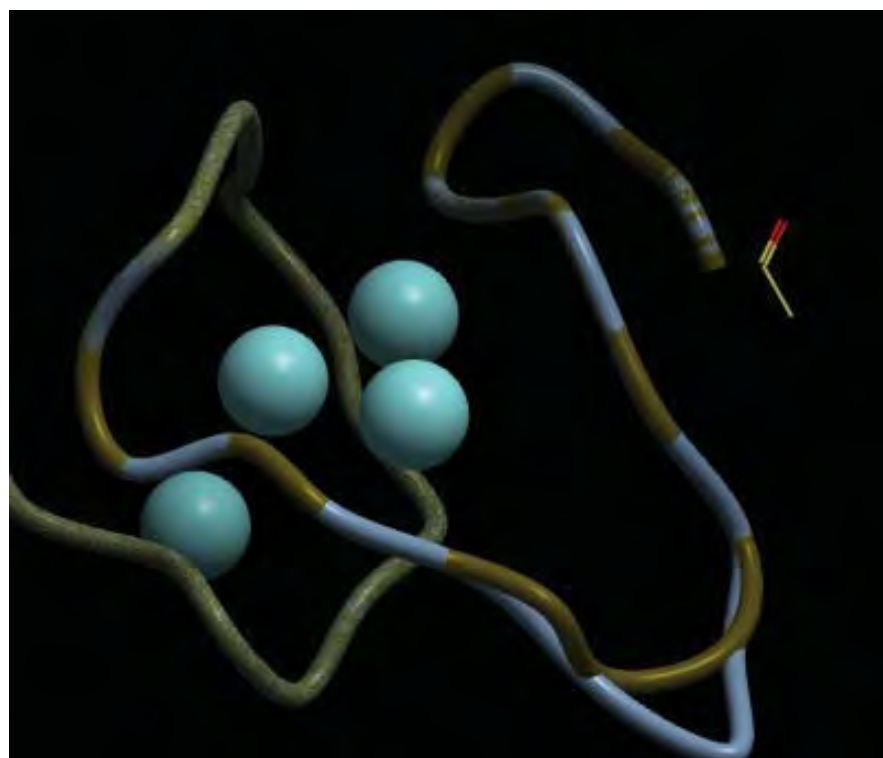


Figure 7. Build Model: 4mt2-rabbit homology. The original 4mt2 is in olive. The new model appears in turquoise. Noticeable differences lie in the boxed section.

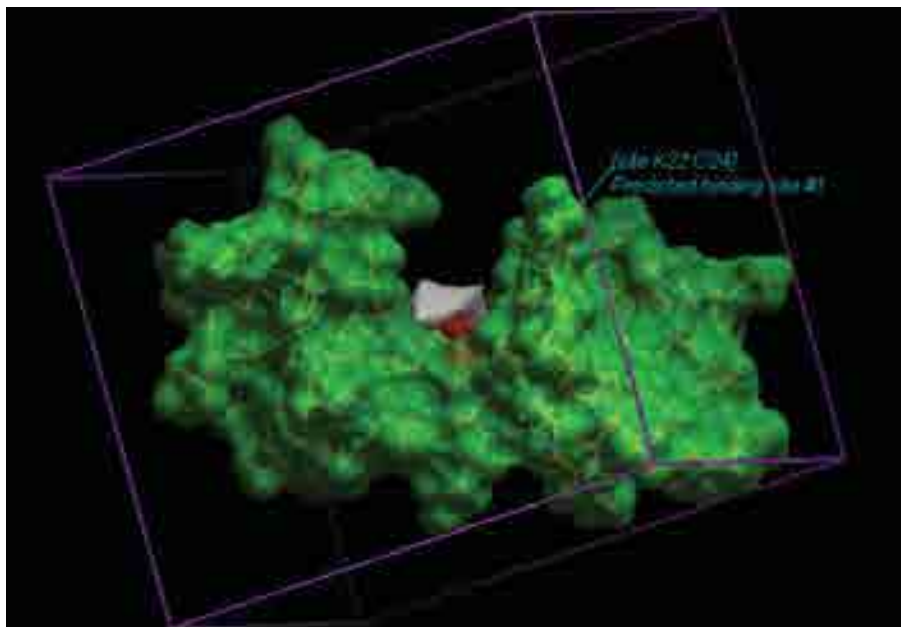


Figure 8. Solution box and projected binding site as seen in ICM-Pro's docking simulation.

To complete the homology, SwissProt P18055 was downloaded in FASTA format. This sequence corresponded to one used by Mason's group. The protein sequence for 4mt2 was extracted using ICM-Pro's sequence extraction option. The two sequences were made parallel via the alignment option, giving a combination that allowed for a protein homology and the subsequent structure to be aligned and predicted to 85% similarity with pP at 25.1 (Figure 4).

After completion of the alignment, a homologous structure was

created using 4mt2 as a 3D template using ICM-Pro's Homology and Interactive Modeling controls (Figure 5).

A secondary modeling was shaped through the same homology command, "Build Model", using default parameters. The resultant structure shows greater variation in the β -domain with almost no change in the α -domain. The differences between the structures were limited by one loop length of 7 amino acids at AA—GDS (Figure 6). This series of non-polar/polar, neutral/negative

amino acids was believed to have no bearing on the overall flexibility of the protein.

Models created from the homology section and modified PDB files were saved. The PDB file was imported into Schrodinger's Maestro 8.5 Protein Preparation Wizard on a CentOS 5.2 Linux computer with D. E. Shaw Research's Desmond molecular dynamics coding. This allowed the fine tuning and adjustment of parameters to create possible trajectories for metallothionein under normalized conditions. A default solution box with disulfide bond detection using OPLS2001 force fields was selected to run under optimized conditions for the default trajectory length of 12 ns (Figure 8).

Discussion and Conclusion

Selected clips and frames of the resultant trajectory in Maestro\Desmond are shown in Figure 9. Though slightly difficult to see, there is enough motility and flexibility in the protein between transitions in the trajectory clip. The protein warps and bends considerably from Figure 9.a to Figure 9.c with multiple overlaps. This behavior suggests some form of covalent ion-transfer is possible. However, for thorough understanding, many more trajectories still need

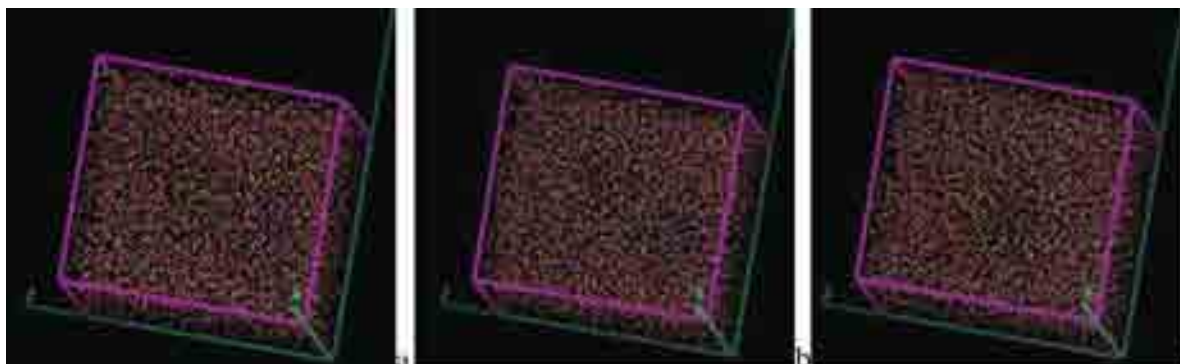


Figure 9. Selected trajectory frames. A: Initial modified protein sequence. B: The trajectory at 6ns C: Final moments in the trajectory

to be done, using differing numbers of zinc ions along with dimers of apo-thionein and metallothionein to examine whether any crossover or binding site matching occurs.

Acknowledgements

This project would not have been possible without continual guidance from Dr. Katherine Kantardjieff, Dr. Qiang (James) Zhao, and the X-ray Crystallography group. The paper would not be in this form if not for the efforts by William Reynolds III and Joyce Park.

References

1.) A Z Mason, N Perico, R Moeller, K Thrippleton, T Potter, D Lloyd, Metal donation and apo-metalloenzyme activation by stable isotopically labeled metallothionein, *Marine Environmental Research*; 2004 August-December; 58(2-5): 371-375

2.) W Braun, M Vasák, A H Robbins, C D Stout, G Wagner, J H Kägi, and K Wüthrich. Comparison of the NMR solution structure and the x-ray crystal structure of rat metallothionein-2. *Proc Natl Acad Sci USA*. 1992 November 1; 89(21): 10124–10128.

3.) F Doz, N Roosen, and M L Rosenblum. Metallothionein and anticancer agents: the role of metallothionein in cancer chemotherapy. *Journal of Neuro-Oncology*. 1993 May 1; 17(2): 123-129.

4.) G Henkel and B Krebs. Metallothioneins: Zinc, Cadmium, Mercury, and Copper Thiulates and Selenolates Mimicking Protein Active

Site Features – Structural Aspects and Biological Implications. *Chem. Rev.* 2004 January 28; 104(2): 801-824

5.) Wikipedia. “Metallothionein.” Revised 2008 Dec. <http://en.wikipedia.org/wiki/Metallothionein>

Subsurface Modeling of Low Porosity Units Restricting Groundwater Recharge to the Regional Aquifer, El Mirage Valley, Mojave Desert, San Bernardino County, California

► Dale R. Dailey

Advisor: Dr. W. Richard Laton, Dr. John H. Foster

California State University, Fullerton

Abstract

El Mirage Valley is located in the Oeste hydrologic sub-basin in the Mojave Desert, just West of Victorville CA and about 25 miles from Interstate 15. The citizens of El Mirage depend almost exclusively on the local groundwater as their source of drinking water. El Mirage Valley contains two aquifers; a shallow aquifer approximately 25 meters (75 feet) thick, which resides only a few meters below the surface; and a deeper Regional Aquifer, which is separated from the shallow aquifer by interbedded low porosity clay and silt units, and is believed to be as much as 125 meters (400 ft) thick. Currently a large portion of the potable groundwater for the township of El Mirage is being pumped from the shallow aquifer, which at current rates will be depleted in the next few decades or degraded to unuseable quality. Using data from well logs in El Mirage, the clay/silt layer was modeled and mapped to measure the unit thicknesses and variation; and assess the potential for artificial aquifer recharge.

To perform this analysis, data for each well in the area was collected from Mojave Water Agency and cataloged into a database. Each well was

then given a unit description according to the average hydraulic conductivity (K value) of the sediments found in the wells, in order to limit the possible values to one of six soil types: clay, silt, sand, gravel, cobbles, and boulders. This was done using the Baseline-Hydrologic Unit Mapping Protocol (B-HUM Protocol®) established by Mojave Water Agency. These wells were then mapped using ArcGIS, and cross sections of the area were created using Crossview™ in order to establish a basic knowledge of the lithology for the area. The well data was then imported into Rockworks, from which profiles and three-dimensional models for the lithology and aquifers were created. These models were compared to the Crossview cross sections for accuracy. Once verified, the models were carefully studied and four potential recharge locations were selected and evaluated based on their location in El Mirage Valley, proximity to the California Aqueduct, and potential interference of the low porosity clays and silts. Based on these results, it was decided that the best potential location for future recharge would be along the southwestern boundary of the study area.

Introduction

Study Area

The Oeste Hydrologic Sub-Basin is located in the Mojave Desert, along the southwestern most part of Mojave Water Agency's jurisdiction zone, approximately 25 miles east of Victorville, and north of the San Gabriel Mountains. El Mirage Valley lies in the northern half of the Oeste Hydrologic Sub-Basin, and contains El Mirage Lake and the township of El Mirage. El Mirage Dry Lake is in close proximity to the Shadow and Adobe Mountains that lie to the North, and Northwest (Figure 1). My study area in particular focuses on the central portion of the valley, surrounding El Mirage and the hypothesized clay layer as previously mapped by the USGS (Huff et al. 2002)(Figure 2).

El Mirage Lake is an ephemeral lake bed, created by runoff from the San Gabriel Mountains along the Sheep Creek alluvial fan. El Mirage Valley contains two aquifers, an upper aquifer that is perched on top of subsurface clay layer(s), and a deeper aquifer, referred to the Mojave River Regional Aquifer. The clay layer splitting the two aquifers was previously estimated (Smith, 2003)

but not modeled or mapped.

Purpose and Goals

The objective of this project is to map, in detail, the subsurface clay layer(s) or subsequent low porosity layers that separate the shallow perched aquifer and the deeper regional aquifer (as defined by Stamos et al., 2001) in El Mirage Valley. Understanding the extent of this clay layer is necessary in order to determine where effective locations for artificially recharge of the deeper aquifer would be, as well as show whether or not natural recharge of the aquifer is presently possible. In order to accomplish this task, the following goals were established:

1. Collect and review all well data for the Oeste Hydrologic Sub-Basin from databases provided by Mojave Water Agency and separate them into useable queries and tables to be used as the base data for mapping and analysis.
2. Using the Baseline-Hydrologic Unit Mapping (B-HUM) protocol previously established for Mojave Water Agency (Environmental Consulting Inc, 2005), categorize the geologic unit descriptions in all wells, and match them with the pre-defined unit names of “clay, silt, sand, gravel, cobbles,” and “boulders” based on the hydraulic conductivity values (K value) for each well section as recorded in the well log database.
3. Export the data tables for geographic location and the updated geologic unit tables into ArcGIS and use them as attribute tables for geographic positioning to allowing them to be useable shape files.
4. Using ArcGIS© and the extension Crossview© create a series of

cross sections, encompassing all the wells in the central portion of the Oeste Hydrologic Sub-Basin, specifically those which lie in El Mirage Valley. Then using principles of sedimentology and stratigraphy, create hand drawn lithology profiles on each cross section to establish the overall lithologic trends for the study area.

5. Using the data originally exported from the Mojave Water Agency database, format and import the data into a form useable in the borehole manager of Rockworks 14© as our principle dataset.

6. Using this data, create computer calculated lithology profiles along the same spacing guidelines as the cross sections made in ArcGIS and compare them to the interpreted lithology profiles to verify accuracy.

7. Once accuracy is verified, use the dataset to create a three dimensional lithology model of the entire study area in Rockworks, from which models of each individual or combined unit types can be made in order to analyze where the aquifers are most easily accessible and where the clay and other low porosity sediments will pose the least amount of interference to artificial recharge attempts.

Previous Work

Previous work in El Mirage Valley includes: Early reconnaissance of the geographic, geologic, and hydrologic conditions of the Mojave Desert region (Thompson 1929); Hydrogeologic reports for the Mojave River Basin and South Lahontan Regional Water Quality Control Board (Badger et al., 1958; DWR, 1960, 1964, 1965, 1966, 1967, 1980, 2003, 2004); geologic mapping of the area (Dibblee 1960, 1968; Morton and

Miller, 2003); USGS groundwater data at various monitoring sites (Huff et al., 2002); a Technical study to evaluate the potential for a long-term Water Management Program between MWA and Metropolitan Water District of Southern California (Bookman Edmonston, 2004); regional water level mapping (USGS, 1994, 1996, 1998, 2000, 2002, 2004); water quality and flow studies throughout the upper Mojave River region (Izbicki et al., 2000, 2005; Izbicki and Michel, 2003; Izbicki, 2004); and a thesis on porosity of subsurface soils in the Oeste Hydrologic Sub-area region (Windfield, 2000).

Collectively, these reports and studies contain the following pertinent information to this study:

1. Groundwater moves northward towards El Mirage Dry Lake from the San Gabriel Mountains through the Sheep Creek Fan, but does not reach the Upper El Mirage Valley (Izbicki and Michel, 2004). Runoff water from the San Gabriel Mountains which originally created El Mirage Lake also no longer reaches the valley area.

2. The groundwater basin is separated into two aquifers: a “shallow,” unconstrained aquifer and a “deep” regional aquifer.

3. Groundwater levels have declined in the area an approximated 15 meters (50 feet) in the last 80 years, and that the groundwater level in the regional aquifer has dropped as much as 53 meters (175 feet) south of El Mirage Lake, possibly causing the 50mm (2 inches) difference in land subsidence measured between 1966 and 1999 (Sneed and Others, 2003).

Background

Symbol	Name	Description
Qa	Quaternary Alluvium	Young unconsolidated alluvium derived from the San Gabriel Mountains, covering all older alluvial deposits to a depth of several hundred feet.
Qc	Quaternary Playa Clays	Brown, sandy clay unit, present at distal end of Sheep Creek Fan.
G	Mesozoic Granite	Granite Units that outcrops in four locations in the study area. Dip estimated at 45°.

Table 1. Breakdown of Major Units in the El Mirage Valley that appear in the study area.

El Mirage and El Mirage Dry Lake

El Mirage is a township just north of Phelan, California, and is without a local water municipality to oversee its water supply, which is almost entirely supplied via groundwater. El Mirage Dry Lake is located in the northwestern portion of the “perched” water table inside the study area. Though an ephemeral lake bed today, this was a deep water deposit in the recent past (exact dates unknown as no age testing has been done in this particular area) as is evident from the clay and silt sediments found in cores from well drilling in the El Mirage Township. During these times it is believed that the lake received runoff water from the San Gabriel Mountains in the southern most part of the basin via the large alluvial fan (known as Sheep Creek Fan). El Mirage Lake is in the center of the Oeste Hydrologic Sub-Basin watershed, yet today runoff waters from Sheep Creek no longer drain into the lake, leaving precipitation, irrigation and septic wastewater as the primary sources of groundwater recharge in the valley proper. (Refer to Figure 1 for all areas referenced in this paragraph.)

Geology

The geology of the area is that typical of desert and alluvial environments. There are three main geologic units in the Oeste Hydrologic Sub Basin (as mapped by Dibblee, 1960) that appear in the study area. The most dominant unit, which covers nearly all of the valley floor, is Quaternary alluvial gravel and sand. The other units are Quaternary playa clays, which appear in the dry lake bed, as well as Mesozoic granite, which outcrops slightly in the southwest quadrant of the study area (figure 3) (Table 1).

Most of the El Mirage Valley, including El Mirage Lake can be seen to have been in the flood plain of the very large alluvial fan (Sheep Creek Fan) to the south. Alluvial environments like El Mirage Valley are comprised surficially of sediments drained from the nearby mountains. The coarse sediments, which require the most energy to move, deposit closer to the source of runoff, with the finer sediments depositing further out. All sediments in Alluvial fan deposits are typically poorly sorted (Boggs, 2006). El Mirage Valley contains sediment layers to an average depth of 151 meters (500 feet) before transitioning to bedrock. It is known that there is a clay layer of undetermined dimen-

sions lying below the upper aquifer. Clay sediments form in deep bodies of water, meaning that at one point El Mirage lake was at significant depth over this area to form clay deposits, and has since dried and been washed over by coarser sediments. It is expected that in the past lake depth fluctuated as precipitation in the area decreased. This would cause the lakes depth to also fluctuate as the lake bottom moved closer and farther from the sheep creek water source. It is expected that the sub-surface lithology for this area will be interbedded and fluctuate between fine and coarse sediments.

The collective soils that make up the surface and upper subsurface layers in El Mirage Valley are Cajon sands, which are found primarily in alluvial fans near the base slopes of mountains in the valley; Manet coarse sand, which is the primary sand type covering most of the valley floor; Manet loamy sand, a deeper, well drained sand found between the three small mountains in El Mirage Valley; and Manet fine sandy loam, which is found along low alluvial fans. (All sediment names and occurrences taken from Soil Survey of San Bernardino County California, surveyed by the United States Department of Agri-

Cajon Sand	Very deep, somewhat excessively drained soil, found on alluvial fans. Forms in alluvium derived dominantly from granitic materials.
Manet Coarse Sand	Very deep, well drained soil, found on alluvial fans. Forms in alluvium derived dominantly from dark-colored micaceous minerals.
Manet Loamy Sand, Loamy Substratum	Very deep, well drained soil, found on alluvial fans. Forms in alluvium derived dominantly from dark-colored micaceous minerals.
Manet Fine Sandy Loam	Very deep, well drained soil, found on low alluvial fans along intermittent drainage ways. Forms in alluvium derived dominantly from dark-colored micaceous minerals.

Table 2. Breakdown of common soils found in El Mirage Valley. All information on soil including type, occurrence, and composition taken from the US Department of Agriculture's "Soil Survey of San Bernardino County California," 1985.

culture, 1985.) A brief breakdown and description of these soil types has been provided (Table 2).

Aquifers

El Mirage is presently known to contain two aquifers, an upper aquifer, and a deeper "regional" aquifer. The upper aquifer is locally perched, and is separated from the regional aquifer by the ambiguous clay layer contained in the subsurface. The clay layer itself first appears between 4-5 Meters (25-50 feet) below the surface, or between 850 and 870 Meters (2850 and 2900 feet) above sea level (Figure 4). The clay layer separating the two aquifers does not outcrop above the surface, making the unit thickness difficult to determine. Also, due to the nature of alluvial fan development, it is likely that the sediment layers will be interbedded, alternating in consistency and bed makeup as discharge levels alternate annually. Currently the upper aquifer, or "perched" aquifer, is the primary source of drinking water for the El Mirage Townships residents. Increased pumping of this aquifer over the past 18 years (since 1990) has also created a large cone of depres-

sion in the central Oeste Sub-area causing an estimated 7.5 meter (25 foot) decline in groundwater levels since 1950. [Sneed et al. 2003, Smith 2003] The deeper regional aquifer resides an average of 38 meters (125 feet) below the surface (Figure 5). This deeper aquifer is thought to contain a significantly more abundant supply of water than the perched aquifer. The primary concern and hindrance in accessing this currently untapped groundwater resource lies in its lack of natural water recharge.

Methods

The clay layer beneath El Mirage is buried beneath Quaternary Aged Alluvium (Henceforth referred to as Qal.) and does not outcrop anywhere above the surface, making use of traditional analysis tools such as geologic maps and cross sections impossible. To create a reliable profile of the subsurface for analysis, a multi-step computer based approach was developed.

The first step in creating the subsurface profile was to gather information on the wells in the Oeste Hydrologic Sub Basin and shape it into a workable dataset for use with other applications. This data was pro-

vided by Mojave Water Agency in the form of an extensive database cataloging all wells in the Mojave Desert. This database was imported into Microsoft Access 2003, where it could be more easily manipulated. Using SQL queries to filter data across multiple tables we were able to extract only the data needed for the wells to be plotted and mapped, such as: name fields, coordinate data, depth information, unit description per depth interval, and water level depth. It quickly became apparent that the descriptions cataloged in the database (which were originally added word for word based off of the driller well logs taken in the field) were far too varied to provide any reliable source of visual translation. To combat this, the database was queried to filter units by their porosity "K" value rather than their unit descriptions. This "K" value had been previously calculated in a study done by Environmental Consulting Inc. in 2005 based off of known average hydraulic conductivity in cm/sec (Sanders, 1998; Environmental Consulting Inc., 2005). The unit descriptions were then changed from their original descriptions to the soil materials derived from the Hydraulic Conductivity (K) for the same wells. This

Soil Material	Average Log10 K (cm/sec)
Clay	-7.5
Silt	-5.0
Sand	-3.0
Gravel	1.0
Cobbles	2.9
Boulders	3.0-5.0
Rock (Bedrock)	5.0+

Table 3. Average Hydraulic Conductivity (K) of Soil Materials as determined by Environmental Consulting Inc. Calculations based off of data by Sanders, 1998.

yielded six reliable values for soil types (Table 3).

The next challenge in building a profile for the clay layer was to somehow create reliable cross sections of the wells. To start, we began by mapping the well locations in ArcMAP, based off of their coordinate data contained in the well database. Once mapped, Crossview, an extension for ArcMAP was used to make the actual cross section slices. Crossview uses the Digital Elevation Model (DEM) for the map area and depth information contained in the well layer's attribute table to create a profile view of the wells with accurate depth information. Then, by categorizing the well units based on the "description" field in the attribute table, the wells units can be uniquely identified, showing the lithology of the sediments into which they are cut. Using Crossview, cross sections were made from west to east and from north to south in one thousand

foot intervals, covering the entire study area. (Refer to Appendix A for examples.) Finally, each cross section was printed out and the lithologic units were drawn and connected by hand. These were used to compare and contrast the lithology profiles created automatically in Rockworks and look for problem areas or unreliable well information.

Once the maps and cross sections of the study area were made, Rockworks 14 was used to tie all the data together and form the three dimensional lithology models to look for potential recharge locations for the aquifers. To create these profiles, the database was once again queried to create tables in a format the Rockworks could work with. These tables were then exported into an excel spreadsheet, at which point our data was added to an exported Rockworks 14 spreadsheet and then imported into the borehole manager of Rockworks. Once the project dimensions

were set, the wells (used interchangeably with boreholes henceforth) were mapped on a location map, showing the borehole locations, names, and topography of the area. A surface grid of the area was also made using the elevation measurements recorded from the DEM field of the original database. Using this location map, lithology profiles were created along the same spacing guidelines as the cross sections developed in Crossview. Using the well SWN numbers, the wells were matched along the same profile lines and compared for lithologic accuracy. By matching the lithology between the hand drawn cross-sections and the computer interpolated lithology profiles made in Rockworks, not only was the accuracy of the lithology profiles verified, but I also found where lithologic inconsistencies existed (Figure 6). The well logs for these inconsistent areas were examined and most were found to be unreliable due to lack of descriptive accuracy (Figure 7). Once the well logs were validated, the lithology profiles were examined for unit trends and interpreted.

The final step for determining the overall profile was to use the collected lithology information contained in the well logs and have Rockworks interpolate the layers into a three dimensional profile. This was done using the built-in modeling options contained in Rockworks. Once all the needed surfaces and grids were programmed and created, the lithology information was computed into two different models. One containing a non-interpolated model (meaning continuity between units not calculated past a certain node distance) and an interpolated model (Figures 8 and 9). Using the new models, the various layers could

be turned on and off and examined for their continuity, unit thickness, and occurrence throughout the project area. By examining the clay and silt units, and their relation to the aquifer, reliable areas for aquifer recharge were determined.

Discussion

The Township of El Mirage uses groundwater as the primary water supply for its citizens industries. They are currently pumping the majority of their water from the perched aquifer in the Oeste Hydrologic sub-basin. This aquifer is convenient in that it is at a shallow depth, making it easily accessible, and is recharged by precipitation and return flow associated with agriculture. At the current rate of usage however, this aquifer will not be a viable long-term resource. It is important for the township to realize that it is a necessity to begin enacting plans to access the Regional Aquifer in the near future, as current usage of the perched aquifer is constantly increasing the contaminant level and depleting this resource.

The Regional Aquifer lies approximately 125 meters (400 ft) below the surface. Its exact dimensions are unknown but based on current water level data it is thought to contain significantly more water than the perched aquifer. Well logs and aquifer models show that the perched aquifers maximum depth lies only about 30-50 meters (100-150 feet) below the surface or 850 meters (2,800 Feet) above sea level (figure 10). The Regional Aquifer trends at roughly 120 meters (400 feet) below the surface or 790 meters (2,600 feet) above sea level, rising slightly in the southern section of the study area (figure 11). It is likely that these

two aquifers merge together to the north and south of El Mirage as they get further and further from the El Mirage dry lake, however, in the El Mirage area they are separated by an extremely low porosity "clay" unit. (The term clay is used in this section to generally describe a unit or units of low hydraulic conductivity, specifically those with a "K" value of less than -5 cm/sec in accordance with the B-HUM protocol used to calculate units. For purposes of this text, "silt" and "clay" will be referred to only as "clay.")

The clay unit separating the two aquifers in the El Mirage township area is of great concern as it prevents natural recharge from reaching the lower aquifer. Clay is a natural hindrance to water flow as it has the lowest hydraulic conductivity for sedimentary structures (Sanders 1998, Fetter 2001, Environmental Inc 2003). As it stands there is no known means of groundwater recharge to this aquifer. Precipitation, as previously mentioned, does not reach the regional aquifer locally due to the restricting clay unit(s), and the runoff from the San Gabriel Mountains via the Sheep Creek Fan no longer reaches the El Mirage area. If the perched aquifer remains the primary water supply for El Mirage it will eventually dry up or become overly contaminated with pesticides and salts, which will leave the citizens of El Mirage without potable drinking water, as well as potentially causing large scale subsidence in the area.

Before pumping from the lower Regional Aquifer can begin, the extent of the clay layer needs to be determined. The unit never outcrops above the surface; so using traditional methods to calculate the unit extent

was not a viable option. To overcome this problem, I used the multiple step process discussed earlier to create a map of all the boreholes with geology measurements to date for that area. Then, using the information contained within, I was able to create several models of the subsurface geology for the area. These models allow for easy manipulation and examination of the subsurface, and give a reasonably reliable foundation for evaluating recharge options.

These models, while extremely helpful, are not without their limitations. The most important thing to note is that the data can only be manipulated and interpreted where it exists. The less well information that is readily available for an area, the less accurate the interpretations and calculations for that area will be. There are many more wells in the southern portion of the southern portion of the study area (Figure 12) making the lithology interpretations in this area significantly more reliable than those in the northern quadrant. Rockwork, however, has the capability to calculate the lithologic extent of specific beds and units over large areas, so long as some data is available. This does not fully alleviate the margin for error in these models, but it does allow them to be examined with a generally acceptable level of confidence.

Through the numerous models that were created, it has been determined that artificial recharge will be the most effective form of groundwater replenishment if the Regional Aquifer is to be used as a water source for the township. The units of lowest hydraulic conductivity are at their thickest in the central and southern portions of the study area. (Figure 13a-d, Appendix C) As they

move northward, the units become an inter-bedded mix of clay and silt, and begin to thin significantly, especially towards the northwest. Although this may seem like a prime location for recharge opportunities, it is far from ideal. Northwest El Mirage is 15 miles north of the California Aqueduct, which means that water will need to be transported a great distance. Also, the clay unit appears to separate the aquifer along the central portion of the study area (Figure 14). There are no water level wells present in the northwestern quadrant so it is presently unknown whether the aquifer split is localized to one area or split across the entire study area.

Conclusions

Using the analysis from the methods developed for this study, four areas have been determined as likely areas for possible recharge. These areas have been categorized based upon the data modeled in the cited figures thus far and have been listed below ranging first with least optimal areas and ending with the most ideal area given the available data.

The first area recommended as a potential recharge location lies in the far north of the project area (Figure 15 and 16, Location 1). Of the four potential areas, this area shows the least promise for successful recharge. This is due primarily to the thickness of low porosity layers surrounding this location. As can be seen in figure 13d, the clay is prominent and well developed in this area. This location is also the farthest from the California aqueduct, which makes transporting water to the area quite difficult and costly. This area does

show promise as a recharge location however due to the level to which the low porosity clays and silts are inter-bedded with the higher porosity sand units. This makes the possibility of recharge more likely, as it will encounter fewer restricting units as water travels down through the layers. It's also outside of El Mirage township, making it more likely to be available for purchase/lease.

The second area is in the southern portion of the study area (Figure 15 and 16, Location 2). This area is much closer to the aqueduct which makes it more easily accessible than location 1. It does, however, suffer from many of the same setbacks. The clay and silt layers are still very thick and prominent in this area. The clay beds are much more thinly spread in this particular area than in the surrounding areas, making them easier to drill through. The sand and higher porosity layers in this area are also thicker than in the areas farther north, which would allow more water to filter through to the Regional Aquifer. The profile of the clay layer to the immediate north is also a concern, as it thickens greatly over the next 3.2 kilometers (2 miles). These obstacles make it wiser to search for a more favorable recharge location.

The third area in the project area which shows promise for recharge lies in the northwest portion of the study area (figures 15 and 16, location 3). This area has significant improvements for recharge possibilities than the previously mentioned locations. The clay layer in this area thins significantly, and is replaced by layers of sand and boulders. These units are much higher porosity than the clay and silt layers, and will allow more water to filter through to the Regional Aquifer. This area also lies

outside of El Mirage Township, making it more likely to be available for purchase/lease. This area is approximately 21 kilometers (13 miles) from the aqueduct, which makes transporting water to this location costly. It is also likely that the plutonic units that outcrop east of this area will interfere with drilling in this area (Figure 16).

The final area lies in the southwest of the study area (figures 15 and 16, location 4). This location is the best candidate for recharge for several reasons. The clay and silt layers thin greatly in this area, and it lies in close proximity to the aqueduct. It is also located outside of El Mirage township making a purchase or lease a possibility and thus an ideal location for a recharge facility. There are, however, factors that might hinder recharge in this area. There are few of the higher porosity units present, like cobbles and boulders, that would allow large amounts of water to filter through to the aquifer. There is also a lack of water level data available for this area, making it difficult at this point to determine the extent to which the Regional Aquifer is present in this area.

Though all of the areas mentioned are possible candidates for aquifer recharge, there is no way to pick a location that is completely reliable without further research and development being done first. More subsurface data is needed in the areas that do not have any wells in order to make the interpreted lithology more accurate and reliable. Additional water level data is also needed to make an accurate map of the Regional Aquifer and verify its trend in the area. The rapidly decreasing water supply in the El Mirage valley area makes gathering this information

a necessity. I feel confident that once the data is available, reliable locations for recharge of the Regional Aquifer will be much easier to identify by using the same methods used in this study.

References

Badger, J.S., Page, R.W., and Dutcher, L.C., (1958). Data on Water Wells in the Upper Mojave Valley Area, San Bernardino County, California, California Department of Water Resources Open File Report 58-8: 234.

Bookman and Edmonston, (2004). Water Management Program Technical Memorandum No. 06.0 December 7, 2004.

Dibblee, T. W., Jr. (1960). Preliminary Geologic Map of the Shadow Mountains Quadrangle Los Angeles and San Bernardino Counties, California. Mineral Investigations Field Studies Map MF-227: United States Geological Survey.

[DWR] California's Department of Water Resources (2006). Access at <http://wdl.water.ca.gov/>.

[DWR] California's Department of Water Resources (1960). Data on Water Wells in the Western Part of the Middle Mojave Valley Area, San Bernardino County, California: Bulletin 91-1 California Department of Water Resources.

[DWR] California's Department of Water Resources (1964). Ground Water occurrence and Quality Lahontan Region., California Department of Water Resources.

[DWR] California's Department of Water Resources (1965). Data on Water Wells in the Western Part of

the Antelope Valley Area, Los Angeles County, California: Bulletin 91-11, California Department of Water Resources: 278.

[DWR] California's Department of Water Resources (1966). Data on Water Wells in the Eastern Part of the Antelope Valley Area, Los Angeles County, California: Bulletin 9-12, California Department of Water Resources: 448.

[DWR] California's Department of Water Resources (1967). Mojave River Groundwater Basins Investigation, Bulletin 84, California Department of Water Resources: 150.

[DWR] California's Department of Water Resources (1980). Ground Water Basins in California, Bulletin 118-80, California Department of Water Resources: 73.

[DWR] California's Department of Water Resources (2003). California's Water, Bulletin 118 Update, South Lahontan Hydrologic Region El Mirage Valley Groundwater Basin, California Department of Water Resources: 4.

[DWR] California's Department of Water Resources (2004). California's Groundwater Bulletin 118, South Lahontan Hydrologic Region Antelope Valley Groundwater Basin, California Department of Water Resources: 5.

Fetter C.W., (2001). *Applied Hydrogeology, Fourth Edition*: New Jersey, Prentice-Hall, Inc.

Huff, J.A., Clark, D.A., and Martin, P., (2002). Lithologic and Ground-water Data for Monitoring Sites in the Mojave River and Morongo River and Morongo Ground-water Basins, San Bernardino County, California, 1992-98, Open File Report 02-354, United States Geological Survey.

Izbicki, J. A. (2004). Source and Movement of Groundwater in the Western Part of the Mojave Desert, Southern California, USA, Water-Resources Investigations Report 03-4313, United States Geological Survey.

Izbicki, J. A., Ball, J.W., Bullen, T.D., and Sutley, S.J. (2005). "Chromium, Chromium Isotopes, an Selected Trace Elements in Rock, Alluvium and Water from Wells in the Western Mojave Desert, Southern California, USA, USGS Draft."

Izbicki, J. A. and Michel, R.L. (2003). Movement and Age of Ground Water in the Western Part of the Mojave Desert, Southern California, USA, Water Resource Investigation Report 03-4314, United States Geological Society.

Laton, R.W., Foster, J., Blazeovic M., Velarde J., and Cruikshank M., (2007). Oeste Hydrologic Sub-Area Hydrogeologic Report.

Morton, D. M., and Miller, F.K. (2003). Preliminary geologic map of the San Bernardino 30' x 60' quadrangle, California, United States Geological Survey.

Sanders, Laura J. (1998). *A Manual of Field Hydrogeology*, New Jersey, Prentice-Hall, Inc.

Smith, G. A., and Pimental, M.I. (2000). Regional water table (1998) and ground-water-level changes in the Mojave River and the Morongo ground-water basins, San Bernardino County, California, United States Geological Survey, Water-Resources Investigation Report 00-4090: 107.

Sneed, M., Ikehara, M.E., Stork, S.V., Amelung, F., and Galloway, D.L. (2003). Detection and Measurement of Land Subsidence Using Interferometric Synthetic Aperture Radar and Global Positioning System, San Bernardino County, Mojave Desert, California, United States Geological Survey, Water Resources Investigations Report 03-4015, Prepared in cooperation with the Mojave Water Agency: 69.

Stamos, C.L., Martin, P., Nishikawa, T., and Cox, B.F., (2001). Simulation of Ground-Water Flow in the Mojave River Basin, California, United States Geological Survey, Water-Resources Investigation Report 01-4002 Version 3: 129.

Thompson, D.G., 1929. The Mojave Desert Region, California: A Geographic, Geologic, and Hydrologic Reconnaissance, United States Geological Survey Water-Supply Paper 578.

[USGS] United States Geological Survey's (USGS) National Water Information System (NWIS) Access at <http://waterdata.usgs.gov/nwis>.

[USGS] United States Geological Survey (1994). Regional Water-Table and Groundwater–Level Changes in the Mojave River and the Morongo Groundwater Basins, Southwestern Mojave Desert, California, USGS

Water-Resources Investigations Report 95-4209.

[USGS] United States Geological Survey. Regional (1996). Water-Table and Groundwater–Level Changes in the Mojave River and the Morongo Groundwater Basins, Southwestern Mojave Desert, California, USGS Water-Resources Investigations Report 97-4160.

[USGS] United States Geological Survey (1998). Regional Water-Table and Groundwater –Level Changes in the Mojave River and the Morongo Groundwater Basins, Southwestern Mojave Desert, California, USGS Water-Resources Investigations Report 00-4090.

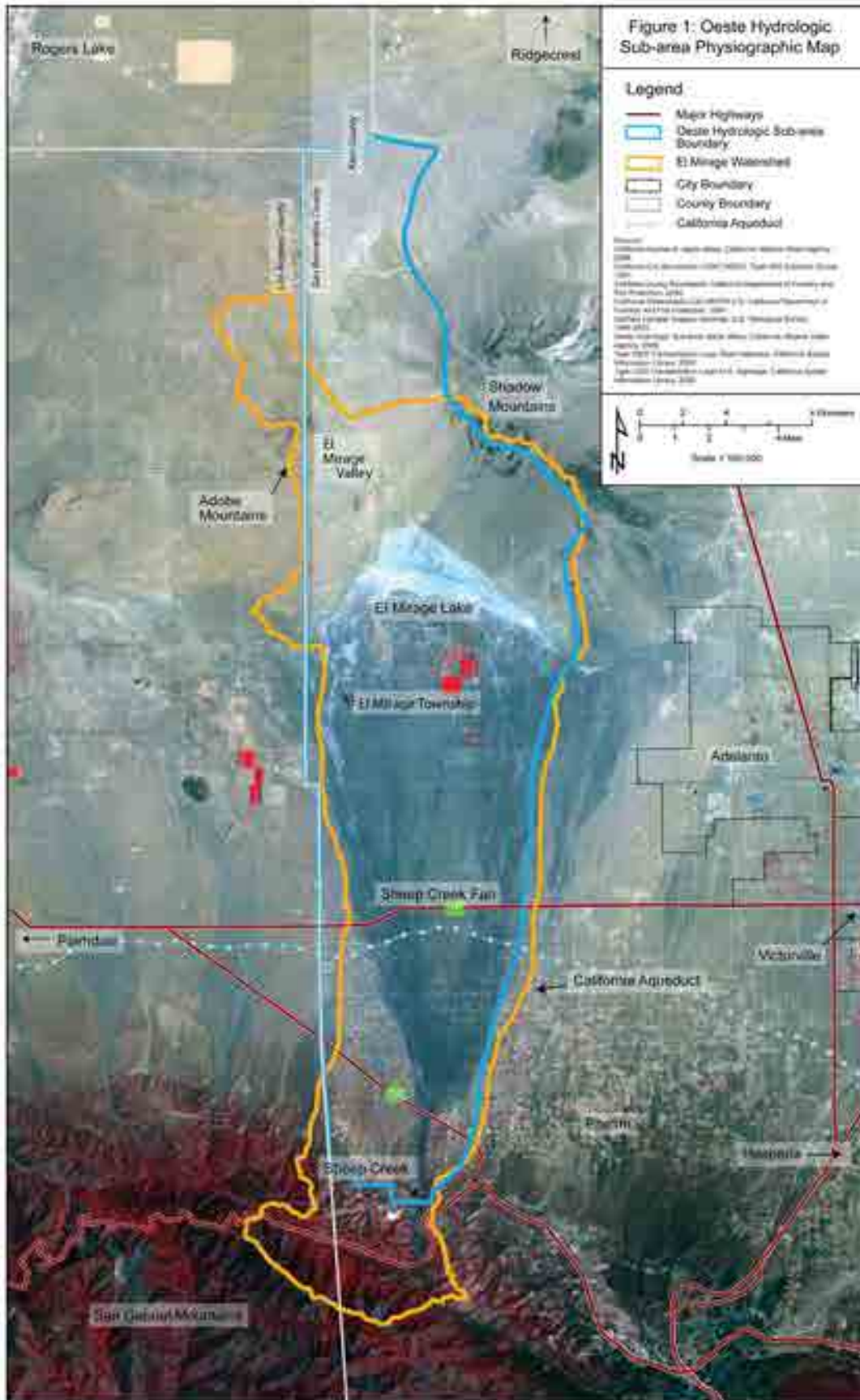
[USGS] United States Geological Survey (2000). Regional Water-Table and Groundwater –Level Changes in the Mojave River and the Morongo Groundwater Basins, Southwestern Mojave Desert, California, USGS Water-Resources Investigations Report 02-4277.

[USGS] United States Geological Survey (2002). Regional Water-Table and Groundwater –Level Changes in the Mojave River and the Morongo Groundwater Basins, Southwestern Mojave Desert, California, USGS Water-Resources Investigations Report 02-5081.

[USGS] United States Geological Survey (2004). Regional Water-Table and Groundwater –Level Changes in the Mojave River and the Morongo Groundwater Basins, Southwestern Mojave Desert, California, USGS Water-Resources Investigations Report 2004-5187.

Winfield, K. A. (2000). Factors Controlling Water Retention of Alluvial Deposits, Western Mojave Desert, MS Thesis, San Jose State University.

Appendix



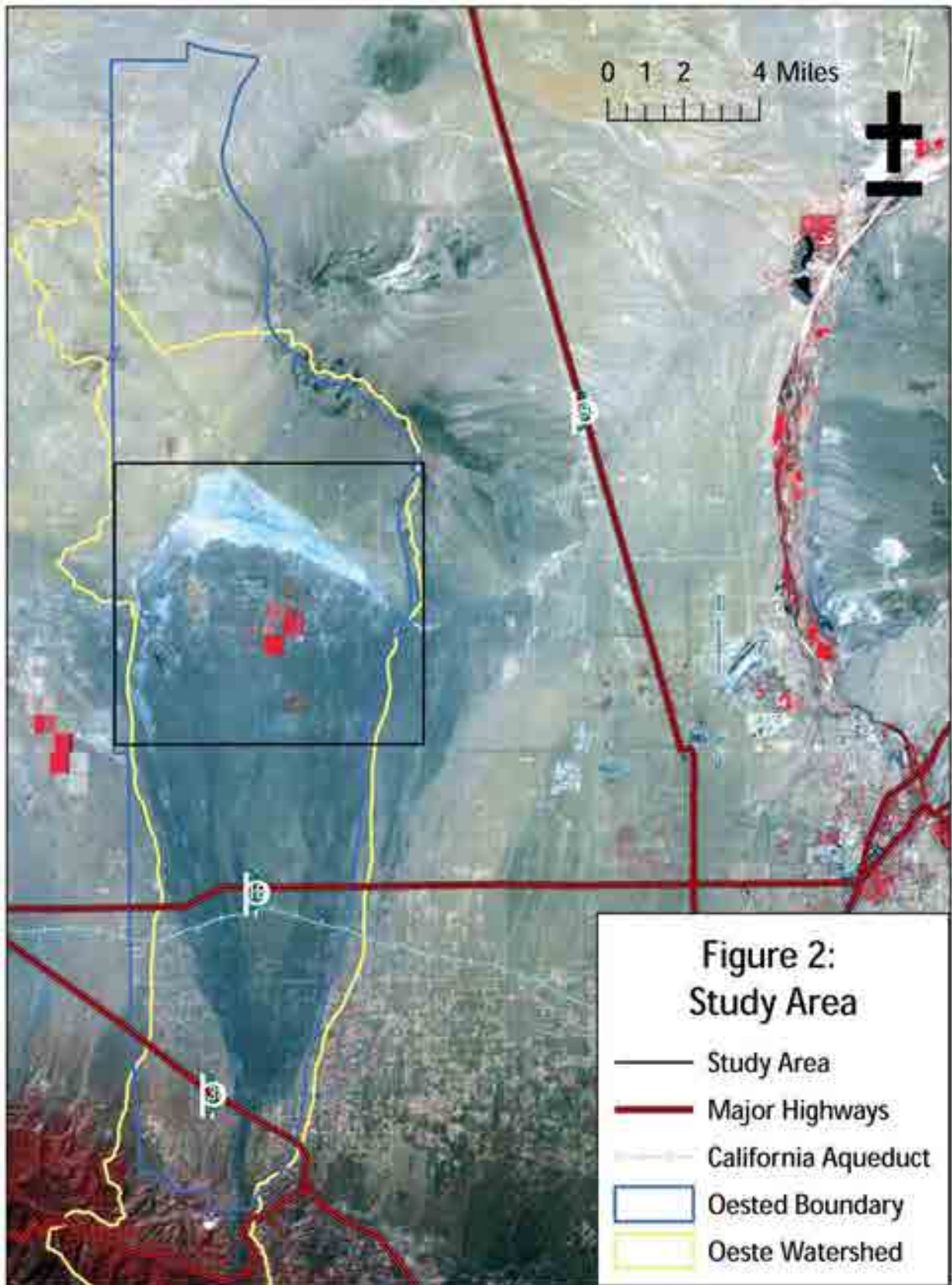


Figure 3: Geologic Map of Project Study Area

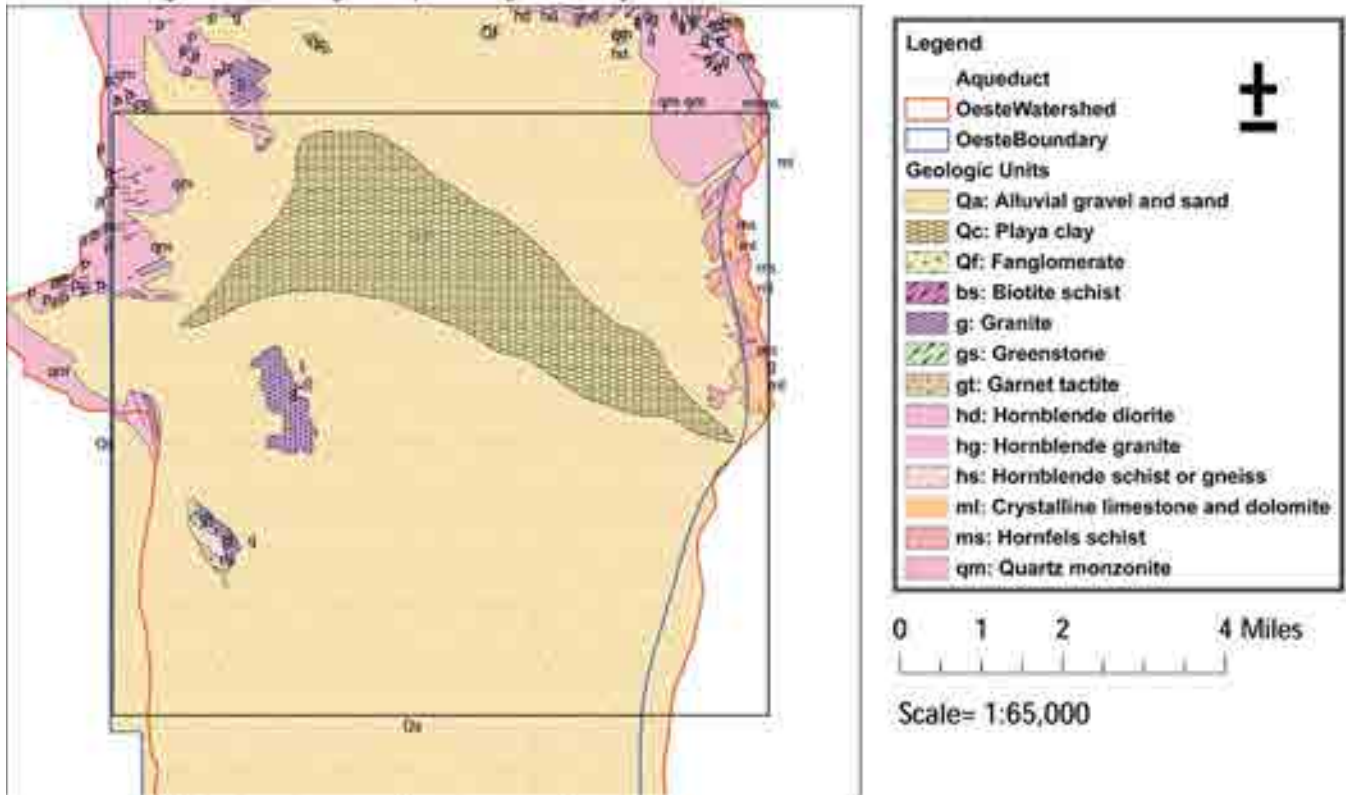


Figure 4: Cross section trending from South to North, showing subsurface geology recorded in driller well logs. The clay unit in red lies at an average elevation of 850 meters (2850 feet) above sea level.

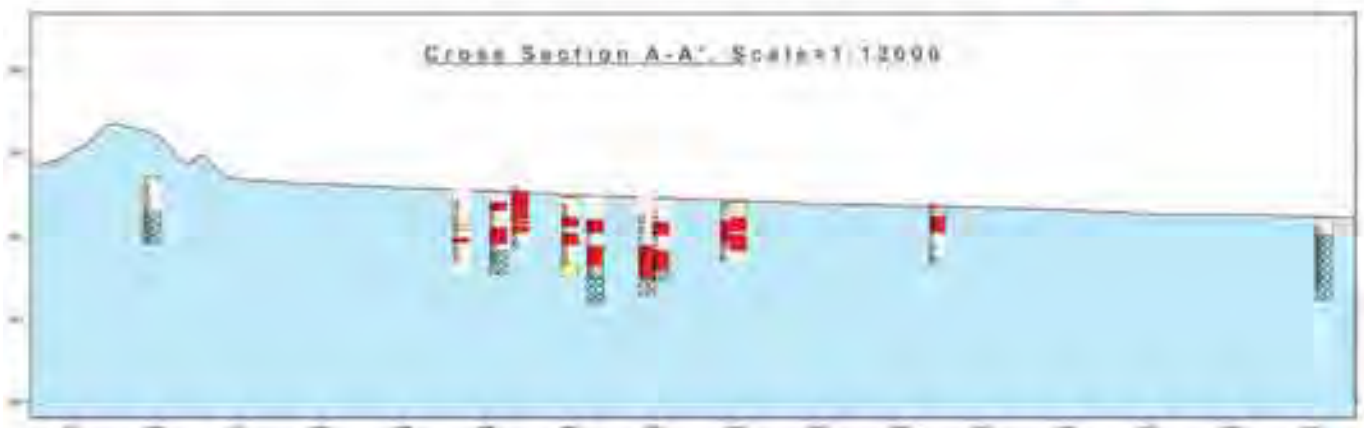
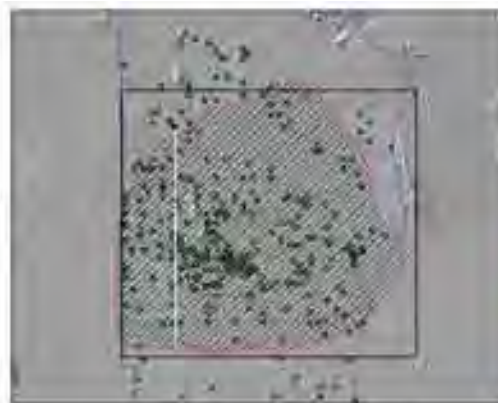


Figure 5a. Profile of Regional Aquifer Showing Surface, Well Lithology, and Water Levels

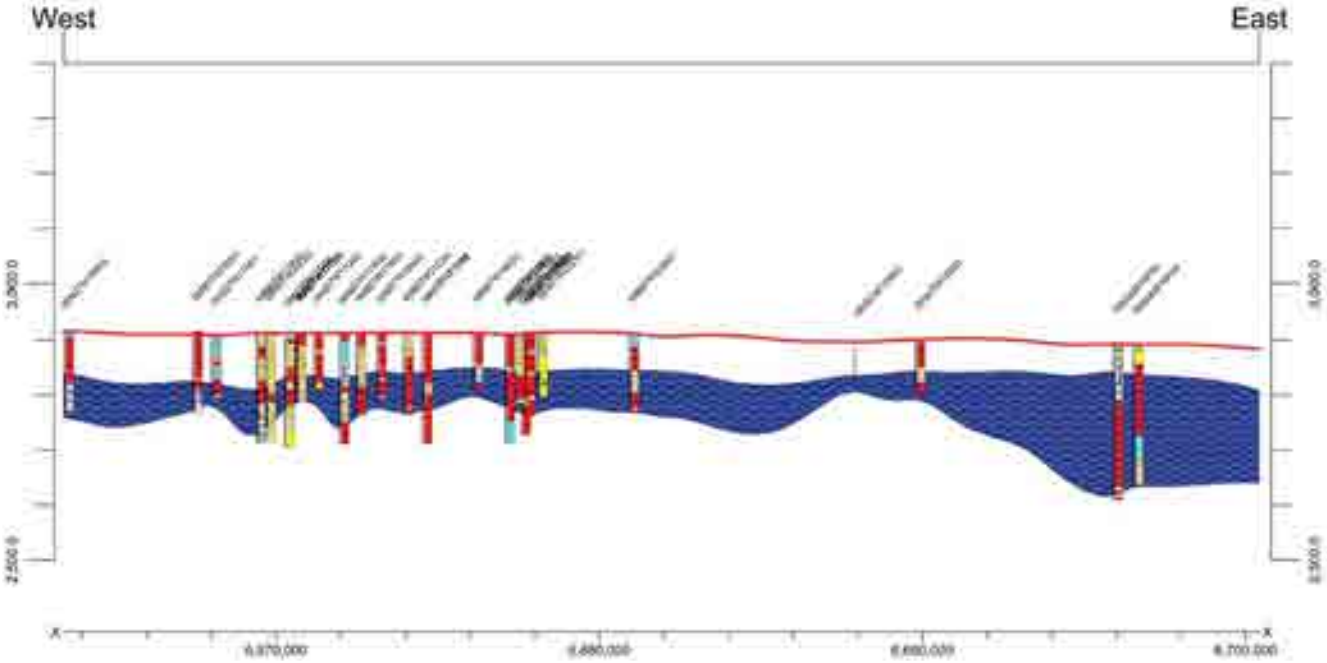


Figure 5b: Location Map for Aquifer Profile

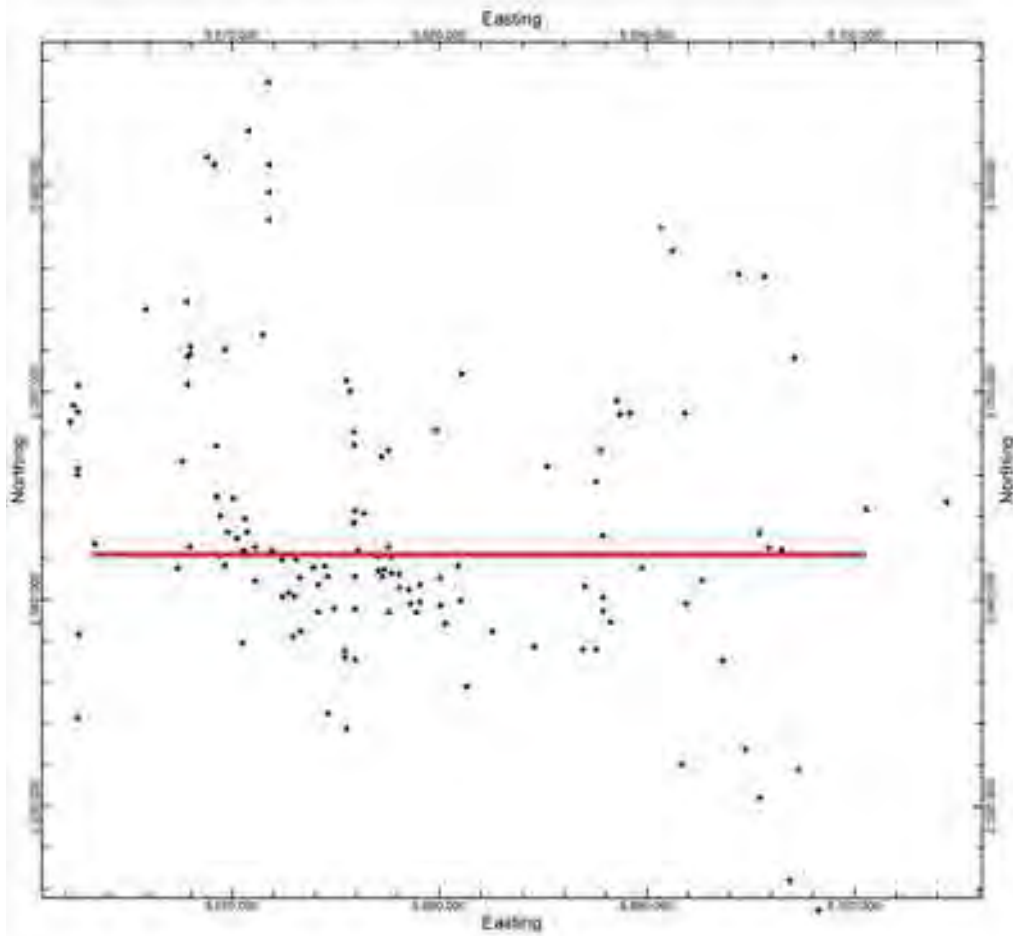


Figure 6: Lithology Profile Showing Unreliable Wells

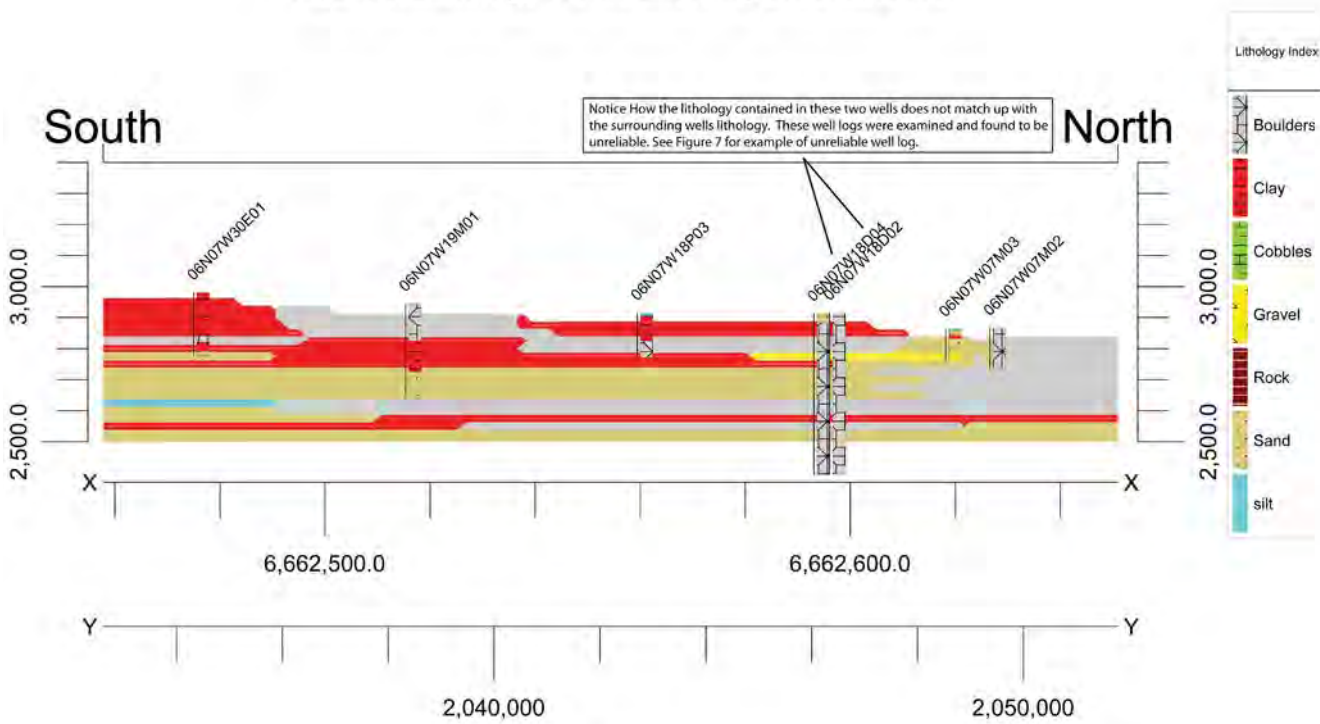


Figure 7: Example of an unreliable well report. Notice that the description for the geology is uninformative and gives no information on the unit type.

ORIGINAL
File with DWR

STATE OF CALIFORNIA
THE RESOURCES AGENCY
DEPARTMENT OF WATER RESOURCES
WATER WELL DRILLERS REPORT

Do not fill in
No. 223927

Well No. 22462W18D08
Other Well No. _____

Form No. _____
Date 07/19/201

This section has been edited to hide the well owner's personal information, and is not relevant to this study.

(2) LOCATION OF WELL (See instructions)
Owner SAN DIEGO, INC Owner's Well Number II
Well address (if different from above) SAME
Frontage LN Back LN Depth 18
Directions (North, South, East, West, True, etc.) FRONT 45° E - 18.7 AC
022-01

(3) TYPE OF WORK
New Well Deepening
Reconstruction
Reconditioning
Horizontal Well
Dewatering (Describe dewatering materials and procedures in item 12)
(4) PROPOSED USE
Domestic
Irrigation
Industrial
Tab Well
Stock
Municipal
Other

WELL LOCATION SKETCH

(5) EQUIPMENT
Pump Reverse
Cable Air
Other Buckets

(6) GRAVEL PACK
Yes No Size 6/16
Diameter of hole 18 IN
Pack thickness 200 in 50 ft

(7) CASING INSTALLED
Steel Plastic Concrete
Type of perforations (if any) of screen:

From ft.	To ft.	Dia. in.	Cores on Wall	From ft.	To ft.	Slot size
<u>000</u>	<u>520</u>	<u>6</u>	<u>1/4</u>	<u>320</u>	<u>420</u>	<u>3/8</u>

(8) PERFORATIONS
Type of perforations (if any) of screen:

(9) WELL SEAL
Was surface slurry seal provided? Yes No If yes, to depth 50 ft
Were struts placed against perforations? Yes No Interval 10 ft
Method of sealing CEMENT

(10) WATER LEVELS
Depth of first water, if known 330 ft
Standing level after well completion 120 ft

(11) WELL TESTS
Was well test made? Yes No If yes, by whom? PROFESSIONAL LAB
Type of test Pump Baller Air SR
Depth to water at start of test 140 ft at end of test 360 ft
Time 3 gallons after 200 strokes WATER TEMPERATURE _____
C. of analysis made? Yes No If yes, by whom? PROF LAB
Was electric log made? Yes No If yes, attach copy to this report

Work started 18 Completed 18

WELL DRILLER'S STATEMENT
This well was drilled under my supervision and this report is true to the best of my knowledge and belief.

Signature _____ (Well Driller)
NAME _____
Address _____
City _____
License No. _____ Date of this report 6-20-88

DWR (68) (REV. 7/78) IF ADDITIONAL SPACE IS NEEDED, USE NEXT CONSECUTIVELY NUMBERED FORM

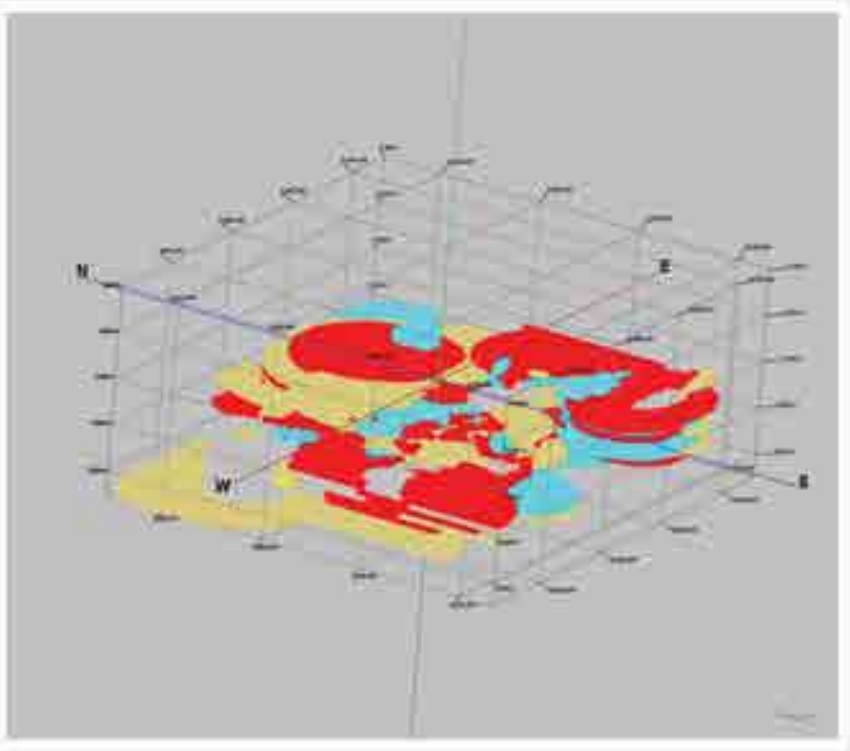


Figure 8: Lithology Model Showing All Units with Non-Interpolated Outliers
 -X and Y Node Spacing=250 Feet
 -Vertical Node Spacing=25 Feet

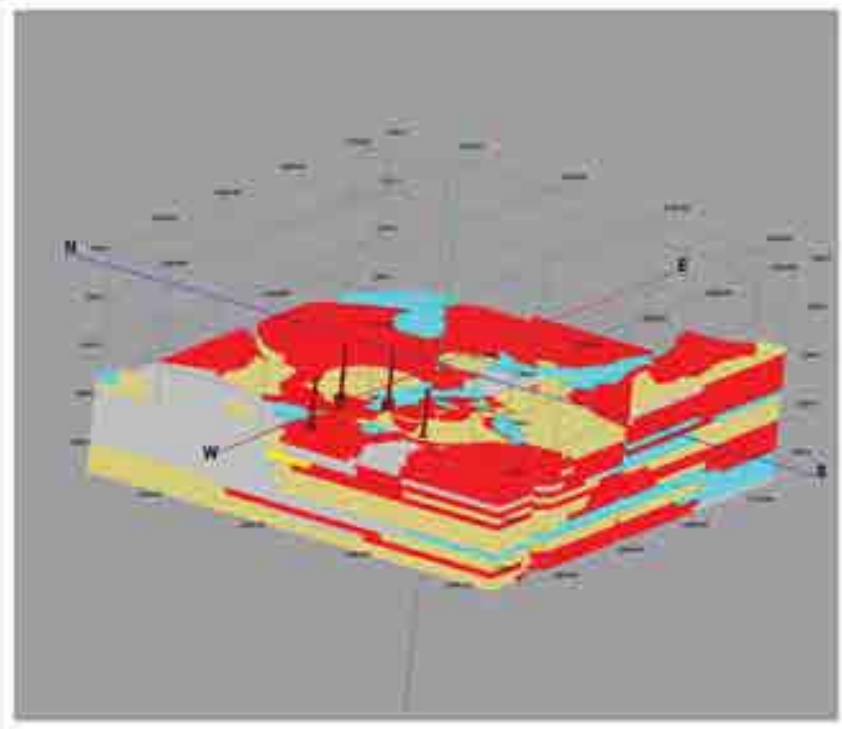


Figure 9: Lithology Model Showing All Units with Interpolated Outliers.
 -X and Y Node Spacing=250 Feet
 -Vertical Node Spacing=25 Feet

Figure 10a: Model Showing Average Depth of Perched Aquifer to be 850 Meters [2800 Feet] Above Sea Level

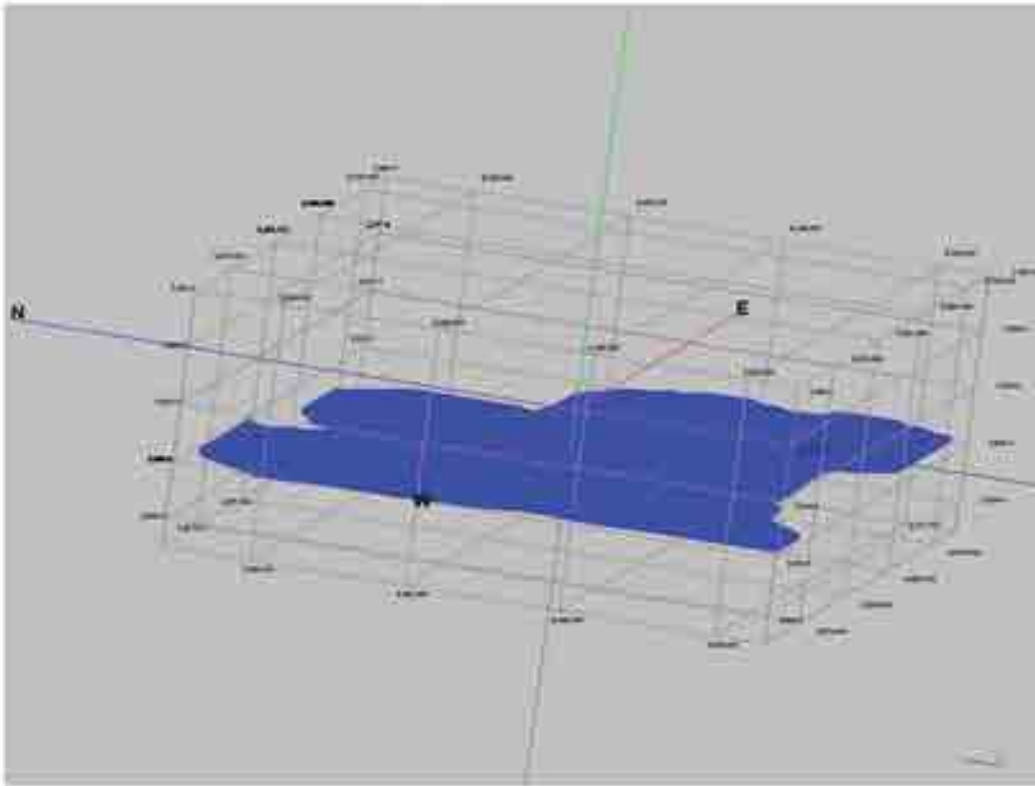


Figure 11a: Model Showing Average Depth of Regional Aquifer to be 790 Meters [2600 Feet] Above Sea Level

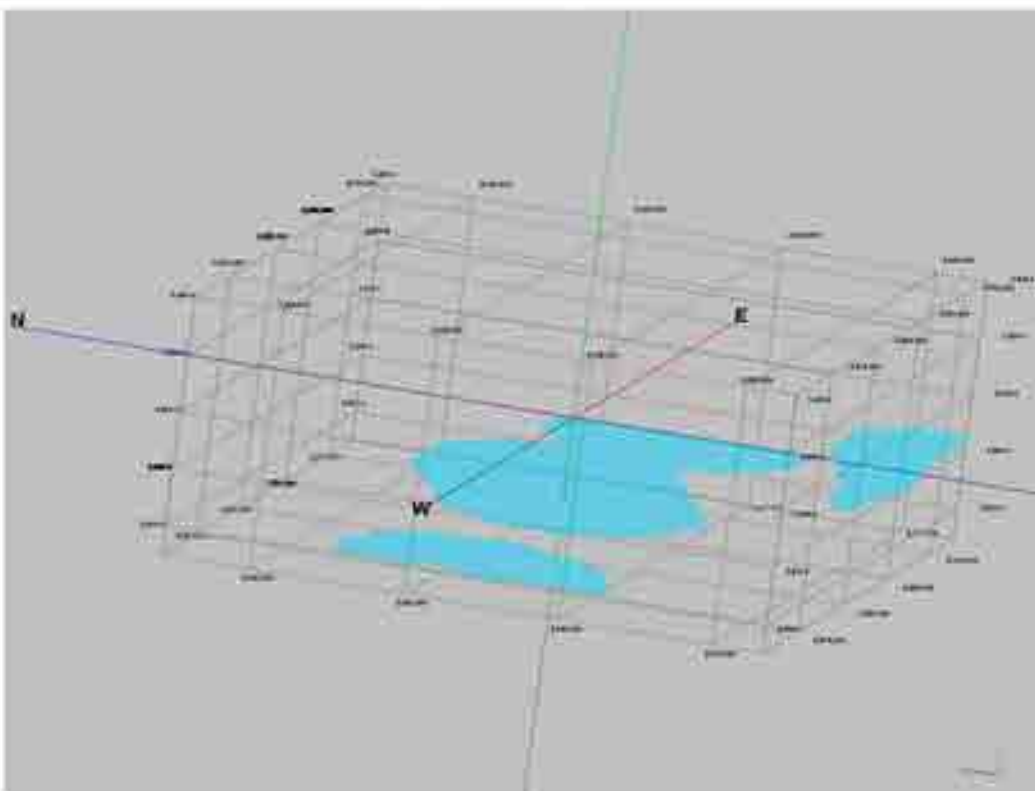


Figure 10b: Model Showing Trends of Both Perched and Regional Aquifers As Viewed from North West

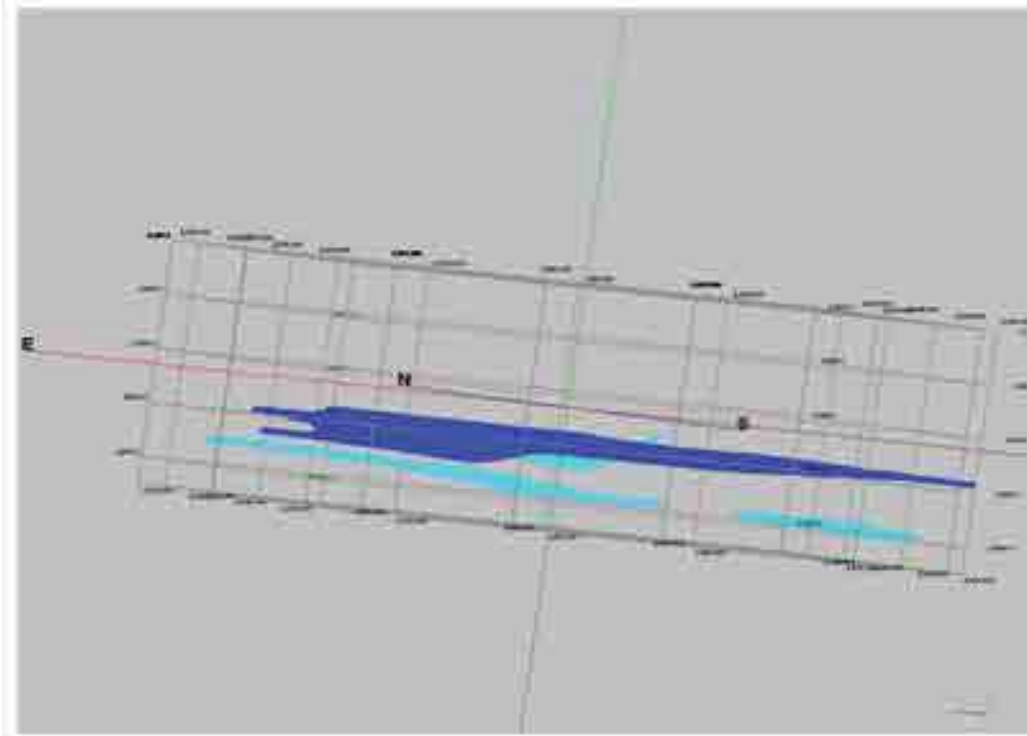
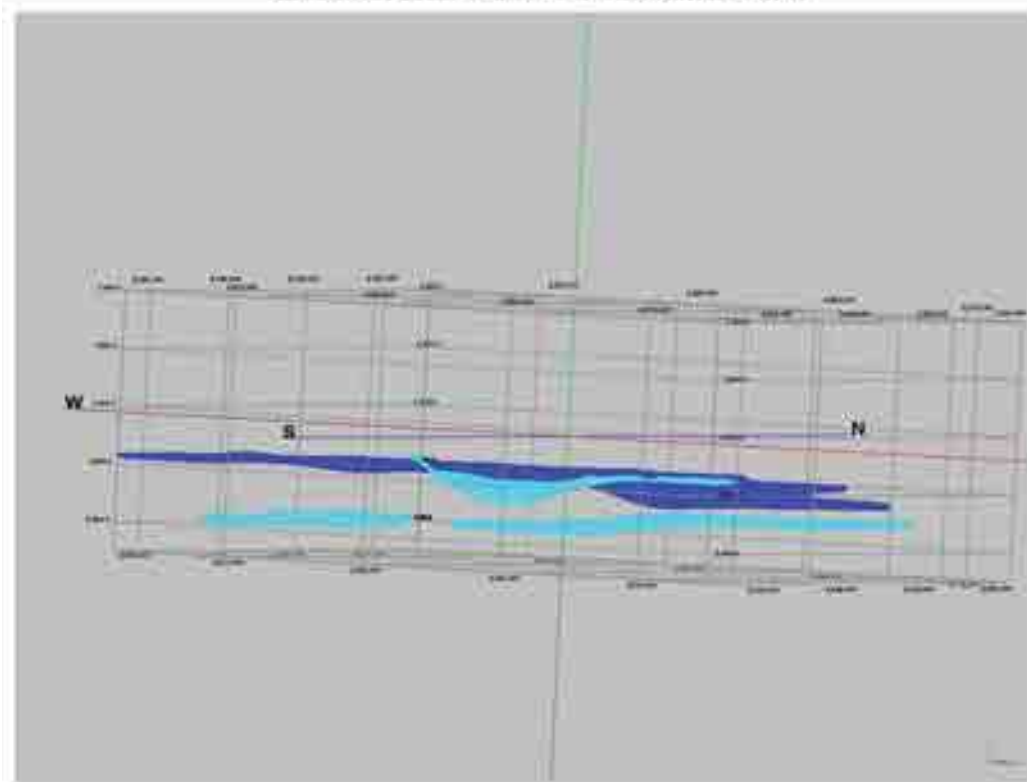


Figure 11b: Model Showing Trends of Both Perched and Regional Aquifers As Viewed from South East



*(Surface Level Approximately 890 Meters [2900 Feet] Above Sea Level)

Figure 12: Oeste Sub-Basin Showing Well Locations

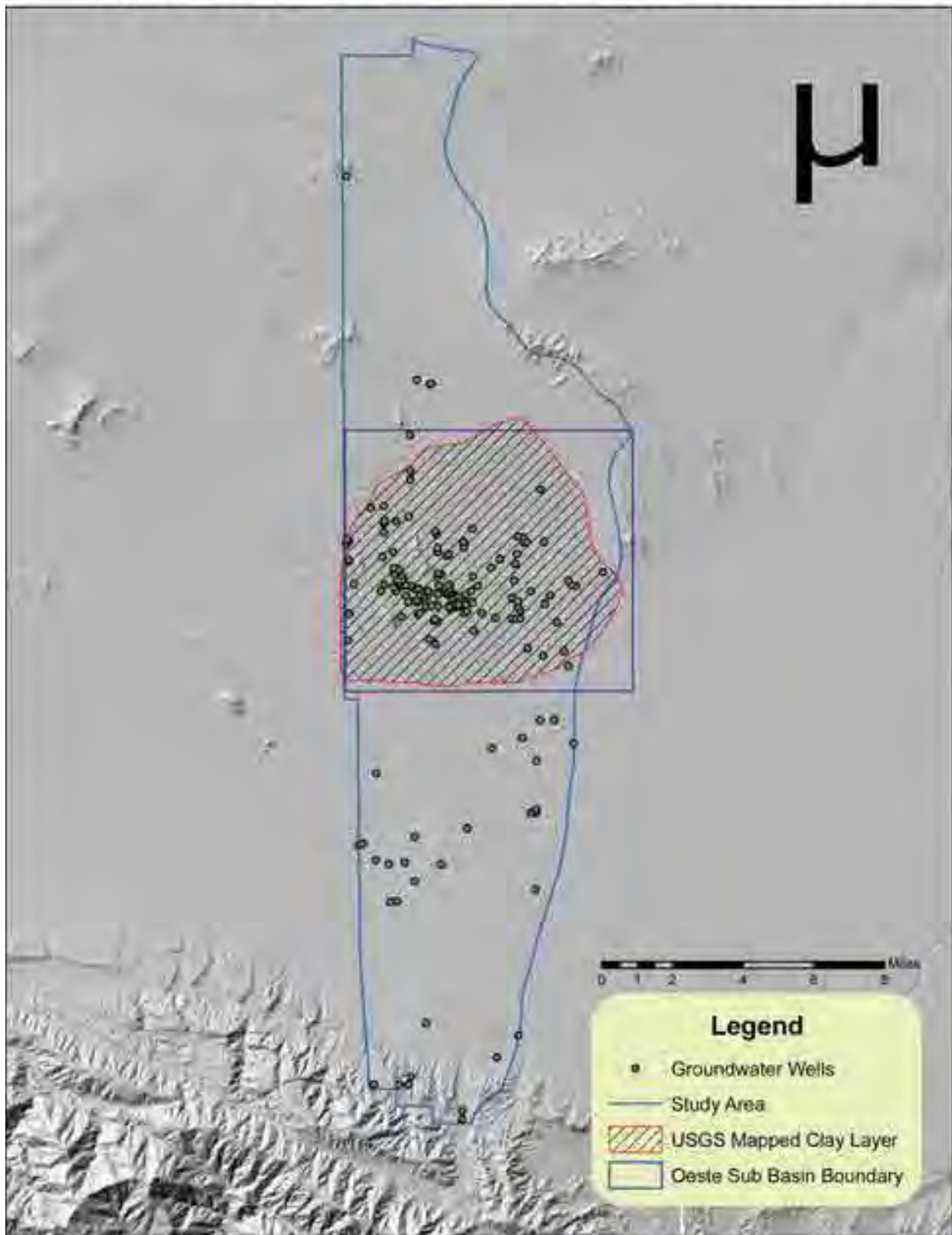


Figure 13a: Clay and Silt Model of Study Area

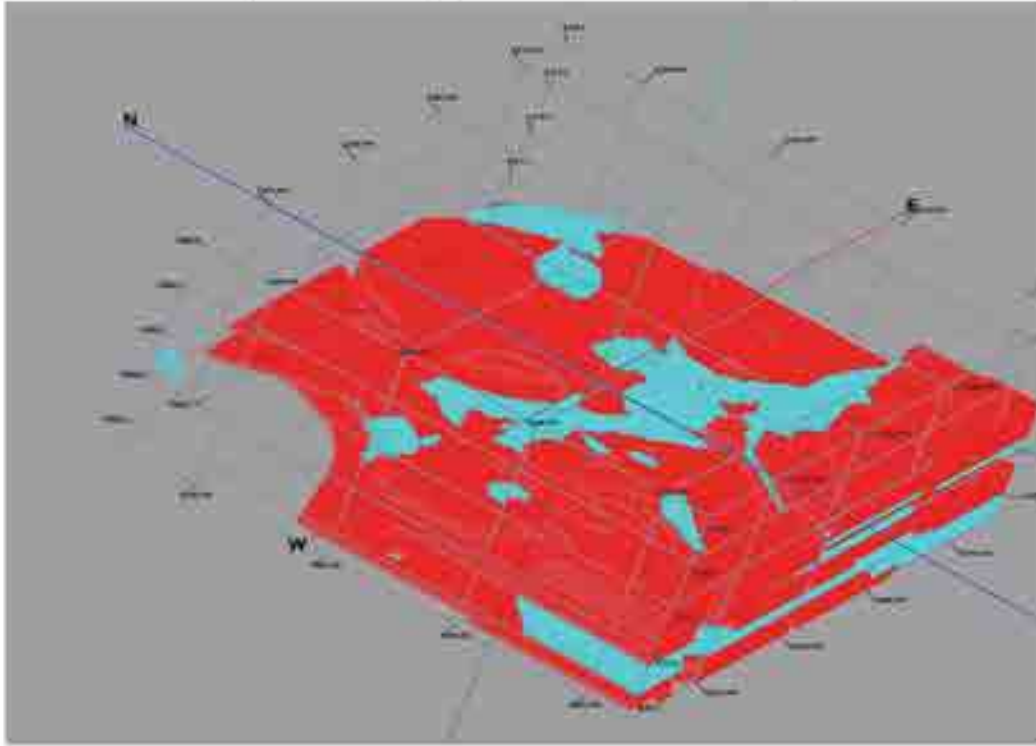


Figure 13b: Clay, Silt and Sand Model of Study Area

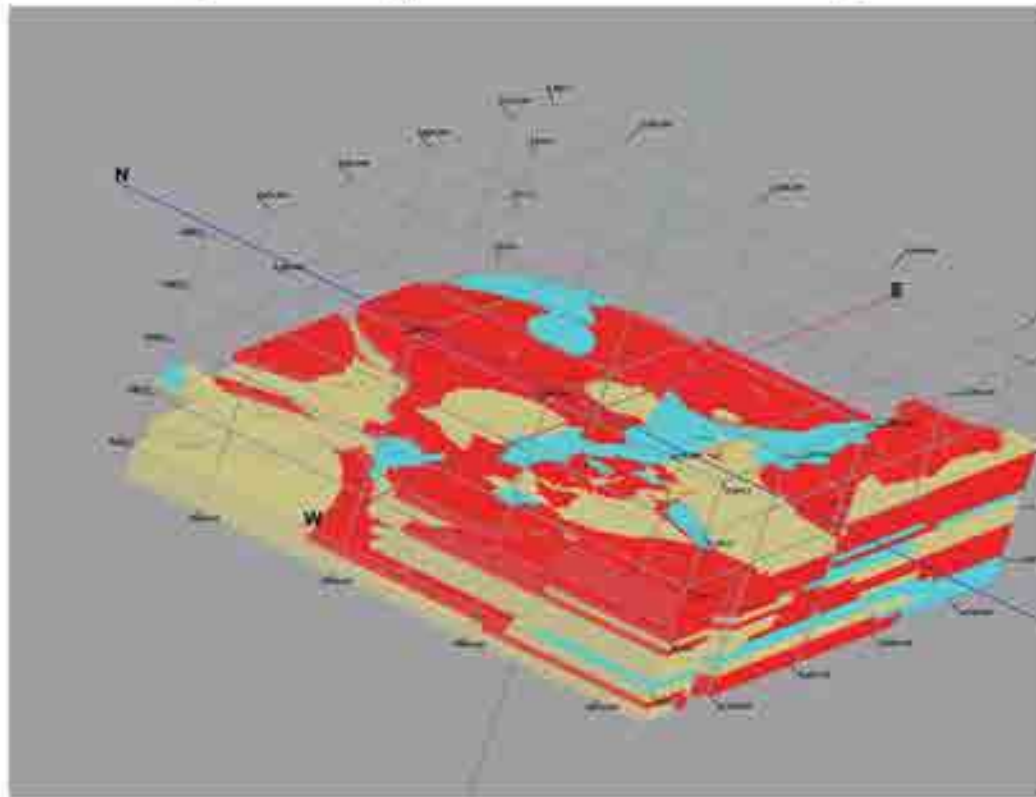


Figure 13c: Clay and Silt Model Alternate Angle

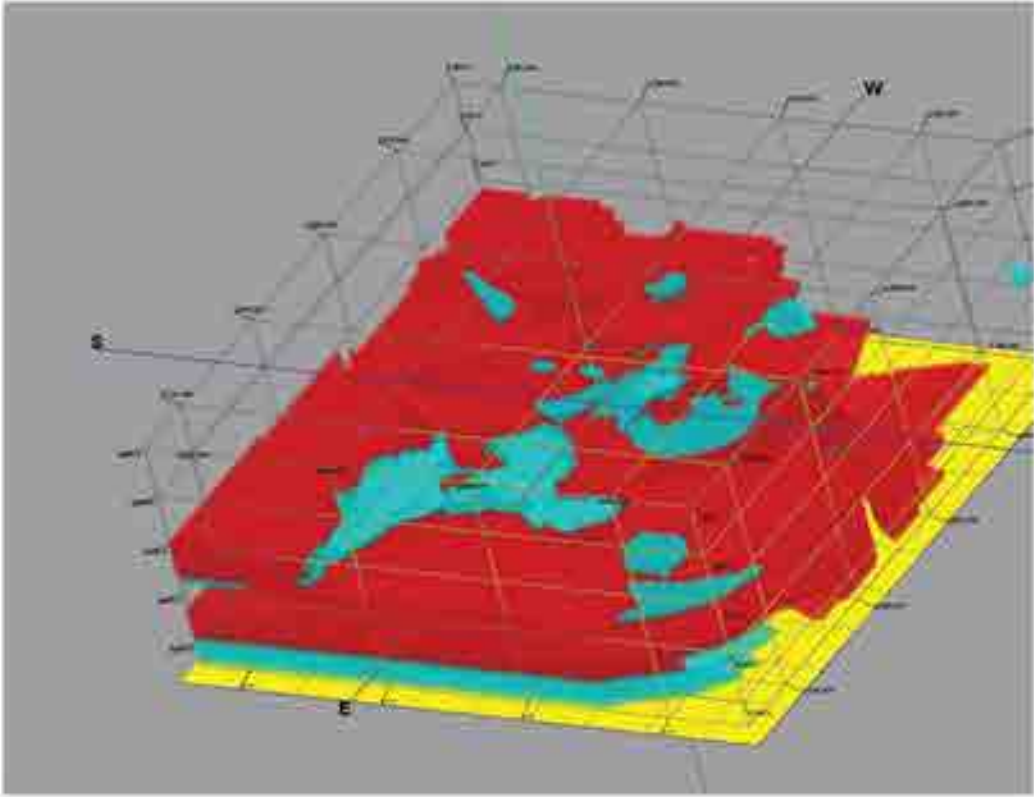
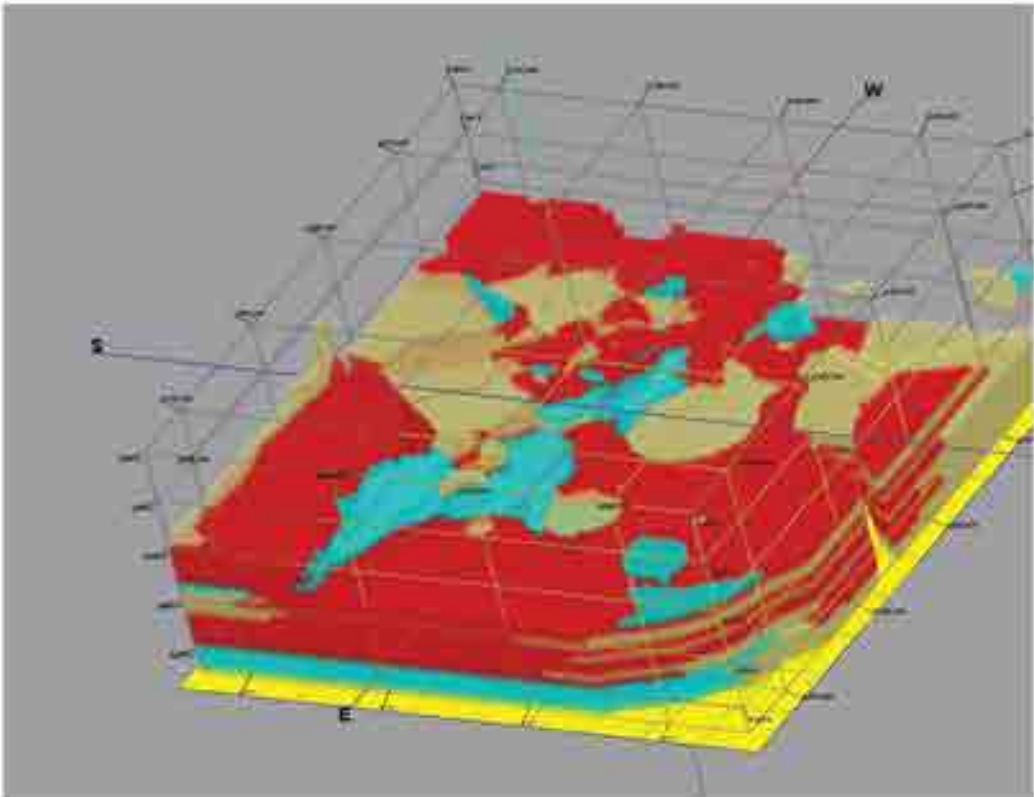
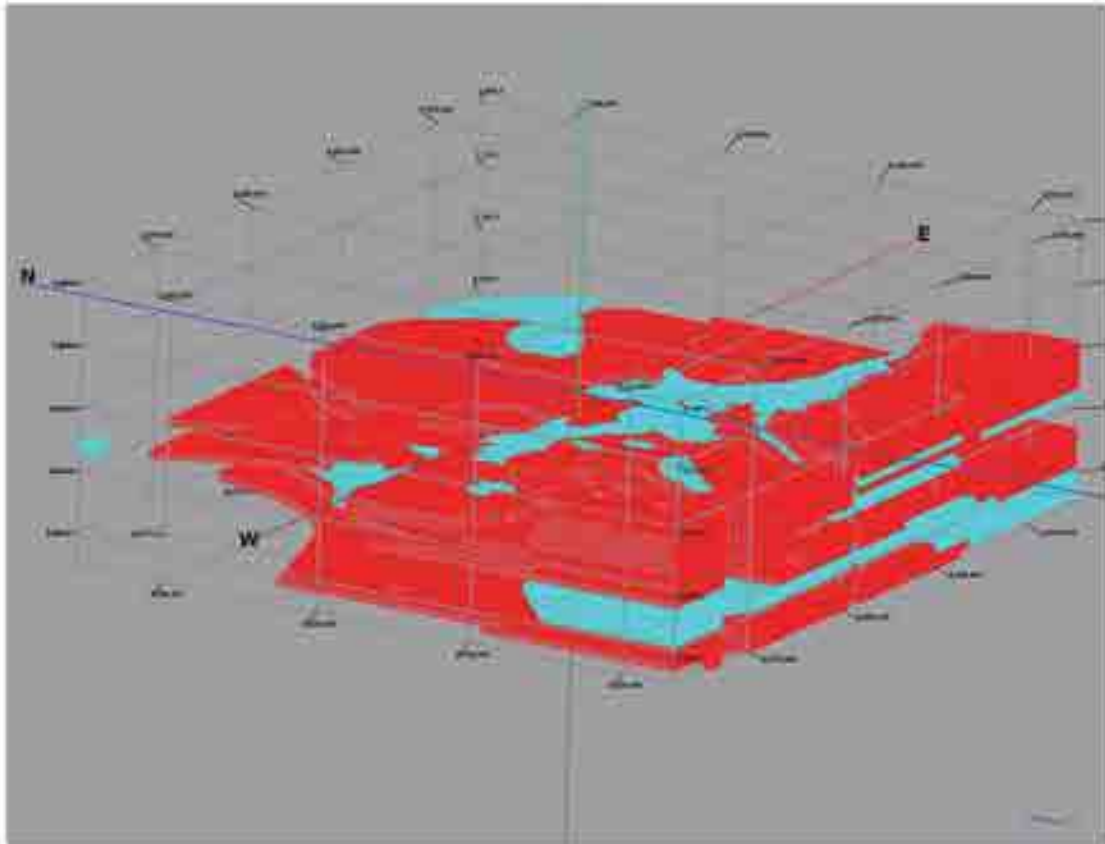


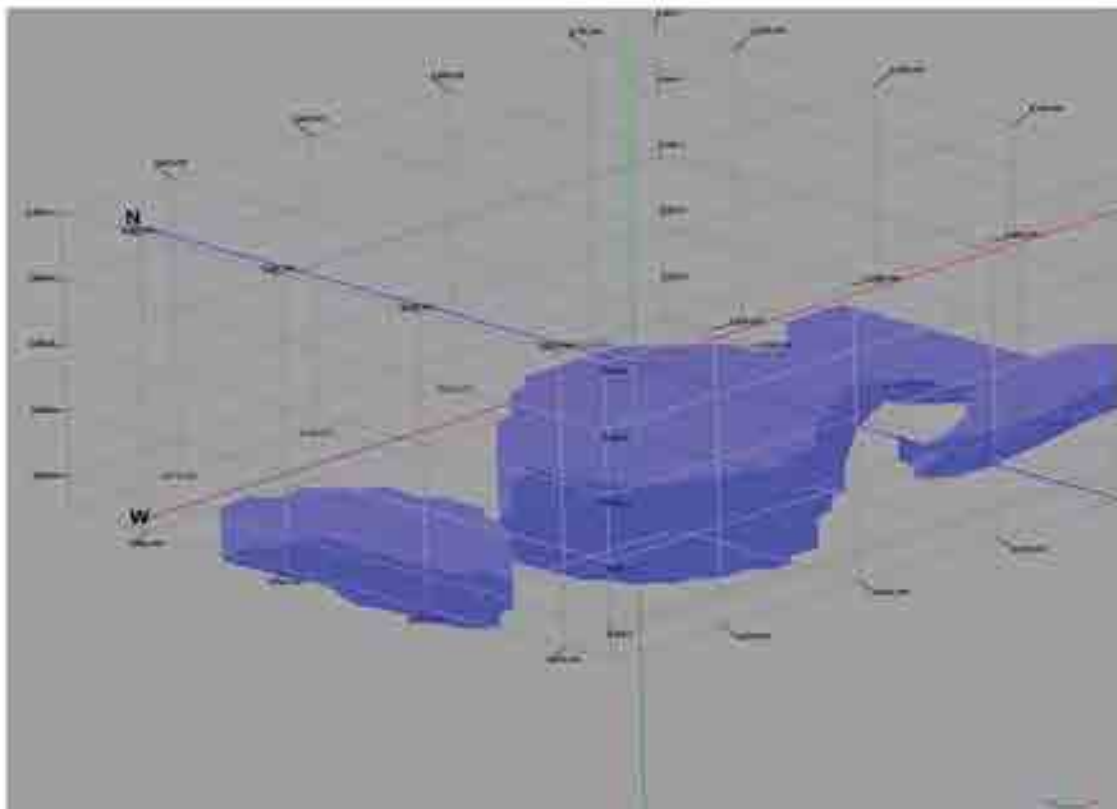
Figure 13d: Clay, Silt and Sand Model Alternate Angle



Lithology Profile Showing Just Clay and Silt Layers



Profile of Regional Aquifer



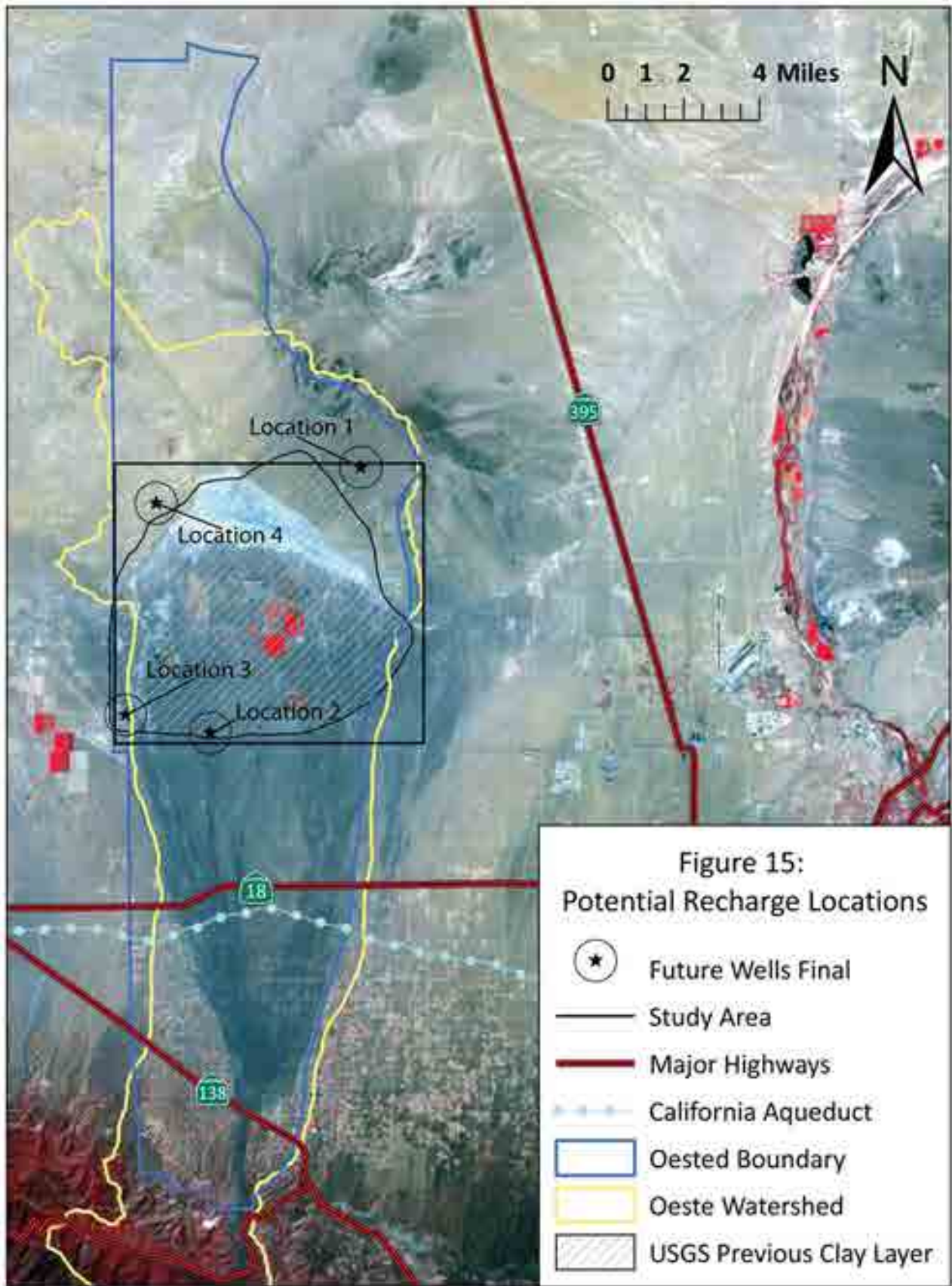
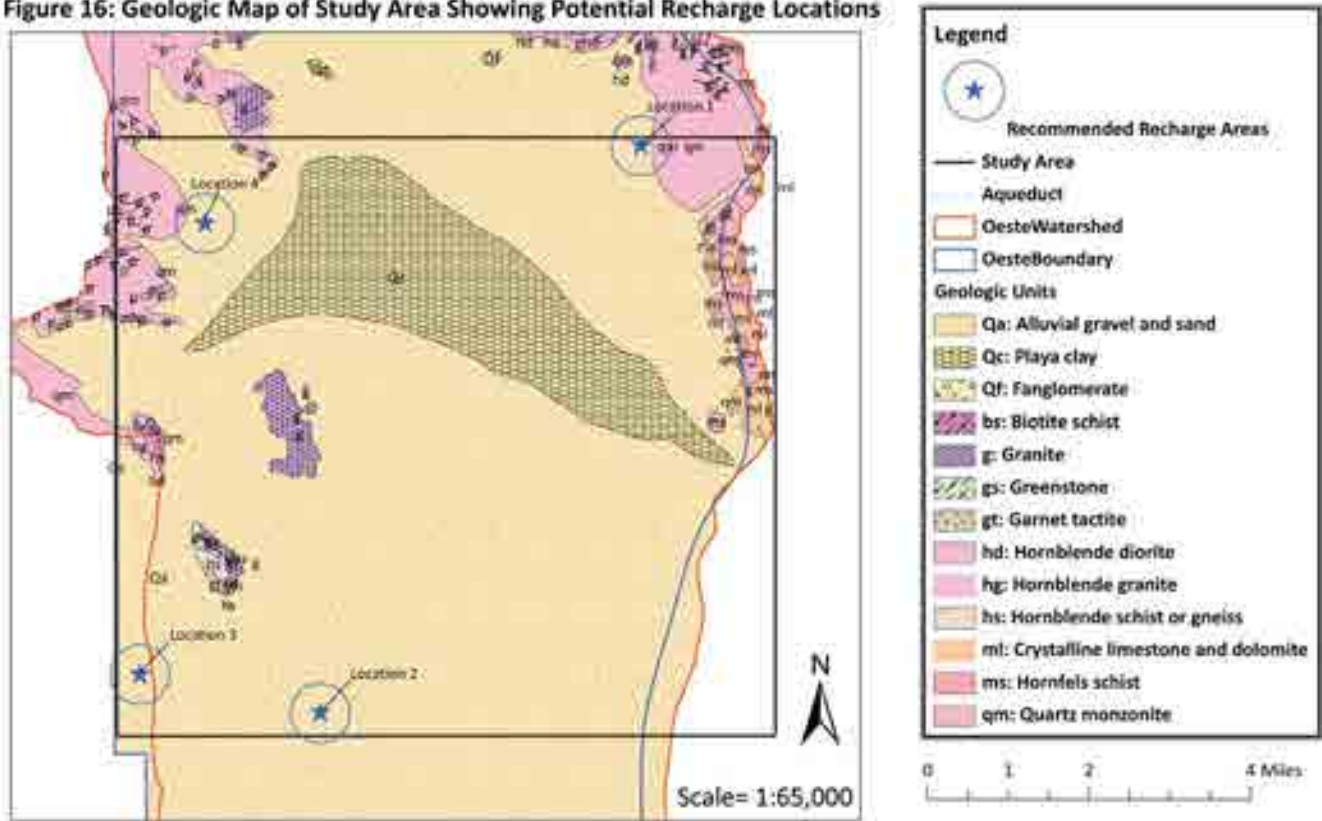


Figure 16: Geologic Map of Study Area Showing Potential Recharge Locations



Dynamic Rupture Propagation path of a Complex fault Geometry

► **Melissa Nunley**

Advisor: **Dr. David Bowman**

California State University, Fullerton

Abstract

The 2001 $M 7.8$ Kokoxili earthquake ruptured the complex fault system of the Kusai segment of the Kunlun fault. King *et al.* [2005] concluded from observing surface ruptures that the complex system obtained a branched structure. This structure began with oblique motion that partitions into two faults with different mechanism. The fault geometry consists of a 70° dipping oblique-slip fault that extends from 15 km to 5km in depth and the branches into a vertical fault and a 45° dipping fault. In our initial models we used a simple regional stress field on all the fault segments, which caused rupture to propagate only to the basal and vertical faults. However, adding a locked patch on the vertical fault causes a stress increase and therefore rupture is allowed to nucleate and propagate on this system. As rupture propagates on the dipping fault, the wedged area in between the upper dipping and upper vertical fault causes the upper vertical fault to rotate and appear to somewhat slip backwards. Our results may have important implications for the dynamics of branched faults and geometrically complex fault systems in general.

Introduction

An important characteristic of seismic hazard evaluation is predicting the path of earthquake rupture on complex fault systems. This point has been emphasized by earthquakes such as the 1992 Landers (Sieh *et al.*, 1993), the 1999 Hector Mine (Scientists from the USGS *et al.*, 2000), and the 2002 Denali Fault (Eberhart-Phillips *et al.*, 2003) events, which all took place on branched fault systems. A point of particular interest in all of these cases has been to attempt to explain why ruptures took one branch while abandoning another. Dynamic earthquake modeling is an important tool in investigating this issue and other issues in rupture propagation. Many dynamic models (e.g Oglesby *et al.*, 2003; Oglesby *et al.*, 2004; Duan and Oglesby, 2007) have addressed the decision of rupture path in branched fault systems. While the details of the models differ, a common result is that the path that rupture takes is a complex product of the fault geometry, regional static stress field, local perturbations of the static stress field, and the dynamic radiated stress field. The assumption has been made in most of these studies that connecting at the vertex are branched faults consisting of a stem and two

limbs. Research has shown it is vital to start with relatively simple computational parameters and simple fault geometry, because even in these cases, rather complex faulting behavior may be produced. However, faults in nature are not necessarily even simply branched: Often fault segments do not necessarily intersect, and in some instances several fault segments may intersect in a branching area.

To accommodate multiple motions from the collision of tectonic plates, parallel and sub-parallel faults form that slip in different directions and have a combined motion that is oblique (King *et al.*, 2005). The term for this phenomenon has been identified as slip partitioning. In 2001 there was an $M 7.8$ earthquake in Tibet, China along the Kusai segment of the Kunlun fault (Figure 1). King *et al.* [2005] concluded from parallel normal and strike-slip surface breaks that the faults originated from a slip partitioning system. Figure 2 displays a SPOT image of the parallel surface ruptures observed in the field. Within the image, the evidence for the normal fault is shown near the base of the mountains in the form of triangular facades (King *et al.*, 2005). Evidence for strike-slip motion and direction of slip in the image is shown when an alluvial is offset. We will use

the fault geometry and mechanism of the system proposed by King *et al.*, [2005] in our models. The goals for our research are to successfully recreate the rupture propagation and decipher why rupture chooses to propagate onto one branch over the other branch.

Methods

We used the dynamic finite element method (Oglesby, 1999; Duan and Oglesby, 2006) to model the dynamics of rupture propagation of the upward branching fault system.

Results

The geometry of a fault or fault system determines the likely path that the rupture will take during an earthquake. Figure 3 displays the obliquely branched fault geometry in cross section. The fault system is 40 kilometers along strike. The basal fault dips 70 degrees. It then divides into an upper dipping fault that dips 45 degrees and also into a vertical fault.

In our initial models we wanted to explore the rupture propagation paths. Rupture is nucleated towards the bottom of the basal fault in all of our models. As rupture propagates upward toward the point of intersection of the faults the geometry of the system determines which fault the rupture will propagate to. Dissecting the fault systems geometry incorporated with each fault's motion can provide an explanation as to why rupture chooses one branch and abandons the other. As the basal fault ruptures it obtains dominantly oblique motion; as rupture propagates to the intersection of the faults the basal fault unlocks the upper vertical fault as it clamps the upper

dipping fault. Rupture propagates onto the upper vertical fault and slip is mainly oblique motion. This rupturing of the upper vertical fault causes the wedged space between the upper vertical fault and upper dipping fault to move slightly northeast, once again clamping the upper dipping fault. Another method to explain why rupture does not propagate to the dipping fault is by examining the normal and shear stresses on the dipping fault. Figure 4 displays the evolution of stresses on all three faults during different times of the earthquake. As rupture evolves on the basal and upper vertical fault the shear stress increases minutely while the normal stress increases (Figure 4a). After the rupture front passes the shear stresses decrease as the normal stress value varies along strike (Figure 4b). Due to the fact that there is not a large enough difference between the normal and shear stress rupture is not allowed to propagate on the dipping fault. Homogenous fault strength throughout the system does not allow slip partitioning to occur.

In attempts to force rupture to nucleate on the upper dipping fault we added heterogeneity in the form of a locked patch on the upper vertical fault (Figure 5). This barrier is 2 kilometers by 3 kilometers and is placed in the middle of the fault. By raising the static frictional coefficient to an unnaturally high value we hope that this will create a locked patch within an area on the vertical fault. In this model as rupture propagates from the basal fault upward, the basal fault unclamps the vertical fault while simultaneously clamping the dipping fault. Rupture is not allowed to propagate onto the upper dipping fault. As rupture propagates throughout the upper vertical fault, rupture passes

around the barrier, which therefore creates a stopping phase of stress waves. This allows rupture to nucleate and propagate throughout the dipping fault. While rupture propagates throughout the upper dipping fault, the wedged block that lies in between the upper vertical fault and upper dipping fault pulls the upper dipping fault slip backwards. This changes the upper vertical fault's original slip from dominantly oblique motion to mainly strike-slip motion. Motion from the basal fault is between the upper vertical and upper dipping faults. This can be further explained by observing the behavior of the shear and normal stresses on each individual fault. As rupture propagates on the upper vertical fault, rupture goes around the asperity without causing it to be displaced. This causes the shear stress to increase while the normal stress decreases on the dipping fault. Due to the fact that there is such a large difference between the two stresses, rupture is therefore allowed to nucleate and propagate on the upper dipping fault. Figure 6 shows the final slip produced by our earthquake. The final slip that is produced on our basal fault is dominantly oblique motion while the slip on the upper vertical fault is mainly strike-slip and the upper dipping fault has primarily dip-slip motion. These results are consistent with the evidence for slip partitioning that was found to occur during the Kokoxili earthquake.

Conclusion

The main priority of our research was to reproduce the rupture propagation that occurs within a complex fault system. Our models associate the role that a heterogeneity or a homogenous strength plays on rupture

propagation within the system. A comparison of final slip for our two models is displayed in figure 7. The fundamental difference between the two models is their final product of motion and displacement. Figure 7a has homogenous fault strength throughout the entire system and in this case slip partitioning does not exist. This occurs when the basal fault ruptures it unclamps the upper vertical fault allowing rupture to propagate while it clamps the upper dipping fault, therefore producing dominantly oblique motions on both the basal faults and upper vertical faults and no motion and slip on the upper dipping fault. This final product does not concur with our evidence for slip partitioning found in the field. Figure 7b has a heterogeneity in the form of a locked barrier located on the upper vertical fault. As rupture propagates upward from the basal fault to the upper vertical fault, the upper dipping fault becomes locked. But as rupture passes around the stuck barrier a stopping phase allows rupture to nucleate and propagate on the dipping fault. The final motion on the upper vertical fault is strike-slip while the upper dipping fault has dominantly dip-slip motion; therefore we have reproduced two different mechanisms for a slip partitioning system. Another difference between the two models is the magnitude of the final slip on the two upper branches. In figure 7a slip is greater than 5 meters in some areas on the upper vertical fault whereas figure 7b shows the upper vertical and dipping faults have slip that is between three and four in most places. However in figure 7b the upper vertical and dipping faults magnitude of slip combined equals the slip on the basal faults.

An implication for importance

within the real world is that complex fault systems are found all over the world and when rupture occurs they produce significantly large earthquakes, so it is important to understand their paths of rupture and propagation which may in turn prevent many injuries and deaths from living near the faults. In the future we plan to explore the rupture propagation and choices for propagation paths of different complex fault geometries.

Acknowledgements

I would like to thank Dr. Bowman and also Dr. Oglesby for their support and guidance. I would also like to thank Harmony Collela for doing the initial research for this project. Also, thank you Southern California Earthquake Center for sponsoring my research.

References

1. Bowman, D., G. King, and P. Tapponnier (2003). Slip partitioning by elastoplastic propagation of oblique slip at depth, *Science* 300, 1121–1123.
2. Colella, H., D. Oglesby, and D. D. Bowman (2005). An oblique/branched fault system: dynamic and static analysis, *EOs Trans. AGU* 86, Fall Meet. Suppl., Abstract S51F-07.
3. Duan, B., and D. D. Oglesby (2005a). Multicycle dynamics of nonplanar strike-slip faults, *Journal of Geophysical Research* 110, doi:10.1029/2004JB003298.
4. Duan, B., and D. D. Oglesby (2005b). The dynamics of thrust and normal faults over multiple earth-

quake cycles: effects of dipping fault geometry, *Bulletin of the Seismological Society of America* 95, 1623-1636.

5. Duan, B., and D. D. Oglesby (2006). Heterogeneous fault stresses from previous earthquakes and the effect on dynamics of parallel strike-slip faults, *Journal of Geophysical Research* 111, doi:10.1029/2006JB004138.

6. Duan, B., and D. D. Oglesby (2007). Nonuniform prestress from prior earthquakes and the effect on dynamics of branched fault systems, *Journal of Geophysical Research* 112, B05308, doi:10.1029/2006JB004443.

7. King, G.C. P., Y. Klinger, D. D. Bowman, and P. Tapponnier (2005). Slip partitioned surface breaks for the Mw 7.8 2001 Kokoxilli earthquake, China. *Bull. Seismol. Soc. Am.*, 95, 731-738, doi: 10.1785/0120040101.

8. Oglesby, D. D. (1999). *Earthquake dynamics on dip-slip faults*, Ph. D. Thesis, University of California, Santa Barbara.

9. Oglesby, D. D., S. M. Day, Y.-G. Li, and J. E. Vidale (2003). The 1999 Hector Mine earthquake: the dynamics of a branched fault system, *Bulletin of the Seismological Society of America* 93, 2459-2476.

10. Oglesby, D. D., D. Dreger, R. A. Harris, N. A. Ratchkovski, and R. Hansen (2004). Inverse kinematic and forward dynamic models of the 2002 Denali Fault Earthquake, Alaska, *Bulletin of the Seismological Society of America* 94, S214-S233.

11. Scientists from the USGS,

SCEC, and CDMG (2000). Preliminary report on the 16 October 1999 M7.1 Hector Mine, California, earthquake, *Seismological Research Letters* 71, 11-23.

12. Tapponnier, P., X. Zhiding, F. Roger, B. Meyer, N. Arnaud, G. Wittlinger, and Y. Jingsui, (2001) Oblique stepwise rise and growth of the Tibet Plateau, *Science*, 294, 1671 – 1677.

Appendix

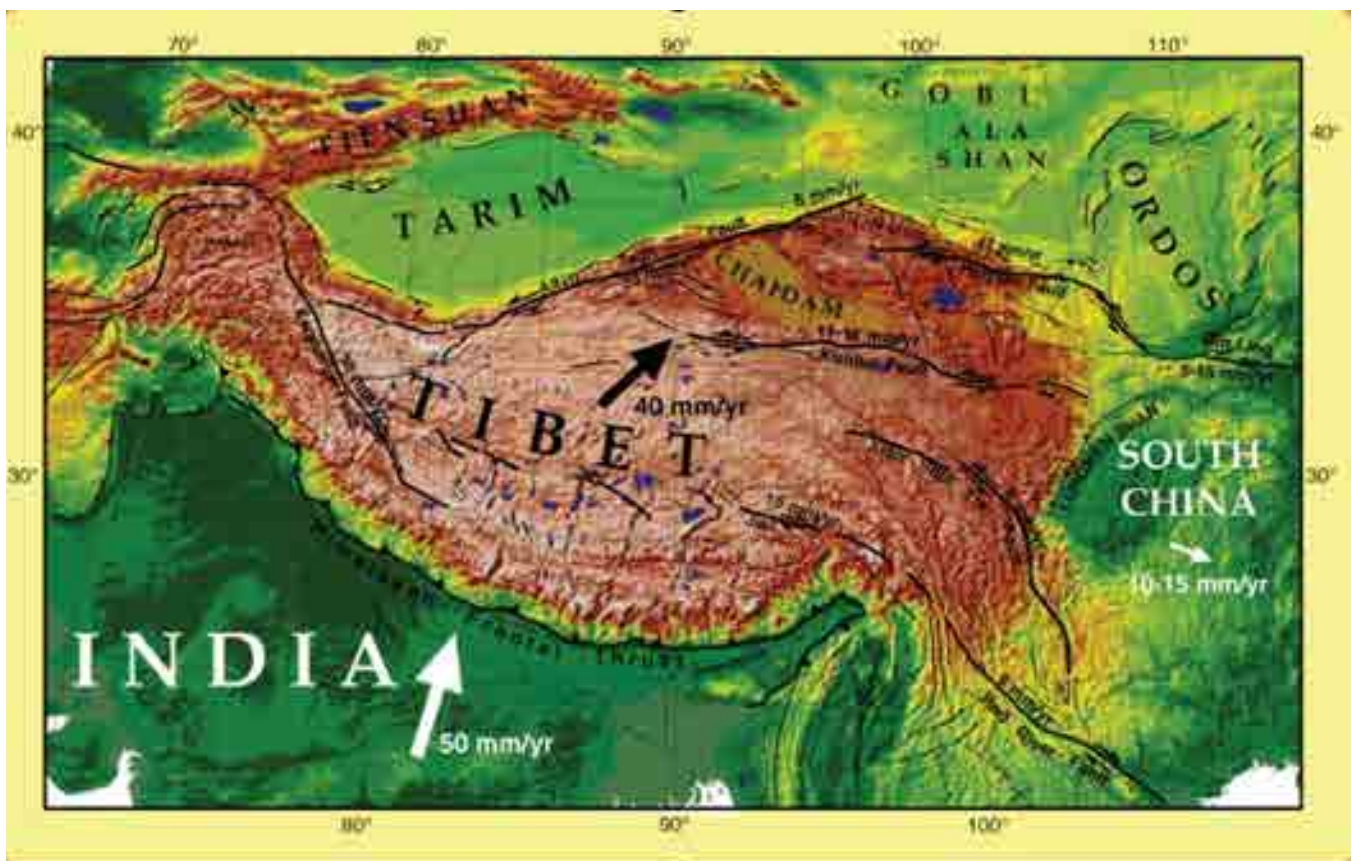


Figure 1 displays where the earthquake occurred in China. Segment that the fault ruptured is shown by the black arrow.

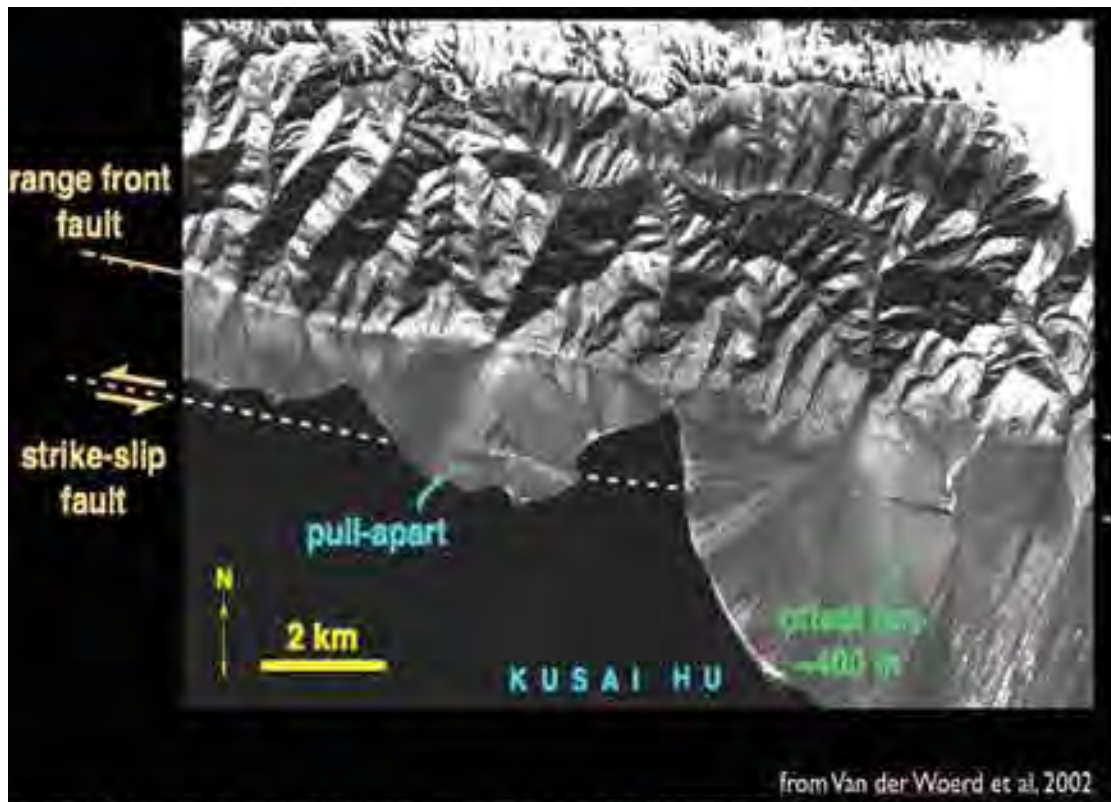
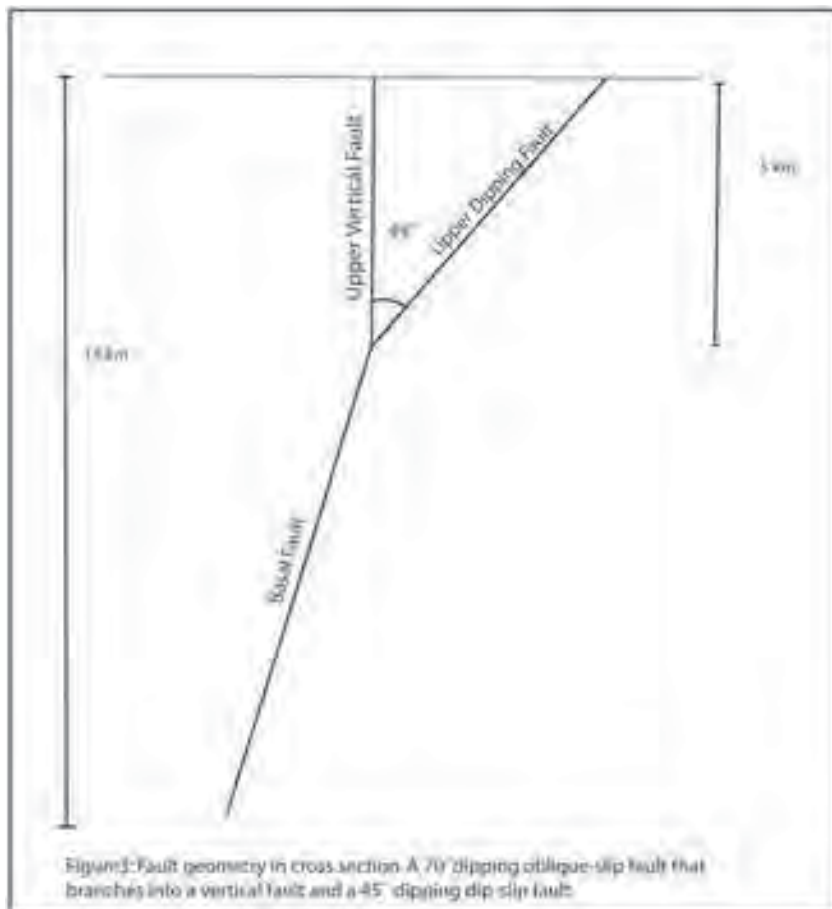


Figure 2 SPOT image of the Kusai Hu Segment of the Kunlun Fault. Image displays two parallel fault scarps from the strike slip and dip slip faults.



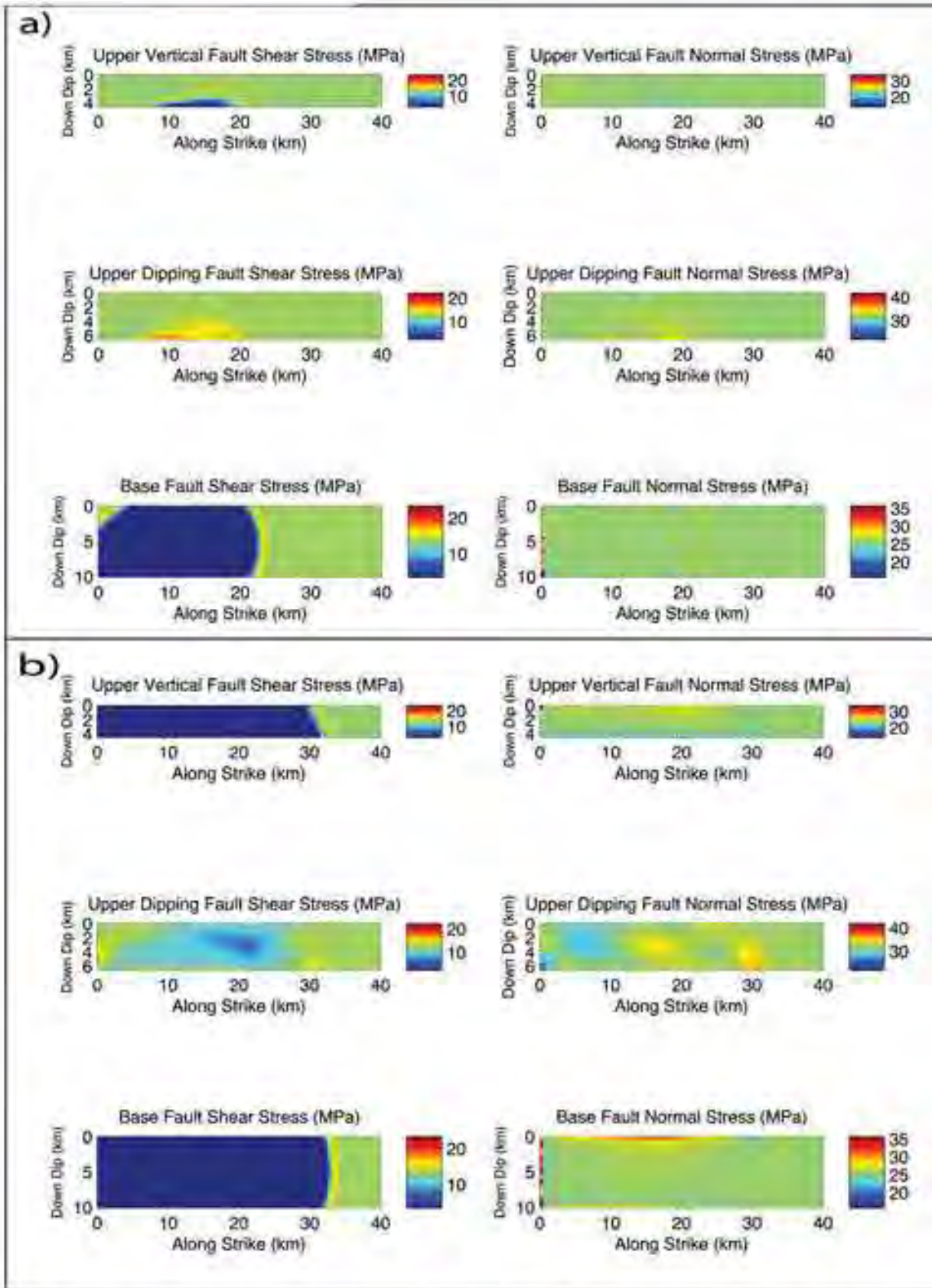


Figure 4 displays the normal and shear stress at different times during propagation. a) The shear stress increases while the normal stress increases minutely. b) The shear stress decreases while the normal stress varies

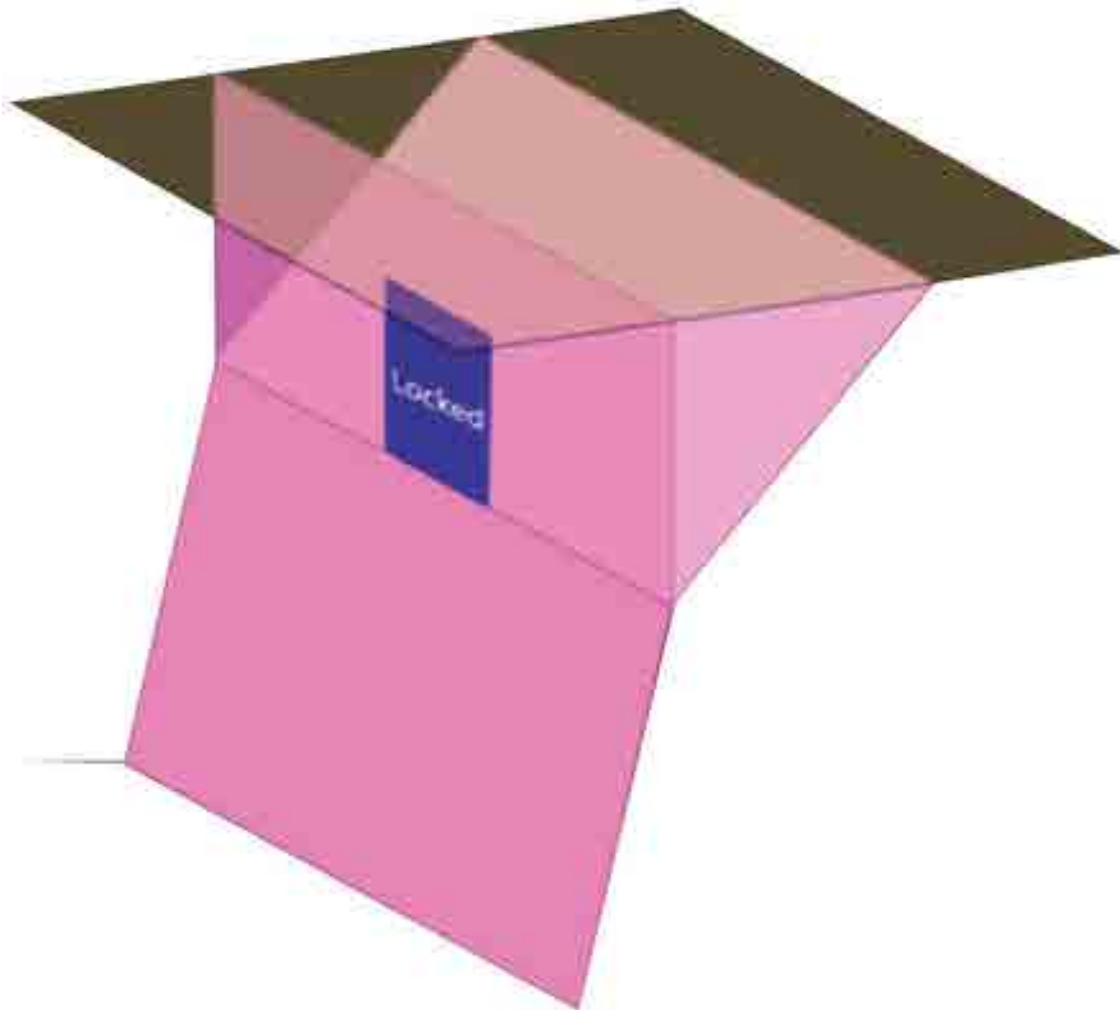
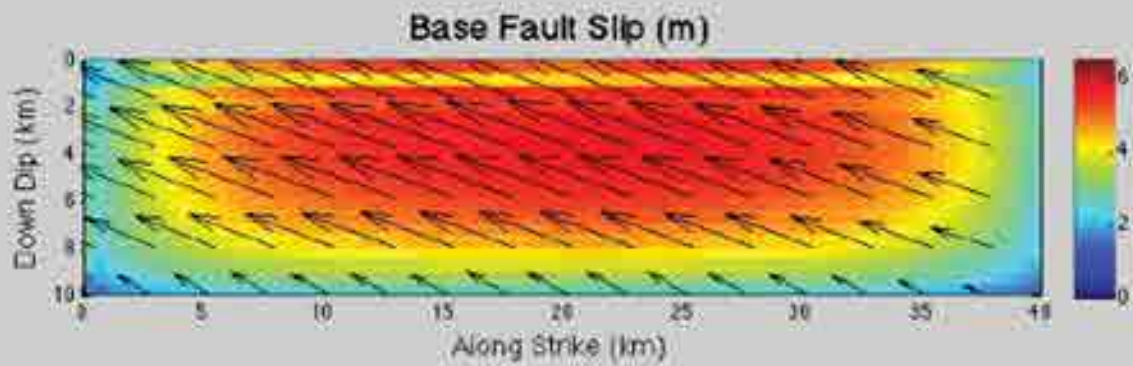
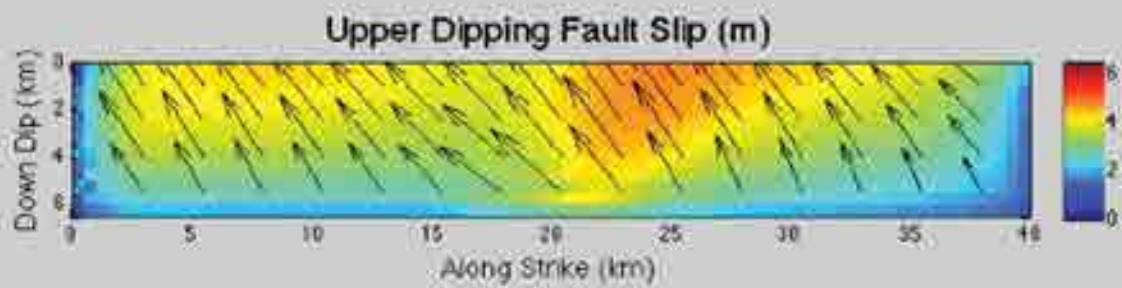
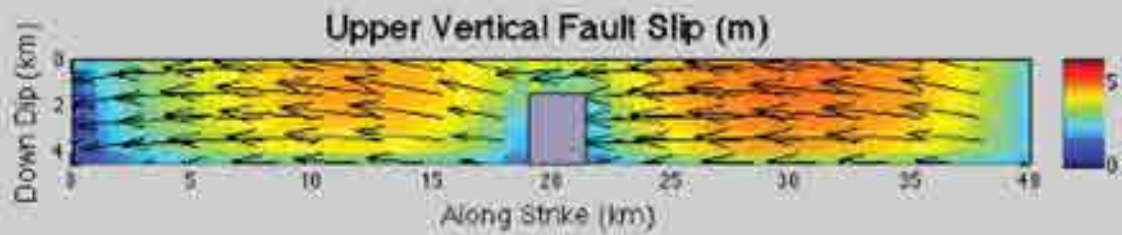


Figure 5 displays placement of barrier along strike. The barrier is placed in the upper vertical fault, towards the branching point of the basal fault. The barrier is 2km by 3km and does not reach the surface.



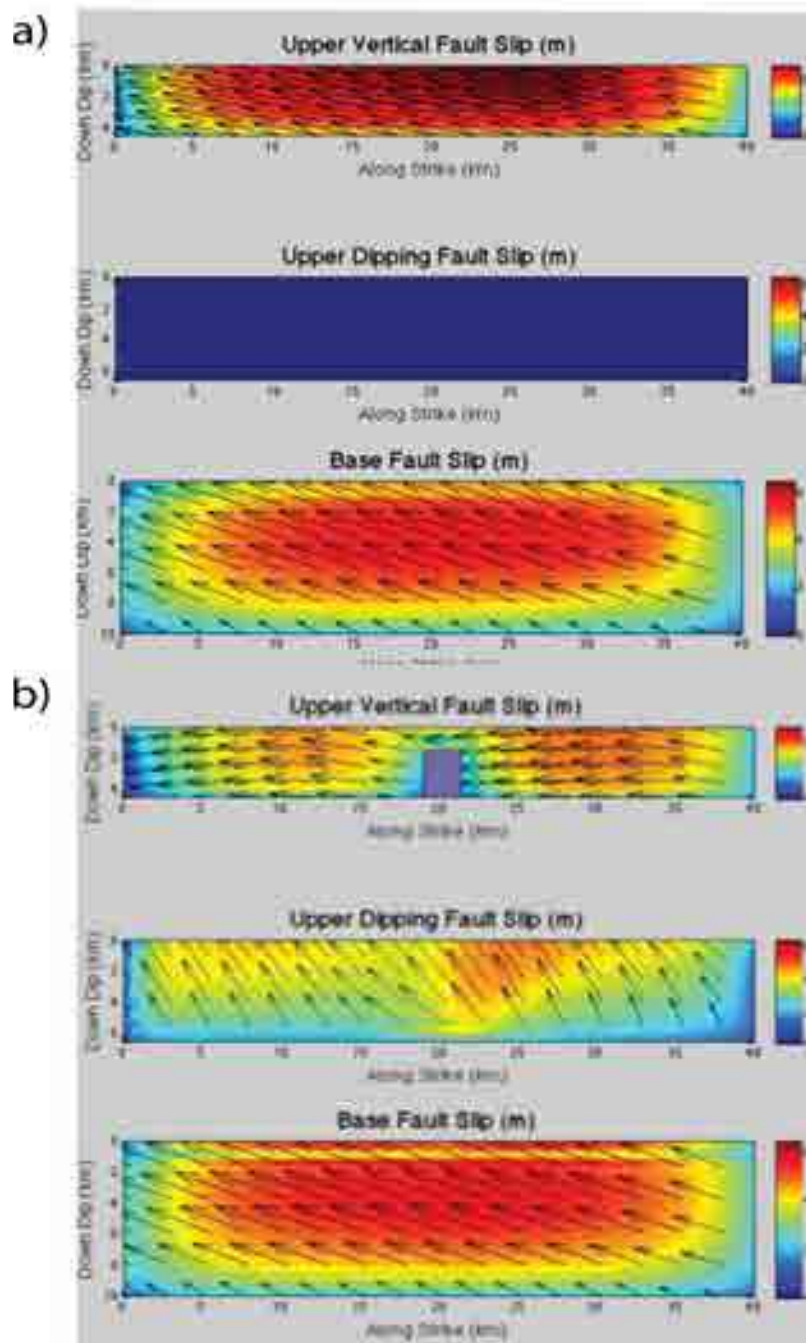


Figure 7 displays a comparisons of slip for the two models. a)Has slip on both the basal and upper vertical fault with the dominate motion oblique. b)Oblique motion on the basal fault, strike-slip on the vertical fault and dip-slip on the dipping fault.

The Unveiling of Math’s Two Most Secret Societies

► **Cristine R. Martin**

Advisor: **Dr. Martin Bonsangue**

California State University, Fullerton

Secret words, secret temples and secret symbols: two societies formed in different times and different regions, but somehow hold many of the same principles and attributes. The Free Masons and the Pythagoreans hold a place in the hall of mysteries not just hundreds of years ago, but still today. This article explores the relationship between the Masons and the Pythagoreans, and considers the Pythagorean influence on both how the Masons came to be and their practices. To know whether or not the Pythagoreans influenced the masons, we must first look into the history of the Pythagoreans and Masons.



Figure 1. Masonic Sword © Christine Martin

The Pythagorean Beginning

The Pythagoreans were a sect that was started by Pythagoras of Samos, ca. 520 BCE. Pythagoras was a man that spent many years of his life studying the world around him. As a young man, Pythagoras spent time in Egypt learning about the pyramids as well as the ancient Egyptian priests and their temples. The ancient Egyptian priests held the belief that knowledge of the society was a precious stone that could be stolen at any moment. These priests had to go through an extensive initiation before they were entrusted to carry on the

knowledge from their predecessors. The Pythagoreans saw knowledge as a sacred ideal, and took precautions to be sure it was not tossed around carelessly, an idea that Pythagoras himself probably obtained from the Egyptian priests.

Pythagoras explored Egypt looking to gain entry into an Egyptian temple and although he failed several times, did eventually succeed after he endured trials of a strict diet and meditated for several days. After this, the Egyptians priests put Pythagoras through many rigorous tests hop-

ing to deter him, but because he prevailed he won their appreciation and was welcomed into their temple (Norfleet, Phil. 1992). Pythagoras spent a little over 20 years in the Egyptian temples studying and adapting to the priest’s way of life (Mackey, A. 1921).

Although there are few specifics known about the Egyptian initiation process, many ideas and assumptions have been generated over the years (Fellows, J.1835). The more sacred or important secrets were not even revealed to all the priests, so it is likely

that little was revealed to Pythagoras (Mackey, A.1921).

When Pythagoras returned to Samos, he founded the Pythagoreans. The Pythagoreans, like the Egyptians, focused on gaining a better understanding of the world around them through religion, astrology, and geometry. In fact, the Pythagoreans looked so highly upon mathematics that they believed it held the key to all things. Similar to the Egyptian priests, access to the Pythagoreans' knowledge was limited to those that were able to pass their initiation process. These members of the Pythagoreans were known to each other by a simple symbol, the pentagram. Another significant belief of this group was in keeping one's soul "clean." Their white togas were to signify innocence and purity, and their restrictive diet was to cleanse their bodies (Fellows, J. 1835).

The Pythagoreans came to an end because of a man's taste for vengeance. Sylo, a wealthy land owner of Crotona, was turned away from the school of Pythagoras. In return he excited a mob of citizens to burn the school down; forty members of the Pythagorean society were burned alive in the fire. The Pythagoreans never formed again (Mackey, A. 1921). Interestingly in the first century B.C. a group called the Neopythagoreans emerged. This group which remained through the Renaissance period, believed that Pythagoras was the father of the development of Greek philosophy (Huffman, Carl. 2008).

The Beginning of the Masons

Masonry can be found throughout the world and is very much in practice today. This organization currently has around 6 million members,



Figure 2. Past Master Masonic Apron © Christine Martin

and has had a number of powerful and memorable members in the past. These include: Louis Armstrong, King Edward VIII, Henry Ford, Wolfgang Amadeus Mozart, Franklin Delano Roosevelt, Mark Twain, and, George Washington (Mackey, A. 1921).

Like the Pythagoreans, this group believes in keeping one's soul clean and pure, and they symbolize this by wearing pure white leather aprons. It is the responsibility of these men to keep their aprons clean at all times. While \Masons do not have an official strict diet, they are expected to lead moral and respectful lives so that others may follow in their footsteps. Masons meet and discuss their issues once a week in their local lodges. Each lodge acts independently of each other, and may have different or additional practices to follow. Depending on the lodge they attend, they may or may not incorporate a healthy diet into their practice. Every lodge and every mason is expected to live by the "compass of virtue and square his actions" so that he may help his neighbors and brothers.

(Mackey, A. 1921).

The Masons seem to have several beginnings but, unlike the Pythagoreans, have no distinct end. While it is certain that Pythagoras is the founder of the Pythagoreans, the Masons have an interesting twist on who their founder is. The founder of the Masons is Hiram Abif (Mackey, A. 1921). Hiram Abif was the architect of King Solomon's temple and known as a Grand Master Mason. Therefore the Masons can trace their history back about 3000 years (ca. 1000 BCE).

Today, the Masons recreate the death of Hiram Abif in one of their initiation processes. During this process the new members are walked through the tragic murder of Hiram. Many of the different initiation processes are meant to force men to rethink their actions and their lives to better themselves. The main objective of this organization is to promote the growth in morals and education of men (McNeil Lodge #440).

While the Masons can date their history back to the time of Solomon's temple, the recent collections of



Figure 3. A Masonic Trowel © Christine Martin

Masons are now called The Free and Accepted Masons (Mackey, A. 1921). Through the years this group claims to have gone through many transitions; perhaps the most significant of these is going from being Operative Masons to being Speculative Masons. The earliest available records of the Masons' existence dates back to the early 16th century and it is of the Operative Masons. This information or records that connect this group to the Templar Knights and Solomon's temple, if such records exist, is most likely only available to Master Masons of a higher degree.

The Connection of these Two Societies

Considering when the Pythagoreans and the Masons began, the possibility that the Pythagoreans influenced the Masons is impossible. Instead, the connection of these two groups is the Egyptians. Hiram Abif spent time in Egypt studying with the priests (Mackey, A. 1921), so the founder of this group was well versed

in the ways of the ancient Egyptian priests. While the Masons date their existence back to King Solomon's temple, Masons also recognize a connection to the Templar Knights as well. In the temple that these knights guarded there were several scrolls of knowledge from the Greek, Egyptian and various other schools (Discovery Channel). These knights had access to these scrolls and passed on their knowledge by word of mouth. It is rumored that though most of these knights were hunted down and killed, some escaped and were the ones that passed down the knowledge. Today in some Masonry meetings some members have swords with them, perhaps to represent the old days and the templar knights, refer to figure 1. By connecting themselves to the Templar knights and to Hiram Abif, the Masons effectively connected themselves to the Egyptians. However the Pythagoreans connection to the Egyptians is more pronounced. Pythagoras, as stated above, spent a little over 20 years in the Egyptian temples. Thus, it does not surprise

that the Pythagoreans practices and beliefs were closely related to the Egyptian's. Therefore we have a connection between these two societies that would create several similarities.

One of these similarities is the respect for numbers and geometry. The Pythagoreans believed that they could unlock the mysteries of the world by the study of numbers and geometry (Mackey, A. 1921). Numbers also play a large role in their symbolic meanings. For example, the Pythagoreans deemed the number five important because it was created by "the union of the first even number, also known as a female number, and the first odd number or male number" (Mackey A. 1921). The number five represented the mixture of order and disorder, life and death, and so forth. To the Masons this number is also significant and is only inferior to 3 and 7 (Mackey, A. 1921). This view of geometry and numbers can also have stemmed from the Egyptians since they were one of the first cultures which cultivated geometry as a quantitative science (Mackey, A.1921).

Both the Masons and the Pythagoreans sent their applicants away to meditate or ponder their beliefs and recent actions before they can even begin the initiation process. It is likely that they both received this action from the ancient Egyptian priests. The idea to keep a clean and pure soul was practiced by the ancient Egyptian priests (Fellows, J. 1835). As the Pythagoreans wore white togas and stuck to a strict diet, the Masons likewise carried out symbolic representation of a clean and pure soul. The Masons, to symbolically represent their clean soul, wear a plain white leather apron. There are different aprons for Masons of dif-

ferent degrees (refer to figure 2), but they are still required to keep their plain white apron and maintain it in good condition; therefore keeping their souls in good condition.

Another similarity between the Masons and the Pythagoreans is in their different levels of acceptance. The three levels of Masons ascending from a lower to a higher degree of knowledge are: Apprentice, Fellow and Master Mason. Within these degrees there are more sub-levels that may vary from different lodges. The Pythagoreans also divided their members into two groups: *akousmatikoi* (listeners), and the *mathēmatikoi* (learners) (Huffman, Carl

2008). They also had three degrees of knowledge: “the first or Mathematic, being engaged in the study of the exact sciences; and the second, or Theoretic, in the knowledge of God and the future state of man; but the third, or highest Degree, was communicated only to a few whose intellects were capable of grasping the full fruition of the Pythagorean philosophy.” (Mackey, A. 1921) This idea of having different levels divided into groups is very likely to have come from the Egyptian priests, as they also had different levels of acceptance.

If the Masons have indeed descended from Hiram Abif and the Templar Knights as many believe,

it would have been unavoidable for them to not have attained some of the same practices and beliefs of the Pythagoreans due to the connection to the Egyptians. How would the Pythagoreans fit into today’s society, and how different from the Masons would they be? One profound difference is the acceptance of women. Women may not join into a Masonic lodge in normal circumstances, though women can join one of the following Masonry based groups: Order of the Eastern Star, the Order of the Amaranth, the White Shrine of Jerusalem, the Social Order of Beauceant or the Daughters of the Nile. The Pythagoreans, however, had no problem accepting women into their society, and would probably still be the same today.

Even though the Masons have labeled some of their lodges after Pythagoras himself, it is only because of the fact that they try to recognize mathematicians that have made a significant difference in geometry. This is due to the significance of geometry in masonry. For example the Masons have also named several lodges after Euclid (Mackey, A.1921). The Pythagoreans did not influence the Masons; rather, merely had a link to the Ancient Egyptian priests.

The Free and Accepted Masons Today

The Masons have general symbols that stand for their beliefs today. Some of these men walk around with rings, pendants, lapel pins or tie clasps with some of the more common masonry symbols on them. Below are some of their more common symbols and their meanings. (McNeil Lodge #440):



Figure 4. Masonic symbols © Christine Martin

The square reminds us to regulate our actions and conduct to be in harmony with the principles of morality and virtue.

The compasses to limit our desires so that we may live respected and die regretted.

The 24 inch rule to allocate our time so as to be used for service to God and distressed Masons.

The gavel to divest our hearts and minds of all of the evils and pettiness of live.

The plumb to walk uprightly before God and man.

The level to deal with all men fairly, and

The trowel to spread the cement of brotherly love.

That cement unites all Masons into one sacred band or society of friends and brothers.

There are several more symbolic references in this group, and only a Mason may know their meanings and purposes. If you have more curiosity about the masons, or you want to become a mason you should ask one. There is no guarantee that any of your questions will be answered. According to the Masons, "To divest it of its secret character would be social suicide, and the death of the Order would follow its legalized exposure." (Mackey, A.) It is likely this expression roots from the Egyptian priests who understood that knowledge was power, and one should be careful about to whom this power is given.

References

Arizona Masonry. <http://www.arizonamasonry.org>

Discovery Channel. (2007, December 3). The Secret History of the Freemasons.

Dunham, W. (1990). *Journey through genius: The great theorems of mathematics*. Wiley science editions. New York: Wiley.

Fellows, J. (1835). *An exposition of the mysteries; or, Religious dogmas and customs of the ancient Egyptians, Pythagoreans, and Druids Also: an inquiry into the origin, history, and purport of freemasonry*. New York: Printed for the author, and sold by Gould, Banks.

Huffman, Carl, "Pythagoreanism", *The Stanford Encyclopedia of Philosophy (Fall 2008 Edition)*, Edward N. Zalta (ed.), URL = <http://plato.stanford.edu/archives/fall2008/entries/pythagoreanism/>

Mackey, A. 33o McClenachan C. 33o (1921). *An Encyclopedia of FREEMASONRY and its Kindred Sciences*. Chicago Illinois: The Masonic History Company

McNeil Lodge #440. <http://www.geocities.com/wduggan/freemasonry.html>

Norreflect, Phil (1992). *Alchemists of the Twentieth Century*. <http://alchemy1961.tripod.com/pythagoras.htm>. 2008.

Nuclear Spin Relaxation via Hole Spins in Semiconductor Nanostructures

► **Alyssa Rodd**

Advisor: **Dr. Ionel Tifrea**

California State University, Fullerton

The use of semiconductor nanostructures in modern electronic devices has allowed for devices that are small enough to make quantum mechanical effects unavoidable [1]. The next step towards more advanced devices is to exploit the quantum properties of the materials from which these devices are composed. Nuclear magnetic resonance (NMR) experiments can be used to gain information about nuclear and electronic systems. In semiconductor structures, electrons will be naturally confined in one or more dimensions creating quasi-two-dimensional systems. The interactions between nuclear spins and electron spins along with the confinement of the electrons will result in a non-uniform nuclear spin polarization [2]. By taking into account a more precise wave function for the electron then previously used and calculating the relaxation time of nuclear spins due to various different interaction mechanisms specific to semiconductor nanostructured samples, a better understanding of how to control the nuclear spin population can be obtained. Specifically, we will address the interaction between nuclear and hole spins in semiconductor nanostructures [3]. Although such an interaction is usually considered to be small, in certain semiconductor nano-

structures it can contribute to about 15% of the nuclear spin relaxation time. Our analysis is theoretical and relies on both analytical and numerical calculations. For the simulation of the electronic wave function in semiconductor nanostructures we will use a state of the art k - p numerical code which gives us the possibility of a very accurate description of the physical phenomena. If we can control the nuclear spin polarization, then we can use the nuclear spins to store data in computer chips. The model we develop will take these effects into account, give NMR data new significance, and result in a new understanding of nuclear spin dynamics. It will hopefully yield a way to control the nuclear spin polarization and ultimately a way to create smaller, faster, more efficient electronic devices.

References

[1] E. I. Gryncharova and V. I. Perel, *Sov. Phys. Semicond.* 11, 997 (1978).

[2] J. H. Davies, *The Physics of Low-Dimensional Semiconductors*, Cambridge University Press 1998.

[3] S. A. Wolf, D. D. Awschalom, R. A. Buhrman, J. M. Daughton,

S. von Molnar, M. L. Roukes, A. Y. Chtchelkanova, and D. M. Treg, *Science* 294, 1488 (2001).

Near Threshold Electron Impact Doubly Differential Cross Sections for the Ionization of Neon and Xenon

► Brent R. Yates & Kyle Keane¹

Advisor: Murtadha A. Khakoo

California State University, Fullerton

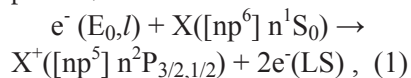
Abstract

Normalized doubly-differential cross sections for the electron impact single ionization of Ne and Xe are presented. The Ne measurements are taken at incident energies of 23.5eV, 25eV, 30eV and 40eV while the Xe measurements are taken at 14eV, 15eV and 20eV. Scattering angles in the experiment range from 15° to 120°. The measurements use a moveable target method for an accurate determination of the experimental background. Normalization of the differential data is initially made to available experimental cross sections for excitation of the ground np^6 to the $np^5(n+1)s$ excited states of the noble gas and then, if necessary after integration, to available experimental total ionization cross sections. We show that our single differential cross sections, derived from integrating the doubly differential cross sections, show a convex profile (frown) for Ne whereas they are concave (smile) for Xe similar to what is observed for He, and we suggest a tentative mechanism for this.

PACS number(s) 34.80.Dp, 25.30.Dh

Introduction

Whereas much experimental and theoretical work has been carried out on the single electron impact ionization of He, e.g. [1, 2], much less work has been carried out for the other rare gases Ne, Ar, Kr and Xe. Of these four, Ar seems to have been more frequently investigated, but even then there remains a paucity of electron impact ionization data. The low energy electron impact ionization of the rare gases plays an important role in the transport of electrons in rare gas discharges [3] which has relevance in plasma applications such as in processing of semiconductor wafers and plasma tubes [4, 5], where rare gases are frequently used as buffer gases. The study of the electron impact ionization of these targets is made more complicated by the dynamics in the change of the $np^6 \rightarrow np^5$ core configuration by the single ionization process, viz.



where X is the rare gas target impacted by an electron with a plane wave (partial wave expansion of the plane wave in the orbital angular momentum (l)) resulting in a two receding electrons with total orbital and spin angular momenta (L,S) [6]. The phys-

ics is made more elaborate to model because of the resultant fine structure in the residual ion X^+ , a spin-orbit coupled P-core and, further, its coupling with the receding electrons (one which depends on the total energy of these electrons) which provides for a more complicated situation than the more studied case of helium. In this experimental investigation of Ne and Xe, we aimed to address the viable angular momentum coupling in the target and between the target and the ionized/projectile electrons for two similar valence shell electron targets, but spectroscopically with different atomic coupling schemes. In the case of Ne, one can expect the coupling to be dominantly LS coupling, whereas for Xe spin-orbit coupling is dominant, as has been shown in other electron impact studies of excitation of the ground state of the rare gases [7,8]. A comparison of cross section data for the electron impact ionization of Ne and Xe would therefore be useful in an attempt to compare the role of LS and spin-orbit interactions in the ionization process.

Presently, the most recent electron impact work on the ionization of Ne was made by Naja et al. [2] which involved an (e, 2e) study of He and Ne at an incident electron energy (E_0) around 500eV. This was a collabora-

tive study between the experimental groups at Orsay of Lahmam-Benanni and at Adelaide of Lohmann, and was supported by theoretical work from an international collaboration of theorists who applied the Distorted-Wave- R Matrix hybrid theory, the Brauner-Briggs-Klar model involving a 3-body Coulomb wavefunction with two outgoing plane waves, as well as the convergent close-coupling approach applied to modeling the electron impact ionization of Ne. We note that the convergent close-coupling approach was used successfully in [1] for He where it has been well-tested at low incident energies near threshold, but has not been as rigorously applied to other rare gas targets. Existence of similarities between He and Ne ionization was recently observed by Murray and Read [9] who observed (coherent) interference minima in Ne similar to that they had observed earlier using the same apparatus for He.

In considering the history of the experimental electron impact ionization of Ne and Xe, the first total cross section measurements were made in 1965 by Rapp and Englander-Golden [10] using an ionization tube system coupled to a McLeod pressure gauge. The accuracy of these measurements has remarkably withstood the test of time. They have been followed by electron impact ionization measurements using various other setups, e.g. pulsed electrons, fast neutral beams, etc. [11-14]. In terms of (e, 2e) triply-differential cross section experiments, the first in Ne were those of Selles *et al.* [6] who made coplanar (e,2e) measurements at near threshold yielding relative triply-differential cross section measurements in the 0.5eV to 2eV range above threshold with equal sharing of the

energy of ionized electrons at 0.25eV, 0.5eV and 1eV. These measurements were followed by non-coplanar (e,2e) measurements of ionization of Ne at $E_0=110.5\text{eV}$ and an out-of-detection-plane angle of 42° by Murray and Read [15]. They observed deep minima similar to earlier work they performed in He and in agreement with theory which coupled the outgoing electrons using a modified Gamow factor [16]. However, this still left the understanding of this deep minimum in terms of being an interference phenomenon an open question. As aforementioned, very recently more coplanar (e,2e) measurements in Ne were carried out by Naja *et al.* [2] at high energy (about $E_0=600\text{eV}$). Doubly-differential cross sections for electron impact on Ne were recently measured by Santos *et al.* [17] at high energy ($E_0=750\text{eV}$), and earlier by Opal and Beatty, [18] $E_0 \geq 750\text{eV}$ and DuBois and Rudd [19] at $E_0 \geq 100\text{eV}$. At these high energies, theory can be expected to be complicated as this region is above the 8th ionization threshold for Ne. Currently, apart from the (e,2e) work of Selles *et al.* [6], there are no other measurements of differential ionization below the second ionization threshold (40.96eV). A variation of the Born approximation by Chang and Altick [20] has been used to compute doubly-differential cross sections at high energy (500eV), and compare their results with the experimental doubly-differential cross sections of Opal *et al.* [18] for Ne, Ar and Kr.

For Xe, the most recent measurements have been the (e,2e) results of Panajotovic *et al.* [21] at $E_0=147.8\text{eV}$ with the aim of investigating the fine-structure effect in the ionization as compared to its excitation [22]. These

measurements are made possible, by the large fine-structure splitting and the heavy target property of Xe. This enables present electron spin polarization sources to be able to facilitate observation of the fine structure effect with spin-polarized electrons and thus test theoretical methods regarding the importance of relativistic interactions in the ionization of Xe. This work follows the measurements of (e,2e) spin-polarized electron scattering (ionization) from Xe of the Münster group of Hanne and co-workers, [22] and the Australian National University (ANU) group of Weigold and co-workers [21]. These investigations (which have looked at the valence electron ionization, i.e. with the Xe+ core left in the $5^2P_{3/2}$ or $5^2P_{1/2}$ state) have shown that including relativistic terms in the scattering such as the Furness-McCarthy exchange potential [21] improved agreement between theory and experiment. However, the reason for this improvement was not clarified. The work of the ANU group has been at $E_0=30\text{eV}$ to 160eV while that of the Münster group has been at $E_0=40\text{eV}$ to 200eV. Electron impact autoionization studies of differential ionization [22,23] currently remain the only measurements below the second ionization threshold of Xe (21.21eV). These electron impact autoionization spectroscopy measurements using (e,2e) [23,24], and observing ejected electron spectra [25] have been made by Martin and co-workers at incident energies of 16eV to 150eV. They observe primarily dipole excitation at high energy and excitation dominated by exchange and non-dipole interactions at low energy. Recently, Ren *et al.* [26] have made (e,2e) measurements of the inner shell ionization of the 4d electrons of Xe at $E_0=1200\text{eV}$ to 2400eV to determine

the momentum distribution of these inner-shell electrons.

It is important to consider the role of relativistic effects at energies below the second ionization threshold of these targets in an effort to understand the role of non-dipole, exchange and spin-orbit interactions in the ionization process. This can, similarly as in the autoionization process, dominate electron impact ionization of heavy targets. In this work, we have selected Ne and Xe and measured doubly-differential cross sections for single ionization leaving the core ion in the unresolved $^2P_{3/2}$ and $^2P_{1/2}$ fine structure states. Our measurements are at E_0 values which range from 1.94eV, 3.4eV, 8.44eV and 18.44eV above the first ionization threshold for Ne, and 1.87eV, 2.87eV and 7.87eV above the first ionization threshold for Xe for scattering angles (q) of 10° to 120° . Presently theoretical calculations for measurements of this type and range are not available.

Experiment.

Our measurements were carried out on a spectrometer comprised of a single hemispherical energy selector in the electron gun, and a single hemispherical energy selector in the scattered electron analyzer. This apparatus has been described in Childers *et al.* [27, 28] where it was used to investigate the electron impact ionization of H and in [1] where it was used for investigating the electron impact ionization of He. However, the present configuration of this instrument bears a complete remounting of the previous system together with a modified collision region in which additional screening of the collision region in the back portion

of the spectrometer further reduced secondary electrons back-scattering into the collision region volume, and entering the scattered electron analyzer when the analyzer was rotated to large θ . This modification has improved the signal to background ratio from that previously observed in [1] by a factor of 50%. This spectrometer operated similarly as in the old setup in [1] with an incident electron current of 50nA to 100nA with a resolution of ≈ 140 meV. In this experiment the electron beam crossed an effusive source of gas emitted by a 2.5cm long molybdenum needle of inner and outer diameters of 1mm and 1.3mm respectively. Surfaces surrounding the collision region (including the needle) were heavily sooted with an acetylene flame to suppress the production of secondary electrons by the primary electron beam colliding with these surfaces. The depth of field of the scattered electron analyzer was restricted to a small region around the collision center (5-6mm region) by using an additional pupil in the input electron lens stack of the detector. The spectrometer was baked to greater than 120°C to maintain stability of the electron beam and the detector, and was housed in double mu-metal shield system which reduced the ambient magnetic field at the collision region to below 5mG.

The experimental setup employed a moveable gas target source [29]. Using the moveable source, it was possible to obtain background-free electron energy loss spectra which enabled us to reliably determine the electron counts under discrete excitation peaks as well as under the ionization continuum. The tip of the needle was 5mm away from the center of the collision region. No variations of the transmitted electron

beam, monitored, using an electron collecting plate arranged downstream of the collision region, were observed as the needle was moved into and out of alignment with the incident electron beam. At $\theta < 10^\circ$, at low residual electron energies (E_R), we observe an additional source of secondary electrons, systematically affecting our background subtraction which suggests the electron beam's changing size (due to space-charge neutralization) at the collision region when the gas beam was moved into and out of alignment. This affects the small angle data more because of the increased electron-gas beam overlap region at small scattering angles. This effect produced an additional source of secondary electrons from the analyzer shielding plates (E_R below 1eV), that could not be systematically removed by subtracting the electron energy loss spectra with the gas in and out of alignment with the incident electron beam. This added an additional 10% uncertainty to the signal for these low E_R electrons.

We calibrated the transmission of our analyzer as follows. First, the detector transmission was made as uniform as possible for electrons with different E_R values by tuning the analyzer, and monitoring the flatness of the helium continuum at $E_0 \approx 30$ eV and $\theta = 90^\circ$. The fact that the helium continuum energy loss spectrum is 'flat' was established by Pichou *et al.* [31], and reconfirmed later by us with atomic hydrogen as a standard [27,28]. At larger E_R values in our experiment (typically exceeding 1eV), the transmission response of the spectrometer was found to be stable during the course of measurements as long as the analyzer was not re-tuned. However, closer to zero E_R this uniform transmission could not

be achieved as reliably as at higher E_R values, and add errors to our DDCSs at small E_R . We were also limited to how much lower than $E_R \approx 0.7\text{eV}$ we could go, because of the zero E_R centered secondary electron peak (see figure 1) which did not always subtract out completely. We note that the spectrometer (electron gun, analyzer and collision region) were baked to temperatures around 120°C using biaxial non-magnetic heaters to maintain this stability. These transmission calibrations were all performed at $E_0 = 30\text{eV}$ for $\theta = 90^\circ$. This calibration provides for a 5.4eV E_R window to calibrate the low E_R electrons (the ionization potential of He is 24.6eV). This can be extended further to the excitation of the $n=2$ states of He giving an increased E_R window of 8.8eV .

For those spectra of Ne taken at impact energies so that the E_R of the ionized electrons exceeded 8.8eV , the transmission was initially flat-extrapolated, because it could not be measured. However, we generally found that simply extending beyond this E_R window did not accurately correct for the transmission in the extrapolated region; a polynomial function that was not flat, but limited to a low order (≤ 2), had to be used to get better agreement with those available in literature (within uncertainties) of integrated total ionization cross sections (TICSs). For this, the spectrometer transmission was extrapolated beyond the He ($n=2$) energy loss region using a polynomial in E (energy loss) of order ≤ 2 , to enable us to flexibly extrapolate outside of the range of this E window to agree with the experimentally available TICSs. We note here also that when the He transmission calibrations did not have to be extrapolated, we did not need to normalize our DDCS to the available

experimental TICSs. At these low E_0 values, a direct comparison between our TICSs and those available expectedly gave satisfactory agreement which affirmed the procedure employed in the analysis of our data. In the case of Xe at 20eV , calibrating for transmission, the interpolation process using the He ionization continuum window at $E_R = 5.4\text{eV}$ and the He ($n=2$) DCSs at $E_R = 8.8\text{eV}$ was found to give a TICS value of about 25% greater than the experimental TICS values. In this case the full Xe ionization continuum region was corrected by this factor – the difference is presently assumed to be due the DCSs (used for our normalization of the DDCS) in [32] being greater by this amount.

Having determined the transmission of the spectrometer, we measured electron energy loss spectra of Ne and Xe at several selected E_0 values in the range below the second ionization threshold of these gases for scattering angles of 10° to 120° , in 10° intervals. Samples of these spectra are shown in figure 1. The spectra were corrected for the transmission of the spectrometer, and then normalized to the available summed differential cross sections (DCSs) for electron impact excitation of the energy levels comprising the excited Ne $2p^5 3s$ configuration at $E = 16.619\text{eV}$, 16.671eV , 16.761eV and 16.848eV from [31] for Ne. For Xe we normalized to the summed DCSs for the lower two energy levels of the Xe $5p^5 6s$ configuration, viz. $6s[3/2]_2$ and $6s[3/2]_1$ states at $E = 8.315\text{eV}$ and 8.437eV , from [32]. For the case of Ne at $E_0 = 23.5\text{eV}$, the 23.5eV DCSs of [31] were determined by linearly interpolating between their existing 25eV and 20eV DCSs. For Xe at $E_0 = 14\text{eV}$, we linearly interpolated the

DCSs of [32] taken at $E_0 = 10\text{eV}$ and 15eV . From the continuum energy loss spectra of the ionization region, we determined normalized doubly-differential cross sections (DDCS)

$$\frac{d^2\sigma_X(E_0, \theta; E)}{d\Omega dE} = \frac{N(E, \text{continuum}) dE}{N(X) \Delta E} \quad (1)$$

where $N(E, \text{continuum})$ is the height of the continuum (number of electron scattering events), at the position E (electron energy loss) in the continuum. ΔE (typically set to $\approx 0.04\text{eV}$) is the energy loss step width per channel in the energy loss spectrum. $N(X)$ is the total number of electron scattering events under the summed, discrete energy loss features for the target X , and $d\sigma_X/d\Omega$ is DCS from Table 1 for the excitation of these summed energy loss features from [31,32]. For Xe, as a check of the DCSs taken from [31,32] we also measured the elastic electron scattering peak and used the elastic scattering DCSs from [33] to further check our normalization of the DDCSs. The elastic scattering check was found to be in good agreement with the results obtained by normalizing to the DCSs from [31].

The value of $N(E, \text{continuum})$ was determined by fitting the ionization energy loss continuum to a polynomial series in E of order ≤ 2 . The calibration of the spectrum was dependent upon an accurate determination of the value of ΔE . This value was determined from the energy loss spectra in which the start energy loss and end energy loss values were recorded. Additionally with ΔE , the location of the helium 2^3S feature in the spectrum at 19.814eV energy loss served to calibrate E for the whole spectrum when the instrument was used with He. The linearity of the

energy loss scale ramp voltage supply was determined in a separate experiment (using a 5-digit voltmeter), and was found to be $\approx 0.2\%$ of the energy loss covered in the full energy loss spectrum. The incident energy of the electron beam was determined from the spectrum by using the cut-off energy loss value (see figures 1) of the continuum. This method served to determine E_0 to an accuracy of $\pm 0.15\text{eV}$. The quoted E_0 values in our DDCSs are an average of these measurements.

Our DDCSs were integrated over θ to obtain singly-differential cross sections (SCDSs), $r \, d\sigma_l/dE(E_0, E)$. These SDCSs were then integrated over E and divided by two (to account for the scattered electron only) to obtain the TICS. Our results compared well with the well-established and accurate total ionization cross sections (with $\pm 3\%$ uncertainties) measured by Rapp and Englander-Golden [10], Wetzel et al. [12] and Krishnakumar and Srivastava [14], for Ne and Xe. In the determination of our SDCSs we visually extrapolated our DDCSs to small and large scattering angles outside of the experimental scattering range. The error in this extrapolation was estimated by repeating the integration, but instead employing flat DDCS extrapolations to $q=0$ and 180° from the endpoints of the angular distribution of the DDCSs. The error estimate was determined from the difference of the two extrapolations and added in quadrature with the mean error of our DDCSs. The SDCSs are expected to be symmetric about the middle of the ionization continuum at the residual energy of $E_R=(E_0-E_1)/2$ where E_1 is the first ionization energy, since the scattered and the total energy of the ionized electron

pair (E_P) equals E_0-E_1 , provided E_0 is below the second ionization energy, i.e. only two free electrons result from the post-collision system. This symmetry property of the SDCS provides a further constraint for our transmission correction that was applied to the experimental energy loss spectra.

Results and Observations.

The resulting DDCSs for Ne and Xe are listed in Tables 2 and 3 together with SDCSs determined from integration of the DDCSs over scattering angle and the resultant total ionization cross section TICS obtained by integrating our the SDCSs over E across the ionization continuum, and dividing by 2 as discussed before. The uncertainties of the DDCSs include errors in the inelastic DCSs used for normalization from [31,32], the error in uncertainty of the spectrometer transmission [5-10%], and statistical errors [2-8%] from determining the background free signal. Selected DDCSs for Ne are plotted in figures 2 and for Xe in figures 3. SDCSs are plotted in figures 4.

Starting with Ne, from figure 2a at 23.5eV incident energy, we note the significantly reduced DDCS (by as much as a factor of about 5) for Ne at small θ as compared to that for He [1] for a comparable energy above threshold. We note here from [10] that the TICS for He is comparable to Ne at these E_0-E_1 values. Intuitively, one would expect Ne to be easier to ionize than He for comparable E_0 above the ionization energies. Examining the TICSs of [10] we see this is not the case. For near-threshold E_0 values, in the region of about 1eV to 5eV above threshold, we observe that the TICSs for Ne are $\approx 15\%$ smaller than the TICSs for He, whereas the

TICSs for Ar, Kr and Xe are, respectively, $\approx 9\times$, $\approx 15\times$ and $\approx 25\times$ those of He. In fact it is only when one gets above the second ionization threshold that the TICSs of Ne overtake He and are $\approx 1.5\times$ greater. This seems to suggest a mechanism where emission of slow ionized electrons by electron impact is somewhat suppressed.

The suppression of slow electrons emitted in the forward direction at low energies is clearly noticeable from both figure 2 and also from the electron energy loss spectrum taken at a higher E_0 value of 25eV , but at a small θ of 10° . This phenomenon, which we observed very early on during the course of this work, made the present experimental work significantly more difficult than earlier for He [1], i.e. to be able to determine the signal at low ER and q for Ne as compared for He. This suppression continues up to $E_0=30\text{eV}$, but improves at $E_0=40\text{eV}$ (see figure 2). We make a suggestion that possibly the $2^2P_{3/2,1/2}$ core is being polarized at low incident energies predominantly in the forward direction by the “fast electron”, and “sucks back” the slow electron. This may also be responsible for suppressing the ionization process overall. Understandably this is a complicated system with a P-core and 2 emerging (correlated) electrons. This is supported by the dipole-type angular distribution of electrons with higher ER, indicating possibly the core polarizability of Ne is involved in setting up the ionization process by the “fast” electron which points the core in the forward direction, and affects the way the other (slow) electron is emitted (or suppressed). This increasingly forward scattering of fast electrons is systematically seen in figure 2 as one proceeds from 25eV to 40eV . At 40eV we note an

interesting reduction of low ER electrons around θ of 25-50°. The reason for this is presently not clear and may be better understood with an (e,2e) investigation in this interesting regime. Certainly the suppression of slow electrons would be of interest to an experimental or theoretical (e,2e) investigation, in terms of the angular distributions of these slow electrons correlated with forward scattered electrons, and would determine what factors cause the TICSs of Ne to be lower than those for He at low E_0 values below the second ionization threshold. From equation 1, the incident electron l values would (at the E_0 values here) certainly exceed $l > 3$ i.e. the contribution in terms of partial waves of terms exceeding the d-wave would be significant. However, after ionization, the low energy of the electron pair would (at near-threshold) cause L to be approximately less than 2, and predominantly S, P or D wave electron pairs would be emitted. Since the angular momentum of the ejected P-electron will contribute $l=1$ to the electron pair, in the event the projectile electron is forward-scattered (thus with most of the pair-energy as observed from the distributions of the high E_R electrons which are mainly forward scattered), this correlation would arguably be smaller and the resultant slow electron would emerge with predominantly $l=1$ (P-electron). This type of electron would predominantly be emitted along the momentum transfer direction for such collisions resulting in low pair-energy of the ionized electrons. Consideration of the collision dynamics for the electron impact ionization of Ne shows that the momentum transfer lies in the region of $0^\circ \leq \theta < 17^\circ$ for $E_0=23.5\text{eV}$ and $E_p=1.91\text{eV}$. For our highest E_0 value of 40eV and $E_p=$

18.41eV the momentum transfer lies in the region of $0^\circ \leq \theta < 42^\circ$. With the slow electron emitted along the direction of the polarization of the core, the core would inhibit its emission ('suck' back the slow electron) and thus this ionization process would have a reduced probability. We stress here that the above is only hypothetical on our part as our observations are limited. This needs to be investigated further in more detail using a near-threshold (e,2e) experiment or a theoretical investigation to observe the slow electron angular distributions in coincidence with a forward-scattered fast electron, to see if the angular distribution of these slow electrons is skewed towards larger θ so that the process of suppression can be directly observed.

For Xe we observe an overall different situation from that of Ne although the alignment of the momentum transfer for Xe is similar to that of Ne (i.e. it stays in the range of $\theta < 17^\circ$). At $E_0=14\text{eV}$, the angular distribution of the DDCSs are closer to He (see DDCSs in [1]) than Ne. In figure 3 at 14eV, the DDCSs exhibit a strong d-wave type angular distribution for all E_R possibly due to resonances (certainly the suppression of low energy forward scattered electrons seen in Ne is not observed here to the same extent), although some (lesser) suppression of low E_R electrons can be seen at the higher $E_0=15\text{eV}$ and 20eV, but not at 14eV. One can expect non-dipole or relativistic mechanisms (exchange and spin-orbit coupling) to favor the distribution in the emission of low ER electrons due to the increased size and atomic mass of Xe as well as the increased spin-orbit coupling in Xe (spin-orbit splitting in the P-core in Xe is 1.306eV) with the continuum

electron, possibly causing the P core to be rotated in the post collision process as compared to Ne (spin-orbit splitting is 0.185eV). The larger spin-orbit splitting in Xe will also affect the emission energy of the ionized electrons at threshold, since the $J=3/2$ core will ionize 1eV below the $J=1/2$ core. This introduces two non-degenerate core E_R energy dependent (dynamic) effects, which will complicate the picture, but may provide some interesting physics on the fine structure behavior in the ionization process.

Figures 4 show the SDCSs for Ne and Xe at different E_0 values. We note that for Xe, the SDCSs follow a similar form as for He, i.e., a concave distribution (or "smile"). On the other hand Ne is different. Apart from our $E_0=23.5\text{eV}$ results, which shows a somewhat flat SDCS, at $E_0=25\text{eV}$, 30eV and also at $E_0=40\text{eV}$ (not shown) the SDCSs are clearly of a convex nature (or "frown"). This suggests a favored overall equal energy sharing between the two outgoing electrons, even at higher energies (where it becomes more pronounced). We can guess for Ne that this could be possibly due to the polarization potential of the ion core aligning along the incident electron beam axis with the emitted energy sharing electrons following a path along the neutral lines of potential symmetrically on either side of the polarized orbital of the ion. For Xe, spin-orbit coupling could likely reduce this alignment, possibly letting electron-electron correlation between the outgoing electrons dominate and frustrate these electrons from coming out with equal energy. Again, an (e,2e) experiment or a theoretical model would be very useful here in shedding more details of the post-col-

lision process, hopefully to enable a better interpretation of the collision dynamics.

Finally, for Ne our TICSs at $E_0=23.5\text{eV}$ and 25eV (see tables 2a,b) compare excellently with those of [10,14] which we consider most reliable. At $E_0=23.5\text{eV}$, our TICS of $19.5\pm 4.1 \times 10^{-19} \text{ cm}^2$ is in excellent agreement with [10] of $20.1 \pm 1.4 \times 10^{-19} \text{ cm}^2$, and at 25eV our TICS of $36.5 \pm 8.0 \times 10^{-19} \text{ cm}^2$ is in excellent agreement with that of [10] of $37.8 \pm 2.7 \times 10^{-19} \text{ cm}^2$ and [14] of $37.7 \pm 3.8 \times 10^{-19} \text{ cm}^2$. At energies above these, we compared to the TICSs in the literature to check the normalization of our extrapolated continuum, as discussed earlier, so a meaningful comparison is not possible. For Xe, the observations are similar. At $E_0=14\text{eV}$, our TICS of $635\pm 145 \times 10^{-19} \text{ cm}^2$ is in excellent agreement with [10] of $569 \pm 40 \times 10^{-19} \text{ cm}^2$ and with [12] of $630 \pm 82 \times 10^{-19} \text{ cm}^2$. At 15eV our TICS of $932 \pm 179 \times 10^{-19} \text{ cm}^2$ is in excellent agreement with that of [10] of $902 \pm 63.1 \times 10^{-19} \text{ cm}^2$ and [12] of $100 \pm 13.0 \times 10^{-18} \text{ cm}^2$. Again at $E_0=20\text{eV}$, comparison with TICS is not possible for the same reasons stated above for Ne.

Conclusions

We present new measurements of doubly-differential cross sections for electron impact ionization of Ne and Xe below the first ionization threshold in order to compare the two targets. The scattered electron signal at the ionization continuum is determined accurately by our moveable source system [1,29] to obtain quantitative DDCSs for these systems at energies close to threshold. From our results, we clearly observe significant differences between the

two targets, and suspect the role of relativistic effects (spin-orbit and spin-exchange processes) and polarization to be responsible for these differences. We observe clearly, for the first time in the literature, convex SCDC profiles, in this case for Ne. However, also interesting is that the SDCS for Xe is instead concave i.e. similar to that well-known for He. It would be interesting to see (e,2e) experiments or a theoretical model to shed more light on this problem. We intend to continue this project to look at Ar and Kr to further see how the DDCSs and SDCS behave.

Acknowledgments.

This work was funded by the NSF under grant number RUI-PHY-0653450. Useful and important discussions with Drs. J. Gregory Childers and James Feagin (California State University Fullerton, California), Dr. James Colgan (Los Alamos National Laboratory, Mew Mexico) Dr. Nicholas L. Martin (University of Kentucky, Lexington, Kentucky) Dr. Don Madison (Missouri Institute of Technology, Rolla, Missouri) and Dr. Klaus Bartschat (Drake University, Des Moines, Iowa) are gratefully acknowledged.

References.

1. E. Schow, K. Hazlett, J. G. Childers, C. Medina, G. Vitug, I. Bray, D. V. Fursa and M. A. Khakoo, Phys. Rev. A 72, 062717 (2005).
2. A. Naja, E. M. Staicu Casagrande, A. Lahmam-Bennani, M. Stevenson, B. Lohmann, C. Dal Capello, K. Bartschat, A. Kheifets, I. Bray and D. V. Fursa, J. Phys. B: At. Mol. Opt. Phys. 41, 1 (2008)

3. A. N Bhoj and M. Kushner, J. Phys. D: Appl. Phys. 37, 2510 (2004).
4. R N Franklin 2003 J. Phys. D: Appl. Phys. 36, 2655 (2003).
5. V. M. Donnelly, Plasma Science, 28, 123 (2004).
6. P. Selles, J. Mazeau and A. Huetz, J. Phys. B: At. Mol. Opt. Phys. 23, 2613 (1990).
7. X. Guo, M. A. Khakoo, D. J. Mathews, G. Mikaelian, A. Crowe, I. Kanik, S. Trajmar, V. Zeman, K. Bartschat and C. J. Fontes, J.Phys. B. Letts., 32, L155 (1999).
8. O. Zatsarinny and K. Bartschat, J. Phys. B: At. Mol. Opt. Phys. 37, 2173 (2004).
9. A. J. Murray and F. H. Read, Phys. Rev. A 72, 062717 (2005).
10. D. Rapp and P. Englander-Golden, J. Chem. Phys. 43, 1464 (1965).
11. J. Fletcher and I. R. Cowling, J. Phys. B: At. Mol. Opt. Phys. 6, L258 (1973).
12. R. C. Wetzels, F. A. Baiocchi, T. R. Hayes and R. Freund, Phys. Rev. A. 35, 270 (1932).
13. D. Mathur and C. Badrinathan, Phys. Rev. A. 35, 1033 (1987).
14. E. Krishnakumar and S. K. Srivastava, J. Phys. B: At. Mol. Opt. Phys. 33, 1055 (1988).
15. S. Murray and F. H. Read, Phys. Rev. A. 63, 012714-1 (2000).

16. J. Rasch, C. T. Whelan, R. J. Allan, S. P. Lucey, and H. R. J. Walters, *Phys. Rev. A* 56, 1379 (1997).
17. A. C. F. Santos, A. Hasan and R. D. DuBois, *Phys. Rev. A* 71, 034701 (2005).
18. R. D. DuBois and M. E. Rudd, *Phys. Rev. A* 17, 843 (1978).
19. C. B. Opal, E. C. Beatty and W. K. Peterson, *At. Data* 4, 209 (1972).
20. D. W. Chang and P. L. Altick, *J. Phys. B: At. Mol. Opt. Phys.* 29, 2325 (1996).
21. R. Panajotovic, J. Lower and E. Weigold, *Phys. Rev. A* 73, 052701 (2006).
22. K. Bartschat, G. F. Hanne A. Wolke and J. Kessler, *Phys. Rev. Letts.* 47, 997 (1981).
23. J. G. Childers, D. B. Thompson and N. L. S. Martin, *Phys. Rev. A* 64, 062703 (2001).
24. J. G. Childers and N. L. S. Martin, *Phys. Rev. A* 66, 012709 (2002).
25. J. G. Childers, B. A. deHarak and N. L. S. Martin, *Phys. Rev. A* 69, 042713 (2004).
26. X. G. Ren, C. G. Ning, J. K. Deng, G. L. Su, S. F. Zhang and Y. R. Huang, *Phys. Rev. A* 73, 042714 (2006).
27. J. Childers, K. James, Jr., M. Hughes, I. Bray, M. Baertschy and M. A. Khakoo, *Phys. Rev. A: Rapid Comm.* 68, 030702R (2003).
28. J. G. Childers, K. E. James, Jr., Igor Bray, M. Baertschy and M. A. Khakoo, *Phys. Rev. A* 69, 022709 (2004).
29. M. Hughes, K. E. James, Jr., J. G. Childers and M. A. Khakoo, *Meas. Sci. and Technol.* 15, 841 (2003).
30. F. Pichou, A. Huetz, G. Joyez and M. Landau, *J. Phys. B* 11, 3683 (1978).
31. M. A. Khakoo, J. Wrkich, M. Larsen, G. Kleiban, I. Kanik, S. Trajmar, M. J. Brunger, P.J.O. Teubner, A. Crowe, C.J. Fontes, R. E. H. Clark, V. Zeman, K. Bartschat, D.H. Madison, R. Srivastava and A. D. Stauffer, *Phys. Rev. A* 65, 062711 (2002).
32. M. A. Khakoo, S. Trajmar, L. LeClair, I. Kanik, C. J. Fontes, R. E. H. Clark and J. R. Abdallah Jr., *J. Phys. B* 29, 3455 (1996).
33. D. F. Register, L. Vuskovic and S. Trajmar, *J. Phys. B: At. Mol. Opt. Phys.* 19, 1685 (1986).

Appendix
Near Threshold Electron Impact Doubly Differential
Cross Sections for the Ionization of Neon and Xenon

E_0 (eV) ? Angle (deg) ?	23.5eV	25eV	30eV	40eV
10	30.9	39.0	142.1	184.0
15	21.9	26.9	105.7	121.0
20	18.1	22.1	58.0	50.0
25	16.2	19.4	35.6	27.1
30	11.9	13.1	19.0	14.2
35	9.89	10.22	13.16	8.93
40	8.80	8.12	7.40	5.77
50	6.19	5.15	4.71	3.99
60	4.50	3.60	3.68	3.06
70	3.30	2.54	2.88	2.17
80	2.55	1.97	2.00	1.54
90	1.69	1.43	1.33	1.05
100	1.46	1.24	1.15	0.90
120	1.50	1.29	1.44	1.09
Error %	15.5	12.8	13.7	13.9

Table 1a

E_0 (eV) ? Angle (deg) ?	14eV	15eV	20eV
10	200	127	414
15	89.8	80.8	228
20	60.7	66.0	158
25	44.2	49.1	131
30	37.2	39.4	85.9
35	36.1	35.7	71.2
40	34.5	35.8	48.5
50	35.5	31.7	32.6
60	34.2	27.9	29.1
70	28.0	21.7	19.2
80	20.5	16.0	9.79
90	14.3	11.4	6.85
100	12.8	12.3	6.66
120	14.0	14.9	5.90
Error %	15.8	13.5	10.6

Table 1b

Table 1. Values of DCSs (used in this work for normalization) for the electron impact excitation of (a) Ne summed levels of the $2p^5 3s$ configuration and (b) the summed $6s[3/2]_2$ and $6s[3/2]_1$ levels (1^{st} half of the $5p^5 6s$ configuration) of Xe used. Units are $10^{-19} \text{cm}^2 \text{sr}^{-1}$. See text for discussion.

E_R (eV) ? Angle (deg) ?	1.9eV Error	1.5eV Error	0.7eV Error
15	1.94 0.38	1.78 0.35	1.12 0.47
20	2.03 0.39	1.81 0.35	1.42 0.45
25	2.14 0.46	2.03 0.43	1.88 0.51
30	2.02 0.38	2.09 0.41	1.94 0.56
35	2.37 0.50	2.46 0.51	2.06 0.58
40	2.46 0.50	2.62 0.60	2.12 0.58
50	1.99 0.38	2.16 0.44	1.94 0.56
60	1.94 0.36	1.76 0.38	1.94 0.50
70	1.94 0.38	1.73 0.35	1.80 0.47
80	1.87 0.35	1.91 0.42	1.92 0.50
90	1.46 0.30	1.43 0.27	1.66 0.44
100	1.40 0.27	1.37 0.28	1.69 0.45
120	1.28 0.23	1.18 0.26	1.38 0.41
SDCS	20.4 4.2	19.5 4.2	20.6 6.1
TICS	19.5 4.1		

Table 2a

E_R (eV) ? Angle (deg) ?	3.4eV Error	2.5eV Error	1.5eV Error	0.7eV Error
10	4.01 0.86	3.15 0.69	2.57 0.56	2.23 0.60
15	3.36 0.69	3.27 0.72	2.74 0.66	2.44 0.63
20	3.49 0.72	3.13 0.60	2.49 0.63	2.41 0.60
25	3.14 0.57	3.09 0.58	2.37 0.51	2.45 0.70
30	2.97 0.54	2.93 0.55	2.48 0.55	1.84 0.48
35	2.57 0.51	2.78 0.52	2.79 0.68	1.82 0.51
40	2.54 0.48	2.35 0.50	2.38 0.52	1.67 0.46
50	1.71 0.36	2.30 0.48	2.27 0.56	1.77 0.45
60	1.56 0.33	2.10 0.45	2.52 0.55	1.89 0.52
70	1.27 0.27	1.88 0.42	2.37 0.51	2.00 0.58
80	1.37 0.28	1.73 0.33	2.27 0.50	1.55 0.38
90	1.44 0.28	1.47 0.27	1.49 0.32	1.52 0.43
100	1.01 0.21	1.33 0.29	1.35 0.29	1.57 0.42
120	1.05 0.22	1.28 0.24	1.26 0.29	1.43 0.37
SDCS	19.0 4.0	22.0 4.6	22.8 5.4	20.5 5.6
TICS	36.5 8.0			

Table 2b

E_e (eV) ? Angle (deg) ?	8.4eV Error	7.5eV Error	6.5eV Error	5.5eV Error	4.5eV Error	3.5eV Error	2.5eV Error	1.5eV Error	0.7eV Error
10	15.0 2.5	12.8 2.2	11.6 2.1	10.1 1.8	7.35 1.31	5.51 1.03	3.19 0.62	2.04 0.44	1.70 0.39
15	10.3 1.8	10.5 1.8	9.00 1.67	6.82 1.47	6.23 1.06	4.89 0.87	2.77 0.53	1.62 0.34	1.66 0.35
20	6.85 1.22	7.44 1.36	6.84 1.14	6.07 1.08	5.28 0.93	4.08 0.73	2.41 0.44	1.63 0.31	1.68 0.34
25	5.23 0.93	5.70 1.08	5.20 0.93	4.88 0.89	4.53 0.83	3.65 0.70	2.61 0.46	1.76 0.30	1.72 0.31
30	3.37 0.63	3.62 0.67	3.82 0.67	3.55 0.66	3.48 0.61	3.09 0.56	2.33 0.41	1.71 0.32	1.78 0.30
35	3.33 0.63	3.39 0.57	3.39 0.59	3.33 0.55	3.03 0.55	2.71 0.48	2.21 0.44	1.64 0.32	1.67 0.26
40	2.07 0.38	2.22 0.42	2.38 0.43	2.40 0.45	2.39 0.41	2.30 0.48	2.12 0.37	1.60 0.29	1.31 0.25
50	1.61 0.27	1.84 0.33	2.03 0.34	1.95 0.33	2.02 0.36	2.06 0.40	1.85 0.34	1.68 0.31	1.27 0.22
60	1.57 0.28	1.89 0.37	2.19 0.38	2.29 0.39	2.37 0.48	2.42 0.48	2.32 0.42	1.89 0.35	1.60 0.31
70	1.14 0.22	1.32 0.26	1.60 0.34	2.21 0.38	2.22 0.37	2.25 0.39	2.36 0.39	1.67 0.34	1.80 0.34
80	1.36 0.23	1.45 0.26	1.67 0.31	1.95 0.37	1.96 0.33	2.14 0.40	2.11 0.40	2.11 0.38	1.79 0.39
90	0.969 0.193	1.10 0.20	1.25 0.22	1.43 0.24	1.55 0.28	1.88 0.32	1.88 0.38	1.73 0.39	1.99 0.39
100	0.807 0.142	1.04 0.19	1.27 0.23	1.36 0.26	1.49 0.29	1.68 0.29	1.74 0.30	1.67 0.29	1.67 0.26
120	0.753 0.137	1.01 0.20	1.37 0.23	1.38 0.28	1.51 0.29	1.68 0.27	1.75 0.33	1.72 0.31	1.62 0.29
SDCS	20.4 3.0	23.3 4.5	26.0 4.0	28.6 5.0	28.8 5.0	26.7 5.1	25.8 5.0	22.4 4.3	20.6 4.0
TICS	103.5 20.5								

Table 2c

E_e (eV) ? Angle (deg) ?	18.4eV Error	18eV Error	18eV Error	14eV Error	12eV Error	10eV Error	8.5eV Error	7eV Error
10	20.8 3.4	18.9 3.3	18.1 3.0	15.2 2.6	15.5 2.9	13.9 2.6	12.6 2.4	8.98 1.94
15	14.1 2.6	13.4 2.5	12.6 2.3	11.1 2.1	10.8 2.1	9.45 1.78	8.19 1.56	5.41 1.03
20	8.07 1.48	7.11 1.31	6.76 1.25	5.61 1.13	5.82 1.05	5.17 0.93	4.61 0.84	3.45 0.63
25	6.24 1.11	4.83 0.82	4.78 0.85	4.57 1.27	4.59 0.88	4.23 0.82	3.85 0.73	2.92 0.58
30	3.32 0.62	3.02 0.57	3.40 0.64	4.88 0.83	3.64 0.66	3.50 0.63	3.28 0.58	2.57 0.48
35	2.60 0.49	2.15 0.40	2.67 0.50	3.53 0.60	3.20 0.54	3.10 0.54	3.08 0.56	2.46 0.45
40	2.13 0.39	1.65 0.31	1.88 0.35	2.70 0.53	2.40 0.47	2.53 0.49	2.53 0.44	2.08 0.38
50	1.37 0.23	1.35 0.22	1.49 0.25	1.69 0.36	2.11 0.41	2.42 0.45	2.58 0.41	2.24 0.41
60	1.08 0.19	1.38 0.25	1.52 0.27	1.90 0.35	2.22 0.41	2.80 0.48	2.62 0.51	2.54 0.46
70	0.889 0.188	1.08 0.21	1.35 0.26	1.47 0.26	1.82 0.32	2.16 0.38	2.42 0.40	2.31 0.39
80	0.950 0.161	0.890 0.161	1.22 0.21	1.34 0.25	1.73 0.32	2.11 0.39	2.43 0.45	2.38 0.45
90	0.840 0.140	0.745 0.128	0.878 0.168	1.06 0.20	1.59 0.30	1.98 0.38	1.89 0.37	1.90 0.37
100	0.814 0.144	0.720 0.127	0.748 0.132	0.983 0.168	1.25 0.22	1.92 0.33	1.80 0.33	1.89 0.33
120	0.705 0.128	0.690 0.125	0.664 0.124	0.862 0.163	1.33 0.22	1.80 0.30	2.13 0.40	2.11 0.39
SDCS	20.5 3.9	19.7 3.7	20.5 3.8	24.5 4.7	27.1 5.2	30.8 5.8	30.8 5.9	28.7 5.5

E_e (eV) ? Angle (deg) ?	8eV Error	8eV Error	4eV Error	3eV Error	2eV Error	1.5eV Error	1eV Error	0.7eV Error
10	11.7 2.3	9.37 1.92	7.79 1.65	6.74 1.38	6.58 1.35	6.52 1.40	7.72 1.76	3.08 0.71
15	7.01 1.34	5.53 1.02	4.80 0.89	3.41 0.83	3.48 0.84	2.90 0.80	3.24 0.82	1.15 0.22
20	2.78 0.51	2.08 0.38	1.65 0.31	1.28 0.24	1.11 0.21	0.872 0.162	0.839 0.143	0.603 0.103
25	2.35 0.44	1.75 0.29	1.37 0.23	1.02 0.17	0.848 0.142	0.561 0.098	0.469 0.085	0.478 0.087
30	2.11 0.38	1.62 0.31	1.30 0.25	1.02 0.19	0.784 0.149	0.700 0.133	0.668 0.112	0.468 0.078
35	2.05 0.38	1.60 0.27	1.32 0.23	1.07 0.18	0.874 0.150	0.827 0.106	0.638 0.147	0.837 0.112
40	1.87 0.33	1.48 0.26	1.06 0.18	0.923 0.159	0.717 0.123	0.527 0.091	0.432 0.081	0.510 0.096
50	1.96 0.36	1.61 0.29	1.38 0.25	1.10 0.20	0.876 0.159	0.746 0.135	0.699 0.114	0.671 0.116
60	2.29 0.42	1.94 0.35	1.71 0.31	1.51 0.28	1.37 0.25	1.32 0.24	1.44 0.28	1.15 0.22
70	2.16 0.36	1.90 0.33	1.75 0.30	1.59 0.28	1.44 0.25	1.35 0.24	1.46 0.25	1.16 0.23
80	2.27 0.40	2.04 0.37	1.92 0.34	1.80 0.32	1.72 0.31	1.72 0.31	1.91 0.32	1.56 0.26
90	1.89 0.36	1.70 0.33	1.84 0.32	1.69 0.31	1.68 0.30	1.65 0.32	1.91 0.35	1.52 0.30
100	1.83 0.32	1.68 0.29	1.64 0.28	1.66 0.29	1.77 0.31	1.98 0.34	2.45 0.42	2.22 0.38
120	2.02 0.38	1.94 0.33	1.78 0.31	1.72 0.31	1.76 0.31	1.89 0.34	1.82 0.34	2.02 0.38
SDCS	29.2 8.6	25.2 4.8	23.7 4.5	21.5 4.1	20.3 3.9	20.7 3.9	19.3 3.7	16.1 3.5
TICS	227 45							

Table 2d

Table 2. (a-d). DDCSs, SDCSs and TICSs for the electron impact ionization of Ne. (a) $E_0=23.5\text{eV}$; (b) $E_0=25\text{eV}$; (c) $E_0=30\text{eV}$; (d) $E_0=40\text{eV}$. Units: DDCSs: $10^{-19}\text{cm}^2\text{sr}^{-1}\text{eV}^{-1}$; SDCSs: $10^{-19}\text{cm}^2\text{eV}^{-1}$; TICSs: 10^{-19}cm^2 .

E_0 (eV) ? Angle (deg) ?	1.5eV Error		1eV Error		0.7eV Error	
10	78.0	17.8	83.7	18.2	80.4	19.2
15	64.8	11.2	67.4	12.0	57.9	13.0
20	48.0	8.9	37.2	7.3	37.3	8.0
25	43.8	7.2	40.9	6.9	34.4	6.5
30	35.8	5.8	35.0	5.9	44.2	9.0
35	34.3	5.9	42.5	7.5	50.2	11.0
40	35.9	6.1	35.1	6.0	45.7	9.1
50	39.4	6.9	40.3	7.4	38.1	8.3
60	51.2	10.0	43.7	7.8	44.5	9.6
70	48.2	9.7	53.2	11.1	38.3	8.1
80	43.0	8.0	48.7	9.3	32.4	6.7
90	36.2	6.8	35.6	7.3	41.1	8.8
100	34.9	6.9	37.0	7.1	40.7	7.3
120	64.7	12.7	57.4	11.5	57.9	11.1
SDCS	670	131	643	129	673	146
TICS	835	146				

Table 3a

E_0 (eV) ? Angle (deg) ?	2.5eV Error		2eV Error		1.5eV Error		1eV Error		0.7eV Error	
10	62.8	12.3	55.7	10.8	50.0	9.3	43.0	8.0	35.2	7.0
15	58.4	11.3	53.3	10.2	44.4	8.1	37.8	6.9	33.5	6.5
20	58.7	10.6	52.5	9.5	48.3	8.7	40.4	7.5	31.0	5.7
25	55.8	10.0	46.1	8.1	45.3	7.9	39.2	7.0	32.0	5.7
30	46.4	8.0	40.7	6.9	38.9	6.2	34.8	6.0	24.7	4.3
35	39.3	6.8	35.6	6.1	34.4	5.8	31.6	5.5	25.1	4.4
40	35.8	8.2	35.0	5.9	28.2	4.9	25.7	4.4	18.5	3.2
50	41.1	7.0	39.1	6.5	42.3	7.0	35.4	6.0	26.0	4.4
60	48.6	8.2	45.3	7.5	44.4	7.3	43.1	7.3	39.6	6.7
70	44.1	7.4	41.6	6.9	42.9	7.1	45.8	7.7	45.3	7.6
80	43.0	7.1	39.6	6.4	41.0	6.6	42.6	7.0	45.6	7.5
90	37.0	6.2	37.1	6.0	34.9	5.7	38.6	6.4	46.9	7.8
100	45.0	7.6	44.3	7.3	47.1	7.7	55.6	9.3	54.2	9.1
120	58.0	9.5	57.0	9.2	56.4	9.0	63.5	10.4	70.7	11.6
SDCS	630	115	597	108	600	107	632	115	676	124
TICS	932	179								

Table 3b

E_0 (eV) ? Angle (deg) ?	7.5eV Error		7eV Error		6eV Error		5eV Error		4eV Error		3eV Error		2eV Error		1eV Error		0.7eV Error	
10	112	23	69.22	16.18	78.0	14.5	89.1	13.0	48.9	9.3	41.0	7.7	39.6	7.3	38.3	7.0	36.3	7.0
15	121	26	110	21	83.9	17.2	72.7	13.3	69.3	12.6	52.7	11.7	59.5	10.9	56.3	10.1	52.6	9.6
20	129	34	122	22	96.6	17.9	67.4	16.1	78.2	14.4	70.1	12.4	67.1	11.9	67.1	10.1	63.6	9.4
25	141	26	127	22	106	16.45	83.2	16.6	84.9	15.1	77.6	13.1	69.6	11.9	58.1	9.7	53.0	9.1
30	108	16	102	17	93.4	15.7	76.9	13.8	72.6	13.5	60.5	9.9	54.6	8.8	50.5	8.3	48.8	8.1
35	103	16	87.84	16.1	86.7	14.71	76.0	13.2	65.6	11.5	57.8	9.0	52.8	8.5	49.9	7.3	45.1	7.5
40	77.8	13.9	74.4	12.6	66.7	11.25	58.0	10.0	49.5	8.6	41.2	8.8	34.1	5.5	28.6	4.6	28.0	4.6
50	68.3	11.8	64.5	10.1	59.0	11.75	53.1	8.0	45.2	7.7	36.1	8.2	38.9	6.1	36.3	6.2	34.0	5.9
60	72.6	12.2	72.5	12.0	69.4	11.36	64.1	10.6	58.5	9.8	54.4	8.7	52.7	8.6	57.8	9.3	49.2	9.6
70	56.3	9.6	56.7	9.36	57.4	9.4	57.6	9.8	58.0	9.8	57.8	9.3	57.3	9.0	56.4	9.1	56.1	9.0
80	27.9	4.3	32.1	5.79	31.5	5.1	32.5	5.4	36.3	6.0	35.7	5.6	34.0	5.3	33.7	5.3	44.5	7.0
90	27.8	4.6	27.8	4.52	27.7	4.5	27.4	4.5	27.4	4.5	28.3	4.6	30.6	4.7	35.2	5.6	37.0	5.8
100	26.4	5.2	32.2	5.30	31.9	5.2	30.6	5.1	31.4	5.1	32.0	5.3	35.0	5.5	43.9	6.9	44.0	7.8
120	29.3	4.8	30.1	4.84	31.6	5.1	33.4	5.5	30.9	5.6	38.6	6.2	44.0	6.9	52.0	8.1	54.1	6.4
SDCS	625	115	603	109	576	103	558	102	639	98.61	632	99.27	547	94.24	568	105	603	106
TICS	2260	420																

Table 3d

Table 3 (a-c). DDCSs, SDCSs and TICSs for the electron impact ionization of Xe.

(a) $E_0=14\text{eV}$; (b) $E_0=15\text{eV}$; (c) $E_0=20\text{eV}$. Units are same as for Table 2.

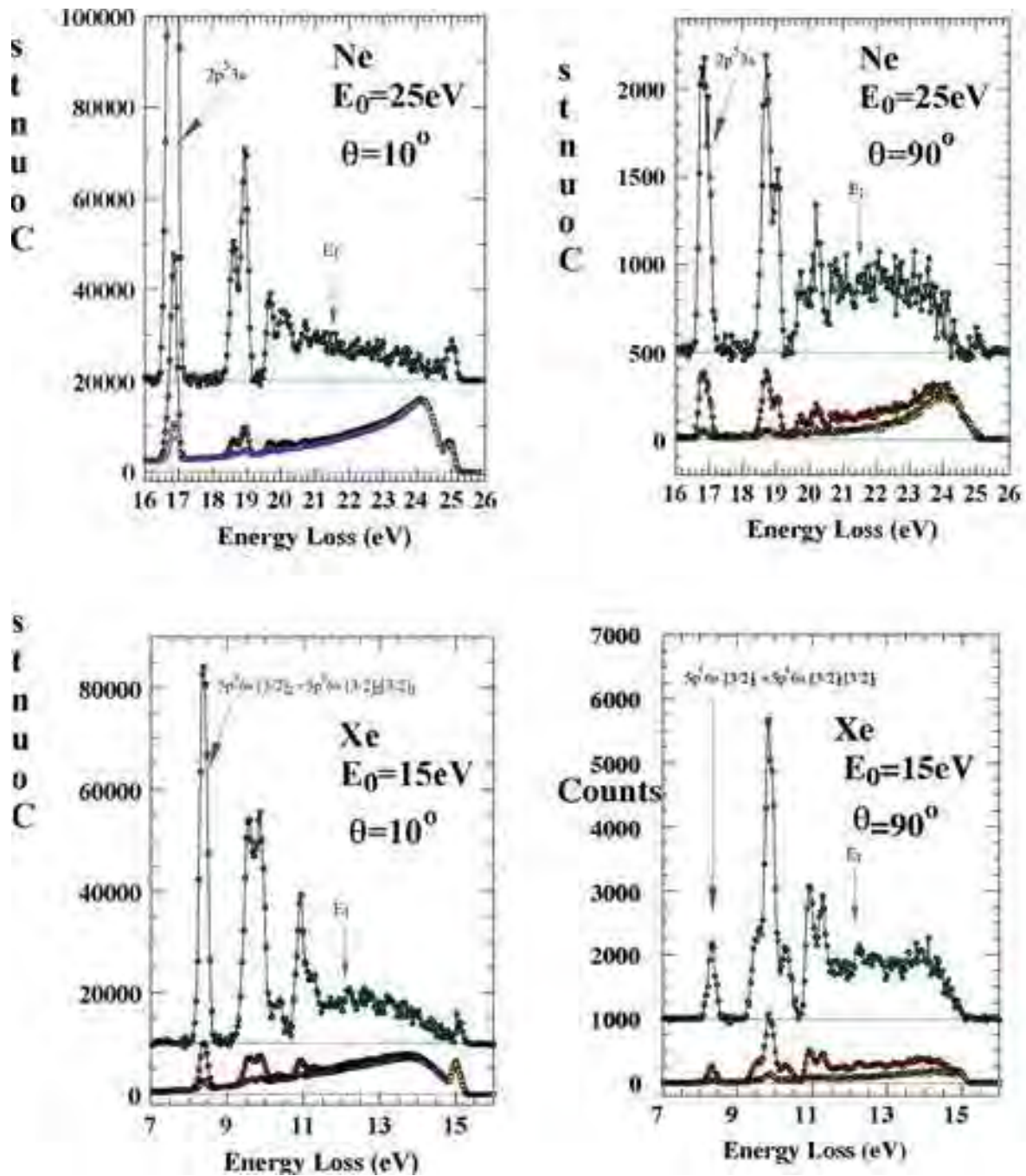


Figure 1. Electron energy loss spectra of Ne and Xe taken at scattering angles of 10° and 90° . Legend: Gas beam aligned with e^- beam (Signal+Background); Gas beam out of alignment with electron beam (Background); Signal+Background spectrum minus Background spectrum (Signal only; $\times 5$ and offset from original spectra). The location of the normalization inelastic peak and the ionization potential (E_i) are arrowed and baselines are indicated by horizontal lines.

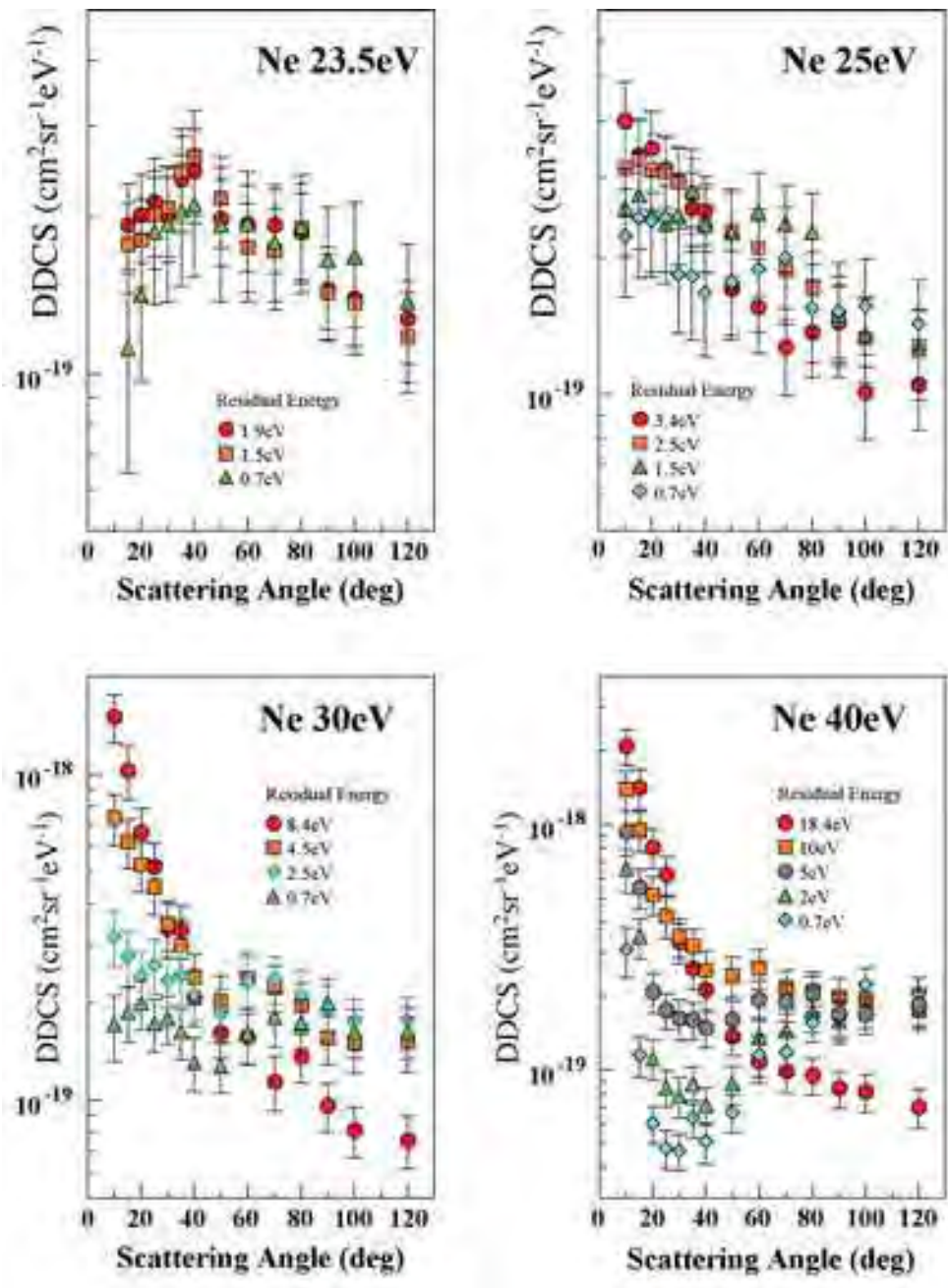


Figure 2. DDCSs for electron impact ionization of Ne at different E_0 values and for selected residual energies E_R .

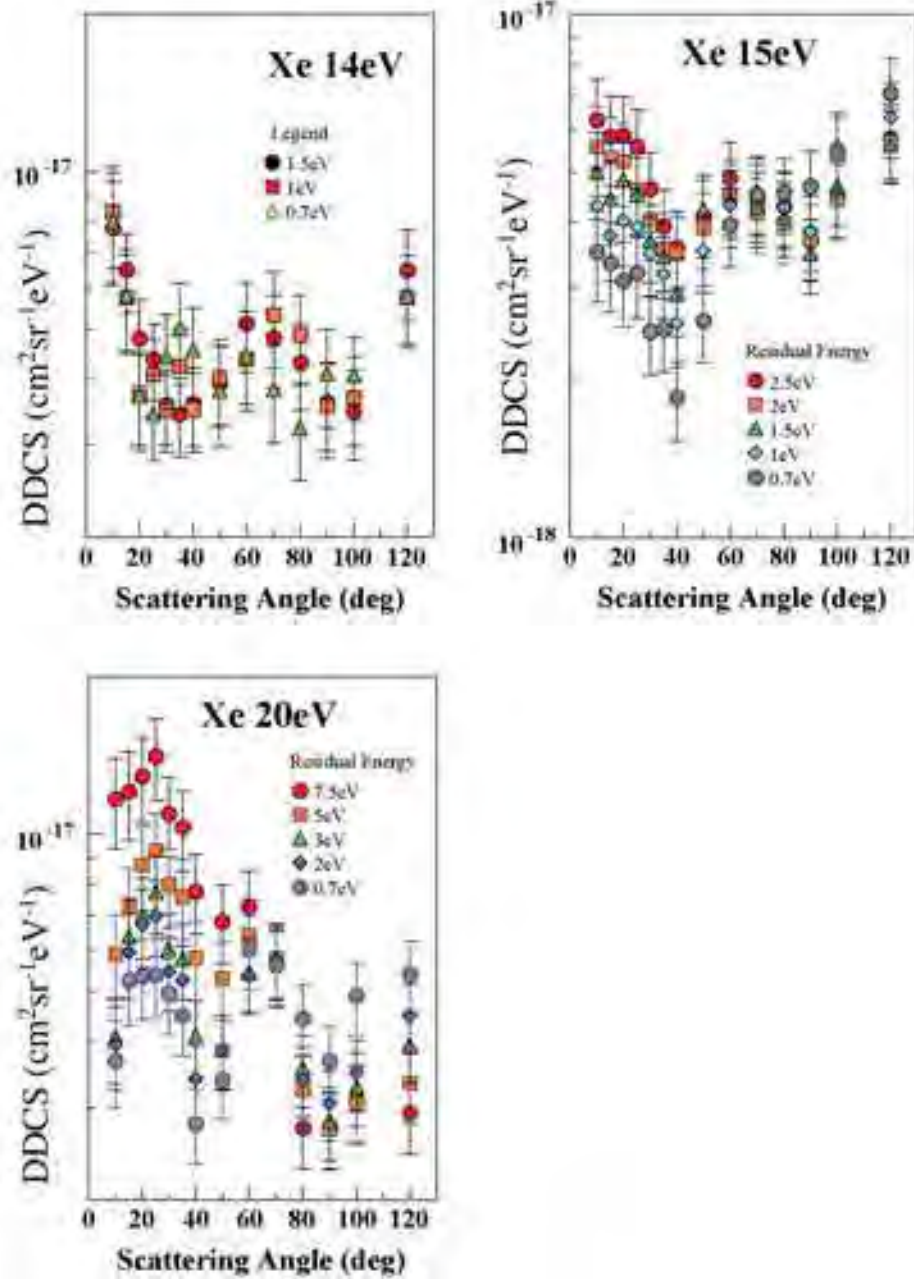


Figure 3. DDCSs for electron impact ionization of Xe at different E_0 values and for selected residual energies E_R .

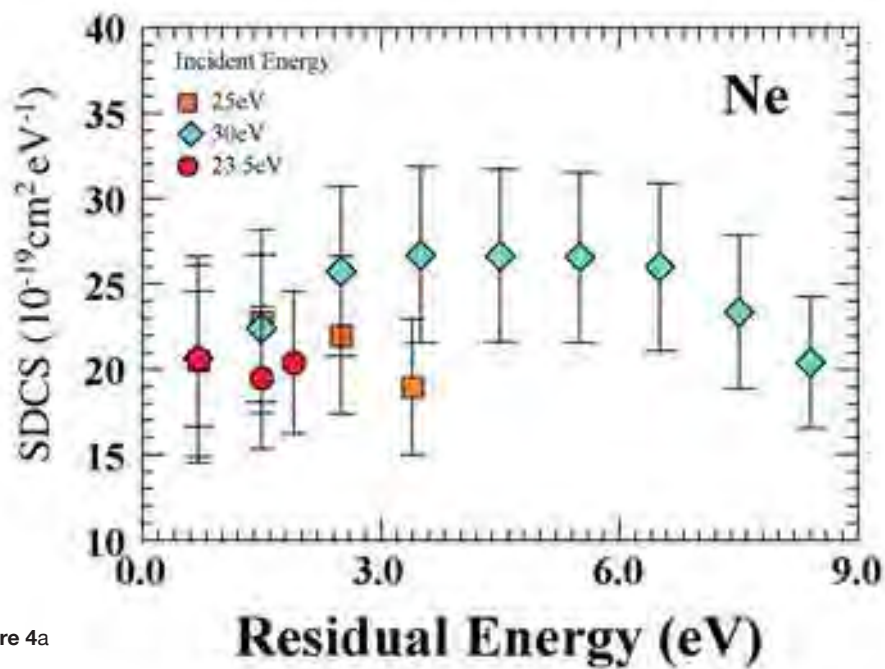


Figure 4a

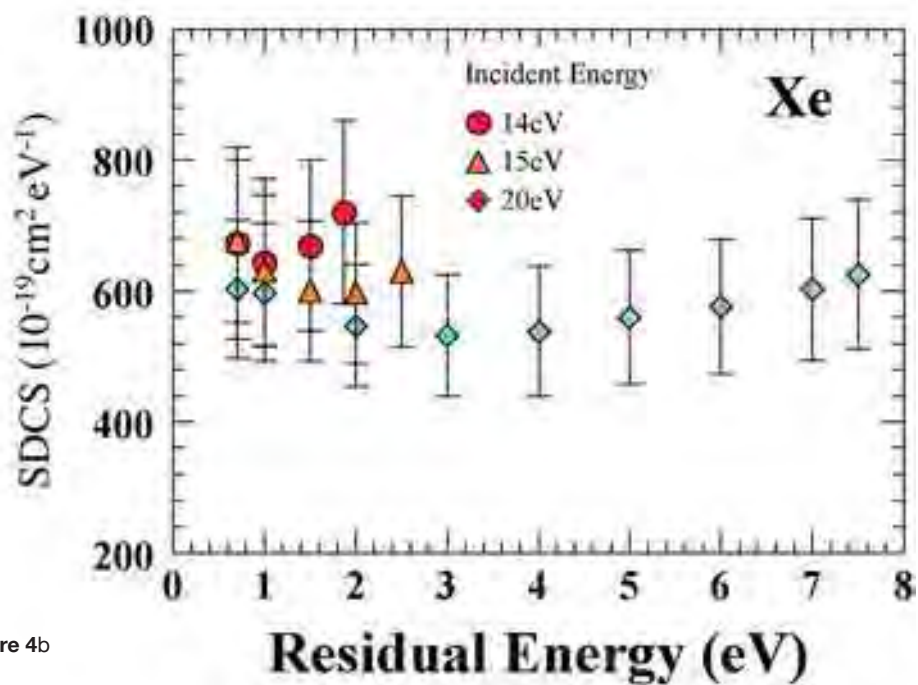


Figure 4b

Figure 4. SDCSs for Ne and Xe at different incident energies. Whereas the SDCS absolute error bars are around 20%, the averaged relative (shape) errors are around 15% See text for discussion.

► Dimensions 2009 Author Biographies



Doreen Emilee Carpio will graduate from California State University, Fullerton in the spring of 2009 with a Bachelor's Degree in Biological Science. Her publication focusing on an antisense strategy to combat bacterial resistance was a direct result of the ten weeks she spent conducting research in Argentina during the summer of 2008 in the Minority Health and Health Disparities International Research Training (MHIRT) Program. Her study was also presented in January of 2009 at the CSU Program for Education and Research in Biotechnology (CSUPERB) symposium in Los Angeles, California. She is currently conducting research on the physiological and anatomical importance of heart anatomy in endothermic fishes in the laboratory of Dr. Kathryn Dickson. Doreen's love of science and children

has caused a strong aspiration to one day become a compassionate pediatrician.



Allyson L. Degrassi is a transfer student from Saddleback Community College where she earned an Associate degree in Environmental Studies. Allyson was accepted into the Southern California Ecology Research Program (SCERP) summer 2008. The works presented here are products of her summer SCERP research projects. In researching with mentor Dr. Kathryn Dickson, Allyson presented on the effects of delayed hatching on the development of grunion larvae at the 2008 Southern California Conference for Undergraduate Research (SCCUR) at Cal Poly Pomona, CA. She is currently working with mentors Dr. Jayson Smith and Dr. Steven Murray

on native and non-native macroalgal nutritional content and their effect on energy budgets of native consumers on urban southern California shores. Allyson will graduate from the Biological Science department spring 2010 with a concentration in marine biology and plans to attend graduate school in the near future.



Carmen J. Cortez was born and raised in Lynwood CA. She is a senior majoring in biological science with a concentration in biodiversity, ecology, and conservation biology. In her third year she was selected to participate in the U.S. Department of Education Ronald E. McNair Post Baccalaureate Achievement Program where she had the opportunity to work with Dr. Sandra A. Banack on an ethnobotanical study

in Mexico. Her participation in this program facilitated her admission to the Southern California Ecosystems Research Program funded by NSF, where she now works with Dr. Darren R. Sandquist on a restoration ecology project working with *Eriastridium densifolium* spp. *sanctorum* and endangered species of the Santa Ana floodplain. Aside from participating in internal research programs, Carmen was also selected to be a scholar for the University of Florida-University of Cape Coast NSF-REU where she conducted research in Ghana, West Africa with Dr. Peter K. Kwabong. Additionally, she worked with Dr. Kevin J. Rice as a scholar for the Summer Undergraduate Research Program at UC Davis. Carmen has been admitted to the Ph.D. graduate group in ecology at UC Davis and the department of botany at the University of Hawaii at Manoa. Her goal is to continue her education and research in ethnoecology and conservation biology and mentor underrepresented students in the sciences as a future professor.



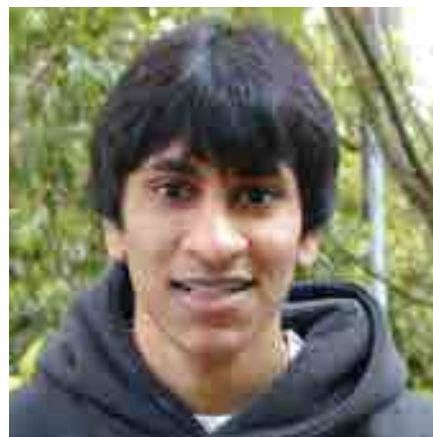
Kimberly Nelson is a biological sciences major in the concentration of biodiversity ecology and conservation at California State University, Fullerton. She is a scholar with

the National Science Foundations UMEB program, the Southern California Ecosystems Research Program (SCERP), run by Dr. Bill Hoese and Dr. Darren Sandquist. As a SCERP scholar, she investigated multiple ecosystems as a summer course and engaged in her own two year research project with Dr. Paul Stapp as her mentor investigating the effects of anthropogenic water inputs on Argentine ant invasion of riparian areas at Starr Ranch Audubon Sanctuary. In the summer of 2008, she participated in the Environmental Scientific Research in Thailand Program, directed by Dr. Richard Deming. In Thailand, she worked with Dr. Chitchol Phalaransk as her advisor in the aquatic insect's laboratory from Chiang Mai University, Thailand and Dr. Richard Deming as her advisor from California State University, Fullerton. She investigated the using of aquatic insects as bioindicators for sustainable water use at three water reservoirs in the village of Ban Pu located in the Li district of Thailand. Kimberly is a proud mother of her daughter Ashley, and is graduating from California State University, Fullerton in May 2009.



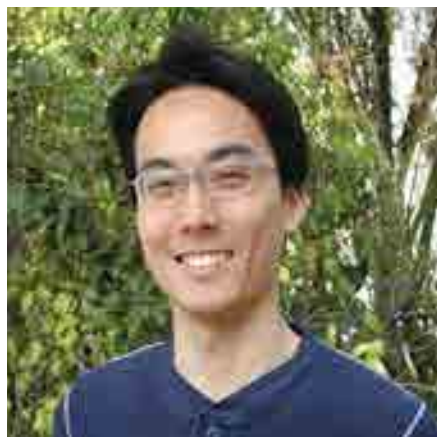
Tracie A. Treybig is a senior at CSUF pursuing a Biological Science

degree in biology with an emphasis in biodiversity, ecology and conservation. She is expected to graduate in spring 2010. Tracie has been a scholar in the Southern California Ecology Research Program (SCERP) since summer 2008. She has presented a poster on the developmental effects of delayed hatching on grunion fish at the National Society for the Advancement of Chicanos and Native Americans in Science conference at Salt Lake City, Utah, in 2008. She is working with mentor Dr. Kathy Dickson to investigate the effects delayed hatching has on grunion larval muscle and skeleton development, and feeding performance. She is especially zealous about the impact humans are making on wildlife and the ecosystem. She aspires to pursue a career in conservation biology to make a lasting impact on the world. She plans to earn a masters or Ph.D in the future.



Tejas Bondade is a senior who will graduate in May from CSUF with a Bachelor of Arts. in Religious Studies and a minor in Chemistry. He has been working in Dr. Kantardjieff's research group since spring 2008. Prior to research in computational biochemistry, he has worked on a protein crystallography project. He is currently involved in designing

Alzheimer's therapeutics using structure guided drug design by means of virtual screening and molecular dynamics.



Steven Hoang was born in the winter of 1981. He studied English with a preference for Old English and literature before Early Modern English. He worked in a clinical research lab at UCLA where he realized that he wanted to make a positive impact on how the medical system worked. He entered CSUF seeking a biochemistry degree in which he hopes will lead to a career in bioethics, policy, and regulation. He spends countless hours drawing and writing in a notebook; you'll never find him without a pen handy.



Dale Dailey will be receiving his B.S. in Geological Science in May. For the last two years, Dale has

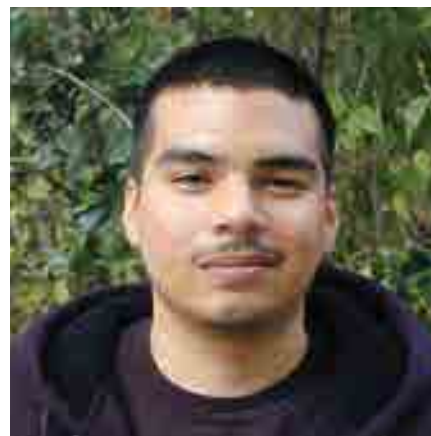
worked diligently with Dr. Richard Laton and Dr. John Foster in the Geological Information Systems lab researching the hydrogeology of the Mojave Desert. In spring of 2008, Dale was awarded the Groundwater Resources Association Scholarship for his undergraduate contributions to the field of Hydrogeology. His research was also presented at the Groundwater Association of California's Collegiate Groundwater Colloquium in September of 2008 and published in *Ground Water*® magazine in early 2009. After graduation, Dale plans on attending Western Michigan University to pursue his Master's degree in Hydrogeology.



Melissa Nunley is an undergraduate student whose major is geology with a minor in mathematics. She will be graduating in spring of 2009. Her plans include receiving her doctorate in geophysics/seismology, while continuing to go more depth in the research she presented in this issue of *Dimensions*. In the future she would like to increase the awareness of the residents in Southern California on the dangers and precautions that should be taken while living near faults that may produce major earthquakes.



Christine Martin is a Math major and will be graduating in May 2009. She plans on getting her single subject teaching credential at CSUF, and eventually attending the masters program at CSUF in the near future. As a teacher she plans on getting her students more involved with math by teaching them some of the history that is behind it.



Ernesto Casillas Jr. is an undergraduate Biological Science major at CSUF. Currently he is a research fellow in the Southern California Ecosystems Research Program, an NSF-funded undergraduate training program. This publication describes the results for one of three SCERP projects that were carried out during the summer of 2008. Ernesto works with faculty mentor Dr. Danielle Zacherl and has extensive experience in the field of larval ecology. He has worked as the lead research on a project that studies the long-

term spatial and temporal variation in larval settlement of the estuarine Olympia oyster, *Ostrea lurida*, the only oyster species native to the west coast of the United States. He is now in the process of developing his multidisciplinary SCERP project that will incorporate ecology, physiology and genetics to study how metals are transported and sequestered within various body organs of the marine gastropod *Kelletia kelletii*. After he completes his B.S., Ernesto plans on attending graduate school to receive his PhD.



Meredith Raith graduated from California State University, Fullerton in spring 2008. While an undergraduate she was accepted into the Southern California Ecosystems Research Program, which allowed her to become familiar with ecological research. From there she joined the laboratory of Dr. Danielle Zacherl lab working in marine environments studying various intertidal organisms. With the completion of her undergraduate degree she spent a semester in Washington studying oceanographic changes within the San Juan Islands. She is now pursuing her graduate degree at CSUF in the Zacherl lab. Her research consists of looking at the taxonomic relationships between various species of oyster belonging to the genus *Ostrea* within the Gulf of California. With

the completion of her graduate degree she wants to pursue work in the conservation and restoration of natural habitats.

Alyssa Rodd is a senior at California State University, Fullerton. She is a member of the school's Honor's Program and a recipient of the Dan Black Scholarship in Physics. She will graduate in Spring 2010 with a BS in physics.

Brent Yates will be graduating in spring 2009 with a Bachelor of Science in Physics and a minor in Computer Science. He has been working with Dr. Murtadha Khakoo since January 2008 researching Low Energy Electron Impact Scattering. Brent has done various tasks in Dr. Khakoo's lab from maintaining equipment to data analysis. After receiving his Bachelor of Science Brent will be continuing his education at California State University, Fullerton for a Master of Science in Physics. He also hopes to earn a Ph.D. in Physics in the future.

Po-Yu Fang grew up in Taiwan. He is pursuing his Bachelor of Science in Biochemistry and expects to graduate in May 2009. He was a member of Dr. Richard Deming and Dr. Karn Sorasaene's research group. His research project was an investigation of the binding affinity of an Iron (III) corrole complex with pyridine and imidazole derivatives. He presented a poster at the 236th ACS National Meeting & Exposition. In addition, Po-Yu also served as both treasurer and event coordinator of the Taiwanese Student Association. Upon graduation, he plans to attend graduate school, and hopes to work in the cosmetics industry in the future.

Dimensions 2009 California State University, Fullerton ► Editors



Top (from left): Troy Cannon, Ali Forghani, Ricardo Ulloa
Bottom (from left): Bahar Ajdari, Kelly Kathe, Joyce Park, Yareli Sanchez